UNIVERSIDAD COMPLUTENSE DE MADRID

FACULTAD DE CIENCIAS FÍSICAS
Departamento de Física Teórica I

TESIS DOCTORAL

Medida de parámetros cosmológicos a partir de los datos de Dark Energy Survey
Measurement of cosmological parameters using data from Dark Energy Survey

MEMORIA PARA OPTAR AL GRADO DE DOCTOR

PRESENTADA POR

Francisco Javier Sánchez López

Director

Eusebio Sánchez Álvaro

Madrid, 2015

Departamento de Investigación Básica
Centro de Investigaciones Energéticas, Medioambientales y Tecnológicas

y

Departamento de Física Teórica I
Facultad de Ciencias Físicas, Universidad Complutense de Madrid

Medida de parámetros cosmológicos a partir de los datos de Dark Energy Survey

Measurement of cosmological parameters using data from Dark Energy Survey

Presentado por
Francisco Javier Sánchez López
para la obtención del grado de Doctor en Física

Dirigido por:
Dr. Eusebio Sánchez Álvaro

Madrid, 9 de Febrero de 2015

Contents

Agradecimientos

La gratitud es la memoria del corazón

Lao Tse

Ciertamente, cuando se termina un trabajo como el de tesis doctoral, uno se da cuenta de lo mucho que debe a numerosas personas. Son muchas las acciones y decisiones puntuales que llevan a una persona a ser quien es y estar donde está, pero sin la ayuda de otras personas, es complicado avanzar y más en un campo tan difícil como la investigación científica.

Me gustaría agradecer especialmente a Eusebio por haberme dado la oportunidad de trabajar con él, por ser más que un director, un amigo. Pienso que me ha ayudado mucho en estos cuatro años y su dedicación ha sido admirable. Gracias por la formación científica y por el enriquecimiento personal que ha supuesto para mí el conocer la historia del CIEMAT a partir de las diversas anécdotas compartidas en los *meetings* de colaboración. Espero que podamos seguir trabajando juntos en el futuro. P.D: Perdón por las más de 70 cartas de recomendación que te he hecho escribir hasta la fecha. También quisiera agradecer a los habitantes del Edificio 2 por su gran acogida durante estos años y al Departamento de Investigación Básica por la oportunidad que me ha otorgado y que me ha abierto puertas que nunca pensé que pudiera abrir. En especial, quiero agradecer a Javier Calonge, Antonio (apareces dos veces), Juanjo y Miguel Cárdenas porque sin su trabajo, yo no podría hacer el mío. También gracias a Sonia por hacer que los trámites burocráticos no sean un infierno y por su gran ayuda. Gracias a Pablo García por darme la oportunidad de dar charlas en institutos lo cual ha sido una gran experiencia para mí. También quiero agradecer al resto del grupo porque sin su ayuda todo mi trabajo no sería posible.

Quiero agradecer a mis colaboradores/sospechosos habituales, David Alonso, al que admiro profundamente y agradezco su ayuda y amistad, creo que además debo agradecer a Mark Zuckerberg por permitirnos hacer algún artículo a través de Facebook; Juan, al que le debo mil gracias por las miles de cartas de recomendación para los *postdoc* que me ha escrito, incluso en fechas intempestivas. Gracias también por contagiar al grupo su enegía y ambición científica y por su magnífico trato durante estos años. Gracias a Nacho S. por toda la ayuda prestada y por tus sabios consejos. Asimismo, agradecer a Ana por su amistad y su apoyo en los momentos difíciles, que los ha habido; también quiero desearte lo mejor para tu tesis y que Pusheen sea contigo, sabes que me puedes seguir mandando gatos y perros varios y te seguiré ayudando en lo que pueda. Gracias a Rafa por ser un becario jefe *chachi* y compartir su sabiduría y anecdotario conmigo. También agradecer a mi predecesor en el cargo, Aurelio, gracias por tus consejos y amistad. Hemos pasado buenos ratos en los *meetings* de colaboración. También quiero agradecer a los disintos miembros de la colaboración DES y, en especial, al grupo de Barcelona de DES-Spain. Gracias a Enrique, Martín y Ramón por su apoyo y valiosos consejos y perdón también por las molestias a la hora de pedir cartas de recomendación (es que la cosa está difícil).

I also want to give special thanks to the people in Fermilab. Special thanks to Scott Dodelson for his great advisory and hosting. I was really comfortable and I found a great work environment there.

Ahora vienen los agradecimientos poco serios (en la forma, no en el fondo). Quiero agradecer a la diversa

fauna (y Gran Nacho C., que no es fauna) que ha compartido este periodo de tesis conmigo: a Bruno, con el que me meto mucho porque es la felicidad en persona, mis mejores deseos y sigue trabajando en ese MC, a Cristina *que nos guía* que se sobrepuso a toda adversidad, a Carmen que amenizaba el despacho con el *Single Ladies* de Beyoncé por aquel entonces, al Gran Nacho C., por su gran sabiduría, su amistad y consejos; a Carlos, alias *el inge*, por ser un gran amigo y por contagiar al resto del grupo esa competitividad y ambición, además por ser un gran defensa, pieza fundamental en ese título de fútbol sala que ganamos. Gracias a Manu por descubrirme grandes vídeos como *Colibritany* y por *indexar* Youtube todos los días. Gracias a Jorge por su ayuda y su buen hacer en el equipo. Gracias a Adrián y José por proveernos de gran sabiduría en el *spam* y las comidas. Gracias a Isabel, que aunque la pobre está siempre de *shift* en el CERN ameniza nuestras vidas con esos vídeos de APM que no tienen precio. Al gran M.A. (no Barracus) que a pesar de ganar premios neutrino al ser indetectable, va ganando presencia (se está acoplando a nuevos campos) y gracias a Antonio por sus goles para el título liguero y sus grandes conversaciones en las comidas (valedoras de un premio). Gracias a *mi becario* Manuelinho, espero que te vaya genial en tu tesis y que sigas el camino que has empezado, mucho ánimo. Ya sabes que para cualquier cosa, me puedes contactar por Facebook y espero que podamos seguir trabajando juntos en el futuro. Gracias a Mariano, bueno, mejor, no gracias por darle vidilla al grupo (sabes que te odiamos). Gracias a Julia por los momentos compartidos. Y a las nuevas incorporaciones: Mar, Diana y Sara, mucha suerte con el camino que habéis empezado, tenéis a vuestro lado un gran equipo de gente y os deseo lo mejor. Gracias al gran Albertismo (alias Escalante), gracias por tu amistad, por tus goles y por esos momentos compartidos. Quiero también decir muchas gracias al gran Edu y la gran Bárbara, por su amistad, apoyo, alegría, revisiones de tesis y consejos varios, por las sesiones de juegos de mesa y karaoke y un larguísimo etcétera que resumo en un muchas gracias.

Gracias también a mi amigo Miguel G., por su amistad y ayuda durante este tiempo. Gracias a mis amigos y *compis* de piso Cristian, David y Mariana, la verdad es que sin vuestro apoyo y amistad no sería lo que soy hoy en día, quien tiene un amigo, tiene un tesoro, y con vosotros tengo uno, y grande. Además, hemos pasado grandes momentos durante este tiempo juntos y espero que os vaya fenomenal y podamos seguir en contacto (espero ir a vuestras respectivas bodas).

Gracias Amanda por tu apoyo incondicional y por tu gran ayuda durante estos últimos meses, sin ti hubiera sido muy complicado avanzar tan rápido como lo he hecho y estar donde estoy, tu ayuda ha sido fundamental, gracias por abrirme las puertas de tu vida. Thanks a lot!

Gracias a mis padres y a mi hermano por toda su ayuda y su apoyo en los momentos buenos, los regulares y los malos, no hay palabras para agradecer vuestra labor durante estos años, por inculcarme los valores que tengo hoy en día y por hacer que el tiempo que paso en casa siempre nos parezca poco. Muchas gracias.

Summary

The worthwhile problems are the ones you can really solve or help solve, the ones you can really contribute something to. No problem is too small or too trivial if we can really do something about it.

R. P. Feynman

The identity of dark energy presents one of the most challenging problems of modern physics. It is responsible for the accelerated expansion of the Universe; however, its defining characteristics are still unknown. Since the discovery of the accelerated expansion of the Universe, the science community is taking great strides, through large collaborations, to shed light on the nature of this elusive form of energy. One of these collaborations is the Dark Energy Survey (DES) (see Chapter 4) in which most of this work has been developed.

The main goal of this thesis is to face the dark energy problem through the study of the large-scale structure of the Universe and to propose new methodologies in order to get some answers about the nature of dark energy, most of it whithin DES. In this thesis several new techniques are presented. These include estimating the transition to homogeneity and fractality of the galaxy distribution in photometric redshift surveys, extracting the scale of the baryon acoustic oscillations in the line-of-sight, extracting cosmological parameters from the angular correlation function in photometric redshift surveys, and a method to estimate the correlation function in a variable-depth survey.

The structure of this work is the following: in Chapter 1 we introduce the ΛCDM model which is the current most widespread to describe the observable Universe. The next one, Chapter 2, gives an introduction to the study of the large-scale structure of the Universe. Chapter 3 addresses the methods developed in this thesis and their results on simulations. Chapter 4 describes the Dark Energy Survey, where most of this work has been developed, and Chapter 5 shows the results of the cosmological measurements for the Science Verification data from DES and the results of the correlation function in a variable-depth data selection. Finally, Chapter 6 gives some concluding remarks about this work.

Chapter 1

The Standard Model of Cosmology: ΛCDM

Big Bang! This is the widely accepted cosmological model for the early development of the Universe. First proposed by Georges Lemaître in 1927 [1], based on Friedmann's equations[1] and confirmed by Hubble's law [2], Big Bang Nucleosynthesis [3], Cosmic Microwave Background (CMB) observations by Penzias and Wilson [4] is the central piece that constitutes the Standard Cosmological Model, namely ΛCDM. It relies on the Big Bang, the inflationary paradigm, the General Theory of Relativity, the Cosmological Principle and the properties of the different components existing in the Universe. This model is in good agreement with observations from very different sources such as light element abundances, type Ia Supernovae brightness, Baryon Acoustic Oscillations (BAO) and the aforementioned CMB.

In this chapter we will describe the ΛCDM model: first we will discuss the Cosmological Principle in section 1.1, then we will focus on the basics of General Relativity in section 1.2. After that, we will describe another ingredient in the standard model of cosmlogy, inflation, in section 1.3. In section 1.4 we will describe the observational basis of the ΛCDM model. Finally, we will discuss the topic of distances in cosmology in section 1.5.

1.1. The Cosmological Principle

Most of the modern cosmological theory is built upon the Cosmological Principle: the hypothesis that all positions and directions in the Universe are essentially equivalent. This homogeneity of the Universe has to be understood in the same sense as homogeneity in a gas: it does not apply to the Universe in detail, but only to a *smeared-out* Universe averaged over large enough regions to include a representative sample of galaxies. At these, and larger scales, the Universe is homogeneous and isotropic. The Cosmological Principle can be formulated as a statement about the existence of equivalent coordinate systems. Suppose that we use the cosmic standard coordinate system to carry out astronomical observations, determining the metric tensor $g_{\mu\nu}$, the energy-momentum tensor $T_{\mu\nu}$, and all other cosmic fields, as functions of the cosmic standard coordinates x^μ. A different set of space-time coordinates x'^μ may be considered equivalent to the cosmic standard coordinates [5], if the whole history of the Universe appears the same in the x'^μ coordinate system as in the cosmic standard coordinate system. That is, at any coordinate point we must have:

$$g_{\mu\nu}(x) = g'_{\mu\nu}(x') \tag{1.1}$$

[1] Lemaître arrived to these equations independently

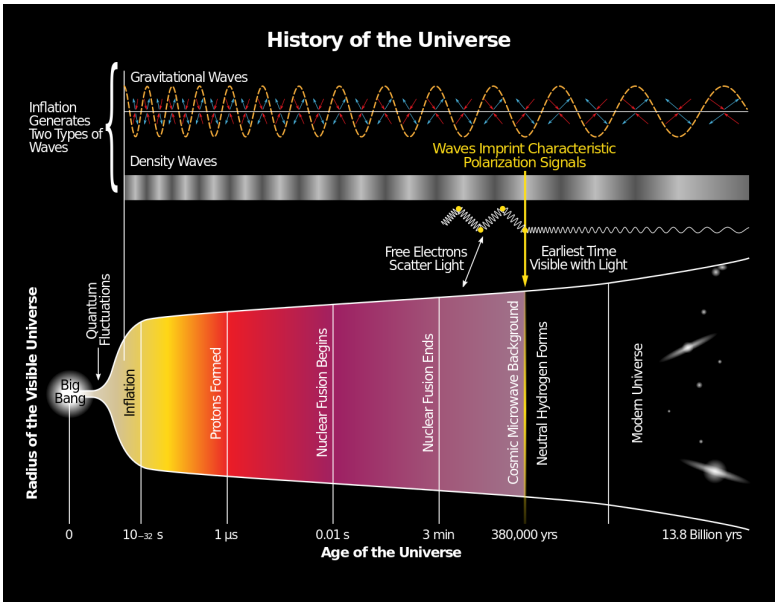

Figure 1.1: Current picture of the evolution of the Universe according to the Standard Model of Cosmology.

$$T_{\mu\nu}(x) = T'_{\mu\nu}(x') \tag{1.2}$$

That is, the coordinate transformation $x \to x'$ must be an isometry and $T_{\mu\nu}$ and so on, must be form-invariant under this transformation. In particular, equation 1.2 will have to hold for the scalar S used to define the cosmic standard time t. Since S is by definition a function only of t, and a scalar, the equation 1.2 reads

$$S(t') = S'(x') = S(x) = S(t) \tag{1.3}$$

and so

$$t' = t \tag{1.4}$$

All coordinate systems that are equivalent to the cosmic standard system necessarily use cosmic standard time. Thus, we can separate the metric into the spatial and temporal parts.

1.2. The General Theory of Relativity and the Friedmann-Lemaître-Robertson-Walker (FLRW) metric

The General Theory of Relativity [6] appeared as a consequence of the incompatibility of Newton's Gravitational theory, which assumes instantaneous action, and the Special Theory of Relativity [7]. This theory is based on:

- The Principle of covariance: Physical laws must have the same form in every coordinate system.
- The Principle of equivalence: Special Relativity laws apply locally for every inertial observer.

The theory states that any presence of matter or energy affects the curvature of the space-time and the mass-energy dynamics, that is:

$$R_{\mu\nu} - \frac{1}{2}Rg_{\mu\nu} + \Lambda g_{\mu\nu} = \frac{8\pi G}{c^4}T_{\mu\nu} \tag{1.5}$$

Where $R_{\mu\nu}$ is the Ricci tensor, R the Ricci scalar, $g_{\mu\nu}$ the metric tensor, $T_{\mu\nu}$ the energy-momentum tensor, G is the gravitational constant and c the speed of light in vacuum. Given a perfect fluid the energy-momentum tensor $T_{\mu\nu}$ can be written as:

$$T_{\mu\nu} = (\rho + p)\, u_\mu u_\nu + p g_{\mu\nu} \tag{1.6}$$

Where ρ is the energy density, p the pressure, and u_μ the *four-velocity*. The most general metric that satisfies the Cosmological Principle can be written as[8]:

$$ds^2 = -dt^2 + a^2(t)\gamma_{ij}(u)du^i du^j \tag{1.7}$$

In spherical coordinates, assuming that the space is spherically-symmetric (isotropy of Cosmological Principle):

$$\gamma_{ij}du^i du^j = e^{2\beta(r)}dr^2 + r^2\left(d\theta^2 + \sin^2\theta d\phi^2\right) \tag{1.8}$$

being $\beta(r)$ an arbitrary function. The spatial part of the Ricci tensor can be written as:

$${}^{(3)}R_{ji} = 2k\gamma_{ij} \tag{1.9}$$

The superscript ${}^{(3)}$ indicates that we are referring to the spatial part only. γ_{ij} is the maximally symmetric metric of the three-dimensional space.

Using the definition of the Ricci tensor we can obtain:

$${}^{(3)}R_{11} = \frac{2}{r}\partial_1\beta(r) \tag{1.10}$$

$${}^{(3)}R_{22} = e^{-2\beta(r)}\left(r\partial_1\beta(r) - 1\right) \tag{1.11}$$

$${}^{(3)}R_{33} = \sin^2\theta\left[e^{-2\beta(r)}\left(r\partial_1\beta(r) - 1\right) + 1\right] \tag{1.12}$$

Thus,

$$\beta = \frac{-1}{2}\ln\left(1 - kr^2\right) \tag{1.13}$$

$$ds^2 = -dt^2 + a^2(t)\left[\frac{dr^2}{1-kr^2} + r^2\left(d\theta^2 + \sin^2\theta d\phi^2\right)\right] \tag{1.14}$$

Equation 1.14 is the so called Friedmann-Lemaître-Robertson-Walker metric (FLRW) which is invariant under $k \to k/|k|$, $r \to \sqrt{|k|}r$ and $a \to a/\sqrt{|k|}$, so the relevant parameter becomes $k/|k|$, usually written as k, with values 1, 0 and -1 that describes a closed, flat and open Universe respectively.
This metric allows different normalizations given by the scale factor $a(t)$. It is common to choose it equal to 1, i.e., $a(t_0) = 1$, at the present time. The specific evolution of $a(t)$ depends on the field equations and the equation of state of each component. The Einstein Field Equations for this metric describe a Universe filled with an ideal fluid:

$$\frac{\dot{a}^2}{a^2} + \frac{k}{a^2} - \frac{\Lambda}{3} = \frac{8\pi G}{3}\rho \tag{1.15}$$

$$2\frac{\ddot{a}}{a} + \frac{\dot{a}^2}{a^2} + \frac{k}{a^2} - \Lambda = -8\pi G p \tag{1.16}$$

Or equivalently,

$$\frac{\ddot{a}}{a} = -\frac{4\pi G}{3}\left(\rho + 3p\right) \tag{1.17}$$

The equations 1.15 and 1.17 are the so-called Friedmann equations. If we define the Hubble parameter $H(a) \equiv \frac{\dot{a}}{a}$ we have:

$$H^2 = \frac{8\pi G}{3}\rho - \frac{k}{a^2} + \frac{\Lambda}{3} \tag{1.18}$$

Using 1.18 and the conservation of energy we can write:

$$\dot{\rho} = -3\frac{\dot{a}}{a}(\rho + p) \tag{1.19}$$

If radiation, matter and energy are barotropic fluids we can define:

$$w \equiv \frac{p}{\rho} \tag{1.20}$$

with a different value for each component. The solution of equation 1.19 is given by:

$$\rho \propto a^{-3(1+w)} \tag{1.21}$$

The value for w depends on the nature of the fluid:

- For a pure non-relativistic *matter* fluid we have $p = \rho_m C^2$, and $C = \sqrt{RT}$ the speed of the matter via thermal scattering. As long as we consider non-relativistic cold matter, $C \ll c$ so $w \approx 0$ and $\rho_m \propto a^{-3}$.
- For *radiation*, $p = 1/3\rho$ thus, $\rho_{rad} \propto a^{-4}$.
- For the *Cosmological Constant*, Λ, using equations 1.18 and 1.19 we see that $p = -\rho$, as long as Λ is constant. Thus, $\rho_\Lambda \propto a^0$.
- For Curvature: In the equation 1.18, the term $-ka^{-2}R_0^{-2}$ behaves like energy density therefore, $\rho_k \propto a^{-2}$.

We can also define the critical density ρ_c. The expression for the critical density is found by assuming Λ to be zero and setting the normalised spatial curvature k equal to zero. Then, using 1.18 we find:

$$\rho_c \equiv \frac{3H_0^2}{8\pi G} \tag{1.22}$$

Moreover, densities of different species are usually expressed using the so-called density parameter Ω_i. It is defined as the ratio of the observed density ρ_i to the critical density ρ_c for each one of the different species: matter, radiation, curvature... We define, as well, the total density parameter Ω as the ratio of the total density to the critical density $\Omega \equiv \rho/\rho_c$. This parameter determines the overall geometry of the Universe. When $\Omega = 1$ the Universe is flat (Euclidean). If $\Omega < 1$ space sections of the Universe are open and if $\Omega > 1$ space sections of the Universe are closed. So we can rewrite the first Friedmann equation 1.18 as follows:

$$H(a)^2 = H_0^2\left(\Omega_{m,0}a^{-3} + \Omega_{\Lambda,0} + \Omega_{rad,0}a^{-4} + \Omega_{K,0}a^{-2}\right) \tag{1.23}$$

Where the subindex 0 denotes the value of each component at the present time. We will drop the use of this subindex for the remainder of this work because, unless otherwise stated, we will refer to present values of each one of these quantities in this thesis. These density parameters have been evolving with time.

The current accepted model of evolution is depicted in Figure 1.2. This scheme summarizes the influence of each component in different epochs in the history of the Universe from the first fraction of a second to the present day. However, it lacks the description of the very beginning of the Universe. Cosmic inflation does this job.

1.3. The Inflationary paradigm

In physical cosmology, cosmic inflation, or just **inflation**, is the period of exponential expansion of the early Universe [9] (see Figure 1.3). Inflation was proposed by Alexei Starobinski [10] (1979/80) in the Soviet Union, and simultaneously by Alan Guth[11] (1980/81) in the United States. These are the *old inflation* models. The modern version of the theory was developed by Andrei Linde [12], and by Andreas Albrecht and Paul Steinhardt[13], which are dubbed as *new inflation*. Inflation is proposed as a solution to some caveats present in the standard Big Bang cosmology which are the flatness problem, the horizon problem, the origin of large-scale structure in the Universe and the monopole problem.

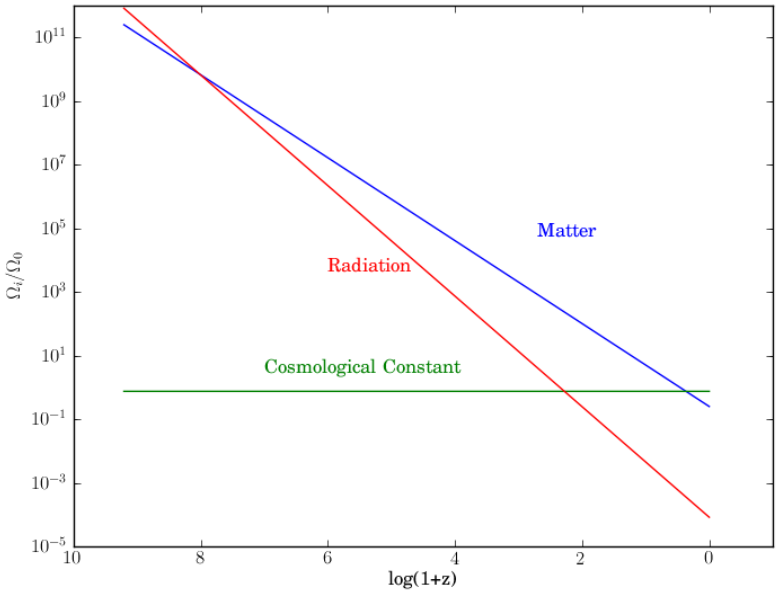

Figure 1.2: Evolution of the radiation, matter and Λ density parameters with time. We can appreciate three different eras: Radation dominated epoch, Matter dominated epoch and DE dominated, depending on the dominant density.

Flatness problem

Present observations show that Ω is very close to 1 at the present time [15], which implies Ω to be unnaturally close to 1 in the past. For example, we require $|\Omega - 1| < \mathcal{O}(10^{-16})$ at the epoch of nucleosynthesis [16] and $|\Omega - 1| < \mathcal{O}(10^{-64})$ at the Planck epoch [17]. This is an extreme fine-tuning of initial conditions. Unless initial conditions are chosen very accurately, the Universe soon collapses, or expands quickly before the structure can be formed. This is the flatness problem.

$$\Omega - 1 = \frac{k}{a^2 H^2} \tag{1.24}$$

If $\Omega = 1$ it remains the same. If $\Omega \neq 1$, then $\Omega = \Omega(t)$. In the matter-dominated epoch:

$$a \propto t^{2/3}, H \propto t^{-1} \Rightarrow |1 - \Omega| \propto t^{2/3} \tag{1.25}$$

And, in the radiation-dominated era:

$$a \propto t^{1/2}, H \propto t^{-1} \Rightarrow |1 - \Omega| \propto t \tag{1.26}$$

Thus, we need some mechanism to avoid this problem or to ensure this extreme fine-tuning.

Horizon problem

Let us define the particle horizon $D_H(t)$ where the light travels from the beginning of the Universe, $t = t_\star$,

$$D_H(t) = a(t) d_H(t), \; d_H(t) = \int_{t_\star}^{t} \frac{dt}{a(t)} \tag{1.27}$$

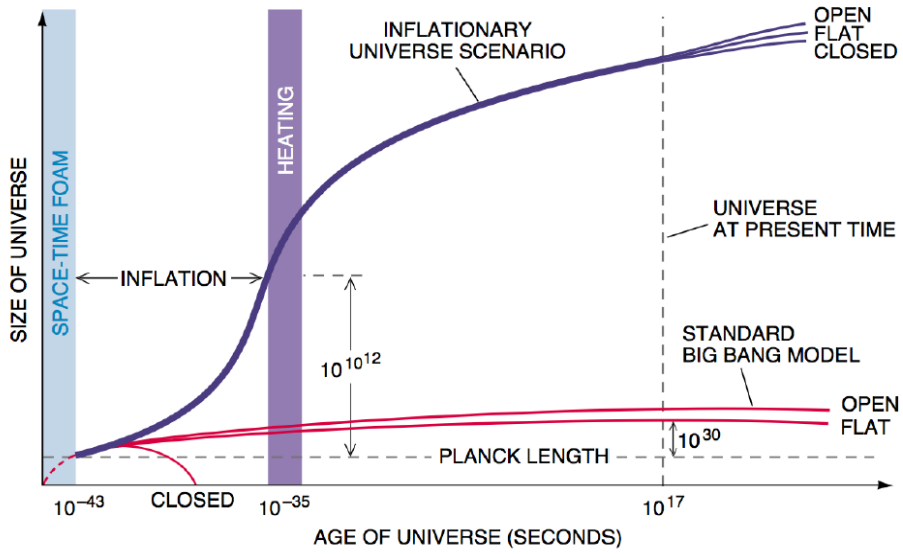

Figure 1.3: Scheme of the evolution of the Universe[14]. We can see the exponential expansion in its very early times.

Where $d_H(t)$ is called comoving distance. Setting $t_\star$=0 we find $d_H(t) = 3t$ in the matter-dominant era. On the other hand, we can observe photons in the CMB emitted at the time of decoupling. The particle horizon at decoupling $D_H(t_{dec})$ corresponds to the region where photons could be causally connected at that time. But we know that:

$$\frac{d_H(t_{dec})}{d_H(t_0)} = \left(\frac{t_0}{t_{dec}}\right)^{1/3} \approx 10^{-2} \tag{1.28}$$

This result implies that the causality regions of photons are restricted to be small. In fact the last scattering surface[2] only corresponds to the angle of order 1°. However, we can observe that photons thermalize to the same temperature in all regions of the Cosmic Microwave Background sky. Finding an explanantion for this extreme isotropy is the horizon problem.
Inflation solves each and every of these problems based on the existence of a period with an exponential expanding Universe. In the following subsection we are going to describe its physics.

1.3.1. Basics of inflation

Inflationary dynamics

Inflation is a period of exponential expansion that fulfills:

$$\ddot{a} > 0 \Rightarrow \rho + 3p < 0 \Rightarrow \frac{d}{dt}\left(aH\right)^{-1} < 0 \tag{1.29}$$

Since we know that inflation ends at some point, the inflationary epoch must be controlled by a dynamic vacuum energy different from Λ. Then, we need a scalar field called the *inflaton* field ϕ. The inflaton action is defined

[2]The last scattering surface corresponds to the source points of the photons we observe in the CMB.

by:

$$S = \int d^4x\sqrt{-g}\left[\frac{1}{2}R + \mathcal{L}_\phi\right] \tag{1.30}$$

Where the lagrangian $\mathcal{L}_\phi$ is given by:

$$\mathcal{L}_\phi = -\frac{1}{2}g^{\mu\nu}\left[\partial_\mu\phi\partial_\nu\phi - V(\phi)\right] \tag{1.31}$$

For FLRW metric, $\sqrt{-g} = a^3$, applying Euler-Lagrange equations to the action we obtain:

$$\ddot{\phi} + 3H\dot{\phi} - \frac{1}{a^2}\nabla^2\phi + V'(\phi) = 0 \tag{1.32}$$

This exponential expansion of the space introduces the term $3H\dot{\phi}$ analogous to a classic friction term with viscosity H.

Also, the energy-momentum tensor of the inflaton is:

$$T^{\mu\nu} = \frac{2}{\sqrt{-g}}\frac{\delta(\sqrt{-g}\mathcal{L}_\phi)}{\delta g^{\mu\nu}} = \partial_\mu\phi\partial_\nu\phi + g_{\mu\nu}\mathcal{L}_\phi \tag{1.33}$$

From where we can extract:

$$\rho = T^{00} = \frac{1}{2}\dot{\phi}^2 + V + \frac{1}{2a^2}\left(\nabla\phi\right)^2 \tag{1.34}$$

$$p = T^{ii} = \frac{1}{2}\dot{\phi}^2 - V - \frac{1}{6a^2}\left(\nabla\phi\right)^2 \tag{1.35}$$

The inflaton ϕ is an homogeneous field, that implies:

$$\frac{\nabla\phi}{a} \to 0 \tag{1.36}$$

This happens at the beginning of inflation. Then, we can write:

$$\rho = \frac{1}{2}\dot{\phi}^2 + V(\phi), \qquad p = \frac{1}{2}\dot{\phi}^2 - V(\phi). \tag{1.37}$$

Where $V(\phi)$ is the potential of the inflaton. If we use equations 1.18 and 1.19 we obtain:

$$H^2 = \frac{8\pi}{3m_{pl}^2}\left[\frac{1}{2}\dot{\phi}^2 + V(\phi)\right] \tag{1.38}$$

$$\ddot{\phi} + 3H\dot{\phi} + V'(\phi) = 0 \tag{1.39}$$

where $G = 1/m_{pl}^2$ and we have neglected the curvature term since conclusions are not affected and calculations become simpler. During inflation:

$$w_\phi = \frac{p}{\rho} = \frac{\dot{\phi}^2/2 - V}{\dot{\phi}^2/2 + V} \tag{1.40}$$

Moreover, $V \gg \frac{\dot{\phi}^2}{2}$ thus, $w_\phi \sim -1$ that implies exponential expasion. $\dot{\phi}$ is maximum when:

$$\frac{\partial V}{\partial\phi} = V'(\phi) = -3H\dot{\phi} \tag{1.41}$$

At this pont:

$$\dot{\phi} = -\frac{V'(\phi)}{3H} \tag{1.42}$$

Since H is very large during inflation compared to V' it implies that the value of $\dot{\phi}$ is small. This occurs as long as the slow-roll approximation is valid:

$$\frac{\dot{\phi}^2}{2} \ll V \rightarrow H^2 \approx \frac{8\pi}{3m_{pl}^2} V(\phi) \tag{1.43}$$

$$\ddot{\phi} \ll 3H\dot{\phi} \Rightarrow 3H\dot{\phi} \approx -V'(\phi) \tag{1.44}$$

Defining the slow-roll parameters as:

$$\epsilon \equiv \frac{m_{pl}^2}{16\pi}\left(\frac{V'}{V}\right)^2, \qquad \eta \equiv \frac{m_{pl}^2}{8\pi}\frac{V''}{V} \tag{1.45}$$

The approximation in 1.43 is valid when:

$$\epsilon \ll 1, \qquad |\eta| \ll 1 \tag{1.46}$$

The inflationary phase ends when ϵ and $|\eta|$ grow up to order of unity. A useful quantity to describe the amount of inflation is the number of e-foldings defined by:

$$N \equiv \ln \frac{a_f}{a_i} = \int_{t_i}^{t_f} H(t)dt \tag{1.47}$$

Where subscripts i and f denote values at the beginning and ant the end of inflation, respectively.

To solve the flatness problem it is required that $|\Omega_f - 1| \leq 10^{-6}$ and assuming $H \approx const$ during inflation we have:

$$\frac{|\Omega_f - 1|}{|\Omega_i - 1|} \approx \left(\frac{a_i}{a_f}\right)^2 = e^{-2N} \tag{1.48}$$

Then $N \geq 70$ is required to solve the flatness problem and a similar value is required to solve the horizon problem.

These are the basic dynamics of inflation. The concrete behaviour depends on the model. Some examples of potential of the inflaton are:

- Chaotic inflation $\rightarrow V(\phi) = \frac{1}{2}m^2\phi^2$ or $V(\phi) = \frac{1}{4}\lambda\phi^4$
- Natural inflation $\rightarrow V(\phi) = m^4\left[1 + \cos\left(\frac{\phi}{f}\right)\right]$
- Hybrid inflation $\rightarrow V(\phi) = \frac{\lambda}{4}\left(\chi^2 - \frac{M^2}{\lambda}\right)^2 + \frac{1}{2}g^2\phi^2\chi^2 + \frac{1}{2}m^2\phi^2$ where we have two fields ϕ and χ.

Solution to the horizon problem

Since the scale factor evolves exponentially during inflation, the physical wavelength, $a\lambda$ grows faster than the Hubble radius, $H^{-1}(\propto t)$. The physical wavelength is pushed outside the Hubble radius so the causality region is stretched on scales much larger than the Hubble radius, thus solving the horizon problem. After inflation, Hubble radius begins to grow faster than the physical wavelength. So it is required that the following condition is satisfied:

$$\int_{t_\star}^{t_{dec}} \frac{dt}{a(t)} \gg \int_{t_0}^{t_{dec}} \frac{dt}{a(t)} \tag{1.49}$$

This implies that the comoving distance that photons can travel before decoupling need to be much larger than after decoupling. This solves the horizon problem.

Models of inflation

Nowadays inflation has a very wide variety of models: R^2, new, chaotic, extended, power-law, hybrid, natural, supernatural, extranatural, eternal, D-term, F-term, brane, oscillating, trace-anomaly driven... [9].

This zoo of models can be classified as follows:

- **Type I** or large field models. These models have a large initial value of the inflaton field ϕ and it rolls down toward the potential minimum at low values of the inflaton field.
- **Type II** or small field models where inflaton field is initially small and then, it evolves toward the potential minimum at larger values of the inflaton field.
- **Type III** or hybrid/double inflation model. In these models inflation typically ends by phase transition triggered by the presence of a second scalar field.

1.3.2. Reheating

After the end of inflation, the Universe enters in the so-called *reheating* stage. In this era, the energy of the inflaton field is transferred to radiation and matter, and the Universe is thermalized. The reheating scenario was originally described by the decay of the inflaton using perturbation theory [9]. Later, it was found that the existence of nonperturbative stage called *preheating* can lead to explosive particle production in a very early stage of reheating [18].

The reheating stage starts when the inflaton reaches the potential minimum and begins to oscillate. Reheating consists of three stages:

1. A preheating stage where particles are produced in a non-perturbative way. The inflaton oscillates coherently and these oscillations produce particles [9].
2. The amplitude of these oscillations decreases, not only due to the expansion of the Universe, but also because of the energy transfer to particles created by the oscillating field. The interaction of the inflaton with the particles produced at earlier stages produces more particles.
3. Thermalization of produced particles.

1.3.3. Consequences of Inflation

Inflation is a mechanism for realizing the cosmological principle. In addition, it accounts for the observed flatness and uniformities. WMAP CMB analysis [19] and Planck CMB analysis [15] shows that the Universe is flat to an accuracy of at least a few percent, and that it is isotropic to a part in 100,000.

In addition, inflation predicts that the structures which do exist in the Universe today formed through the gravitational collapse of perturbations that were formed as quantum mechanical fluctuations in the inflationary epoch. The detailed form of the spectrum of perturbations, a nearly-scale-invariant Gaussian random field, is very specific and has only two free parameters, the amplitude of the spectrum and the spectral index, which measures the slight deviation from scale invariance predicted by inflation. Inflation predicts that the observed perturbations should be in thermal equilibrium with each other. This structure for the perturbations has been confirmed by the WMAP spacecraft and other cosmic microwave background experiments [19] and galaxy surveys [20]. These experiments have shown that the observed inhomogeneities have exactly the form predicted by theory. Moreover, there is evidence for a slight deviation from scale invariance. The spectral index, n_s is equal to one for a scale-invariant spectrum. The simplest models of inflation predict that this quantity is between 0.92 and 0.98 [21, 22]. From the data taken by Planck, $n_s = 0.9667 \pm 0.0040$ [15] ruling out exact scale invariance at over 5σ. These are considered important confirmations of the inflationary theory.

Inflation also predicts the existence and value of the so-called *B-modes* of the polarization of the CMB. Measurement of B-modes could provide evidence of the gravitational radiation produced by inflation, and could also show whether the energy scale of inflation predicted by different models is correct. Although it is unclear if the signal will be visible, or if contamination from foreground sources will interfere with these measurements. Forthcoming measurements, such as those of 21 centimeter radiation (radiation emitted and absorbed from neutral hydrogen before the first stars turned on), may measure the power spectrum with even greater resolution than the cosmic microwave background and galaxy surveys, however it is not known if these measurements will be possible or if interference with radio sources on earth and in the galaxy will be too high [23].

1.4. Observational basis of the Standard Model

The success of the ΛCDM model resides on being able to explain very different observables such as the existence and structure of the Cosmic Microwave Background [15], the large-scale structure in the distribution of galaxies, the light-elements abundances (H, He, Li), and the accelerating expansion of the Universe. In addition, the model has made a number of successful predictions such as the existence of the Baryon Acoustic Oscillation (BAO) feature[3], the polarization of the CMB, and the statistics of the weak gravitational lensing.

1.4.1. CMB

The cosmic microwave background is the oldest light we can observe in the Universe. It was emitted when the photons decoupled from baryons in the primordial baryon-photon plasma when the Universe was ~ 380000 years old ($z_{dec} \sim 1100$), when the temperature of the Universe was about 3000 K, corresponding to about 0.25 eV. This energy does not correspond to the ionization energy of the hydrogen, 13.6 eV. This is due to the fact that the number density of photons is much larger than the number density of baryons. When the energy spectrum of photons is typically represented by a Blackbody, at 13.6 eV there are a lot of photons with energies higher than 13.6 eV that can ionize the hydrogen atoms. However, in a Blackbody distribution with a peak at 0.25 eV, even the tail of the distribution would not reach sufficient energy values to ionize hydrogen.

Precise measurements of the CMB are critical to cosmology since small variations on the model could have a great impact on the CMB. The CMB has a thermal black body spectrum at a temperature of 2.72548 ± 0.00057 K [15]. The temperature of the background radiation has evolved since the emission of the CMB as:

$$T_r = 2.72548(1 + z) \tag{1.50}$$

The spectral distribution $dE_\nu/d\nu$ peaks at 160.2 GHz (see Figure 1.4) in the microwave range of frequencies. The CMB shows a nearly uniform pattern in all directions (isotropy), but the tiny residual variations show a very specific pattern. In particular, the spectral distribution at different angles of observation in the sky contains small anisotropies, which vary with the size of the region examined. They have been measured in detail, and match what would be expected if small thermal variations, generated by quantum fluctuations of matter in a very tiny space, had expanded to the size of the observable Universe we see today. Although many different models might produce the general form of a black body spectrum, no model other than the Standard Model has yet explained the fluctuations.

The CMB was first predicted in 1948 by Alpher and Herman [25], and Gamow[26] to understand the production of light elements. They were able to estimate the temperature of the CMB to be 5K. This prediction was rediscovered by Zel'dovich in the early 1960s [27]. The first detection of the CMB was made by Penzias

[3]BAO will be explained in full detail later in this work, in section 2.2

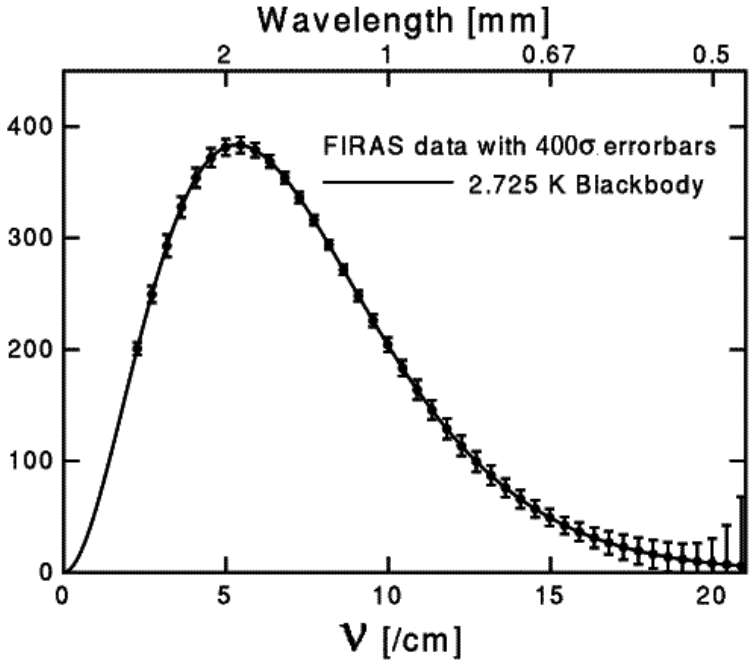

Figure 1.4: CMB spectrum from FIRAS instrument in COBE [24]. It peaks in the microwave range of frequencies and correspond to a perfect black body radiation of 2.725 K. Note that error bars are mutiplied by 400 in order to make them visible.

and Wilson [4]. Harrison, Peebles, Yu and Zel'dovich realized that the early Universe would have to have inhomogeneities at the level of 10^{-4} or 10^{-5} [27][28][29]. The NASA COBE mission [24] confirmed the primary anisotropy in 1992. After COBE measurements, many measurements of the CMB anisotropies have been performed. Specifically, WMAP [19] and Planck [15] missions measured anisotropies with a much higher resolution imposing strong constraints on the cosmological parameters.

Anisotropy of the CMB

The anisotropy of the CMB (see Figure 1.5) is divided into two types: primary anisotropies, due to effects occuring at the last scattering surface and before; and secondary anisotropies, due to interactions of the CMB with hot gas or gravitational potentials, which take place between the last scattering surface and the observer.

The structure of the primary anisotropies of the CMB (Figures 1.5 and 1.6) is principally determined by:

- Baryon acoustic oscillations (see section 2.2 for more details): Before decoupling, the radiation pressure of the photons tends to erase anisotropies, whereas the gravitational attraction of the baryons tend to increase them. The competition of these two forces create acoustic oscillations. Depending on the density of dark matter, dark energy, baryons, and spatial curvature of the Universe, these peaks have well known positions. Thus, BAO encode a lot of cosmological information.

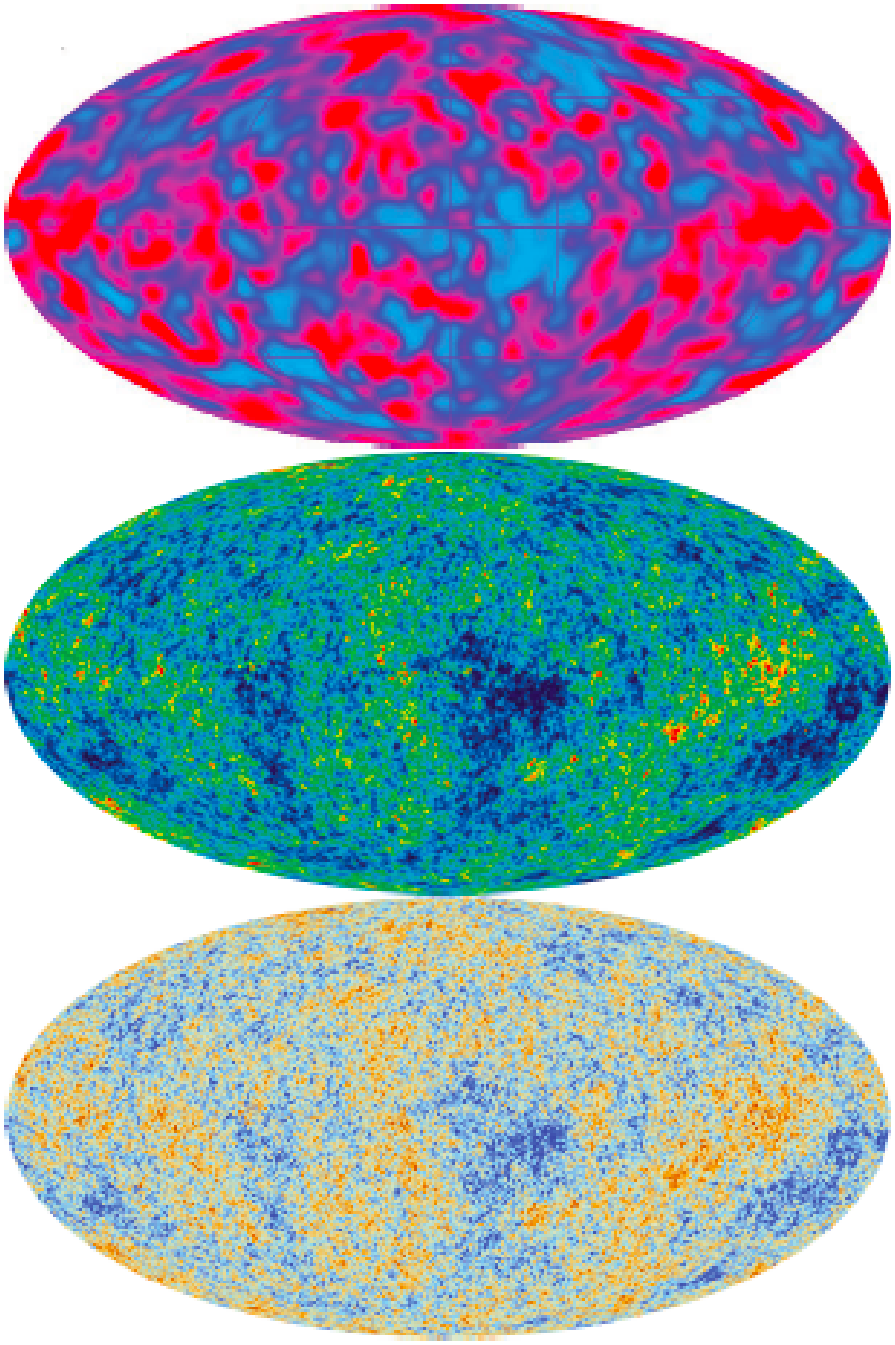

Figure 1.5: CMB anisotropies as measured by COBE [24], WMAP [19] and Planck [15].

- Diffusion damping or Silk damping [30]: Before decoupling, baryons and photons move as a single fluid. The imperfections or anisotropies in this fluid arise due to photon interactions. However, photons travel some distance (their mean free path in the baryon-photon fluid) before interacting. Thus, anisotropies are damped.

The present abundance of free charges in the intergalactic medium (IGM) is very low. If the IGM was ionized at very early times when the Universe was still dense enough, CMB anisotropies would suffer the following effects: small scale anisotropies are smeared-out and Thomson scattering induces polarization anisotropies on large angular scales. This broad angle polarization is correlated with the broad angle temperature perturbation. Two other effects induce secondary anisotropies: the Sunyaev-Zel'dovich effect, where clouds of high-energy

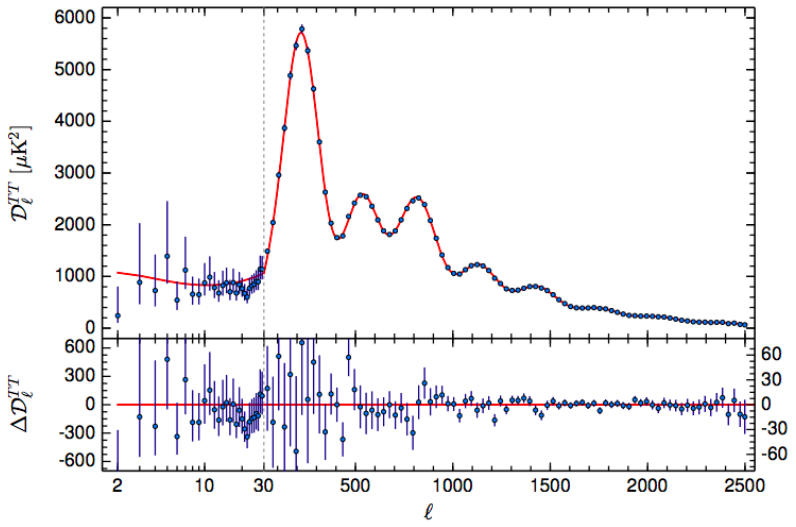

Figure 1.6: Best fit CMB power spectrum given by Planck mission [15].

electrons scatter the radiation [31], and the Sachs-Wolfe effect, which causes CMB photons to be redshifted due to gravitational fields [32].

The explanation of the isotropy, homogeneity, and evolution of CMB and its anisotropies, is a major success of ΛCDM.

1.4.2. Light element abundances

Another strong observational basis of the standard model is the light element abundances. ΛCDM makes a prediction about the abundance of light elements created during the so-called *Big Bang nucleosynthesis* (BBN) or *primordial nucleosynthesis*. This era began at temperatures of around 10 MeV and ended at 100 keV. The temperature/time relation in this era is given by [33]:

$$tT^2 = 0.74(10.75/g_\star)^{1/2} \tag{1.51}$$

where t is the time in seconds, T the temperature in MeV, and $g_\star$ the effective number of particle species, that is 10.75 in the Standard Model. The key parameter necessary to calculate the BBN is the number of photons

per baryon because photons and baryons participate in the generation of Deuterium D and ^{4}He. The main reactions in the BBN are depicted in Figure 1.7. It is very useful to define the quantity η_{10}:

$$\eta_{10} = 10^{10}(n_B/n_\gamma) = 274\Omega_B h^2 \tag{1.52}$$

Where n_B is the number density of baryons, n_γ the number density of photons, Ω_B the density parameter of baryons, and h the Hubble parameter. As it can be seen in Figure 1.8 light elements abundances are strongly dependent on η_{10}.

The current observations are in agreement with the theretical predictions as it can be seen in the Figure 1.8

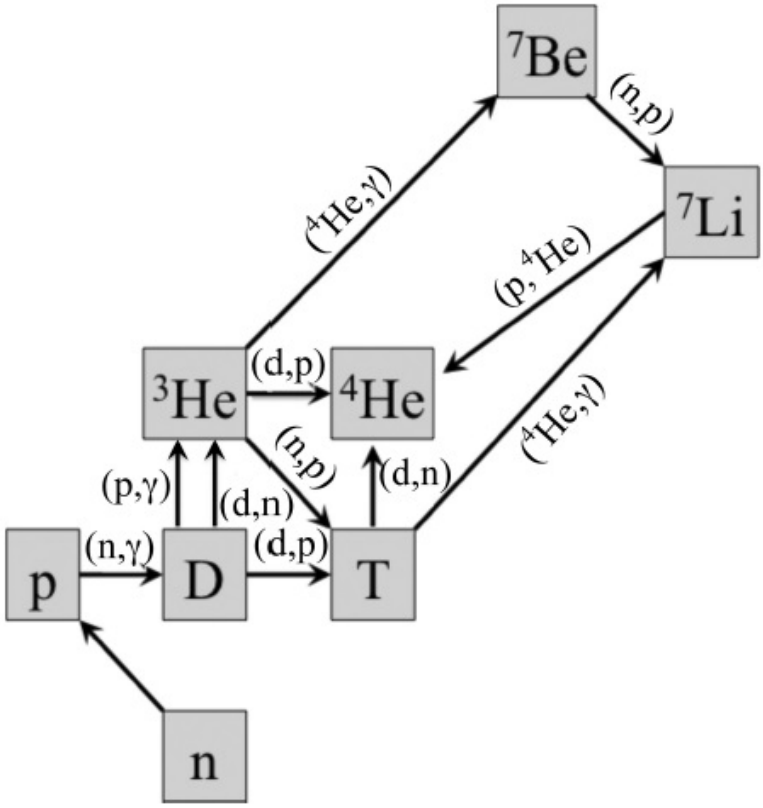

Figure 1.7: Reaction chains occured during the BBN [33].

1.4.3. Accelerating Universe and Supernovae

In the local Universe there exists a linear relation between the distance to a galaxy and its recession velocity due to the cosmos expansion as dictated by Hubble's law [2]. This linear relation is not valid for higher redshifts, and furthermore, in 1998, while measuring distances to type Ia supernova, it was discovered that the Universe was undergoing accelerating expansion. One of the most recent measurements of the Hubble diagram using supernovae is depicted in Figure 1.9. We can measure distances using luminosities of supernova explosions. It is known that the luminosity of type Ia supernova explosions has a standarizable evolution. For this reason, they are *standard candles*. This evolution can be used to measure distances and to infere cosmology. The supernovae Ia Hubble diagram led to the discovery of dark energy, and gave basis for the formulation of ΛCDM, which, obviously describes very well these measurements.

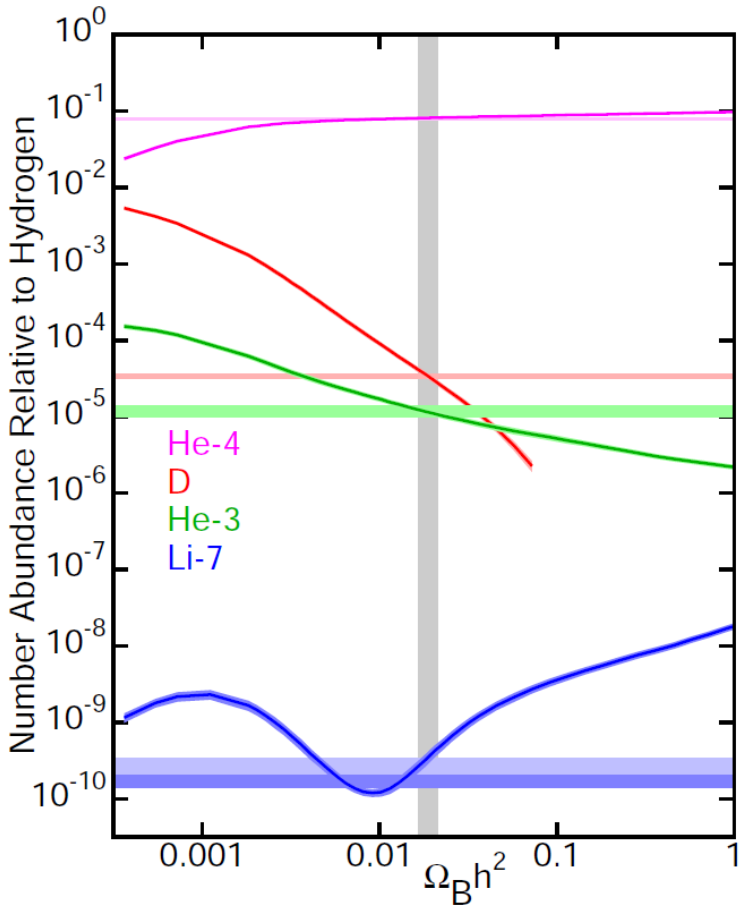

Figure 1.8: Relative abundances of light elements depending on the value of $\Omega_B h^2$. Theoretical predictions are the dark colored lines, light horizontal lines correspond to measurements and the light vertical line corresponds to the $\Omega_B h^2$ value measured by Planck [15]. As it can be seen, the predictions are in good agreement with the observed values.

1.4.4. Cosmological parameters

ΛCDM relies on six independent parameters: the physical baryon density Ω_b, the physical dark matter density Ω_{cdm}, the dark energy density Ω_Λ, the scalar spectral index n_s, the curvature fluctuation amplitude Δ^2_R, and the reionization optical depth τ. The values of these parameters (depicted in Figure 1.10) are not predicted by theory, although, most versions of cosmic inflation predict $n_s < 1$. From these parameters, the other model values, including the Hubble constant H_0 and the age of the Universe t_0 can be calculated. The current best-fit values for these and other parameters can be found in table 1.1. Combination of SN from SNLS [34] and SDSS-II [35], BAO from [36], [37], and [38] CMB from Planck 2013 data [39], and CMB polarization from WMAP [19] are depicted in Figure 1.11. This combination results in a $\chi^2/ndof = 684.1/738$, or equivalently, $p = 0.922$ [20].

From these six parameters it is possible to derive other parameters such as Ω_k or H_0. There are extensions to ΛCDM. For example, the wCDM model, where dark energy evolution is parametrized by the ratio between pressure and density. In these models, w is parametrized as $w(a) = w_0 + (1-a)w_a$. If $w_0 = -1$ and $w_a = 0$ we recover the cosmological constant case. These parameters describe properties of dark matter and dark energy in the Universe, two mysterious components that we are going to describe in the next sections.

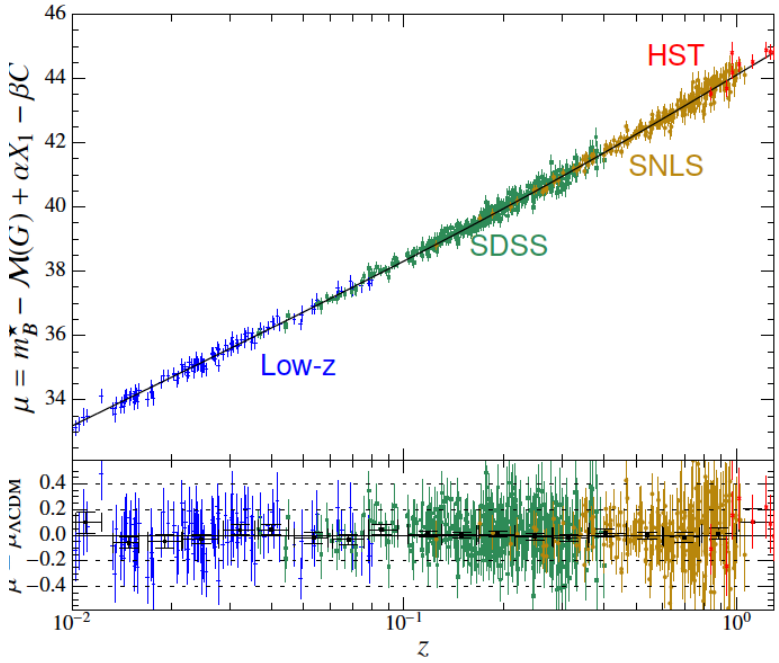

Figure 1.9: Hubble diagram with the best-fit ΛCDM cosmology for a fixed $H_0 = 70$ km s^{-1} Mpc^{-1} is shown in black. Figure from [20].

Parameter	WMAP9+BAO+H_0	Planck 2015
$\Omega_b h^2$	0.02266 ± 0.00043	0.02230 ± 0.00014
$\Omega_c h^2$	0.1157 ± 0.0023	0.1188 ± 0.0010
Ω_Λ	0.712 ± 0.010	0.6911 ± 0.0062
$10^9 \Delta^2_{\mathcal{R}}$	$2.427^{+0.078}_{-0.079}$	2.142 ± 0.049
n_s	0.971 ± 0.010	0.9667 ± 0.0040
τ	0.088 ± 0.013	0.066 ± 0.012

Table 1.1: Best-fit values for cosmological parameters from WMAP [19] and Planck [15].

1.4.5. Dark matter

In the Standard Model of cosmology the so-called *dark matter* plays a major role. Most of the matter in the Universe has this nature. The concept of dark matter originally arises to solve the problem of the rotation velocity of galaxies among others (see Figure 1.12). Fritz Zwicky in 1933 [40] applied the virial theorem to the Coma cluster and found that the total mass was 400 times bigger than the observable mass. However, it was not until the 1980s, when it was well-established that galaxies were dark-matter dominated by observations of Vera Rubin [41]. These observations were made in the late 1960s and early 1970s.

Galaxy and structure formation and CMB put constraints on the nature of dark matter. It should be composed of non-relativistic particles, this is the so-called *cold dark matter*. The fundamental constituents of dark matter are still unknown, but there are many candidates:

- Massive compact halo objects (MACHOs): These are objects composed by baryonic matter which emit little or no light such as unassociated planets, neutron stars and black holes. BBN and gravitational lensing studies allow MACHOs to be only a small fraction of the total dark matter.

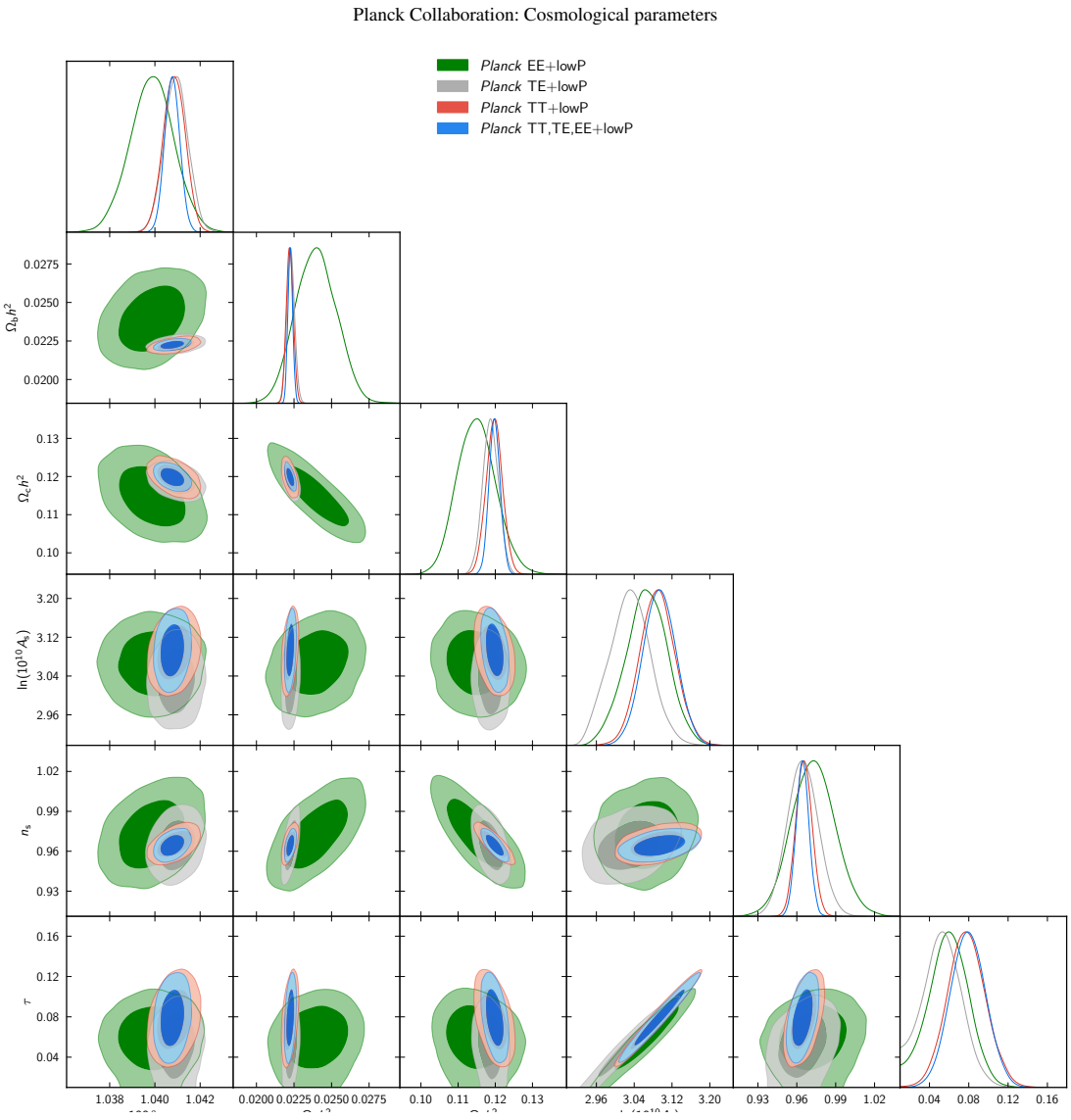

Figure 1.10: Base ΛCDM parameter constraint contours for Planck [15].

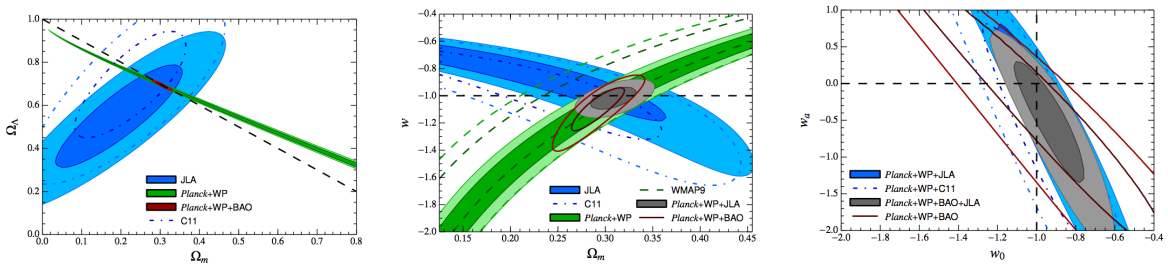

Figure 1.11: Cosmological parameter constraints combining WMAP CMB polarization, Planck CMB anisotropies, SN and BAO from [20].

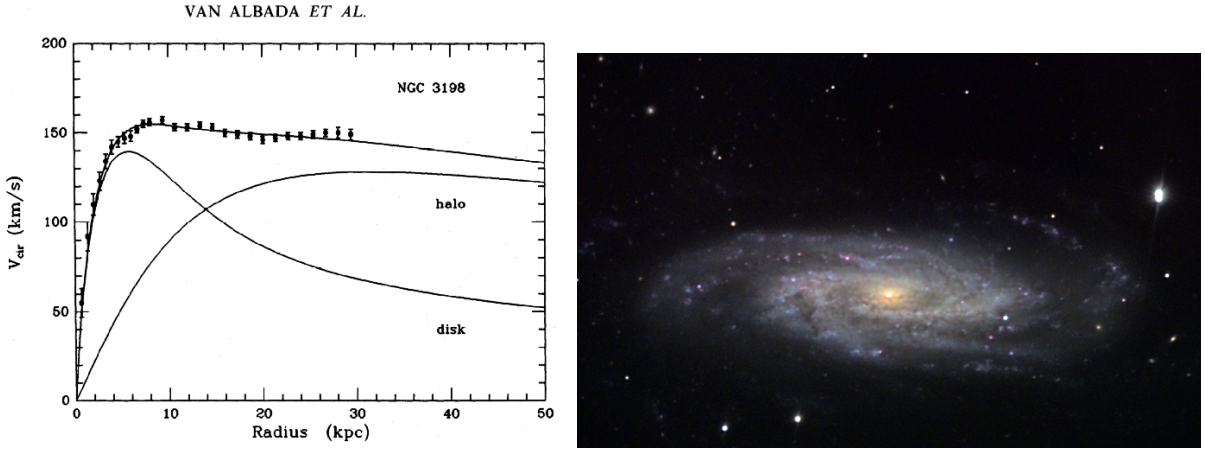

Figure 1.12: Measurements of NGC 3198 rotational speed of stars from [42] (left) and NGC 3198 galaxy (right).

- Robust associations of massive baryonic objects (RAMBOs): These are clusters of white and brown dwarfs. They only could be a small fraction of the total dark matter for the same reason as MACHOs [43].
- New particles: There are many candidates from the particle physics point of view. The most plausible candidates are WIMPs (Weakly Interactive Massive Particles) and axions.

There are many experiments to explore the nature of dark matter, that can be split into three categories:

1. Direct detection: These experiments are usually located at underground laboratories to minimize the cosmic ray background. They try to detect interactions from dark matter particles (most of them use WIMPs as candidates for modelling) with a particular nucleus. They use cryogenic (CDMS [44] among others), or noble liquid detectors (for example ArDM [45]) as well as, NaI crystals (DAMA/LIBRA) or CaF_2 (CANDLES).

2. Indirect detection: These experiments look for products from dark matter annihilation or decay. These processes could be detected indirectly through an excess of gamma rays, antiprotons or positrons emanating from regions of high dark matter density. In this category we can find AMS [46], Fermi Gamma-Ray Space Telescope [47], PAMELA [48], MAGIC, CTA, among others.

3. Production in laboratory: Some SUSY models predict dark matter particles that could be potentially detected in the following years of operation of the LHC [49]. For example, in the case of WIMPs, since they are weakly interacting and neutral, they are not expected to produce any discernible signal in LHC detectors. However, their presence in an event would be inferred from an imbalance of the total momentum.

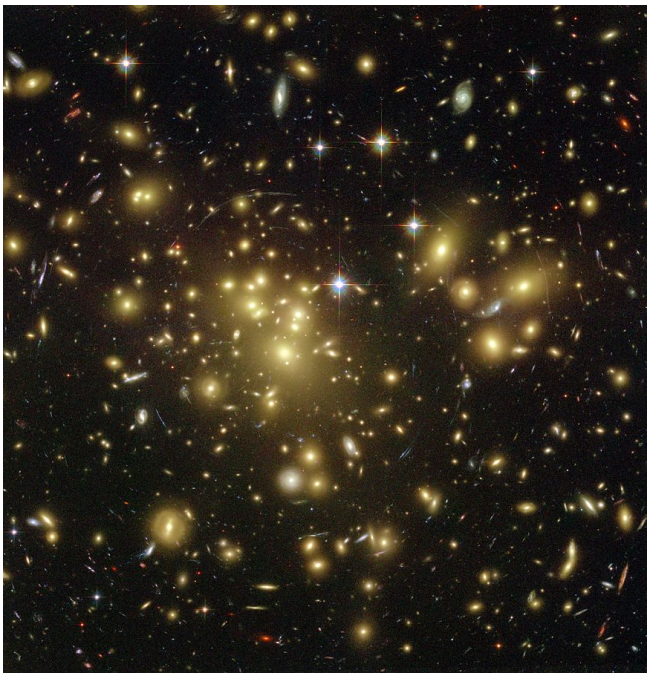

Figure 1.13: Strong gravitational lensing observed by the Hubble Space Telescope (HST) in Abell 1689.

There is an international effort dedicated to the search of dark matter. It is expected that many of these candidates will be found or excluded in the next 10 years.

1.4.6. Dark energy

The last ingredient to enter in the cosmological recipe and also the most mysterious is *dark energy*. Most of Universe's energy density is in the form of dark energy, i.e., it is the most abundant component. The nature of dark energy is unknown. We only know that it behaves like a negative pressure being the ultimate responsible of the accelerated expansion of the Universe. Its properties are compatible with being the *vacuum energy*, but all of the predictions from particle physics theories fail to match their expected value with the observations by tens of orders of magnitude. However, all current data are perfectly described by dark energy being the cosmological constant ($w = -1$), although sensitivity is still limited. There exist many other proposals to explain the nature of the dark energy such as *phantom dark energy* ($w < -1$), *quintessence* ($-1 < w < -1/3$), where w is the equation of state parameter and was defined in equation 1.20. Current experiments like DES and future experiments such as LSST or Euclid will try to clarify its nature.

The dark energy equation of state is generally parametrized as:

$$w = w_0 + w_a(1 - a) = w_0 + w_a \frac{z}{1 + z} \tag{1.53}$$

There are other possibilities to explain the nature of the dark energy. For example, there are alternative theories that state that General Relativity is incomplete at large scales [50].

1.4.7. Probes of dark energy

There are two main approaches to test it: Using geometrical probes, these probes are based on distances measurements; or using probes based on evolution, these probes are based on measuring the evolution of struc-

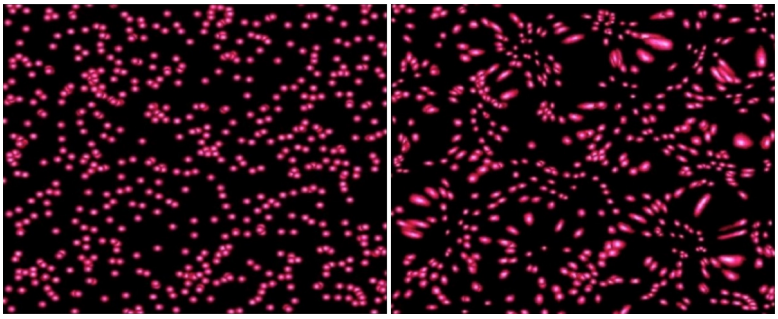

Figure 1.14: Effect of lensing in an image. The left picture corresponds to the unlensed image and the right is the resulting lensed image. Credit: LSST, Smoot Lensing Subgroup (http://aether.lbl.gov/Weak_lensing/weak_theory.html)

tures in the Universe.

It was back in 2006 when the Dark Energy Task Force (DETF) identified the four observational techniques that dominate current and future dark energy experiments [51]. These techniques are:

1. Baryon Acoustic Oscillations (BAO): It constitutes a strong geometrical as a *standard ruler*. BAO can be detected in the spatial distribution of galaxies. The BAO technique is sensitive to dark energy through its evolution with redshift. The physics of BAO will be covered deeper later in this work (2.2).

2. Type Ia supernova observations: Supernova explosions constitute a major geometrical probe by relating luminosity and distance. This is the most mature technique. Dark energy was discovered using it, and since then, a large improvement on the precision has been achieved as it is depicted in the Figure 1.9.

3. Galaxy clusters: This method is both a geometrical probe and an evolution probe. The number of galaxy clusters dN_c/dz is sensitive to dark energy through [52]:

$$\frac{d^2N_c(z)}{dzd\Omega} = \frac{c}{H(z)}d_A^2(1+z)^2\int_0^\infty f(M,z)\frac{dn_c(z)}{dM}dM \tag{1.54}$$

   Where $dn_c(z)/dM$ is the cluster density with mass M in comoving coordinates, $H(z)$ is the Hubble parameter, $d_A(z)$ the angular diameter distance (see 1.5) and $f(M,z)$ is the probability of detection. The main problem of this probe, from the theoretical point of view, is that $dn_c(z)/dM$ is not precisely characterized from first principles and it is usually based on the Press-Schechter formalism [53]. From the observational point of view, major difficulties are associated to mass calculations and cluster location procedures.

4. Weak lensing: This is also a geometrical and evolution probe. Light trajectory is perturbed during its travel towards the observer due to the pressence of mass, thus, galaxy images are altered in shape and in apparent brightness. This effect is depicted in Figure 1.14. The statistical properties of galaxy shapes are related to the mass field and to the cosmological parameters [52]. This is one of the most powerful probes but requires a detailed analysis of data and it is also strongly affected by systematics.

1.5. Distances and redshift

Since most cosmological probes are related to distance measurements it is mandatory to know the relation between the cosmological models and distances. Let us consider the extension to ΛCDM model wCDM. We can

rewrite the Friedmann equation as follows:

$$H(z) = H_0 \left[\Omega_m(1+z)^3 + \Omega_k(1+z)^2 + \Omega_\gamma(1+z)^4 + \Omega_\Lambda(1+z)^{3(1+w_0+w_a)} e^{-3w_a \frac{z}{1+z}}\right] \tag{1.55}$$

Where H_0 is the Hubble constant, which relates the recessional velocity of galaxies with the distance and it is generally expressed as:

$$H_0 = 100h \text{ Mpc}^{-1} \text{ kms}^{-1} \tag{1.56}$$

Where h is the adimensional Hubble constant and z is the redshift. Distances in cosmology are generally measured from *redshift*. The redshift z of an object is the fractional change of frequency of its emitted light resulting from the expansion of the Universe:

$$z \equiv \frac{\nu_e}{\nu_o} - 1 = \frac{\lambda_o}{\lambda_e} - 1 \tag{1.57}$$

Related to $H(z)$ is the *comoving distance*. The comoving distance is the distance measured in a comoving frame of reference, in other words, it factors out the expansion of the Universe giving a distance that does not change in time due to expansion. It is computed as follows:

$$d_C(z) = \chi(z) \equiv c \int_0^z \frac{dz'}{H(z')} \tag{1.58}$$

In the case of a flat Universe. For different curvatures we can write:

$$d_M = \begin{cases} d_H \frac{1}{\sqrt{\Omega_k}} \sinh\left(\sqrt{\Omega_k} d_C/d_H\right) & \Omega_k > 0 \\ d_C & \Omega_k = 0 \\ d_H \frac{1}{\sqrt{|\Omega_k|}} \sin\left(\sqrt{|\Omega_k|} d_C/d_H\right) & \Omega_k < 0 \end{cases} \tag{1.59}$$

Where d_H is the Hubble distance

$$d_H \equiv \frac{c}{H_0} \tag{1.60}$$

The *angular diameter distance* d_A is dened as the ratio of an object's physical transverse size to its angular size. Thus, an object with a physical transverse size $s_\perp$ substends an angle $\Delta\theta$ with the following relation:

$$\Delta\theta = \frac{s_\perp}{d_A} \tag{1.61}$$

We can also recover information about $H(z)$ if we know the physical radial size of a given object $s_\parallel$ and the observed redshift difference Δz,

$$H(z) = \frac{c\Delta z}{s_\parallel} \tag{1.62}$$

And we relate the angular diameter distance with the comoving distance through,

$$d_A = \frac{d_M}{1+z} \tag{1.63}$$

These are the basic ingredients to deal with the ΛCDM model. In the following sections we will explain in detail some of the most usual tools to study the large-scale structure of the Universe.

Chapter 2

Large-scale structure of the Universe

Most of the work in this thesis is focused on galaxy clustering, thus, it is necessary to introduce some basic concepts about the way to characterize the matter distribution in the Universe, its evolution and features.

2.1. The matter distribution in the Universe

Inhomogeneities in the distribution of matter in the Universe give us information about its origin, evolution, and the nature of its components. Inflationary models predict density perturbations which are generated by Gaussian quantum fluctuations in a scalar field. Thus, density perturbations are a Gaussian random field [54], [55] completely described by the power spectrum, $P(k)$, which is defined as follows:

$$\langle\hat{\delta}(\vec{k})\hat{\delta}(\vec{k}')\rangle = (2\pi)^3\delta^D(\vec{k}-\vec{k}')P(\vec{k}), \tag{2.1}$$

where δ^D is the Dirac delta and $\hat{\delta}(\vec{k})$ is the density contrast defined as:

$$\hat{\delta}(\vec{k}) = \frac{\rho(\vec{k})}{\bar{\rho}} - 1 \tag{2.2}$$

where $\rho(\vec{k})$ is the density in Fourier space. We can also write:

$$\hat{\delta}(\vec{r}) = \frac{\rho(\vec{r})}{\bar{\rho}} - 1 \tag{2.3}$$

with $\rho(\vec{r})$ the density in real space, and $\bar{\rho}$ the mean density. We also define the density contrast in real space and in redshift space similarly. Originally, fluctuations are suppossed to be isotropic, that is, $P(\vec{k})$ only depends on the modulus of $\vec{k}$, $|\vec{k}| = k$. As already mentioned, inflation also predicts the functional form of $P(k)$:

$$P(k) \propto k^{n_s}, \text{ with } n_s \sim 1 \tag{2.4}$$

This has been confirmed by observations. The most recent measurement, by Planck [15], is: $n_s = 0.9603 \pm 0.0073$. These density perturbations may be modified by amplification due to gravitational instability, pressure, and dissipation.

There are two standard approaches to deal with density perturbations:

1. The particle free path is short and matter can be described as an ideal fluid.
2. The particles free path is very long (for example when we deal with stars or galaxies) and we assume the particles moving in the potential ϕ of a smoothly varying particle density function, thus, we can apply Vlasov equation [56].

We will focus on the first case since this work is mainly focused to large scales, where this approximation is very accurate. The equations for an ideal fluid are:

$$\left(\frac{\partial \rho}{\partial t}\right)_{\vec{r}} + \nabla_{\vec{r}} \cdot \rho \vec{u} = 0 \tag{2.5}$$

$$\rho \left[\left(\frac{\partial \vec{u}}{\partial t}\right)_{\vec{r}} + (\vec{u} \cdot \nabla_{\vec{r}})\, \vec{u} \right] = -\nabla_r p - \rho \nabla_{\vec{r}} \Phi \tag{2.6}$$

$$\nabla^2_{\vec{r}} \Phi = 4\pi G \rho \tag{2.7}$$

The $\vec{r}$ subscript indicates the spatial variable is the proper distance $\vec{r}$ and $\vec{u}$ is the proper velocity. So, if we want to express these equations in terms of peculiar velocity $\vec{v}$:

$$\vec{u} = \dot{a}\vec{x} + \vec{v}(\vec{x}, t) = (\dot{a}/a)\, \vec{r} + \vec{v}\,(\vec{r}/a, t) \tag{2.8}$$

Defining $\vec{x} = \vec{r}/a$ we can write:

$$\left(\frac{\partial}{\partial t}\right)_{\vec{r}} \rho(\vec{r}/a, t) = \frac{\partial \rho}{\partial t} - \frac{\dot{a}}{a} \vec{x} \cdot \nabla \rho \tag{2.9}$$

$$\nabla_{\vec{r}} \cdot \rho \vec{u} = \frac{1}{a} \nabla \cdot [\rho(\vec{v} + \dot{a}\vec{x})] \tag{2.10}$$

Where $\nabla = \nabla_{\vec{x}}$. Decomposing the density as:

$$\rho(\vec{x}, t) = \rho_b(t)(1 + \delta(\vec{x}, t)) \tag{2.11}$$

we can obtain the equations for the non-homogeneous perturbation $\delta(\vec{x}, t)$ of the homogeneous background $\rho_b(\vec{x}, t)$. If we sum equations 2.9 and 2.10 we obtain:

$$\left(\frac{\partial}{\partial t} - \frac{\dot{a}}{a}\vec{x}\nabla\right) \rho_b(1 + \delta) + \frac{1}{a} \nabla \left[\rho_b\,(1 + \delta)\,(\dot{a}\vec{x} + \vec{v})\right] \tag{2.12}$$

For the homogeneous part we have:

$$\dot{\rho}_b + 3\frac{\dot{a}}{a}\rho_b = 0 \tag{2.13}$$

and for the perturbation:

$$\dot{\delta} + \nabla\left[(1 + \delta)\vec{v}\right] = 0 \tag{2.14}$$

On the other hand, expressing 2.6 in terms of $\vec{x}$ and $\vec{v}$ we obtain:

$$\ddot{a}\vec{x} + \frac{\partial \vec{v}}{\partial t} + \frac{1}{a}\,(\vec{v} \cdot \nabla)\, \vec{v} + \frac{\dot{a}}{a}\vec{v} = -\frac{1}{\rho a}\nabla p - \frac{1}{a}\nabla\left(\phi - \frac{1}{2}a\ddot{a}x^2\right) \tag{2.15}$$

Where again, we can consider the homogeneous potential Φ and its perturbation, $\phi = \Phi + \frac{1}{2}a\ddot{a}x^2$. Thus, we obtain the fluid equations in expanding coordinates

$$\frac{\partial \vec{v}}{\partial t} + \frac{1}{a}\,(\vec{v} \cdot \nabla)\, \vec{v} + \frac{\dot{a}}{a}\vec{v} = -\frac{1}{\rho a}\nabla p - \frac{1}{a}\nabla\phi \tag{2.16}$$

$$\dot{\delta} + \frac{1}{a}\nabla \cdot (1 + \delta)\, \vec{v} = 0 \tag{2.17}$$

$$\nabla^2 \phi = 4\pi G \rho \delta \tag{2.18}$$

If we calculate the divergence of 2.16 and we take the derivative with respect time 2.17 and add them we get:

$$\frac{\partial^2 \delta}{\partial t^2} + 2\frac{\dot{a}}{a}\frac{\partial \delta}{\partial t} = \frac{\nabla^2 p}{\rho a^2} + \frac{1}{a^2}\nabla \cdot (1 + \delta)\, \nabla\phi + \frac{1}{a^2}\frac{\partial^2}{\partial x^\alpha \partial x^\beta}\left[(1 + \delta)\, v^\alpha v^\beta\right] \tag{2.19}$$

2.1.1. Linear approximation

If we assume that the density field is slightly perturbed from the background, *i.e.*,

$$\delta \ll 1, \ \ (vt/d)^2 \ll \delta \tag{2.20}$$

where d is the coherence length for spatial variations of δ, v is the characteristic fluid velocity and $t \sim (G\rho)^{1/2}$. The expansion of equations 2.16, 2.17 and 2.19 neglecting non-linear terms transform into

$$\frac{\partial^2\delta}{\partial t^2} + 2\frac{\dot{a}}{a}\frac{\partial\delta}{\partial t} = \frac{\nabla^2 p}{\rho a^2} + 4\pi G\rho\delta \tag{2.21}$$

$$\frac{\partial\delta}{\partial t} + \frac{1}{a}\nabla\cdot\vec{v} = 0 \tag{2.22}$$

which are the equations that describe the behaviour of the density perturbations in an expanding Universe. The solution of this equation can be written as:

$$\delta(\vec{x},t) = f_1(\vec{x})D_1(t) + f_2(\vec{x})D_2(t) \tag{2.23}$$

Where $D_1 f_1$ is the growing mode and $D_2 f_2$ the decaying mode. We are interested in the growth of structure so, we focus on the growing mode $D_1 \equiv D$ that can be written as [56]:

$$D(a) = \frac{5}{2}\Omega_M H_0^2 H(a)\int_0^a \frac{da'}{\left[a'H(a')\right]^3} \tag{2.24}$$

This expression is normalized to $D(a\to 0)\to a$. The usual normalization is $D(1)=1$. Thus,

$$D_+(a) = D(a)/D(1) \tag{2.25}$$

In linear theory, each Fourier mode evolves independently, $\delta_k(t)\propto D_+(t)$, and the shape of the power spectrum is preserved, but its amplitude grows as $D_+^2(t)$. Thus, we can write:

$$P(k,t)\propto k^{n_s}D_+^2(t) \tag{2.26}$$

If we want to relate the power spectrum in this regime with the primordial power spectrum predicted by inflation we should keep in mind that, at early stages, pressure inhibits the growth of structure on scales smaller than the distance travelled by an acoustic wave during the free-fall collapse time of a perturbation. If there are collisionless particles of hot dark matter, they can travel rapidly through the background and this free streaming can damp away perturbations completely. Radiation and relativistic particles may also cause kinematic suppression of growth. The coupling of photons and baryons can also cause dissipation of perturbations in the baryonic component. The net effect of these processes, for the case of statistically homogeneous initial Gaussian fluctuations, is to change the shape of the original power spectrum in a manner described by the transfer function $T(k)$. The power spectrum $P(k,z)$ is then related to its primordial form $P(k)$ via:

$$P(k,z) = P(k)T^2(k)D_+(z) \tag{2.27}$$

There are numerical expressions to obtain the transfer function [57], [58] taking all these effects into account. In practice, the usage of codes such as `CAMB` [59] and `CMBFAST` [60] to evaluate this transfer function is the usual way to work. The actual distribution of matter δ_M is not accessible, since we observe only the distribution of galaxies δ_G. These quantities are related by:

$$\delta_G = b(k,z)\delta_M \tag{2.28}$$

Where $b(k,z)$ is known as the *bias* parameter. Thus, we can write the galaxy power spectrum as follows:

$$P_G(k,z) = b^2(k,z)P_M(k,z) \tag{2.29}$$

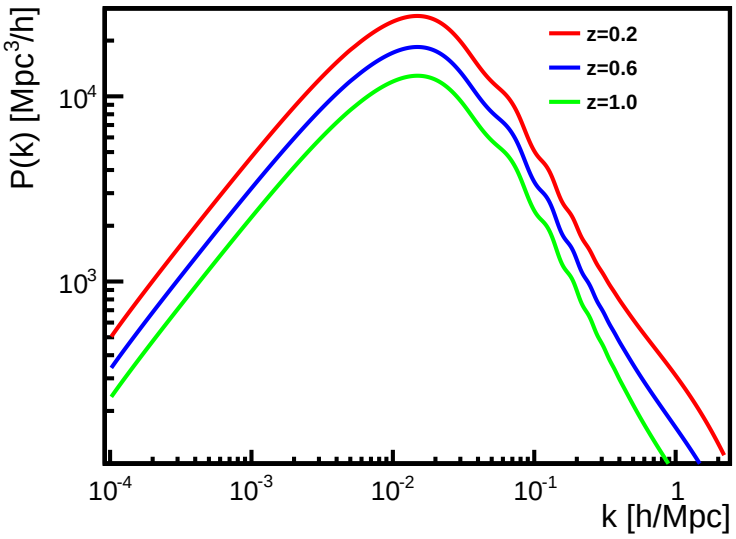

Figure 2.1: Example of power spectrum obtained with `CAMB` for different redshifts. These curves were computed for a flat ΛCDM Universe with Planck cosmological parameters.

As aforementioned, the power spectrum gives a full description of a Gaussian random field in the Fourier space but we are interested in real space. The Fourier transform of the power spectrum is the two point correlation function $\xi(\vec{r})$.

$$P(\vec{k}, z) = \int d^3\vec{r}\xi(\vec{r}, z) \exp\left(i\vec{k} \cdot \vec{r}\right) \tag{2.30}$$

The two point correlation function $\xi(\vec{r})$ is the excess of probability of finding one galaxy pair at a distance $\vec{r}$ compared to an uniform random field with the same mean density [56]. Thus, the expected number of galaxies with one galaxy in dV_1 and other in dV_2 in a field with a mean number of galaxies per unit volume $\bar{n}$ is:

$$\langle n_{pair} \rangle = \bar{n}^2 \left[1 + \xi(\vec{r})\right] dV_1 dV_2 \tag{2.31}$$

This means that $\xi(\vec{r})$ measures the excess of clustering of galaxies at a separation $\vec{r}$. If $\xi(\vec{r})$=0, galaxies are uncorrelated (randomly distributed). If $\xi(\vec{r}) > 0$, we have clustering, and if $\xi(\vec{r}) < 0$, we have anti-clustering. The most usual way to normalize the amplitude of the matter perturbations is through the σ_8 parameter, which is defined as the variance of the linear matter density contrast in spheres with a radius R of 8 Mpc h^{-1} at redshift 0. This can be calculated as:

$$\sigma_R^2 \equiv \frac{1}{2\pi^2} \int_0^\infty k^2 \left|W(kR)\right|^2 P(k, z) dk, \text{ where } W(kR) \equiv 3\frac{\sin kR - kR\cos kR}{k^3 R^3} \tag{2.32}$$

2.1.2. Correlation function

The two point correlation function $\xi(\vec{r})$ is one of the most used and powerful tools in modern cosmology. Under the assumption of isotropy, the correlation function can be written just as a function of the distance r, but there are some effects that make it anisotropic. It is useful to define certain coordinate systems to describe the correlation function. These coordinates are depicted in Figure 2.2. Given two space positions positions $\vec{x}_1$ and $\vec{x}_2$ of two points of the space the coordinates of the Figure 2.2 are defined as follows:

- θ: the angle subtended by both lines of sight.

$$\cos\theta \equiv \frac{\vec{x}_1 \cdot \vec{x}_2}{x_1 x_2} \tag{2.33}$$

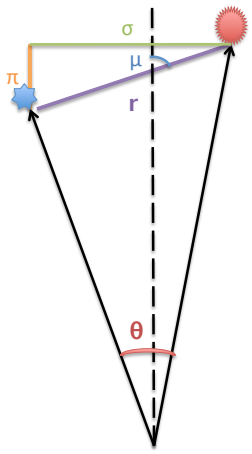

Figure 2.2: Different coordinates to describe the 3D anisotropic correlation function.

- $r \equiv |\vec{x}_1 - \vec{x}_2|$: the relative distance between both points.

$$r \equiv \sqrt{x_1^2 + x_2^2 - 2x_1 x_2 \cos\theta} \tag{2.34}$$

- μ: the angle of the separation vector with respect to the line of sight.

$$\mu \equiv \frac{(\vec{x}_1 - \vec{x}_2)\cdot(\vec{x}_1 + \vec{x}_2)}{|\vec{x}_1 - \vec{x}_2|\,|\vec{x}_1 + \vec{x}_2|} = \frac{|x_1^2 - x_2^2|}{\sqrt{x_1^4 + x_2^4 + 2x_1^2 x_2^2(1 - 2\cos^2\theta)}} \tag{2.35}$$

- π: the projection of the separation vector along the line of sight.

$$\pi \equiv r\mu \equiv \frac{|x_1^2 - x_2^2|}{\sqrt{x_1^2 + x_2^2 + 2x_1 x_2 \cos\theta}} \tag{2.36}$$

- σ: the projection of the separation vector on the plane transverse to the line of sight.

$$\sigma \equiv r\sqrt{1 - \mu^2} \equiv \frac{2x_1 x_2 \sin\theta}{\sqrt{x_1^2 + x_2^2 + 2x_1 x_2 \cos\theta}} \tag{2.37}$$

The most usual representations are $\xi(r, \mu)$ and $\xi(\sigma, \pi)$ but, these are not directly observable quantities. One must assume an underlying cosmological model to compute them. It is possible to define a coordinate system based on observable quantities only. We use the difference in redshift of the objects Δz, and the angle subtended by both lines of sight θ. It is possible to express the correlation function as a function of these quantities as $\xi(\theta, \Delta z)$.

It is also useful, mainly when using photometric redshifts[1], to define the angular correlation function $\omega(\theta)$, which is just a projection of $\xi(\vec{r})$ onto the sphere:

$$\omega(\theta) \equiv \langle \delta(\hat{n}_1)\delta(\hat{n}_2)\rangle = \int_0^\infty dz_1 \phi(z_1) \int_0^\infty dz_2 \phi(z_2)\xi(z_1, z_2, \theta) \tag{2.38}$$

Where $\phi(z)$ is the selection function that represents the true redshift distribution of the objects to be projected on the plane where the correlation function is computed. In the case of having a photometric redshift bin between z_{p1} and z_{p2} [61]:

$$\phi(z) \propto \frac{dN}{dz} \int_{z_{p1}}^{z_{p2}} dz_p \frac{dN_p}{dz_p} \mathrm{P}(z_p|z) \tag{2.39}$$

The angular correlation function is defined in the sphere $\mathcal{S}^2$ and thus, we can express it in terms of spherical harmonics. Given $\delta(\hat{n})$ a projection of the density fluctuations in the line of sight direction $\hat{n}$ defined by:

$$\delta(\hat{n}) = \int dz \phi(z) \delta(\hat{n}, z) \tag{2.40}$$

It can be decomposed as:

$$\delta(\hat{n}) = \sum_{l\geq 0} \sum_{m=-l}^{l} a_{lm} Y_{lm}(\hat{n}) \tag{2.41}$$

where Y_{lm} are the spherical harmonics and the a_{lm} verify [62]:

$$\langle a_{lm} a_{l'm'} \rangle = \delta^K_{ll'} \delta^K_{mm'} C_l \tag{2.42}$$

Thus,

$$C_l = \frac{1}{2l+1} \sum_{m=-l}^{l} a_{lm}^2 \tag{2.43}$$

and we can express the angular correlation function as a sum of C_l [62]:

$$\omega(\theta) = \sum_{l\geq 0} \left(\frac{2l+1}{4\pi} \right) P_l(\cos\theta) C_l \tag{2.44}$$

where P_l are the Legendre polynomials of order l. Equivalently [62]:

$$C_l = \frac{1}{2\pi^2} \int 4\pi k^2 dk P(k) \Phi_l^2(k) \tag{2.45}$$

Where:

$$\Phi_l(k) = \int dz \phi(z) D(z) j_l(kr(z)), \tag{2.46}$$

and j_l are the spherical Bessel functions of order l. The C_l play the role of the power spectrum for the projected quantities. They are the angular power spectrum. The spherical harmonics formalism is very useful because, under the assumption of Gaussian fluctuations, the a_{lm} coefficients follow a Gaussian distribution and the C_l are uncorrelated [62], so,

$$\mathrm{Cov}_{ll'} = \mathrm{Var}(C_l)\delta^K_{ll'} = 2\frac{C_l^2}{2l+1} \tag{2.47}$$

[1]The photometric redshift is an estimation of the redshift using photometry instead of spectroscopy. It provides a faster redshift estimation but with a higher uncertainty and thus, we lose some information along the line of sight, but on the other hand, we have larger statistics. This technique is used in surveys such as DES.

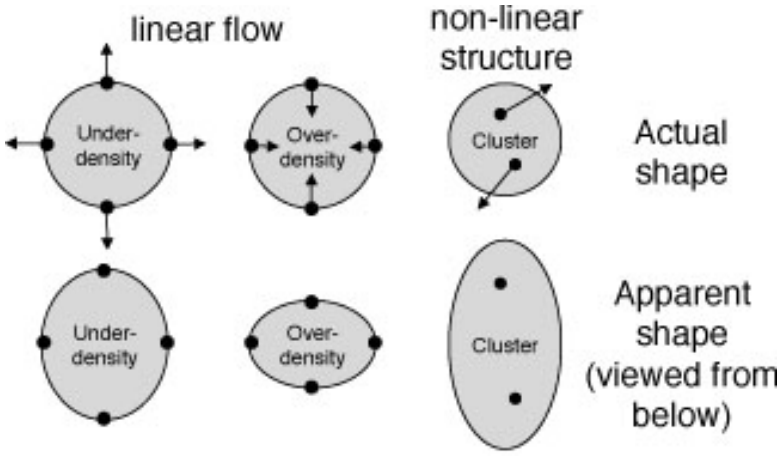

Figure 2.3: Schematic representation of effects due to Redshift Space Distortions (RSD) [64].

If we observe only a fraction of sky f_{sky} the covariance of the correlation function will be given by [62]:

$$\mathrm{Cov}_{\theta\theta'} = \frac{2}{f_{sky}} \sum_{l\geq 0} \frac{2l+1}{(4\pi)^2} P_l(\cos\theta) P_l(\cos\theta') \left(C_l + \delta^D(\theta - \theta') \frac{1}{\bar{n}} \right)^2 \tag{2.48}$$

Where $\bar{n}$ is the number of objects per steradian and represents the Poisson noise contribution.

2.1.3. Redshift space distortions

In astronomy, distances to objects are determined using their luminical information, *i.e.*, we cannot directly measure distances to galaxies. The most usual technique to determine distances is the redshift measurement. The redshift of one galaxy will be a combination of the redshift due to the cosmic recession and its redshift due to the peculiar velocity. In redshift space we have:

$$\vec{s}(\vec{r}) = \vec{r} - v_r(r) \frac{\vec{r}}{r} \tag{2.49}$$

Where $\vec{s}$ is the position in redshift space of an object, $\vec{r}$ is the real space position of that object with the observer at the origin, and v_r is the radial component of the peculiar velocity of that object. Thus, two galaxies at the same distance have different redshifts if they have different velocities. At low scales objects will appear elongated. This effect is known as Finger of God (FOG) [63]. On the other hand, when we are dealing with large scales, the galaxies appear to be closer to each other due to their coherent peculiar velocities induced by gravitational collapse. This translates to a stretching of structures at large scales, this is known as the Kaiser effect [63]. These effects can be seen in Figure 2.3 [64].

If we assume that the patch of the Universe where clustering is measured is sufficiently far away, that the line-of-sight is approximately constant (Kaiser approximation), the effect can be modelled as [63]:

$$P_s(k) = \left(1 + \beta\mu_k^2\right)^2 P(k), \tag{2.50}$$

where the subscript s denotes redshift space, $\mu_k = \cos\theta$ in this space, and β is proportional to the velocity growth factor, f, and to the galaxy bias:

$$\beta = \frac{f(z)}{b(z)} \equiv \frac{1}{b(z)} \frac{d\ln D_+}{d\ln a} \tag{2.51}$$

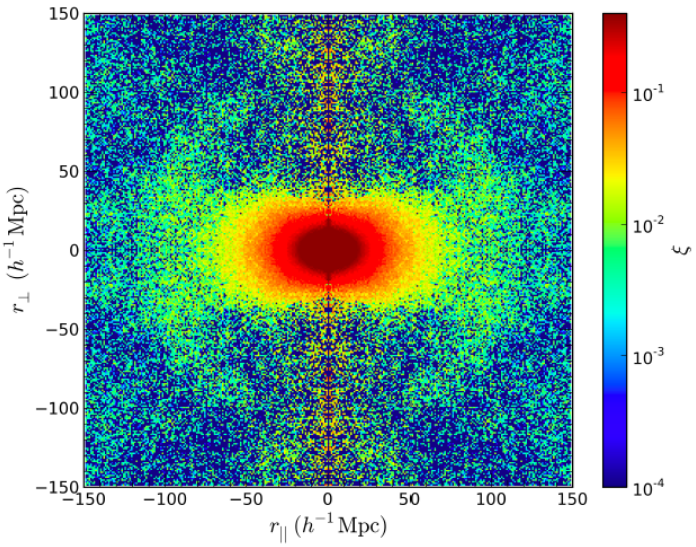

Figure 2.4: Effect of RSD in the correlation function along the line-of-sight and the transverse directions as measured for SDSS-III DR11 galaxies in [66].

$f(z)$ is usually parametrized as $f(z) \approx \Omega_m^\gamma(z)$, where γ is the gravitational growth index. For the General Relativity case $\gamma = 0.55$ [56].
A useful expansion is [65]:

$$\left(1+\beta\mu_k^2\right)^2 = \left[1+\frac{2}{3}\beta+\frac{1}{5}\beta^2\right]\mathcal{P}_0(\mu_k) + \left[\frac{4}{3}\beta+\frac{4}{7}\beta^2\right]\mathcal{P}_2(\mu_k) + \frac{8}{35}\beta^2\mathcal{P}_4(\mu_k) \tag{2.52}$$

where $\mathcal{P}_l$ are the Legendre polynomials of degree l. Moreover, we can write $\xi(\vec{r})$ in terms of (r,μ) and expand the correlation function in terms of the Legendre polynomials as follows,

$$\xi(r,\mu) = \sum_l \xi_l(r)\mathcal{P}_l(\mu) \tag{2.53}$$

ξ_l is defined as:

$$\xi_l(r) = \frac{i^l}{2\pi^2}\int dk P(k)k^2 j_l(kr), \tag{2.54}$$

where $j_l(kr)$ is the spherical Bessel function of order l. Thus, the redsfhift space correlation function including Redshift Space Distortions can be written as:

$$\xi_s(r,\mu) = b(z)^2\left\{\left[1+\frac{2}{3}\beta+\frac{1}{5}\beta^2\right]\mathcal{P}_0(\mu)\xi_0(r) + \left[\frac{4}{3}\beta+\frac{4}{7}\beta^2\right]\mathcal{P}_2(\mu)\xi_2(r) + \frac{8}{35}\mathcal{P}_4(\mu)\xi_4(r)\right\} \tag{2.55}$$

The effect in the correlation function consists in the stretching that can be seen in the Figure 2.4.

2.1.4. Non-linear clustering

New generation galaxy surveys give an unprecedented statistical power and allow us to reach very low scales. At these low scales ($\Delta_l \equiv 4\pi k^3 P(k)_l \geq 1$) we are entering the extremely nonlinear regime. The non-linear terms

that we have neglected in the fluid equations, start to be sizeable. There are many different approaches to deal with this. The standard perturbation theory expands the power spectrum:

$$P(k,z) = D_+^2(z)P_0(k)T^2(k) + P_{1loop}(k,z) + P_{2loop}(k,z) + \cdots \tag{2.56}$$

Where P_{1loop} and P_{2loop} are higher order corrections. This expansion is valid at large scales where fluctuations are small, but it breaks down when approaching this nonlinear regime if truncation is present. There exists another approach called Renormalized Perturbation Theory (RPT) [67]. This approach is represented by Feynman diagrams constructed in terms of the initial conditions, *i.e.*, perturbation spectrum, the vertex describing nonlinearities and the propagator describing the linear evolution. The corrections to the linear spectrum organize themselves into two classes of diagrams, one class corresponding to mode-coupling effects, and the other one to a renormalization of the propagator. Unlike the standard perturbation theory, this approach has as an advantage that each term in the remaining mode-coupling series dominates at some characteristic scale and is subdominant otherwise. The power spectrum can be written as [67]:

$$P(k,z) = G^2(k,z)P_{linear}(k) + P_{MC}(k,z) \tag{2.57}$$

where $G(k,z)$ is known as the propagator and P_{MC} is the mode coupling term. We can write:

$$G(k,z) = \frac{\langle \delta(k,z)\delta_0(k')\rangle}{P_0(k)} = D_+(z) - f(k)D_+^3(z) + \cdots \tag{2.58}$$

$f(k)$ is [67]:

$$f(k) = \int \frac{1}{504k^3q^5}\left[6k^7q - 79k^5q^3 + 50q^5k^3 - 21kq^7 + \frac{3}{4}(k^2-q^2)^3(2k^2+7q^2)\ln\frac{|k-q|^2}{|k+q|^2}\right]P_0(q)d^3q \tag{2.59}$$

In the low-k limit $G(k,z)$ can be written as:

$$G(k,z) \approx D_+(z)\left(1 - \frac{61}{210}k^2\sigma_v^2 D_+^2(z)\right), \tag{2.60}$$

with σ_v defined as:

$$\sigma_v^2 \equiv \frac{1}{3}\int d^3q \frac{P_0(q)}{q^2} \tag{2.61}$$

In the large-k limit [67]:

$$G(k,z) \approx D_+(z)\exp\left(-\frac{1}{2}k^2\sigma_v^2\left(D_+(z)-1\right)^2\right) \tag{2.62}$$

In this approach we can rewrite the correlation function as:

$$\xi(r,z) = \left[G^2 \otimes \xi_0\right](r,z) + \xi_{MC}(r,z) \tag{2.63}$$

The term ξ_{MC} is computed using mode-coupling diagrams in perturbation theory as described in [67]. Since G is approximately Gaussian in Fourier space, it induces an attenuation of any feature in the correlation function and a displacement of the local maximum of the correlation function[2]. The mode coupling term also induces a displacement of the maximum but is much lower [68] as it can be seen in Figure 2.6.

In practice, a common approach to deal with nonlinearities is to resort to `HALOFIT` [69]. This is a fitting formula based on a suite of high-resolution N-body simulations and decomposes the dimensionless power-spectrum $\Delta^2(k) = k^3P(k)/(2\pi^2)$ as:

$$\Delta^2(k) = \Delta_Q^2(k) + \Delta_H^2(k) \tag{2.64}$$

[2]This maximum is due to the Baryon Acoustic Oscillations that will be introduced later in this chapter (see section 2.2

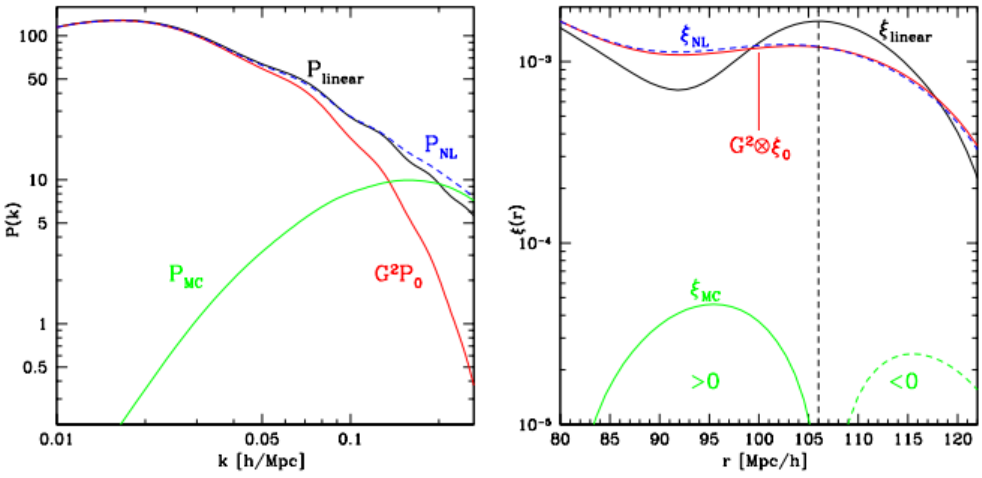

Figure 2.5: Power spectrum (left) and correlation function (right) for dark matter in ΛCDM cosmology at $z = 0$. Black line corresponds to the linear prediction, blue line is the non-linear including Mode Coupling terms (green) and propagator terms (red).

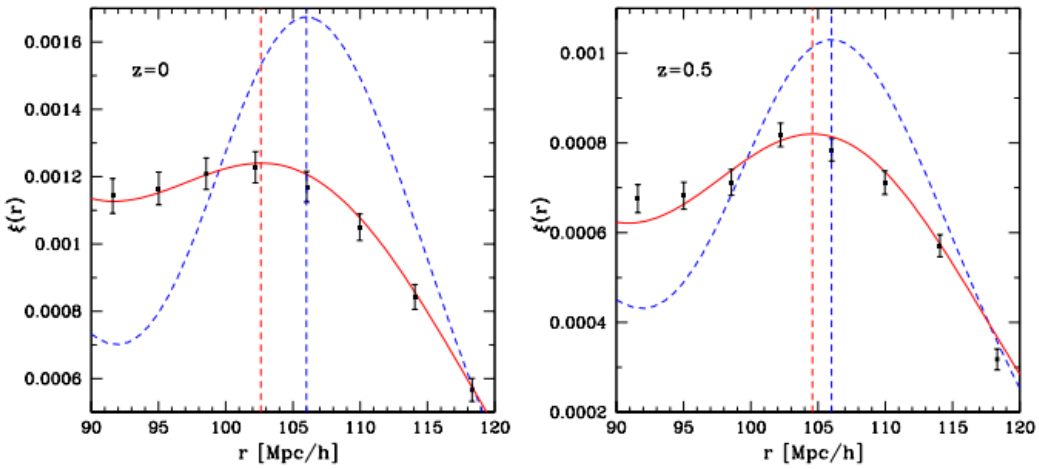

Figure 2.6: Displacement of the local maximum for different redshifts due to nonlinearities. Red line is non linear theory and blue dashed line corresponds to linear theory.

The first term is called the two-halo term that dominates at large scales, whereas the second term is referred to as the one-halo term that is important at small scales. The two-halo term $\Delta_Q^2(k)$ is given by [69]:

$$\Delta_Q^2(k) = \Delta_L^2(k) \left[\frac{\left(1 + \Delta_L^2(k)\right)^{\beta_n}}{1 + \alpha_n \Delta_L^2(k)} \right] e^{-f(y)} \tag{2.65}$$

where the subscript L stands for linear,

$$f(y) = \frac{y}{4} + \frac{y^2}{8} \tag{2.66}$$

and y is the dimensionless wavenumber $y = k/k_\sigma$. The nonlinear scale k_σ^{-1} is defined by

$$\sigma^2(k_\sigma^{-1}) = 1 \text{ with } \sigma^2(R) = \int d\ln k \Delta_L^2(k) e^{-k^2 R^2} \tag{2.67}$$

The one halo term is [69],

$$\Delta_H^2(k) \frac{\Delta_H'^2(k)}{1 + \mu_n y^{-1} + \nu_n y^{-2}} \text{ with } \Delta_H'^2(k) = \frac{a_n y^{3f_1(\Omega_m)}}{1 + b_n y^{f_2(\Omega_m)} + [c_n f_3(\Omega_m) y]^{3-\gamma_n}} \tag{2.68}$$

The parameters $a_n, b_n, c_n, \gamma_n, \alpha_n, \beta_n, \mu_n$ and ν_n are given by polynomials as functions of the effective spectral index n_{eff} and the curvature C defined as

$$n_{eff} + 3 = - \left. \frac{d\ln\sigma^2(R)}{d\ln R} \right|_{\sigma=1}, \; C = - \left. \frac{d^2 \ln\sigma^2(R)}{d\ln R^2} \right|_{\sigma=1} \tag{2.69}$$

The best fit parameters for these expressions can be found at [69].

2.2. Baryon Acoustic Oscillations

In the early Universe, before recombination and decoupling, the Universe consisted of a hot plasma of photons and baryons which were tightly coupled. The competing forces of radiation pressure and gravity set up oscillations in the baryon-photon fluid. These are the so-called Baryon Acoustic Oscillations (BAO). When the plasma ionized, the mean free path for a photon was much smaller than the horizon of the Universe. Photons behave just like a fluid coupled to charged particles and the photon perturbation Θ obeys Boltzmann's equations. In this situation the perturbation can be written as [65]:

$$\dot{\Theta}_0 + k\Theta_1 = -\dot{\Phi} \tag{2.70}$$

$$\dot{\Theta}_1 - \frac{k\Theta_0}{3} = \frac{k\Psi}{3} + \dot{\tau} \left[\Theta_1 - \frac{i v_b}{3} \right] \tag{2.71}$$

Where Θ_0 and Θ_1 are the monopole and the dipole of the photon perturbations, τ the photon mean free path and v_b the velocity of baryons. Ψ is the perturbation to the Newtonian potential and Φ the perturbation to the spatial curvature. We have also the velocity equation for baryons given by [65]:

$$v_b = -3i\Theta_1 + \frac{\mathcal{R}}{\dot{\tau}} \left[\dot{v}_b + \frac{\dot{a}}{a} v - _b + ik\Psi \right] \tag{2.72}$$

at which $\mathcal{R} = 3\rho_b / 4\rho_\gamma$. This term can be approximated by:

$$v_b \approx -3i\Theta_1 + \frac{\mathcal{R}}{\dot{\tau}} \left[-3i\dot{\Theta}_1 - 3i\frac{\dot{a}}{a}\Theta_1 + ik\Psi \right] \tag{2.73}$$

From these equations we obtain:

$$\dot{\Theta}_1 + \frac{\dot{a}}{a}\frac{\mathcal{R}}{1+\mathcal{R}}\Theta_1 - \frac{k}{3(1+\mathcal{R})}\Theta_0 = \frac{k\Psi}{3} \tag{2.74}$$

differentiating equation 2.70 and inserting in the last expression we obtain:

$$\ddot{\Theta}_0 + k\left[\frac{k\Psi}{3} - \frac{\dot{a}}{a}\frac{\mathcal{R}}{1+\mathcal{R}}\Theta_1 + \frac{k}{3(1+\mathcal{R})}\Theta_0\right] = -\ddot{\Phi} \tag{2.75}$$

Finally using equation 2.70 we have:

$$\ddot{\Theta}_0 + \frac{\dot{a}}{a}\frac{\mathcal{R}}{1+\mathcal{R}}\dot{\Theta}_0 + k^2c_s^2\Theta_0 = -\frac{k^2}{3}\Psi - \frac{\dot{a}}{a}\frac{\mathcal{R}}{1+\mathcal{R}}\dot{\Phi} - \ddot{\Phi} \equiv F(k,\eta) \tag{2.76}$$

$F(k,\eta)$ is the forcing function (function of k and the conformal time η) and c_s is the sound speed given by:

$$c_s = c\sqrt{\frac{1}{3(1+\mathcal{R})}} \tag{2.77}$$

In the case of a baryon-free relativistic fluid $c_s = c/\sqrt{3}$. Hence, we have acoustic waves propagating within the plasma until photons and baryons decouple. When the temperature of the Universe drops off to 3000 K, baryonic matter starts recombination to create neutral atoms and radiation decouples from baryons. Moreover, acoustic waves *freeze* at a distance given by the acoustic horizon. Baryon overdensity attracts dark matter also by gravitational interaction but photons stream away freely, and thus, we will have an excess of probability of finding objects at the sound horizon distance. This process is depicted in Figure 2.7. Given the sound speed of the equation 2.77 we have that the acoustic horizon is given by:

$$r_s(z_{dec}) = \frac{c}{\sqrt{3}}\int_0^{1/(1+z_{dec})} \frac{da}{a^2H(a)\sqrt{1+(3\Omega_b/4\Omega_\gamma)a}} \text{ Mpc h}^{-1} \tag{2.78}$$

at which z_{dec} is the redshift at decoupling and is analitically described by [58]:

$$z_{dec} = 1291\frac{(\Omega_m h^2)^{0.251}}{1+0.659(\Omega_m)^{0.828}}\left[1+b_1\left(\Omega_b h^2\right)^{b_2}\right] \tag{2.79}$$

$$b_1 = 0.313\left(\Omega_m h^2\right)^{-0.419}\left[1+0.607\left(\Omega_m h^2\right)^{0.674}\right] \tag{2.80}$$

$$b_2 = 0.238\left(\Omega_m h^2\right)^{0.223} \tag{2.81}$$

The BAO overdensity translates to a bump or peak in the correlation function at the sound horizon distance $r_s \approx 110$ Mpc h^{-1} (See Figures 2.6, 2.4). As aforementioned, those oscillations froze out after recombination and, hence, the BAO scale constitutes a standard ruler, since it is constant in comoving coordinates and we can use it in order to test the geometry of the Universe. The BAO is a three-dimensional process, hence, it is possible to measure the BAO scale in 3D, both in the angular and in the radial directions. If we are able to measure angular and radial BAO scale for different epochs, we can also trace the evolution of the Universe (see Figure 2.8). This bump in the correlation function translates into wiggles in the power spectrum (see Figure 2.1).

Status of the BAO measurement

The first significant detection of the BAO signal using the distribution of galaxies was made by Eisenstein *et al.* in 2005 [70] using 46748 Luminous Red Galaxies (LRGs) from SDSS project. Since then, many other measurements have been made [71], [72], [73]. The first measurement of BAO using photometric information

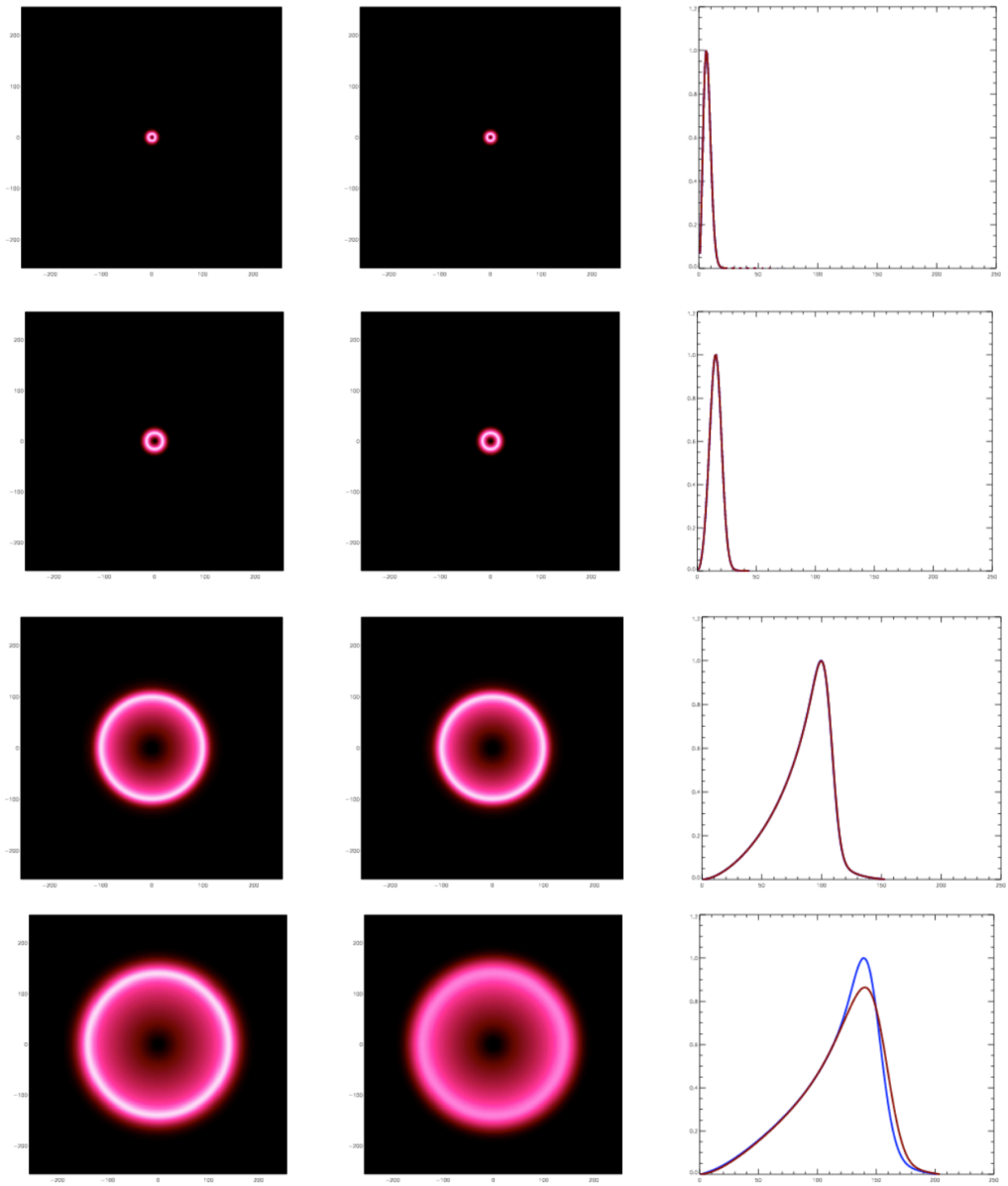

Figure 2.7: Starting with a perturbation (top panel) baryons (left panels/blue in the plots at the right) and photons (center panels/red in the plots at the right) are coupled and the pressure drives out the sound wave. Photons and baryons travel together until decoupling (third panel). Then photons stream away freely (bottom panel). Figure from Martin White.

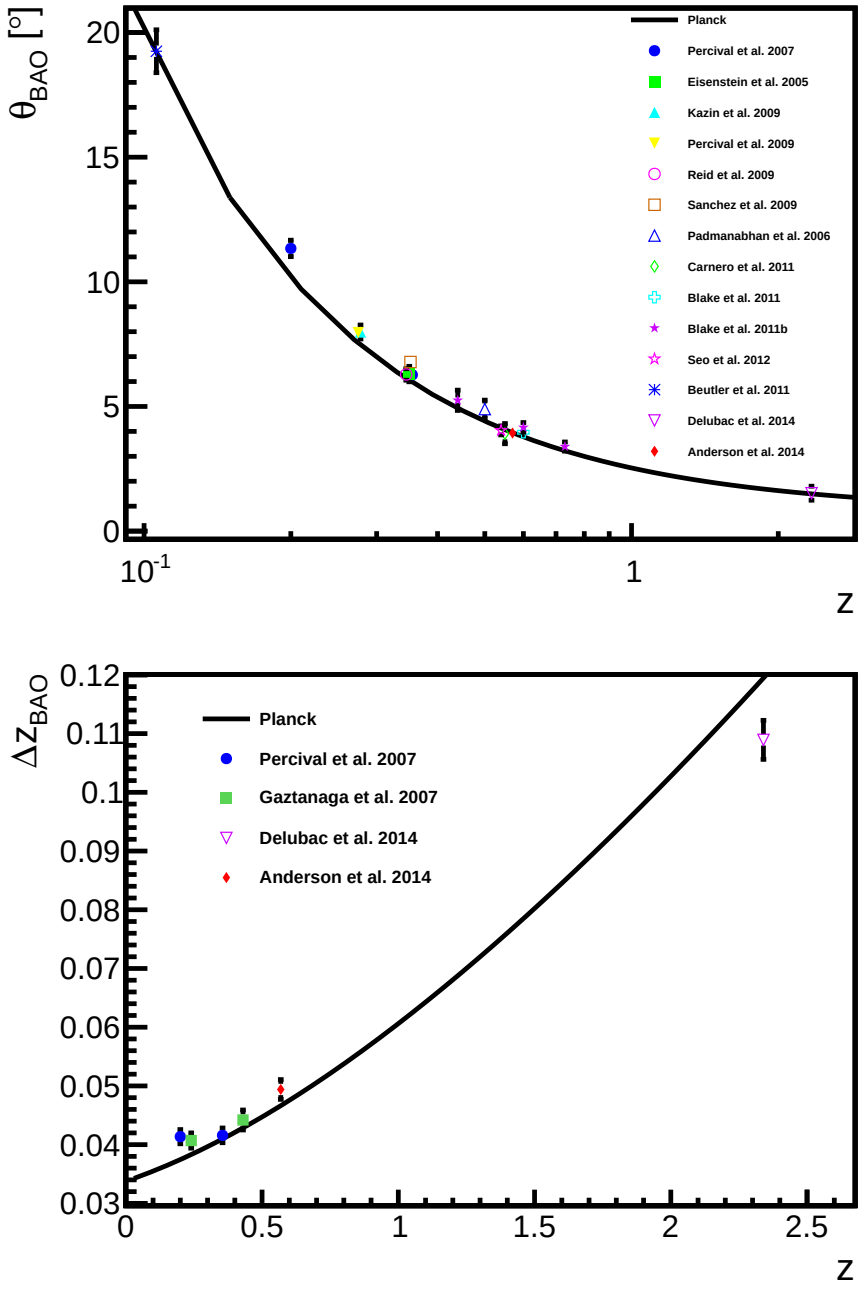

Figure 2.8: Status of the angular and radial BAO measurement and evolution of theses scales with redshift.

was made by Padmanabhan *et al.* using SDSS DR3 [74] and there are also measurements of BAO from quasars using the Lyman-α forest [75]. Today, a precise diagram of distance versus redshift has been built up to $z \sim 0.7$ which can be seen at Figure 2.8. Future galaxy surveys will extend this until $z \sim 1.5$. This is going to be one of the main cosmological probes of the Dark Energy Survey (DES). Using quasars complementary measurements, this diagram can be extended up to $z \sim 2$. We have introduced the underlying theory to study the Large Scale Structure (LSS) of the Universe and, in the following chapter, we will present and test to probe it.

Chapter 3

LSS with Galaxy Surveys: Simulations

In this chapter the different methods developed to study the Large Scale Structure of the Universe are presented as well as their implementation in galaxy surveys. First we show the study of a model independent way to extract the radial and angular BAO. Afterwards, we present a method to test the Cosmological Principle in photometric redshift galaxy surveys. We also present a study of the angular BAO, and finally, we introduce a method to study $\omega(\theta)$ and extract cosmological information oriented to DES. The latter study will be repeated with real DES data in the next chapter.

3.1. Baryon Acoustic Oscillations: MICE

In the preceding chapters we have described the power and robustness of the Baryon Acoustic Oscillation scale measurement. Since it is a fixed scale in comoving distance and consitutes a *standard ruler*, it is a powerful tool for cosmology. However, the most usual approach to measure BAO is through the assumption of a fiducial cosmology. This has the inconvenience of being model-dependent. In this context we developed a new technique to extract the BAO scale from galaxy surveys. We describe in this section, this novel technique for the radial BAO and combine it with a similar, model-independent approach for the angular BAO. The combined constraining power on cosmological parameters is compared with the standard method used in the literature.

3.1.1. Introduction

We have developed and tested a new, model independent method to recover the radial BAO scale [76] using a large N-body simulation capable of reproducing the geometry (e.g. area, density and depth) and general features of a large galaxy survey. The simulated data were kindly provided by the MICE project team, and consisted of a distribution of dark matter particles (galaxies, from now on) with the cosmological parameters fixed to a flat ΛCDM model with $\Omega_m = 0.25$, $\Omega_\Lambda = 0.75$, $\Omega_b = 0.044$, and, $n_s = 0.95$. The redshift distribution of the galaxies is shown in Figure 3.1. The simulation covers one octant of the full sky in the redshift range $0.1 < z < 1.5$, and contains 55 million galaxies in the lightcone. This simulation [1], has a comoving size $L_{box} = 3072\ h^{-1}$ Mpc and more than 8×10^9 particles ($m_p = 2.3 \times 10^{11} h^{-1} M_\odot$). More details about this simulation can be found in [77], [78] and [79]. The simulated catalog contains the effect of redshift space distortions, fundamental for the study of the radial BAO scale. Data with similar characteristics are expected in future large galaxy surveys, such as DESI [80] or EUCLID [81].

The main challenge for this radial BAO determination resides in the fact that this measurement needs a very large survey volume. We tried to extract the radial BAO peak from catalogs with smaller areas (200, 500 and 1000 sq-deg), finding a very small significance, or no detection at all in most cases. This is due to the fact

[1] http://www.ice.cat/mice

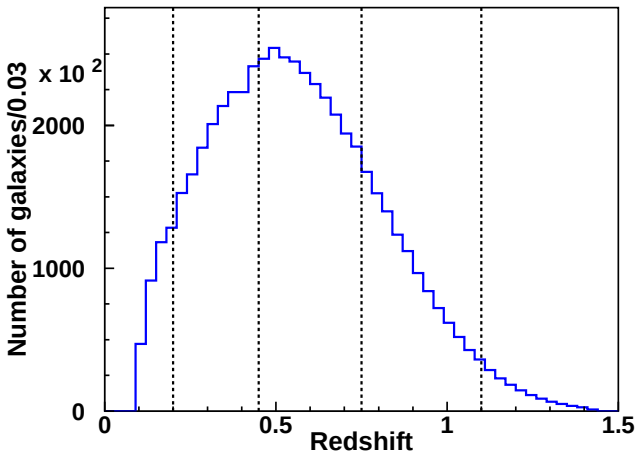

Figure 3.1: $N(z)$ in the used MICE catalog. The simulation contains 55 million galaxies in the redshift range $0.1 < z < 1.5$. The vertical dashed lines show the limits of the redshift bins used in the analysis.

that the statistical error related to the cosmic variance is specially large for the radial correlation function, and therefore it can only be reduced by increasing the volume explored.
It is in this light that we divided the catalog in four different redshift bins. These bins are large enough to enclose a big volume but, not too large in order to avoid a large projection effect [76]. We apply the method described in [76] for each bin and obtain the correlation functions using the Landy-Szalay estimator [82]. We count pairs of galaxies within certain radial separation, this radial separation it's just the redshift difference of two collinear galaxies in a given redshift bin. The corresponding results are shown in Figure 3.3. We have used an angular pixel with a size of 0.25 square degrees, in order to retain enough number of galaxy pairs in the collinear direction. The generation of the random catalog is made taking into account the $N(z)$ distribution of objects in the simulation. The reason behind this choice is that, if we don't consider the $N(z)$ distribution, we are introducing a false structure (induced by the underlying distribution) that would bias the results. Then, we fit these points to the sum of two exponentials and a Gaussian around the BAO peak:

$$\xi_{\parallel}(\Delta z) = A + Be^{-C\Delta z} + De^{-E\Delta z} + Fe^{-\frac{(\Delta z - \Delta z_{BAO})^2}{2\sigma^2}} \tag{3.1}$$

Errors have been computed using two different approaches. The first one relies in the theoretical expression in equation 3.2 [76]:

$$C_{\parallel}^{\xi}(\pi_1, \pi_2) \equiv \frac{1}{\pi^2} \int_0^{\infty} dk_{\parallel}\, \bar{\cos}(k_{\parallel}\pi_1)\, \bar{\cos}(k_{\parallel}\pi_2)\, \left[\mathfrak{P}_{\parallel}(k_{\parallel}, \Delta\sigma)\right]^2, \tag{3.2}$$

This equation is just a generalization of the Gaussian errors presented in chapter 2. This estimate relies on the model used for the computation, but we expect little variation of the error with the cosmological model. The other one, is using many realizations, dividing the total area in patches of different sizes and computing the corresponding dispersions and covariance matrices. This method can be applied in real data and also, keeps the analysis fully model independent. We have then obtained the error for the total area, scaling this estimates to the full area of the measurement. Both determinations agree in the region of interest for the BAO scale measurement, as shown in Figure 3.2. There is a disagreement for small scales, which is coming from the incomplete description of the non-linearities in the theoretical calculation, where the mode-mode coupling effects are neglected, and from boundary effects in the realizations. The statistical significance of the BAO observation is computed by measuring how different is the F parameter of the fit from zero using its statistical error. In the first bin it is very low ($\sim 1.4\sigma$) and it is consequently not considered in the cosmological analysis. This is due to the combination of two factors: on the one hand, the large cosmic variance for lower redshifts

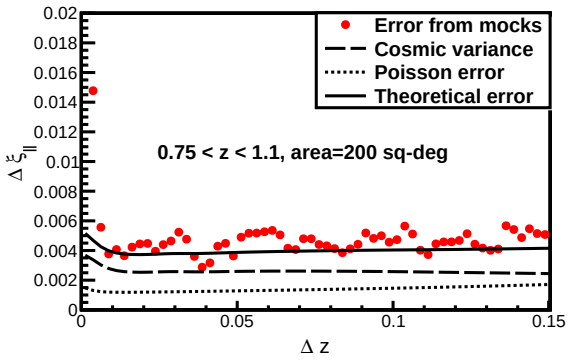

Figure 3.2: Comparison of the different estimates of the error in the radial correlation function are shown. The estimates are MC samples (dots) and theoretical calculation (solid line). They agree in the region of interest for the BAO analysis. The disagreement at low scales comes from the incomplete description of the non-linearities, where the mode-mode coupling effect is neglected, and from some boundary effects in the realizations, but it does not affect the BAO scale measurement since it is outside the fitting region. The different contributions to the total error are shown. They come from Poisson shot noise (dotted line) and cosmic variance (dashed line). The contribution of the Poisson shot noise is non-negligible.

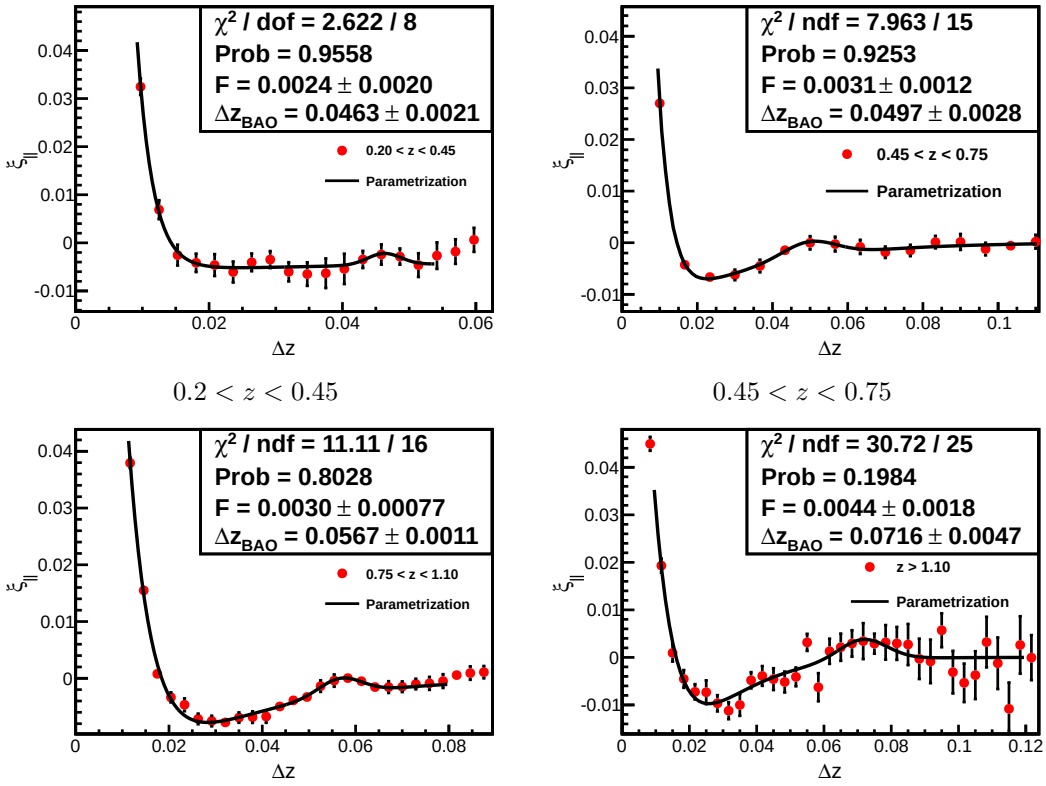

Figure 3.3: Radial correlation functions measured in the MICE simulation for the 4 redshift bins, for an angular pixel of 0.25 sq-deg, compared with the proposed parametrization (solid line). The statistical significance of the BAO detection in the first bin is very low, thus, it is not used in the cosmological analysis.

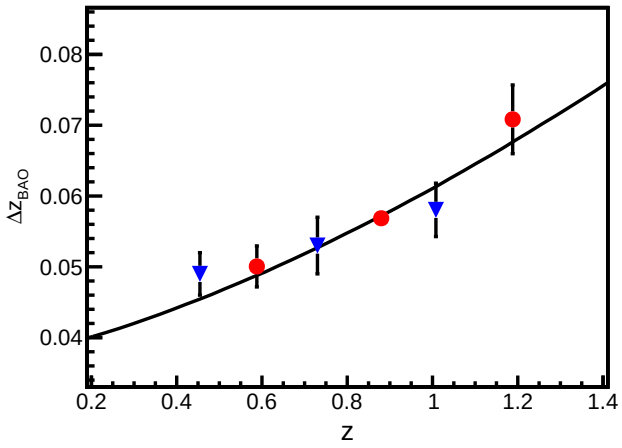

Figure 3.4: Measured radial BAO scale as a function of the redshift in MICE. Dots are the nominal bins and triangles correspond to displaced bins, and are measured only as a cross-check. All measurements are in good agreement with the theoretical prediction (solid line).

and, on the other hand, the large projection effect. The measured values of the BAO scale as a function of the redshift can be seen in Figure 3.4 as dots. The results for three alternative bins shifted with respect to the nominal ones are also shown as triangles. These have not been used to obtain cosmology results, since they are fully correlated with the red ones. They are only shown for illustration and verification purposes. We have used in this analysis the center of the redshift bin to obtain the prediction of the model, although what is really observed is the average within the bin. We have verified that they are very close if the $N(z)$ distribution is smooth, as it is in this case.

3.1.2. Systematic Errors

Systematic error estimation is one of the key elements for every analysis. We estimated those systematic uncertainties that affect the determination of the radial BAO scale using this method. There is one specific systematic effect associated to the method, which is coming from the size of the angular pixel which defines what we call collinear galaxies. Other systematic errors are generic and will be present in any determination of the BAO scale: the influence of the non-linearities, the starting and end point of the fit to the correlation function and the possible influence of the galaxy bias in the measurement.

Size of the Angular Pixel

The specific systematic error associated to this method is the possible influence that the size of the angular pixel has on the determination of the radial BAO scale, since it determines which galaxies are considered collinear in the analysis. The effect of different pixel sizes on the radial correlation function can be seen in Figure 3.5. The radial correlation function clearly changes on small scales, but this effect does not change the position of the BAO peak (Figure 3.5). These small scale effect comes from the smoothing of the correlation function due to the inclusion in the calculation of galaxy pairs which are not exactly collinear. For a larger angular pixel, the effect is larger. However, the scale where this effect acts is fixed by the angular pixel size, which is very far away from the BAO scale, that remains, therefore, unaffected, since the parametrization is able to absorb the change in the slope of the function.
In order to quantify this influence on the determination of the BAO scale as a systematic error, we have repeated

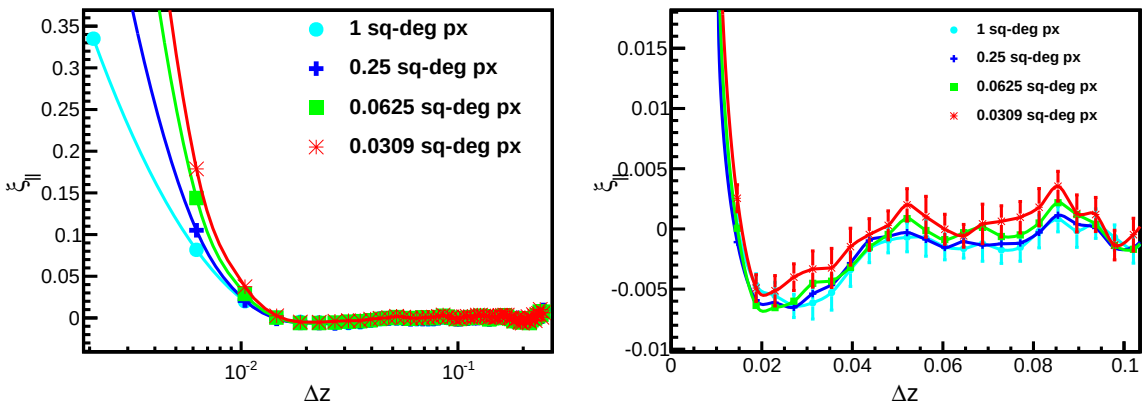

Figure 3.5: Effect of the angular pixel size on the radial correlation function. The finite size of the angular pixel induces a change on the slope of the correlation function at small scales (top), but when a zoom around the position of the BAO peak is done, it is clear that this effect does not change the position of the BAO peak (bottom). The effect is shown for pixels of sizes 0.0309 (stars), 0.0625 (squares), 0.25 (crosses) and 1 (dots) square degrees. The 0.25 sq-deg pixel has been used to obtain the cosmological parameters. The change in the slope arises from the smoothing effect produced by the inclusion in the calculation of galaxy pairs which are not exactly collinear. This effect does not affect the determination of the BAO scale.

the full analysis for different pixel sizes. The obtained results are shown in Figure 3.6. The radial BAO scale is recovered with high precision for any angular pixel size, even for sizes as large as 1 square-degree, which corresponds to a range of two orders of magnitude. The associated systematic error can be estimated to be $\delta(\Delta z_{BAO}) = 0.20\%$, much smaller than the statistical error for the nominal pixel size of 0.25 sq-deg, which is shown as error bars.

Non-linearities

Another systematic effect is the error due to the uncertainty in the goodness of the parametrization for different theoretical effects (non-linearities at the scale of the BAO peak). This value has been computed obtaining a global error of 0.10%. This was estimated in a conservative way as the difference between the Δz_{BAO} measured using linear and non-linear $\xi_{\parallel}(\Delta z)$, for the same redshift bins of the analysis. Non-linearities are computed using the RPT formalism [67], excluding mode-mode coupling, since it only affects small scales, far enough from the BAO scale. The contribution of these uncertainties to the systematic error can be estimated as $\delta(\Delta z_{BAO}) = 0.10\%$.

Galaxy Bias

The galaxy bias can influence the determination of the BAO scale only through the changes in the goodness of the parametrization of the correlation function for different biases. To estimate the contribution of the galaxy bias, we have repeated the analysis with different values of the bias, to obtain the propagation of the uncertainty in the galaxy bias for the selected galaxy population to the measured value of the radial BAO scale. The influence on the peak position is small, and we can estimate the associated systematic error as $\delta(\Delta z_{BAO}) = 0.15\%$. Moreover, we have tested the effect of a scale dependent bias, introducing artificially the effect in the correlation functions, using an approximate Q-model [83]. The bias variation with Δz in the fitted region of $\xi_{\parallel}(\Delta z)$ ranges from 1% to 6%, but the measurement of the BAO scale is insensitive to these changes. We estimate the systematic error in the presence of a scale dependent bias as $\delta(\Delta z_{BAO}) = 0.20\%$.

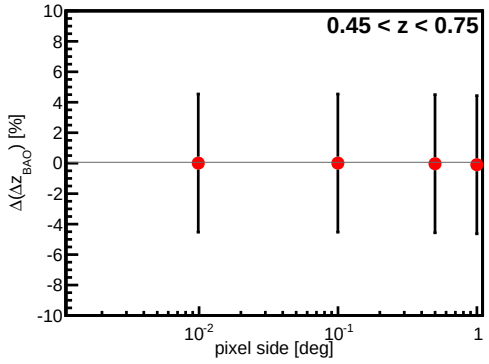

$0.45 < z < 0.75$

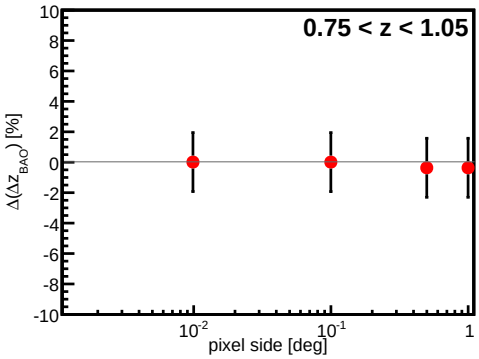

$0.75 < z < 1.05$

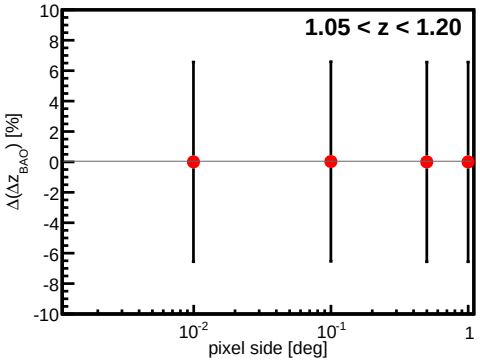

$1.05 < z < 1.2$

Figure 3.6: Variation of the radial BAO scale determination as a function of the angular pixel size for different redshifts. Results are stable, and the maximum variation is always of a few parts per mille, very well below 1%, even if the range in pixel sizes covers two orders of magnitude. The error bars indicate the size of the statistical error for the nominal pixel size of 0.25 sq-deg, including Poisson shot noise and cosmic variance, for the used simulation, that covers 1/8 of the sky.

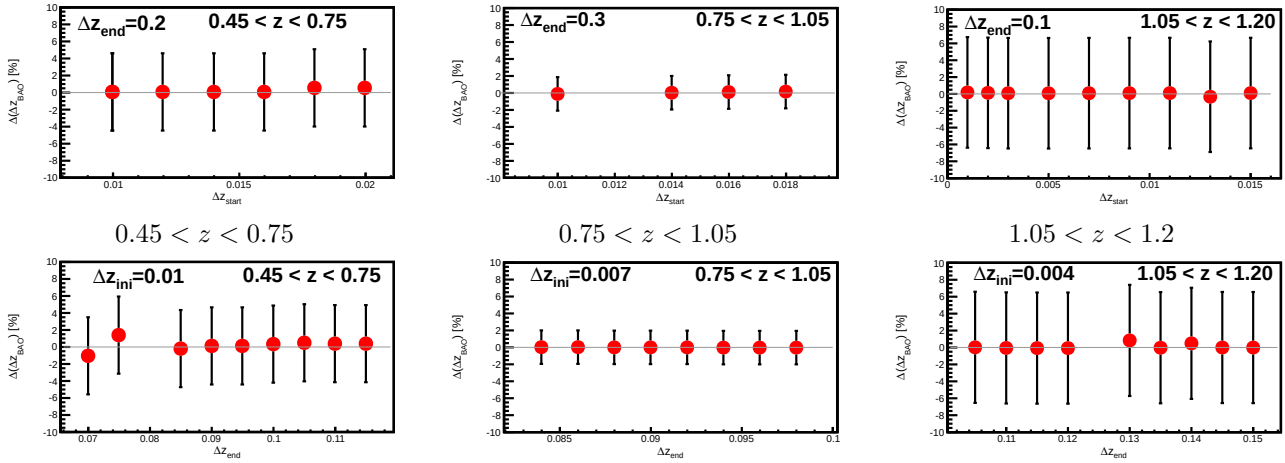

Figure 3.7: Δz_{BAO} evolution as a function of the starting and end point of the fitted region. Results are stable, confirming that the systematic error is small. The error bars indicate the size of the statistical error, including Poisson shot noise and cosmic variance, for the used simulation, that covers 1/8 of the sky.

Starting and End Point of the Fit

To compute the systematic error associated to the parametrization method, we used theoretical radial correlation functions with the same bin widths and central redshifts as those in the analysis of the MICE simulation. The error associated to the method comes from the possible influence in the obtained Δz_{BAO} of the range of Δz used to perform the fit. To evaluate the error, we have varied this range for the 3 redshift bins where we have a significant detection of the BAO scale, and performed the fit for each range.
We should choose a starting point at angles smaller than the BAO peak, where physics are determined by non-linearities, and an end point after the peak, beyond the effects of cosmic variance may be relevant. By varying these two points we can study how much the result varies with this decision. Results can be seen in Figure 3.7, where the obtained Δz_{BAO} is shown for different starting points and end points of the fit, for the 3 redshift bins. In all cases, the uncertainty is of the order of 0.1%. We assign this value as the associated systematic error. This uncertainty is much smaller than the statistical error, including Poisson shot noise and cosmic variance, which is depicted as error bars.

Total Systematic Error

The different sources of the systematic errors are completely independent, and therefore, we can compute the total systematic error by summing quadratically these contributions, resulting on a value of $\delta_{SYS}(\Delta z_{BAO}) = 0.33\%$.

There are some other potential systematic errors, the gravitational lensing magnification, which introduces a small correlation between redshift bins, or those mainly associated to the instrumental effects which could affect the used galaxy sample. However, these effects are expected to be much smaller than the considered ones and we have neglected them in this analysis.

3.1.3. Cosmological Constraints

The evolution of the measured radial BAO scale, including the systematic errors, with redshift is shown in Figure 3.4. The cosmological model of the simulation is the solid line. The recovered BAO scale is perfectly compatible with the true model, demonstrating that the method works.

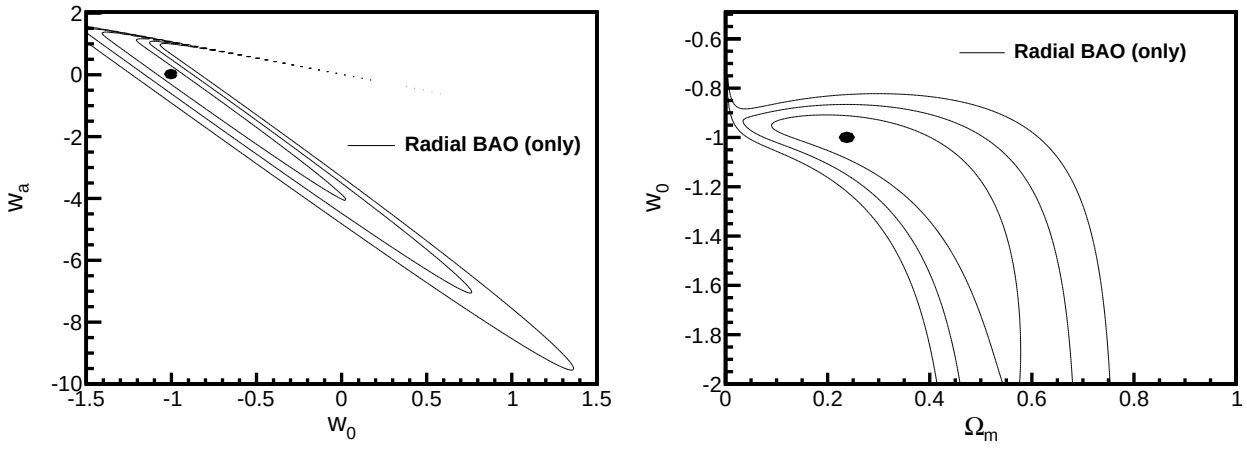

Figure 3.8: Contours at 1σ, 2σ and 3σ C. L. on the plane (w_0, w_a) (left) and on the plane (Ω_M, w_0) (right) obtained from the analysis of the radial BAO scale. The dot shows the value of the parameters for the MICE cosmology. No combination with any other cosmological probe is included. The other parameters have been fixed to the values of the MICE cosmology.

When these measurements are translated into constraints on the cosmological parameters, we obtain the results depicted in Figure 3.8, where the contours for 1σ, 2σ and 3σ C. L. in the (w_0, w_a) plane are shown at the left panel. The right panel shows the same contours in the (Ω_M, w_0) plane. To obtain the constraints on the cosmological parameters, we have performed a χ^2 fit to the evolution of the measured radial BAO scale with the redshift to the model,

$$\Delta z_{BAO} = r_S(\Omega_M, w_0, w_a...)\ H(z, \Omega_M, w_0, w_a...), \tag{3.3}$$

where r_S is the sound horizon scale at the baryon drag epoch and $H(z, \Omega_M, w_0, w_a...)$ is the Hubble parameter. We leave free those cosmological parameters which are shown in the Figures, while all other parameters have been kept fixed to their values for the simulation. The cosmology of the simulation is recovered, and the plot shows the sensitivity of the radial BAO scale alone, since no other cosmological probe is included in these constraints.

3.1.4. Measurement of the angular BAO scale

We also measured the angular BAO scale in in this simulation in order to combine the angular and radial scales to obtain the full power of this model independent BAO method. To do that we used the approach present in [73] for 10 redshift bins of 0.1 binwidth, starting at redshift 0.2 up to redshift 1.2. We find statistically significant results in 9 of them. Results are presented in Figure 3.10. An important point is that the redshifts for this galaxy sample are spectroscopic, consequently, the systematic error associated to the photometric redshift quoted in [73] does not affect these measurements.

3.1.5. Combination of radial and angular BAO scales

We have combined the results of this analysis with the radial BAO scale, using the same approach of the previous section. For the angular analysis, the BAO scale is described as

$$\theta_{BAO} = \frac{r_S(\Omega_M, w_0, w_a...)}{(1+z)\ d_A(z, \Omega_M, w_0, w_a...)}, \tag{3.4}$$

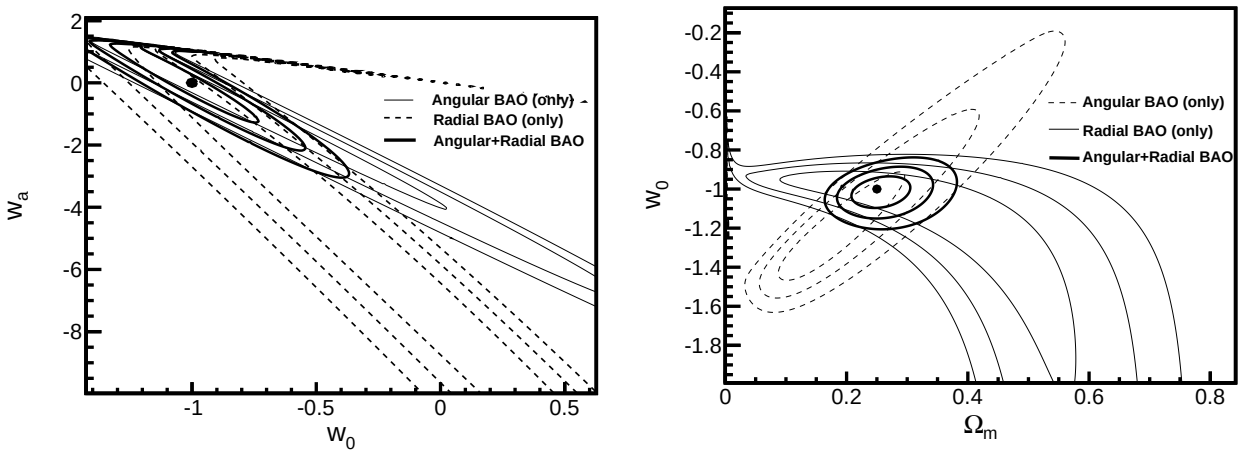

Figure 3.9: Contours at 1σ, 2σ and 3σ C. L. on the plane (w_0, w_a) (left) and on the plane (Ω_M, w_0) (right) from radial BAO (thin solid lines), angular BAO (thin dashed lines) and the combination of both (thick solid lines). The dot shows the value of the parameters for the MICE cosmology. No other cosmological probe is included in this result, showing the high sensitivity that the BAO standard ruler can achieve. The other parameters have been fixed to their values in the MICE cosmology.

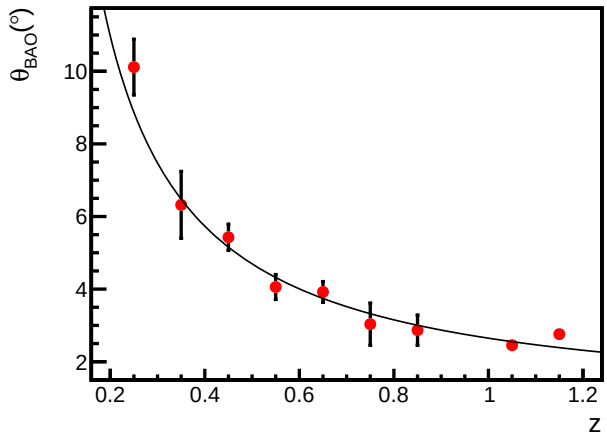

Figure 3.10: Measured angular BAO scale as a function of the redshift in the MICE simulation using the method described in [73]. Dots are the measured values of θ_{BAO} and the solid line is the prediction for the cosmology of the simulation.

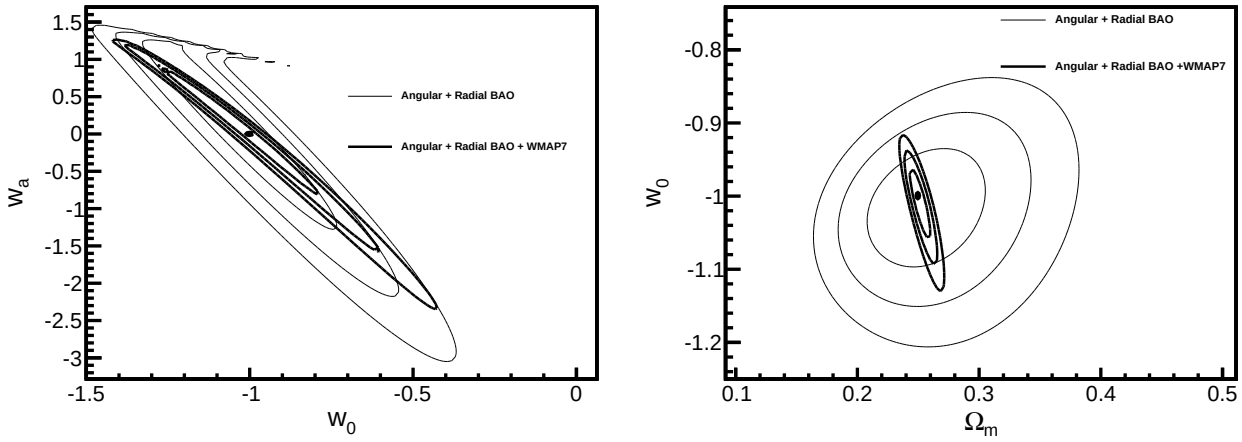

Figure 3.11: Contours at 1σ, 2σ and 3σ C. L. on the plane (w_0, w_a) (left) and on the plane (Ω_M, w_0) (right) from BAO (both radial and angular), depicted as thin solid lines, and adding also the CMB distance measurements, depicted as thick solid lines. The dot shows the value of the parameters for the MICE cosmology. The covariance matrix of WMAP7 has been used, while the central value of the measurement has been taken at the MICE cosmology. The other parameters have been fixed to their values in the MICE cosmology.

where $d_A(z, \Omega_M, w_0, w_a...)$ is the angular diameter distance. The constraints on the (w_0, w_a) plane coming from this determination of the angular BAO scale can be seen in Figure 3.9 (left) as thin dashed lines, and correspond to the 1σ, 2σ and 3σ C. L. contours. The sensitivity of the angular BAO scale is complementary to that of the radial BAO, shown as the thin solid lines. When combined, the contours represented by the thick solid lines are found. The same constraints for the (Ω_M, w_0) plane are shown in the right panel of Figure 3.9. These constraints are as precise as what is usually quoted for the BAO standard ruler, which is based on the use of the monopole of the 3-D correlation function. It is important to remark that these constraints are obtained only with the BAO standard ruler, independently of any other cosmological probe, which shows the real power of the standard ruler method when the full information is used.
We provide also the combined result of BAO, both radial and angular, with the distance measurements from CMB using the WMAP7 covariance matrix [84] and assuming the measurements correspond to the MICE cosmology. The combination has been performed following the procedure as detailed in [85]. The corresponding contours at 1σ, 2σ and 3σ C. L. are presented in Figure 3.11 both in the plane (w_0, w_a) (left) and in the plane (Ω_M, w_0) (right) as thick solid lines, and compared with the result using only BAO (both radial and angular), which is presented as the thin lines. As before, the other parameters have been kept fixed. There is an important improvement in the precision of the determination of the corresponding parameters in both cases. It is larger in the (Ω_M, w_0) plane, showing that a precise measurement can be achieved when all the information provided by the BAO scale is included in the fit.

3.1.6. Comparison with Other Methods

In order to compare our results, obtained combining radial and angular BAO scale determinations, with the standard approach of measuring the position of the sound horizon scale in the monopole of the two-point correlation function, we performed on our mock catalog the same analysis that was carried out to obtain the result by the BOSS collaboration [38]. We calculated the three-dimensional correlation function $\xi(r)$ using the Landy and Szalay estimator in the three wide redshift bins used for the analysis of the radial BAO ($0.45 < z < 0.75$, $0.75 < z < 1.10$ and $1.10 < z$). We chose these wide bins in order to maximize the number of pairs that contribute to the measurement of the monopole, since this is one of the key advantages of the standard method. In order to calculate $\xi(r)$, redshifts must be translated into distances. We have used the true cosmology of the

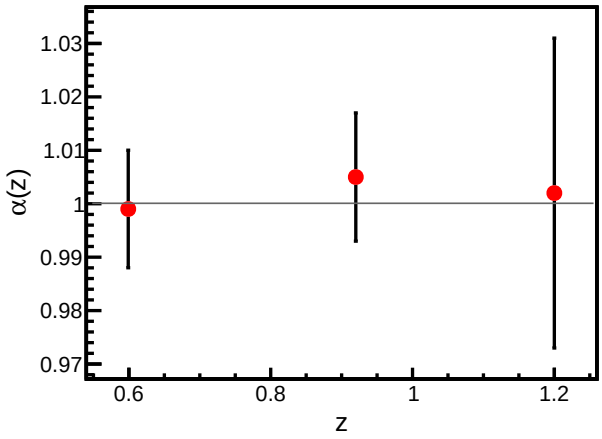

Figure 3.12: Values of the scaling parameter α measured from the three bins of the MICE mock catalog. The input cosmology ($\alpha \equiv 1$) is recovered well within errors.

MICE simulation to ensure that our results will not be biased by this choice.
The covariance matrix was calculated using the Gaussian approach [86]. This calculation was validated by comparing it with the errors computed from subsamples of the total catalog, and both estimations were found to be compatible within the range of scales needed for the analysis. As it is done in [38], we fit the model

$$\xi_{\rm fit}(r) = B^2\,\xi_{\rm th}(\alpha\, r) + a_0 + \frac{a_1}{r} + \frac{a_2}{r^2}, \tag{3.5}$$

to the estimated correlation monopoles. Here, $\xi_{\rm th}(r)$ is a template theoretical correlation function corresponding to the fiducial cosmological model used to translate redshifts into distances in the survey, in our case the MICE cosmology. This template was calculated from the `CAMB` [59] linear power spectrum for the MICE cosmology, and corrected for non-linearities via the RPT damping factor. We are mainly interested in the fitting parameter α, which relates real and fiducial scales:

$$\frac{d_V(z)}{r_s} = \alpha\,\frac{d_V^{\rm fid}(z)}{r_s^{\rm fid}}, \tag{3.6}$$

where $d_V(z) \equiv ((1+z)^2\, d_A^2(z)\, z/H(z))^{1/3}$ is the volume-averaged distance [70] and r_s the sound horizon scale. Since the true cosmology was used to translate redshifts into distances, the value of α must be compatible with 1. The statistical uncertainty in α was calculated following the same method used in [38].
We have not studied the different sources of systematic errors for this measurement, and no systematic contribution has been added to the errors. On the one hand this provides a more conservative comparison with our approach, since the results quoted in section 3.1.5 do contain systematics. On the other hand, there exist several potential systematics that are specific for the standard method, such as the effect of the fiducial cosmology used to obtain the three-dimensional positions of the galaxies, or the choice of template used to perform the fit. Studying this effect would be extremely interesting, but we have postponed this analysis for a future work. As we have seen before, the systematic errors that are common to both approaches (bias, RSDs, non-linearities, fitting limits) are clearly subdominant compared to the statistical uncertainties.

The cosmological constraints drawn in the $(\Omega_{\rm M}, w_0)$ and (w_0, w_a) planes from the values of α measured from the correlation functions are shown in Figure 3.13. The Figure also shows the contours corresponding to the combination of radial and angular information, described in the previous section, for comparison. Plots show that the constraining power of both methods is very similar. There is a degenerate direction in the $(\Omega_{\rm M}, w_0)$ plane for the standard method, which coincides with the orientation of the contours for the angular BAO shown in Figure 3.9 (right panel). This is a reasonable result: most of the information in the angle-averaged BAO

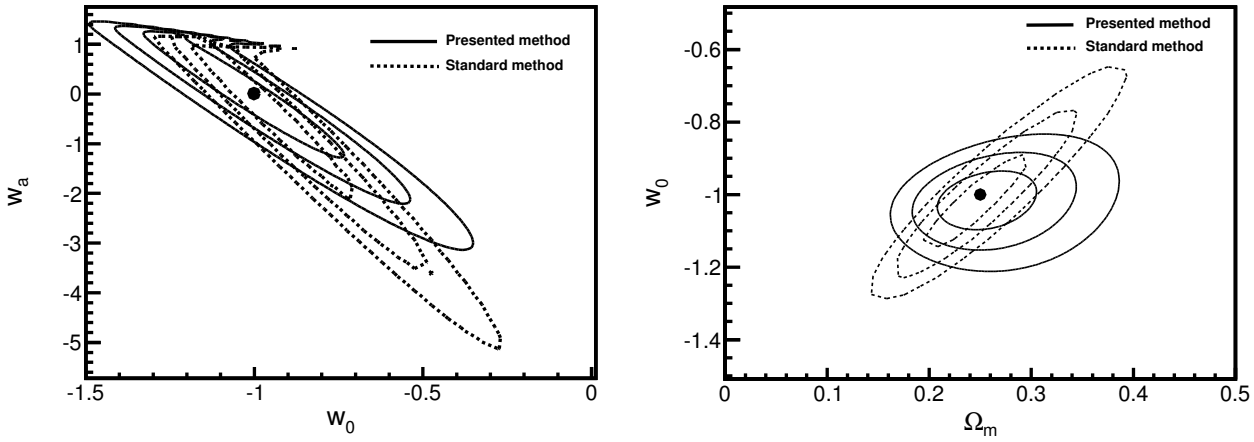

Figure 3.13: Contours at 1-σ, 2-σ and 3-σ confidence level in the planes (w_0, w_a) (left panel) and $(\Omega_{\rm M}, w_0)$ (right panel). The solid contours correspond to our combination of independent radial and angular BAO information, while the dashed lines correspond to the results drawn from the standard analysis of the angle-averaged BAO. The different correlation between parameters is due to the different treatment of the redshift space distortions.

signature comes from the angular part, since there are two transverse dimensions and only one longitudinal. On the other hand, our combined approach seems to be able to obtain better constraints on the evolution of the dark energy equation of state. This could be due to the fact that the radial BAO enables us to measure the evolution of the expansion rate alone, which is a local quantity, unlike the angular diameter distance, which is an integrated one depending on the expansion history. Although the degenerate directions are very similar for both methods, they are not exactly the same. The reason is the different treatment of the redshift space distortions, which are ignored, to first approximation, in the standard method when the angular average is performed. However, they are fully taken into account in our proposal, where the angular and radial correlation functions have very different shapes, mainly because of the redshift space distortions.

3.1.7. Conclusions

We developed and tested a new method to measure the BAO scale in the radial two-point correlation function. This method is adapted to the observational characteristics of galaxy surveys, where only the angular position on the sky and the redshift are measured for each galaxy. The sound horizon scale can be recovered from the non-linear radial correlation functions to a very high precision, only limited by the volume of the considered survey, since the systematic uncertainties associated to the determination of the BAO scale are very small, around 0.3%. On the other hand, the method is fully cosmology independent, since it relies only on observable quantities and, consequently, its results can be analyzed in any cosmological model.

The method has been tested with a mock catalog built upon a large N-body simulation provided by the MICE collaboration, in the lightcone and including redshift space distortions. The true cosmology is recovered within 1-σ. An evaluation of the main systematic errors has been included in this study, and we find that the method is very promising and very robust against systematic uncertainties. Note that this analysis over the MICE simulations is done on dark matter particles, instead of galaxies. This simplification is not an essential limitation to the method presented here, as we have shown that both the modelling and the error analysis are quite generic.

We have compared the cosmological constraints obtained by combining radial and angular BAO information

with those obtained by performing the standard analysis of the angle-averaged BAO signature on the same dataset and with the same fitting technique. Both methods seem to yield comparable constraints, with the advantage that our method is entirely based on purely observable quantities (redshifts and angles) and is therefore completely model-independent.

3.2. Observational validation of the Cosmological Principle

The measurement of the BAO is a strong cosmological tool since it gives a lot of information about the cosmological parameters. However, it cannot give us information about other Standard Model aspects such as the Cosmological Principle, which is assumed as an axiom for some cosmological analysis and needs to be tested as well. Thus, we introduce and test here a novel technique to probe the Cosmological Principle in photometric redshift galaxy surveys [112].

3.2.1. Introduction

As it was already mentioned in Chapter 1 the Standard Model of Cosmology is based on the Cosmological Principle. Thus, the validity of the Cosmological Principle is of paramount relevance, and therefore it is extremely important to verify it using unbiased observational probes. In this model, the homogeneous regime is only reached asymptotically on large scales, and is evidently not realized on small scales, as it can be seen in the form of the spectrum of matter perturbations and their evolution via gravitational collapse. Large-scale homogeneity is usually assumed without proof when analyzing certain cosmological probes [87]. This is often a reasonable approach, since it would not be possible to obtain many observational constraints without doing so. However, in order to be able to rely on these constraints, we must verify the validity of the Cosmological Principle independently in an unbiased way. This is not an easy task, since homogeneity must sometimes be assumed in order to cope with certain observational effects. These issues will be further explained in section 3.2.2. At the end of the day, we must ensure that the method used is able to distinguish homogeneous from non-homogeneous models to a reasonable level of precision. A robust and popular method to study the transition to homogeneity in the matter density field at late times is to analyze the fractality of the galaxy distribution in a redshift survey. Furthermore, fractal dimensions can be used to quantify clustering, since they depend on the scaling of the different moments of galaxy counts in spheres, which in turn are related to the integrals of n-point correlation functions.

As it has been said, the homogeneous regime is reached, within the standard ΛCDM model, at very large scales, and therefore a large survey volume is necessary in order to safely claim a detection of this transition. In this sense, photometric galaxy redshift surveys such as DES [51] provide a good framework for this study, since they are able to observe large numbers of objects distributed across wide areas and to further redshifts than their spectroscopic counterparts. The main caveat of these surveys is that, due to the lack of precision in the redshift determination, a large part of the radial information is lost, and we are only able to study angular clustering in different wide redshift slices. Hence, in order to study the fractality of the galaxy distribution with a photometric survey, the methods and estimators used in previous analyses must be adapted to draw results from angular information alone. This approach has as an advantage that, since angular positions are pure observables (unlike three-dimensional distances, which can only be calculated assuming a fiducial cosmology), the results obtained are completely model independent. We propose an observable, the angular homogeneity index $H_2(\theta)$, which could be used by photometric surveys to study the fractal structure of the galaxy distribution. In section 3.2.2 we describe one of the most popular observables used in the literature to study the fractality of the galaxy distribution, the correlation dimension D_2,and propose a way to adapt this quantity to the data available in a photometric galaxy survey.

Here, the angular homogeneity index $H_2(\theta)$ is presented and modelled in the ΛCDM cosmology. In section 3.2.3 we analyze the fractality of a set of ΛCDM mock galaxy surveys using the method described before and study the different effects that may influence this measurement. The ability of our method to distinguish

different inhomogeneous models is studied in section 3.2.4 by using it on different simulated inhomogeneous distributions. Finally, the main results of this work are discussed in section 3.2.5.

3.2.2. Fractality

There exist different statistical quantities that can be studied in order to quantify the fractality of a point distribution, such as the box-counting dimension, the different Minkowski-Bouligand dimensions or the lacunarity of the distribution (see [88] for a review of these). Here, we will focus on the Minkowski-Bouligand dimension of order 2, also called the correlation dimension, for the three-dimensional case. A simple modification of this observable will then allow us to study the fractality of the distribution from its angular projection.

The fractal dimension

For a given point distribution, let us define the correlation integral $C_2(r)$ as the average number of points contained by spheres of radius r centerered on other points of the distribution. For an infinite random point process in three dimensions, this quantity should grow like the volume

$$C_2(r) \propto r^3, \tag{3.7}$$

thus, we define the correlation dimension of the point process as

$$D_2(r) \equiv \frac{d\log C_2}{d\log r}. \tag{3.8}$$

Hence, if the galaxy distribution approaches homogeneity on large scales, D_2 must tend to 3 for large r.

For the canonical ΛCDM model, departures from this value are due to two different reasons. First, since the galaxy distribution is clustered due to the nature of gravitational collapse, there exists an excess probability of finding other galaxies around those used as centers to calculate D_2. Secondly, in practice, the point distributions under study are finite in size, and this introduces an extra contribution due to shot-noise. These two contributions have been modelled by [89] for the correlation integral:

$$\begin{aligned} &C_2(r) = \overline{N}(r) + [\Delta C_2(r)]_{\rm cluster} + [\Delta C_2(r)]_{\rm sn} \\ &[\Delta C_2(r)]_{\rm cluster} = \overline{N}(r)\,\bar{\xi}(r), \\ &[\Delta C_2(r)]_{\rm sn} = 1, \end{aligned} \tag{3.9}$$

and the correlation dimension

$$\begin{aligned} &D_2(r) = 3 + [\Delta D_2(r)]_{\rm cluster} + [\Delta D_2(r)]_{\rm sn} \\ &[\Delta D_2(r)]_{\rm cluster} = -3\,\frac{\bar{\xi}(r) - \xi(r)}{1+\bar{\xi}(r)}, \\ &[\Delta D_2(r)]_{\rm sn} = -\frac{3}{\overline{N}(r)}, \end{aligned} \tag{3.10}$$

where $\bar{\xi}(r)$ is the volume-averaged two-point correlation function of the distribution

$$\bar{\xi}(r) \equiv \frac{3}{r^3}\int_0^r s^2\xi(s)\,ds \tag{3.11}$$

and $\overline{N}(r) \equiv 4\pi\bar{n}\,r^3/3$ is the average number of objects inside spheres of radius r. Since the contribution due to shot noise will always be present in any finite distribution, we will substract it by hand in this work, and focus only on the clustering term.

The angular homogeneity index

The observables described in the previous section can be adapted straightforwardly to point distributions projected onto the 2-dimensional sphere. Instead of spheres of radius r, we will consider here spherical caps of radius θ.

In analogy with the three-dimensional case, we can define the angular correlation integral $G_2(\theta)$ as the average number of points inside spherical caps of radius θ centered on other points of the distribution. For a homogeneous distribution, this quantity should grow like the solid angle inside these spherical caps. However, since this volume $V(\theta) = 2\pi\,(1-\cos\theta)$ does not grow as a simple power of θ, a logarithmic derivative of G_2 with respect to θ would not capture the approach to homogeneity in a simple manner, independent of the angular radius. Therefore, we have preferred to define the homogeneity index $H_2(\theta)$ as the logaritmic derivative with respect to the volume:

$$H_2(\theta) = \frac{d\log G_2(\theta)}{d\log V(\theta)}, \tag{3.12}$$

which should tend to 1 if homogeneity is reached.

As in the three-dimensional case, these quantities can be modelled for a finite weakly clustered distribution:

$$G_2(\theta) = 1 + \overline{N}(\theta)\,[1+\bar{w}(\theta)], \tag{3.13}$$

$$H_2(\theta) = 1 - \frac{\bar{w}(\theta) - w(\theta)}{1+\bar{w}(\theta)} - \frac{1}{\overline{N}(\theta)}, \tag{3.14}$$

$$\overline{N}(\theta) \equiv 2\pi\,\bar{\sigma}\,(1-\cos\theta), \tag{3.15}$$

where $\bar{\sigma}$ is the mean angular number density of the distribution, $w(\theta)$ is the angular two-point correlation function and $\bar{w}(\theta)$ is defined in analogy to $\bar{\xi}(r)$:

$$\bar{w}(\theta) \equiv \frac{1}{1-\cos\theta}\int_0^\theta w(\theta')\,\sin\theta'\,d\theta'. \tag{3.16}$$

We will be interested in the departure of H_2 from its homogeneous value: $\Delta H_2(\theta) \equiv 1 - H_2(\theta)$. This quantity must not be mistaken with the statistical error on the determination of H_2, which we label σ_{H_2} here.

Measuring the transition to homogeneity

When trying to measure the fractal dimension or the homogeneity index from a realistic galaxy survey, different complications arise, mainly related with the artificial observational effects induced on the galaxy distribution, which must be correctly disentangled from the clustering pattern and from a possible fractal-like structure. For instance, unless a volume-limited sample is used, we will have to deal with a non-homogeneous radial selection function. Furthermore, the angular distribution of the survey galaxies will always contain imperfections, which may come, for example, from survey completeness, fiber collisions and star contamination for a spectroscopic survey, or CCD saturation in photometric catalogs. Although it would be desirable to be able to deal with these effects without making any extra assumptions about the true galaxy distribution, in order to make sure that our method of analysis is not biased towards a homogeneous solution, this is often not possible. The most popular method to circumvent these issues in the calculation of the two-point correlation function, is to use random catalogs that incorporate the same artificial effects as the data, and a similar approach may be used for our purposes. In this work we have considered three different estimators for D_2, which are described below.

For the i-th galaxy of the survey, let us define $n_i^d(<r)$ as the number of galaxies in the survey inside a sphere of radius r centered around i, and $n_i^r(<r)$ as the same quantity for an unclustered random distribution. For

N_c galaxies used as sphere centers, we can define the scaled counts-in-spheres $\mathcal{N}(r)$ as

$$\mathcal{N}(r) \equiv \frac{1}{N_c} \sum_{i=1}^{N_c} \frac{n_i^d(< r)}{f_r \, n_i^r(< r)}, \tag{3.17}$$

where $f_r \equiv D/R$ is the ratio of the number of galaxies in the survey to the number of points in the random catalog. Varying the prescription to estimate n_i^r and to select galaxies as sphere centers, we can define three different estimators:

1. **E1**. In the most conservative case, in order to avoid any assumptions about the galaxy distribution, around each galaxy we may only use spheres that fit fully inside the surveyed volume. Thus, the number of centers will be a function of r. Also, assuming that there are no other artificial effects in the galaxy distribution, we may estimate $n_i^r(< r)$ theoretically as

   $$n_i^r(< r) = \overline{N}(r) = \frac{4\pi}{3} r^3 \, \bar{n}_d, \tag{3.18}$$

   where $\bar{n}_d$ is the survey's mean number density and we have assumed $f_r = 1$.

   This estimator is very idealistic and problematic to use in a realistic scenario, in which observational effects are not negligible.

2. **E2**. While still using only complete spheres, we may use a random catalog that incorporates the same observational effects as the data to estimate $n_i^r(< r)$. This way we are able to study the fractality of a survey that is not volume limited, as well as to incorporate small-scale observational effects, without assuming anything about the galaxy distribution outside the survey.

3. **E3**. In order to maximize the use of the survey data, we may use all galaxies as sphere centers for all radii. This implies using spheres that lie partly outside the surveyed region, a fact that is accounted for by using a random catalog to estimate $n_i^r(< r)$ in those same spheres.

Once $\mathcal{N}(< r)$ is estimated, it can be directly related to the correlation integral through

$$C_2(r) = \overline{N}(r) \, \mathcal{N}(< r) - 1, \tag{3.19}$$

where we have explicitly substracted the shot-noise contribution. C_2 can then be used to calculate the fractal dimension through equation (3.8).

Two final points must be made regarding the use of random catalogs in order to deal with observational effects. First, we must be very careful to incorporate in these only purely artificial effects in order to minimize a possible bias of our estimator towards homogeneity. Even doing so, it is clear that the only way to avoid this bias is by using the estimator **E1** on a volume-limited survey using only regions that are 100% complete and free of any observational issues, however this is too restrictive for any realistic galaxy survey. This approach is impractical and, therefore, we have only considered the estimators **E2** and **E3** in the rest of this work. These estimators contain an extra contribution due to the finiteness of the random catalogs used to estimate $n_i^r(< r)$ (i.e., they are biased). This bias can only be suppressed by using many times more random objects than points in the data ($f_r \ll 1$). Note that in the limit of infinite random objects, and in the absence of artificial inhomogeneities, **E1** and **E2** are equivalent.

As it is shown in section 3.2.4, we have tested that the use of the least conservative estimator **E3** does not introduce any significant bias towards homogeneity by using it on explicitly inhomogeneous data. Since this estimator makes the most efficient use of the data, we have used it for most of the analysis presented in sections 3.2.3 and 3.2.4, and it will be assumed unless otherwise stated.

The estimators for $H_2(\theta)$ from a finite projected distribution can be constructed in analogy with the ones

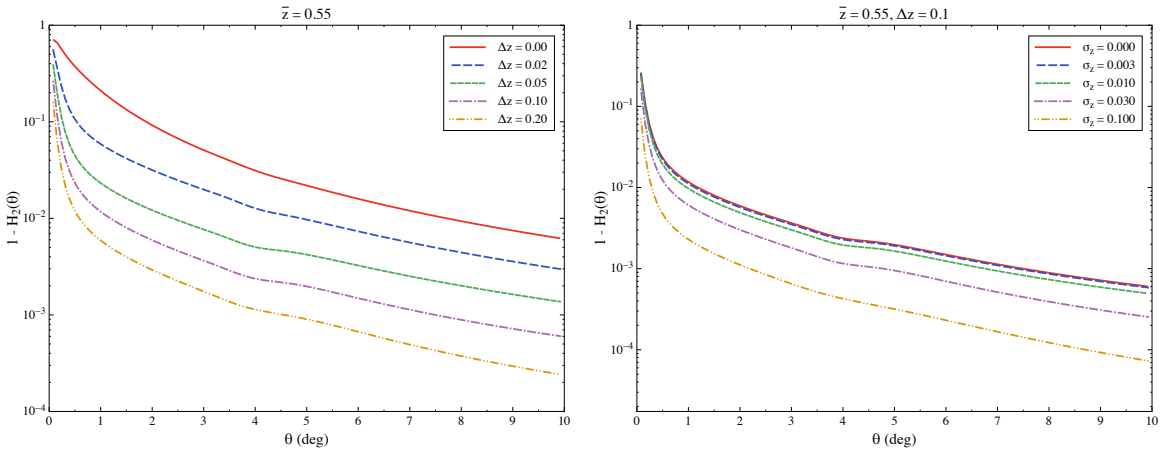

Figure 3.14: $\Delta H_2(\theta)$ as a function of θ for varying redshift bin size (left panel) and photometric redshift uncertainty (right panel). The use of thick redshift bins and photometric redshifts produces a more homogeneous distribution when projected on the sphere, reducing the amplitude of the correlation.

presented above for three-dimensional distributions. In this case, they are based on calculating the scaled counts-in-caps

$$\mathcal{N}(<\theta) \equiv \frac{1}{N_c} \sum_{i=1}^{N_c} \frac{n_i^d(<\theta)}{f_r\, n_i^r(<\theta)}, \tag{3.20}$$

using different prescriptions for N_c and $n_i^r(<\theta)$.

Modelling $H_2(\theta)$

As we have seen, the angular homogeneity index is directly related, to first order, with the angular two-point correlation function $w(\theta)$. Thus, in order to forecast the ability of a given galaxy survey to study the transition to homogeneity, we need to be able to model $w(\theta)$ correctly. This modelling has been covered previously in chapter 2. The effects of a non-zero photometric redshift error can be included in the selection function by convolving the true-z $\phi(z)$ with the photo-z probability distribution function. For the Figures shown in this section we used the flat ΛCDM parameters

$$(\Omega_M, \Omega_\Lambda, \Omega_b, h, \sigma_8, n_s) = (0.3, 0.7, 0.049, 0.67, 0.8, 0.96) \tag{3.21}$$

as a fiducial cosmology.

Projection effects and bias Different effects have an influence in the way the galaxy distribution approaches homogeneity. In the case that concerns us, that of data projected on the sphere, this projection effectively homogenizes the distribution. This is easy to understand: consider a pair of galaxies subtending a small angle but separated by a large radial distance. While they are far away, and therefore almost uncorrelated, they appear close when projected. This effect is obviously larger for wider redshift bins, and therefore $H_2(\theta)$ will approach 1 faster as we increase the binwidth. This effect is shown in the left panel of Figure 3.14. The effect of a large photo-z error is similar: the photo-z shifts galaxies from adjacent redshift bins, effectively making the bin width larger (see right panel of Figure 3.14).

On the other hand, galaxy bias modifies the homogeneity index in the opposite way. A positively biased population ($b > 1$) is more strongly clustered and therefore will reach the homogeneous regime on larger scales. This can be seen in Figure 3.15.

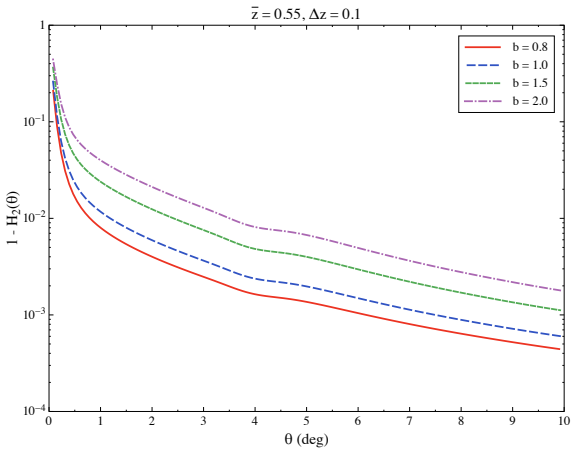

Figure 3.15: $\Delta H_2(\theta)$ as a function of θ for varying galaxy bias. A biased galaxy population will be more tightly clustered, and therefore will show a more evident departure from homogeneity.

Non-linearities As we said, homogeneity is reached in the standard cosmological model on relatively large scales. Therefore one might think that the modelling of the small-scale non-linear effects should be irrelevant. However, the angular homogeneity index (or the correlation dimension in 3D) depends on an integral quantity (number counts *inside* spheres), and therefore contains information about those small scales which may propagate to larger angles.

This is shown in Figure 3.16, where the angular homogeneity index for the bin $z \in (0.5, 0.6)$ has been plotted using different prescriptions to describe non-linearites. The solid red line shows the prediction using the `HALOFIT` [69] fitting formula (which provides the best fit to the mock data in section 3.2.3). The dashed blue line corresponds to the prediction in renormalized perturbation theory (RPT) [67] of the damping of the BAO wiggles due to non-linear motions, given by

$$\Delta P^{NL}_{\rm wiggles}(k) = \Delta P^{L}_{\rm wiggles}(k)\, \exp(-\sigma_v^2 k^2/2), \tag{3.22}$$

where $\Delta P_{\rm wiggles}$ is the BAO contribution to the power spectrum and

$$\sigma_v = \frac{1}{6\pi^2} \int_0^\infty P^L(k)\, dk. \tag{3.23}$$

As it can be seen, the extra clustering amplitude on small scales contributes as a visible offset in H_2 up to scales of $\mathcal{O}(1\,\mathrm{deg} \sim 20\,\mathrm{Mpc}/h)$.

Dependence on cosmological parameters Since the evolution of the matter perturbations depends on the background cosmological parameters, we can expect that some cosmological models will approach homogeneity faster than others. We have studied this dependence using our model for $H_2(\theta)$. Our aim is not to use the form of $H_2(\theta)$ to obtain precise cosmological constraints, since we do not think that this quantity contains more information than the two-point correlation function $w(\theta)$, for which there exist many different methods in the literature [73, 90]. However, we think that a qualitative characterization of the homogeneity index for different types of models is instructive and may give us some hints about how model-independent our results area.

In Figure 3.17 we have plotted $H_2(\theta)$ varying the values of the matter parameter Ω_M (left panel) and the dark energy equation of state w (right panel), from their fiducial values (eq. 3.21). As expected, larger values of Ω_M enhance the amplitude of inhomogeneities on small scales (i.e., make ΔH_2 larger). Likewise, more negative

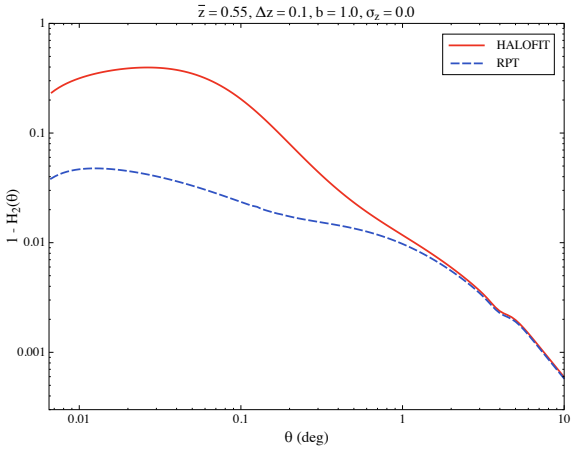

Figure 3.16: $\Delta H_2(\theta)$ as a function of θ for two different non-linearities prescriptions. Since the $H_2(\theta)$ depends on an integral quantity, it contains information about small scales. Thus, it is important to describe non-linear effects correctly. The solid red line corresponds to the prediction using the HALOFIT fitting formula, which fits well our mock catalogs. The prediction including only the damping of the BAO wiggles (dashed blue line) overpredicts $H_2(\theta)$ on small scales, although this offset decreases for larger angles.

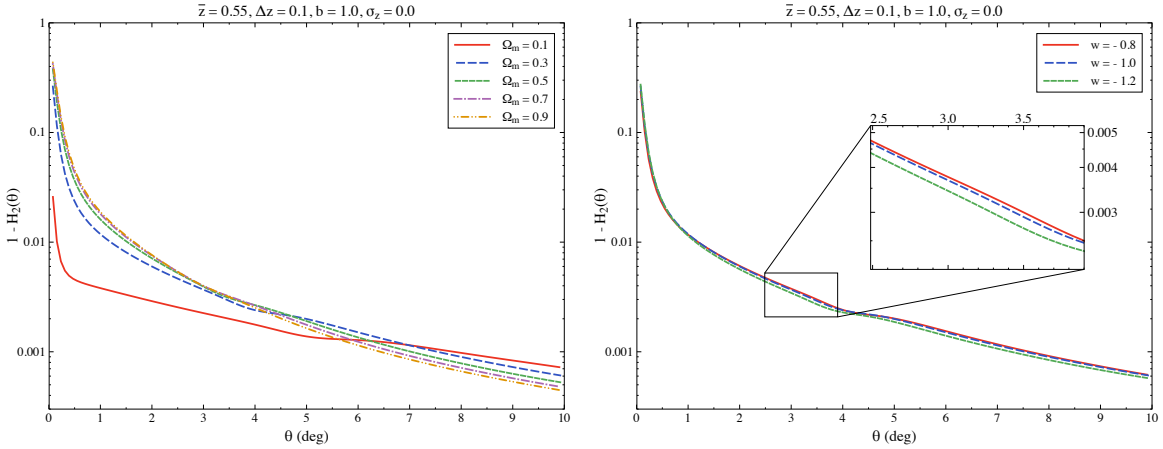

Figure 3.17: $\Delta H_2(\theta)$ as a function of θ for varying Ω_m (left panel) and dark energy equation of state w (right panel).

values of w accelerate the expansion and damp the growth of perturbations, shifting H_2 closer to 1. In any case we observe a mild dependence of H_2 on the cosmological parameters, and hence we expect that the results presented here should not vary qualitatively for any viable homogeneous cosmological model.

Defining homogeneity

As it has been discussed, even though the standard cosmological model postulates a homogeneous and isotropic Universe, this homogeneous regime is only approached asymptotically on large scales or in early times. Thus, there is no straightforward prescription to define the scale at which homogeneity is reached. Two different definitions have been used in the literature:

- One possibility is to define the scale of homogeneity as the scale at which the difference between our measurement of D_2 or H_2 (or, in general, any observable characterizing fractality) and its homogeneous value ($D_2 = 3$, $H_2 = 1$) is comparable with the uncertainty in this measurement. The caveat of this definition is that this uncertainty will depend on the characteristics of the survey (area, depth, number density, etc.), and therefore different surveys will measure a different scale of homogeneity.

- Another approach is to define that homogeneity is reached when the measured fractal dimension is within a given arbitrary fraction of its homogeneous value. For example, a value of 1%. The advantage of this definition is that all surveys should measure the same scale of homogeneity, while its caveat is the arbitrariness of the mentioned fraction. Furthermore, using this kind of prescription would not be viable in our case, since, as we have seen, projection effects reduce the departure from homogeneity, and therefore the same fixed fraction cannot be used for different bins.

For the data analyzed in the next section, we have chosen to follow the first prescription, defining the homogeneity scale as the angle at which

$$\Delta H_2(\theta) \leq q\, \sigma_{H_2}(\theta), \tag{3.24}$$

where σ_{H_2} is the error on H_2 and q is an $\mathcal{O}(1)$ number. Since the errors associated to the estimator **E2** are significantly larger than the errors for **E3** (see section 3.2.3), we have used $q = 1$ for the former and $q = 2$ for the latter. Note that the value of $\theta_{\rm H}$ given by this definition should be interpreted as a lower bound on the scale of homogeneity, and not as a scale beyond which all inhomogeneities disappear.

At the end of the day, the scale at which homogeneity is reached is not a well defined quantity, nor is it of vital importance. Instead, the main aim of this kind of studies is to establish whether homogeneity is reached or not, focusing on defining the limits of our ability to detect a departure from large-scale homogeneity.

3.2.3. Measuring the homogeneity index

In order to assess the performance of the different estimators for $H_2(\theta)$ in a realistic scenario, we have used them on a set of simulated galaxy surveys corresponding to a canonical ΛCDM model.

Lognormal mock catalogs

Lognormal fields were proposed by [91] as a possible way to describe the distribution of matter in the Universe. More interestingly for our purposes, lognormal fields provide an easy and fast method to generate realizations of the density field in order to produce large numbers of mock catalogs. This technique has been used by different collaborations to estimate statistical uncertainties and study different systematic effects in galaxy surveys, and has been proven to be a remarkably useful tool. The physics and mathematics of lognormal realizations, as well as their limitations, have been widely covered in the literature [91, 92]. 100 lognormal realizations were generated for the cosmological model of equation (3.21) inspired by the measurements by the

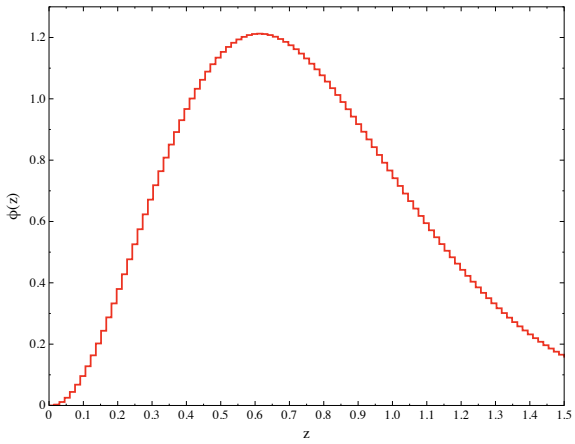

Figure 3.18: Selection function as a function of redshift used for the lognormal catalogs, given by eq. (3.25).

Planck collaboration in 2013 [39]. Each catalog contains 1.2×10^8 galaxies distributed over one octant of the sky ($\simeq 5000\,\mathrm{deg}^2$) in the redshift range $0 < z < 1.4$ with a selection function

$$\phi_{\mathrm{true}}(z) \propto z^2\, e^{-\left(\frac{z}{0.5}\right)^{1.5}}, \tag{3.25}$$

shown in Figure 3.18. The density field was generated in a box of size $L_{\mathrm{box}} = 3000\,\mathrm{Mpc}/h$ with a grid of size $N_{\mathrm{side}} = 2048$, yielding a spatial resolution of $l_{\mathrm{grid}} \simeq 1.5\,\mathrm{Mpc}/h$. All the catalogs contain redshift space distortions, and a Gaussian photometric redshift error was generated for each galaxy with $\sigma_z = 0.03\,(1+z)$. Since the effect of a linear galaxy bias factor is well understood and very easy to model in theory, all the catalogs were generated with $b = 1$.

Results

The angular homogeneity scale $\theta_H(z)$ In order to better understand the approach to homogeneity of a projected galaxy survey, we have computed $H_2(\theta)$ from the 100 lognormal catalogs using the two estimators **E2** and **E3**. Then, the lower limit on the angular homogeneity scale was estimated, as described in section 3.2.2, as the angle for which the amplitude of the departure of H_2 from homogeneity is smaller than q times the error on H_2 (with $q = 1$ for **E2** and $q = 2$ for **E3**). These errors were calculated as the standard deviation of the 100 lognormal realizations (see section 3.2.3).

The comoving three-dimensional homogeneity scale is related to the angular scale θ_H through

$$r_H(z) \equiv (1+z)\, d_A(z)\, \theta_H(z), \tag{3.26}$$

where $d_A(z)$ is the angular diameter distance to redshift z.

These results are summarized in table 3.1, and can be visualized in Figure 3.19. The numbers given in this table for θ_H correspond to the mean value obtained from the 100 lognormal mocks, and the errors correspond to the standard deviation. Two main observations must be made:

- First, since the two estimators make a different use of the data, they have different variances, and therefore each of them measures a different lower bound on the homogeneity scale. While all the galaxies in the survey are used as centers for spherical caps of any angular aperture in the case of **E3**, only those caps that fit fully inside the field of view are used for **E2**. Thus, in this case the variance will grow faster for larger scales, and homogeneity is reached on smaller angles. This is explicitly illustrated in Figure 3.21.

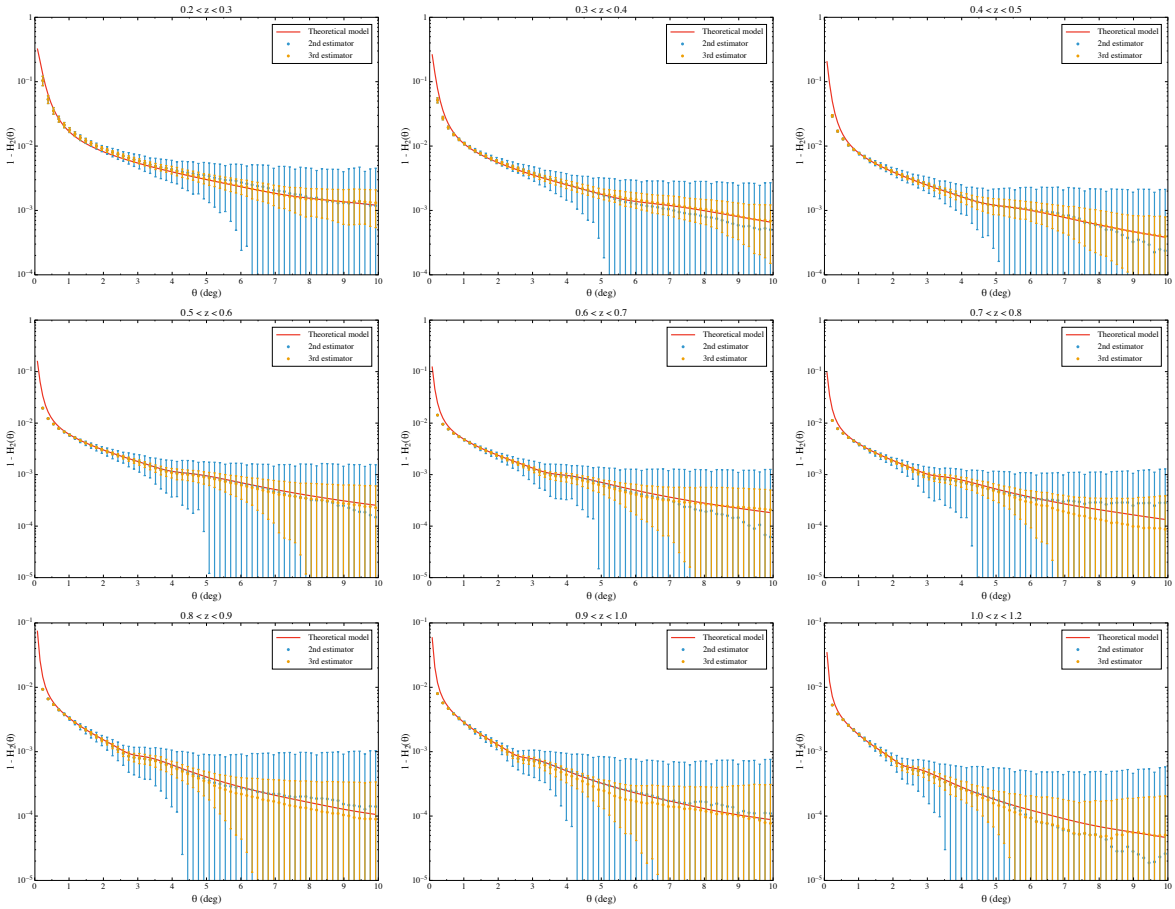

Figure 3.19: $\Delta H_2(\theta)$ as a function of θ calculated from the 100 lognormal realizations for the 9 redshift bins given in table 3.1. The data contains Gaussian photometric errors with $\sigma_z = 0.03\,(1+z)$. The blue dots with error bars correspond to the mean and standard deviation of the 100 mocks for the estimator **E2**, while the yellow dots correspond to estimator **E3**. The solid red line shows the theoretical model described in section 3.2.2.

	E2		E3	
Bin limits	$\theta_H >$	$r_H >$	$\theta_H >$	$r_H >$
$0.2 - 0.3$	6.1	75	7.5	93
$0.3 - 0.4$	5.6	94	7.8	131
$0.4 - 0.5$	5.5	11	7.1	149
$0.5 - 0.6$	5.0	126	6.3	158
$0.6 - 0.7$	4.9	140	6.0	174
$0.7 - 0.8$	4.7	151	5.6	182
$0.8 - 0.9$	4.7	169	5.4	192
$0.9 - 1.0$	4.8	185	5.3	206
$1.0 - 1.2$	4.2	180	4.8	207

Table 3.1: Lower bound on the scale of homogeneity calculated for the nine redshift bins of the 100 lognormal realizations. The angular scale of homogeneity θ_H is given in degrees, while the corresponding comoving distance is given in Mpc/h.

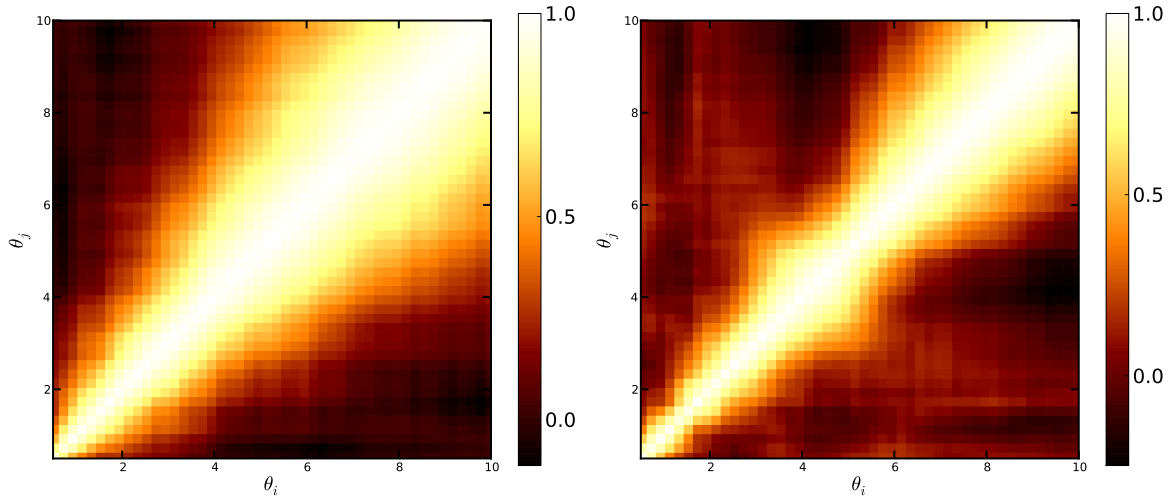

Figure 3.20: Correlation matrix $\rho_{i,j} \equiv C_{i,j}/\sqrt{C_{i,i}C_{j,j}}$ of H_2 for **E2** (left) and **E3** (right). Note that the errors are correlated over relatively wide ranges of scales, specially on large angles.

- Secondly, the comoving scale corresponding to the angular homogeneity scale for each bin seems to increase with redshift. This result is precisely the opposite of what intuition would predict: since the amplitude of matter perturbations decreases with redshift, the matter distribution is more homogeneous at earlier times, and should reach homogeneity on smaller scales at larger redshifts. This paradox is due to the fact that the definition that we have used for the scale of homogeneity is based on statistical principles, and not on the physical meaning of homogeneity. For this and other reasons we believe that producing a number for θ_H or r_H is not as relevant as setting a lower limit to the departure from large-scale homogeneity that can be allowed given our observational capabilities.

Statistical uncertainties We have studied the full covariance matrix of the angular homogeneity index $H_2(\theta)$ for the different estimators. The covariance between the angular bins θ_i and θ_j is calculated from the measurements of H_2 in the 100 lognormal mock catalogs as

$$C_{i,j} = \frac{1}{N_m - 1}\sum_{n=1}^{N_m} H_2^n(\theta_i)H_2^n(\theta_j) - \overline{H_2(\theta_i)}\,\overline{H_2(\theta_j)}, \tag{3.27}$$

where $N_m = 100$, H_2^n is the measurement on the n-th catalog and $\overline{H_2}$ is the arithmetic mean over all the catalogs. Figure 3.21 shows the diagonal errors $\sigma_i \equiv \sqrt{C_{i,i}}$ for the bin $z \in (0.5, 0.6)$ using the estimators **E2** and **E3**. As it was noted before, the errors corresponding to **E2** are significantly larger than those of **E3** for large scales, due to the smaller number of galaxies used as centers of spherical caps for those angles.

The correlation matrix $\rho_{i,j} \equiv C_{i,j}/\sqrt{C_{i,i}C_{j,j}}$ is shown, for the same two estimators and the same bin, in Figure 3.20. As it is shown in the Figure, the measurements of H_2 are statistically correlated over wider ranges of scales as we go to larger angles, especially in the case of **E2**. Therefore, if any likelihood analysis is to be done on H_2, the full covariance matrix must be used.

Projection effects

As it has been said before, using wider redshift bins damps the amplitude of the correlation function and makes the projected galaxy distribution more homogeneous (i.e., H_2 gets closer to 1). However, the amplitude of the error on the correlation function (or on H_2) will also be damped, and it is therefore interesting to study

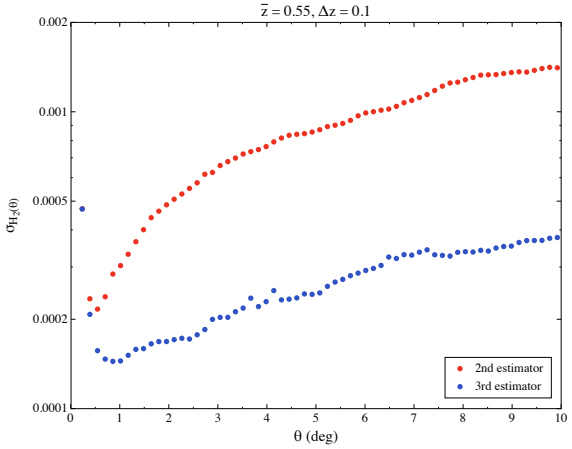

Figure 3.21: Diagonal errors on $H_2(\theta)$ as a function of θ for estimators **E2** (red) and **E3** (blue). Since with **E3** all galaxies are used as centers of spherical caps for all θ, the errors are significantly smaller than in the case of **E2**.

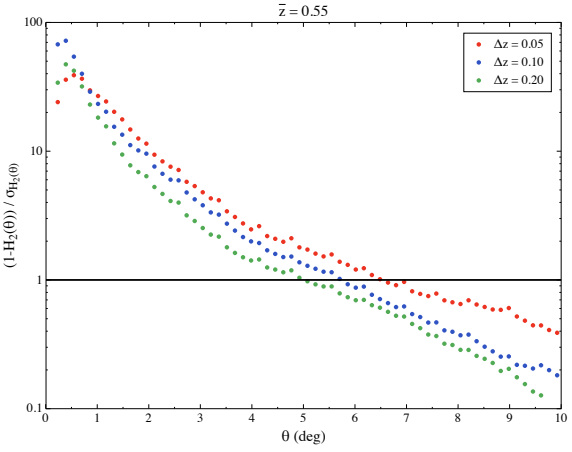

Figure 3.22: Departure from homogeneity ΔH_2 divided by the uncertainty on σ_{H_2} as a function of θ for a redshift bin centered on $\bar{z} = 0.55$ with different binwidths. As it could be expected, projecting on wider bins moves the scale of homogeneity towards smaller angles.

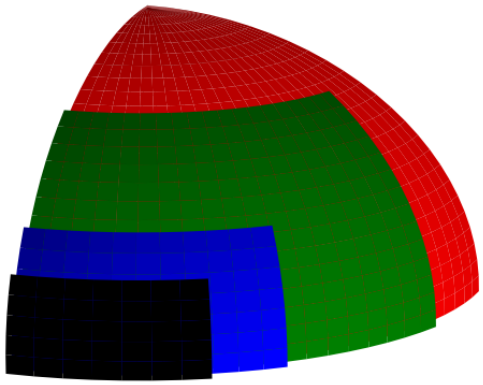

Figure 3.23: The four survey cases considered in section 3.2.3, covering $5000\,\mathrm{deg}^2$ (red), $3000\,\mathrm{deg}^2$ (green), $1000\,\mathrm{deg}^2$ (blue) and $500\,\mathrm{deg}^2$ (black).

whether the two dampings compensate each other and to quantify the effect on the scale of homogeneity. This has been done in Figure 3.22. The homogeneity index $H_2(\theta)$ has been calculated at $\bar{z} = 0.55$ using different redshift binwidths: $\Delta z = 0.05, 0.1, 0.2$, and the ratio $\Delta H_2/\sigma_{H_2}$ has been plotted for different values of θ. According to our definition, the homogeneity scale is reached when this ratio becomes 1 for **E2** (the same result holds for **E3**). As it can be seen, the damping of ΔH_2 due to projection effects is not compensated by the corresponding damping on σ_{H_2}, and the homogeneous regime is reached on smaller scales for wider bins, as could be intuitively expected. Since the use of photometric redshifts effectively increases the width of the redshift bin, it produces a similar effect.

Fraction of the sky In order to study the effects related to the area covered by a given survey, we considered a fiducial redshift bin $0.5 < z < 0.6$ and restricted the data from our mock catalogs to regions of different areas. Specifically, we have considered surveys covering $\sim 5000\,\mathrm{deg}^2$ (one octant of the sky) $\sim 3000\,\mathrm{deg}^2$, $\sim 1000\,\mathrm{deg}^2$ and $\sim 500\,\mathrm{deg}^2$. For simplicity we have used simply connected fields of view with the shapes shown in Figure 3.23. This is an ideal scenario, and therefore the results shown here would correspond to the most optimistic ones any survey of the same area could obtain. The total area covered by a given survey affects the measurement of $H_2(\theta)$ in two ways.

First, the sample variance should be inversely proportional to $\sqrt{f_{\mathrm{sky}}}$ [62], and therefore the uncertainty in H_2 will grow for smaller areas. This is illustrated in the left panel of Figure 3.24, which shows the magnitude of the errors on H_2 for the 4 different areas. Secondly, the survey size limits the maximum scale that we are able to probe, and may prevent us from reaching the homogeneous regime. In order to illustrate this point, we have performed the following exercise: inside each of the regions shown in Figure 3.23, we have randomly placed a large number points. Then, for different values of θ, we have estimated the fraction of spherical caps of radius θ centered on these points that lie fully inside the surveyed region. The result is shown in the right panel of Figure 3.24. In view of this result we have established three different criteria to define the largest scale θ_{max} that can be probed in a survey:

1. θ_{max} corresponds to the radius of the largest spherical cap that fits inside the surveyed region.

2. θ_{max} is the angle for which the fraction shown in the right panel of Figure 3.24 is 10%.

3. The same as above for a fraction of 50%.

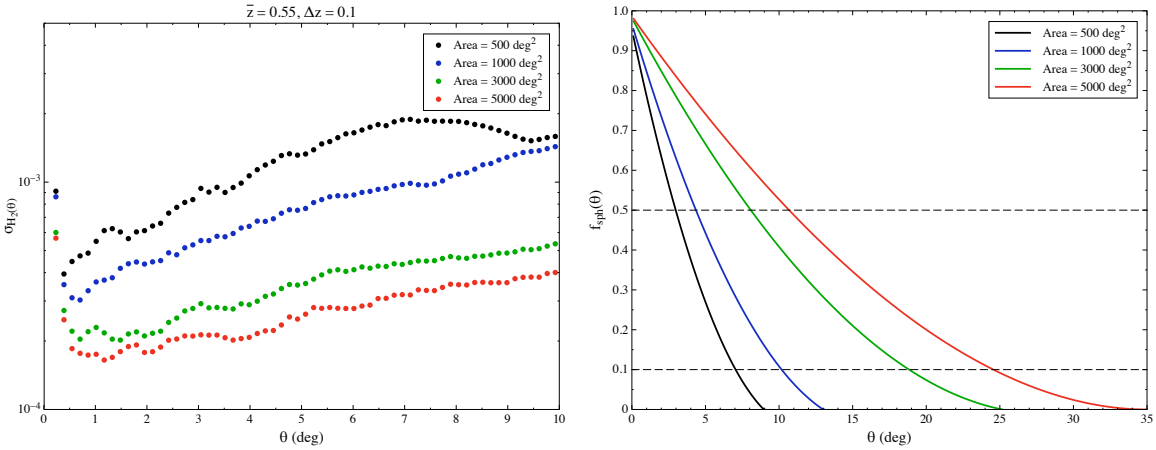

Figure 3.24: *Left panel*: Errors on $H_2(\theta)$ for the four surveys described in Figure 3.23 as a function of θ. *Right panel*: Fraction of complete spheres of different radii in the same four surveys as a function of θ. The horizontal dashed lines correspond to the last two criteria considered below to determine the maximum angular scale to be used.

3.2.4. Robustness of the method

It has been argued [93] that fractal distributions may look homogeneous when projected onto the celestial sphere, and therefore it is necessary to verify that we are indeed able to distinguish a 3D fractal from an asymptotically homogeneous distribution using only angular information, and to what level so. In order to address these questions, we have analyzed different inhomogeneous models which, we know, should not approach homogeneity. Two different models were explored: 2-dimensional random walks on the sphere and the 3D β-model.

Spherical Rayleigh-Levy flights

A random walk in 3 dimensions is an iterative point process in which the distance between one point and the next one is drawn from a probability distribution independently of all previous jumps. In the particular case of a heavy-tailed Pareto distribution

$$P(r > R) = \begin{cases} 1 & R < R_0 \\ \left(\frac{R}{R_0}\right)^{-\alpha} & R \geq R_0 \end{cases} , \tag{3.28}$$

these walks are called *Lévy flights* and exhibit a fractal behavior with $D = \alpha$ for $\alpha \leq 2$ [94].

We have generated random walks on the sphere by following a similar process. We first choose a starting point on the sphere at random, and draw an angular distance θ_d from a probability distribution. The next point is selected at this distance in an arbitrary direction from the first one, and the process is repeated. For our walks we have chosen a distribution similar to the one given above in the three-dimensional case

$$P(\theta_d < \theta) = \begin{cases} 1 & \theta < \theta_0 \\ \left(\frac{1-\cos\theta}{1-\cos\theta_0}\right)^{-\alpha} & \theta \geq \theta_0 \end{cases} . \tag{3.29}$$

It must be noted that with this procedure we are generating an inhomogeneous distribution directly in the 2-dimensional sphere, and not projecting a 3-dimensional set. However, we know for sure that this distribution must asymptotically reach some $H_2(\theta) \neq 1$, and therefore we can use it to verify that the use of random catalogs

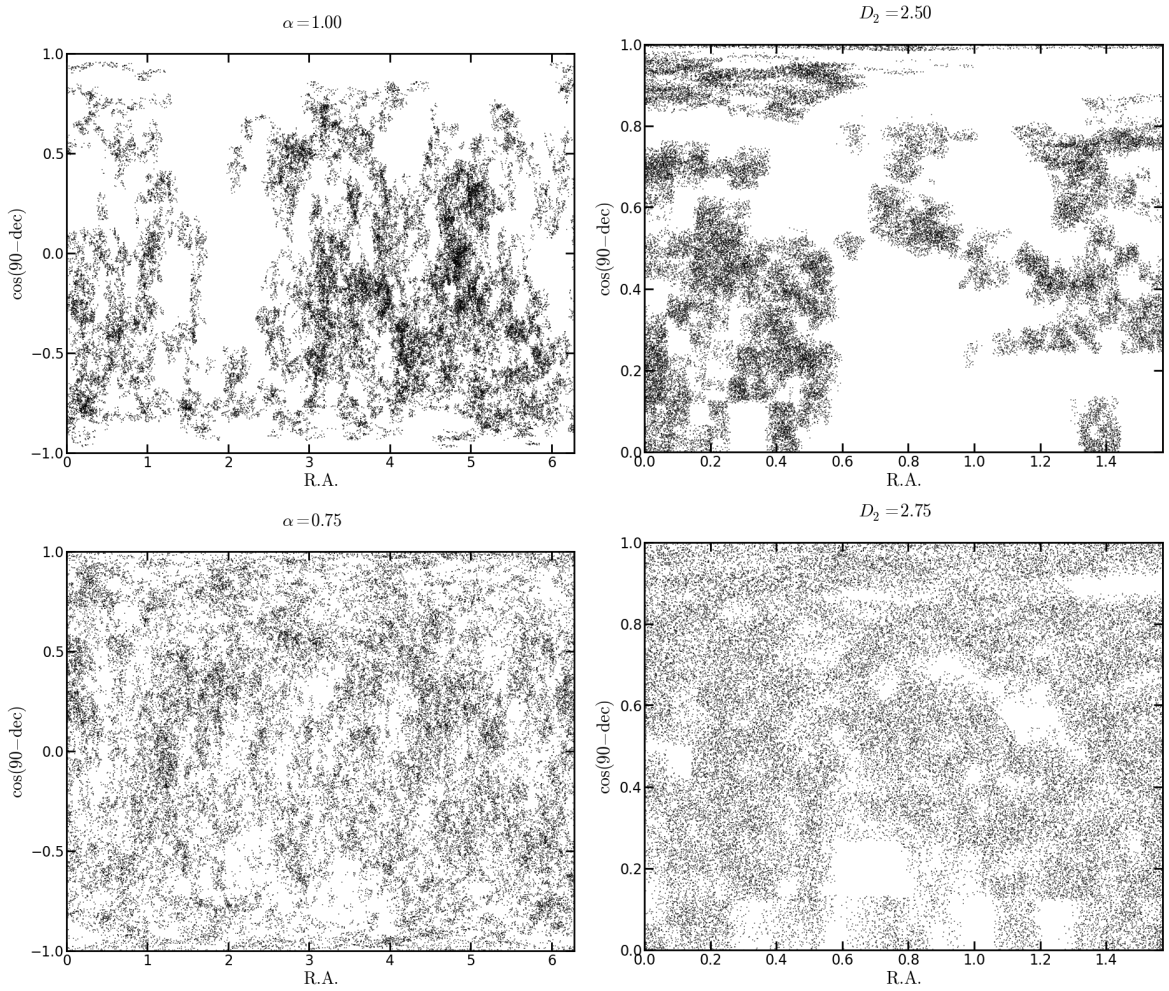

Figure 3.25: Sky maps for the 2D Rayleigh-Levy flights (left) and the β-model catalogs at $0.5 < z < 0.6$ (right). The plots are ordered top-down from more to less inhomogeneous.

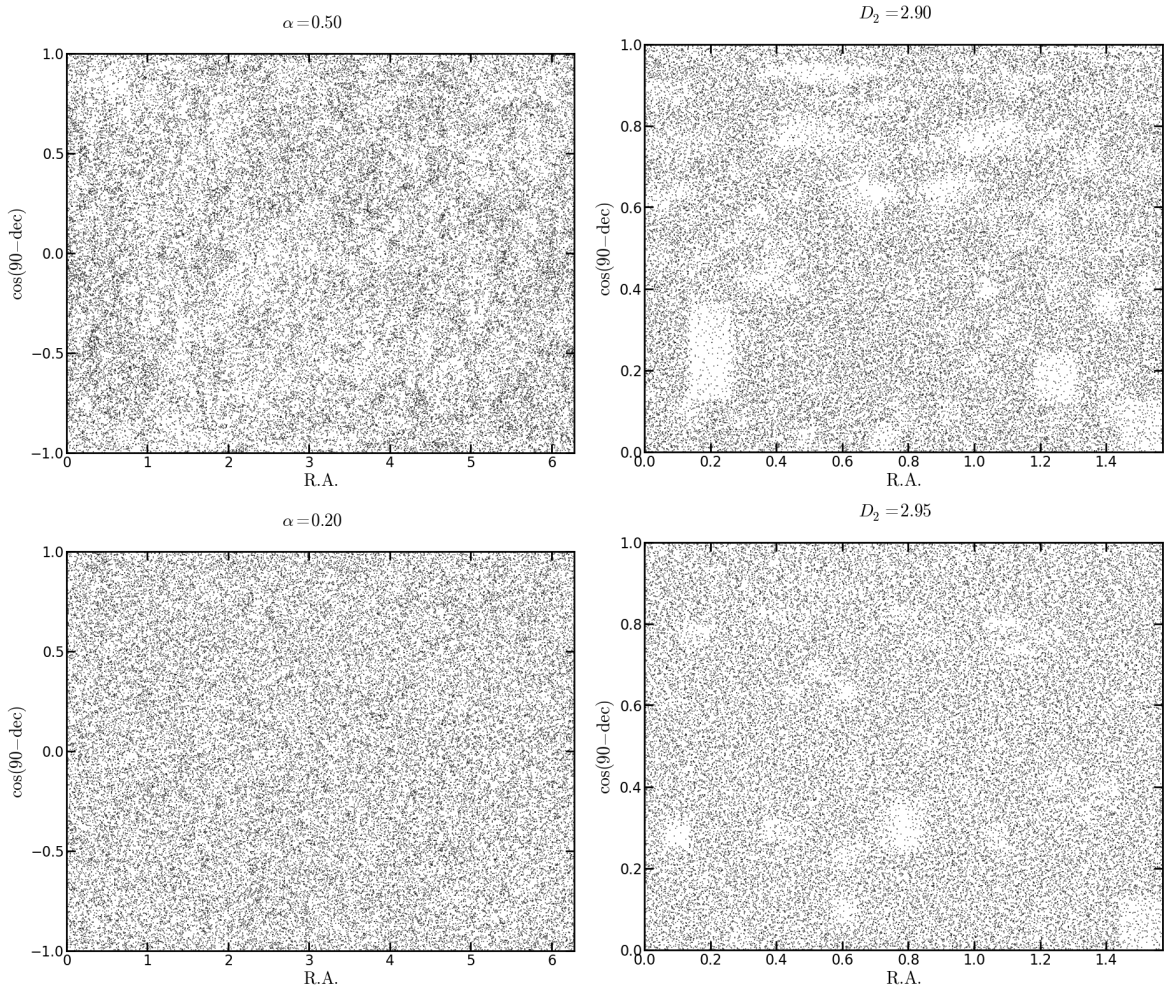

Figure 3.26: Sky maps for the 2D Rayleigh-Levy flights (left) and the β-model catalogs at $0.5 < z < 0.6$ (right). The plots are ordered top-down from more to less inhomogeneous.

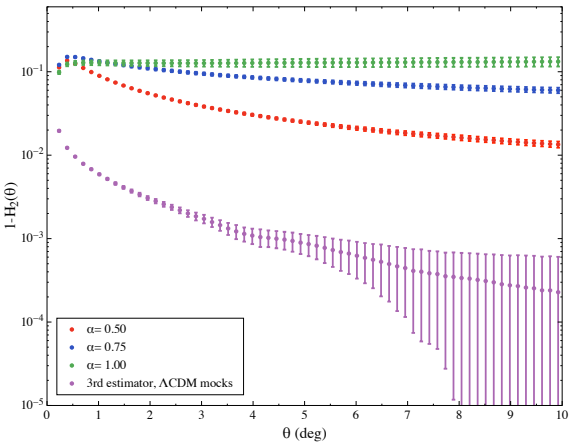

Figure 3.27: $\Delta H_2(\theta)$ as a function of θ for three sets of 2D Rayleigh-Levy flights with $\alpha = 1.0$ (green), $\alpha = 0.75$ (blue) and $\alpha = 0.5$ (red), together with the result from the lognormal catalogs for the bin $0.5 < z < 0.6$ (purple). We can distinguish these models from a ΛCDM model.

does not bias our results. To do so we have considered values of $\alpha = 0.5, 0.75$ and 1, generating 20 random walks containing 10^6 objects in all cases. Figure 3.25 (left column) shows the 2D distribution of some of these walks for different values of α, showing that the degree of inhomogeneity increases with α. For $\alpha = 0.5$ the distribution is visually indistinguishable from a homogeneous one. We have calculated $H_2(\theta)$ and its error from these random walks using the **E3** estimator. The results are shown in Figure 3.27 together with those corresponding to the ΛCDM lognormal catalogs. In all cases the asymptotic value of H_2 is different from 1 and can be clearly distinguished from the ΛCDM prediction, showing that, at least within the range of scales explored, our method is not biased towards homogeneity.

β-model

The fractal β-model is a multiplicative cascading fractal model based on the following process: take a cubic box of side L and perform $N_{\rm side}$ equal divisions per side. Then, give a probability $p < 1$ to each of the $N_{\rm side}^3$ sub-cubes of surviving to the next iteration and randomly choose those which survive according to this probability. In the next iteration you follow the same process on each of the surviving sub-cubes. In the n-th iteration, the average number of surviving cells will be $N_{\rm surv} = (N_{\rm side}^3\, p)^n$. Equating this to $N_{\rm side}^{n\,D}$ we obtain that this set has a fractal dimension

$$D = 3 + \log_{N_{\rm side}} p. \tag{3.30}$$

We explored different values for D ranging from 2.5 to 3, generating multiple realizations of this process for each value. These catalogs were produced by running the process outlined above on a cubic box of the same size as the one used for the lognormal catalogs, using $N_{\rm side} = 2$. The catalog is then subsampled to the desired number density and the three-dimensional distances to each object are translated into redshifts using our fiducial cosmological parameters. This is, of course, not correct, since the distance-redshift relation for this model need not be that of FRW, however it is not clear which relation should be used. In any case, our aim is to explore whether a three-dimensional inhomogeneous model could be noticed when projected onto the sphere, and, for this purpose, our choice of $\chi(z)$ is as good as any other. The redshift of each object is then perturbed with a Gaussian photo-z error with $\sigma_z = 0.03\,(1+z)$, and the point distribution is projected in different redshift bins.

The projected distributions of some of these catalogs for a redshift bin $0.5 < z < 0.6$ are shown in Figure 3.25 (right panel). Figure 3.28 shows the value of $H_2(\theta)$ and its error calculated from these catalogs for a the same bin, together with the ΛCDM result from the lognormal catalogs. As is evident from this Figure,

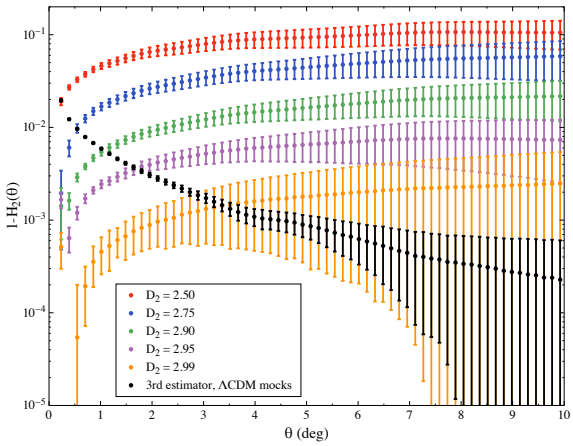

Figure 3.28: $\Delta H_2(\theta)$ as a function of θ for the β-model projected onto the redshift bin $0.5 < z < 0.6$ for different values of D_2 from 2.5 (top) to 2.99 (bottom), together with the ΛCDM prediction obtained from the lognormal mocks (black). In spite of the 2D projection, we are still able to distinguish the inhomogeneous nature of the β-model from an asymptotically homogeneous model for $D \lesssim 2.95$.

when projected, these catalogs still retain their inhomogeneous nature, and can be clearly distinguished from an asymptotically homogeneous ΛCDM model for values of D_2 that are remarkably close to 3. For instance, only with the results drawn from the bin $0.5 < z < 0.6$ we would be able to set the limit $D_2 \gtrsim 2.95$.

LTB models

In general, there is no direct connection between the three dimensional fractal dimension D_2 and the homogeneity index H_2 of the projected data. An extreme example of this would be an inhomogeneous but spherically symmetric distribution in which the observer sits exactly at the center of symmetry. Although the distribution is inhomogeneous in three dimensions ($D_2 \neq 3$), the central observer will measure a homogeneous distribution for the projected data ($H_2 = 1$).
This is precisely the case of Lemaître-Tolman-Bondi (LTB) void models. A complete description of these models can be found in [95]. In an LTB model the observer is placed very close to the center of a very large ($\mathcal{O}(1)$ Gpc) spherical underdensity. With this setup it is possible to reproduce many of the observational effects that can be adscribed to a Dark Energy component without introducing any exotic species or new physics in the model. The price to pay for this is relatively high, since in order to match the observed high isotropy of the distribution of CMB anisotropies, the observer is bound to be within a comparatively small distance ($\mathcal{O}(10)$ Mpc) from the center of the void. LTB models have been tested against multiple cosmological observations [96] and are basically ruled out. However, they provide an explicit example of an inhomogeneous model that can *not* be distinguished from a homogeneous distribution with our method. This is shown in Figure 3.29, in which we compare the homogeneity index $H_2(\theta)$ measured from the ΛCDM mock catalogs with the values measured from an N-body simulation of an LTB model. These simulations are described in [97], and the data shown in Figure 3.29 correspond to the best resolved simulation, labelled $\mathcal{H}$ in the aforementioned paper. The errors shown for the LTB data points have been calculated by splitting the simulation into 8 octants of the sky and then calculating the standard deviation from the mean of the angulat homogeneity index of the 8 octants.

3.2.5. Summary & Discussion

We have studied the possibility of measuring the transition to homogeneity using photometric redshift catalogs. The method presented here is an extension of the usual fractal studies that have previously been performed using three-dimensional distances by several collaborations. Photometric redshift uncertainties erase much of

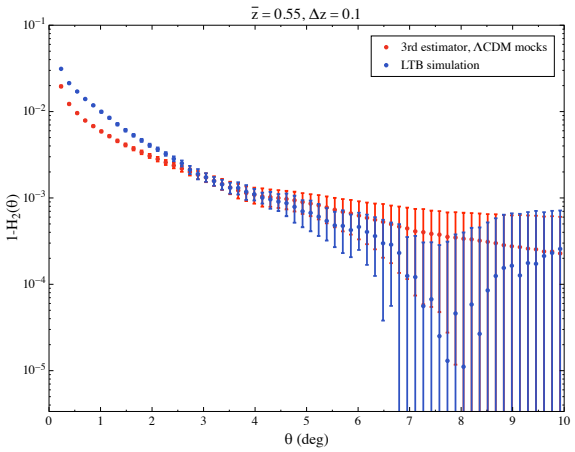

Figure 3.29: $\Delta H_2(\theta)$ as a function of θ for an LTB void model (blue) compared to the ΛCDM value (red). Since the LTB metric preserves spherical homogeneity around the central observer, the inhomogeneity of these models can not be measured using the method described here.

the clustering information along the radial direction. Thus, our method is based on measuring the fractality of the projected galaxy distribution, using angular distances only. This method is assumption-free, since it relies only on observable quantites (as opposed to three-dimensional distances, which requires a fiducial cosmological model), and in this sense provides a way to test the Cosmological Principle in a model-independent way. In the era of precision cosmology, testing this fundamental assumption is extremely important, and the upcoming galaxy surveys, covering large volumes of the Universe, will make this possible.

We have tested that our method is not biased by the use of random catalogs to correct for artificial effects induced on the observed galaxy distribution. We have done so by using our method on different synthetic inhomogeneous catalogs. We have verified that, not only is our method unbiased in practice, but it is in fact capable of discriminating some fractal models with relatively large fractal dimensions, in spite of the loss of information due to the radial projection. Our method is unable to detect the large-scale inhomogeneity along the line of sight, and therefore can not be used to constraint a particular type of inhomogeneous models preserving the isotropy around a central observer.

We have modelled and studied how different effects would affect the measurement of the angular homogeneity index $H_2(\theta)$ in a ΛCDM cosmology. We have studied the influence of the redshift bin width, photometric redshift errors, bias, non-linear clustering, and surveyed area. The level to which a given survey will be able to constrain the transition to homogeneity will depend mainly on two factors:

- The total surveyed area: this regulates the size of the statistical uncertainties.

- The compactness of the surveyed region: this determines the largest angular scale that can be measured.

In particular, a DES-like survey should be able to easily discriminate certain fractal models with fractal dimensions as large as $D_2 = 2.95$. We believe that this method will have relevant applications for present and upcoming large photometric redshift surveys, such as DES or LSST.

3.3. BAO and LSS in Photometric Surveys: BCC

3.3.1. Introduction

The final test for the methods presented before is to show that we can measure an unknown cosmology from a given data set. This was the idea behind the Blind Cosmology Challenge (BCC), DES collaborators were provided with different simulations with unknown underlying cosmological models. Each working group was encouraged to test its analysis in a way as close as possible as in real DES data. We obtain the BAO scale from the angular two point correlation function and then, we retrieve the cosmological parameters related to each simulation.

3.3.2. BCC simulations

The analysis has been made for two simulations, called Aardvark and Buzzard[2]. Both are 10313 sq-deg (quarter of sky) catalogs to full DES depth and include the DES footprint (5000 sq-deg). Both catalogs contain galaxies that have a signal to noise greater than 5 in at least one DES band.
These are the characteristics of these simulations:

- 10313 sq. degrees, including mask to 5000 sq. degree footprint.
- 1.36 billion galaxies to the DES 5-sigma limit.
- Shear at galaxy positions using algorithm appropriate for full sky; 6.2 arcsec ray tracing.
- Galaxy magnitudes and shapes include impact of shear and magnification.
- Magnitudes in DES, SDSS, 2MASS, DEEP, VHS, VIKING, VIDEO, CFHTLS, RCS, NDWFS, WISE, HSC, BCS, LSST, WFIRST and Euclid bands.
- Multiple photometric redshift catalogs included.
- Star and quasar catalogs included.

The only difference between these two simulations is that Aardvark is a semiblind cosmology challenge, it is based in a flat ΛCDM model whereas Buzzard is a completely blind cosmology.

3.3.3. Analysis

We perform a cosmological analysis based on the extraction of the position of the BAO peak as presented in [73] and in the previous section 3.1. The idea of this analysis is to perform it as it will be done in DES data. Thus, we require galaxies to be inside the provided footprint and impose a 10σ detection in i or z bands (i.e. we require `MAGERR_I` or `MAGERR_Z` to be less than 0.1 where the `MAGERR` variables are just the errors in the magnitudes provided in the simulations). In order to be as close as possible to the real data analysis, we use the values of ArborZ photo-z provided for both simulations. After these cuts we have 3.0×10^8 galaxies in our selection for Aardvark and 2.7×10^8 in Buzzard.

[2] `http://www.slac.stanford.edu/~risa/des_bcc/`

Quality tests

We performed some basic quality tests: we checked the redshift distribution, $N(z)$, the magnitude distributions $N(mag)$, the distributions of magnitude versus its error (mag vs $magerr$), color-color distributions and maps. Figure 3.30 shows the redshift distribution for ArborZ [98]. We have studied the magnitude histograms (Figures 3.31 and 3.32) and magnitude error versus magnitude histograms (Figures 3.33 and 3.34). We also analyzed the spatial distribution of objects in both simulations. This can be seen in the maps plotted in Figures 3.35 and 3.36 for Aardvark and Buzzard respectively.

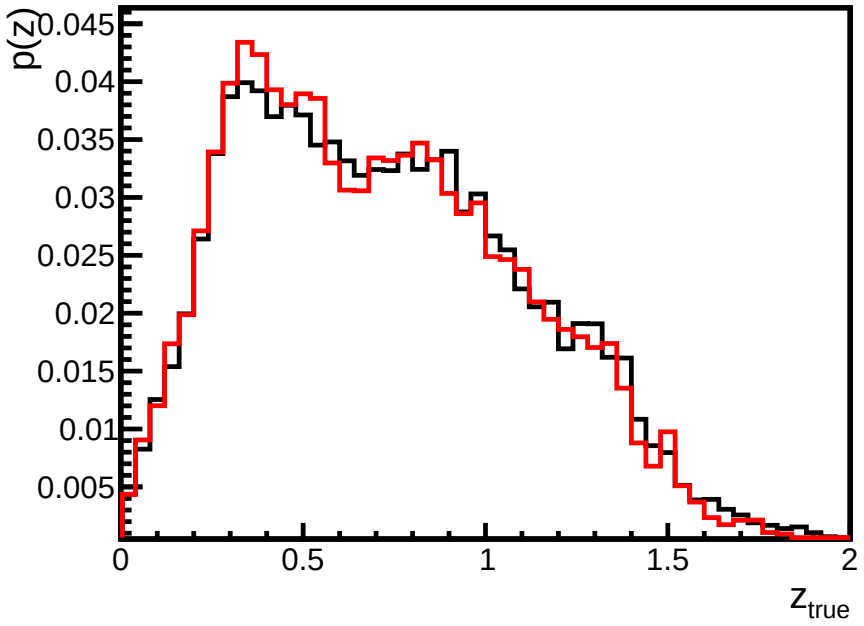

Figure 3.30: Normalized $N(z)$ distribution of Aardvark (black) and Buzzard (red) simulations using ArborZ.

Even though we haven't attempted any kind of color selection, we inspected the color-space distributions to verify that they looked reasonable (Figure 3.37). All of them behave as expected and were ready for the cosmological analysis.

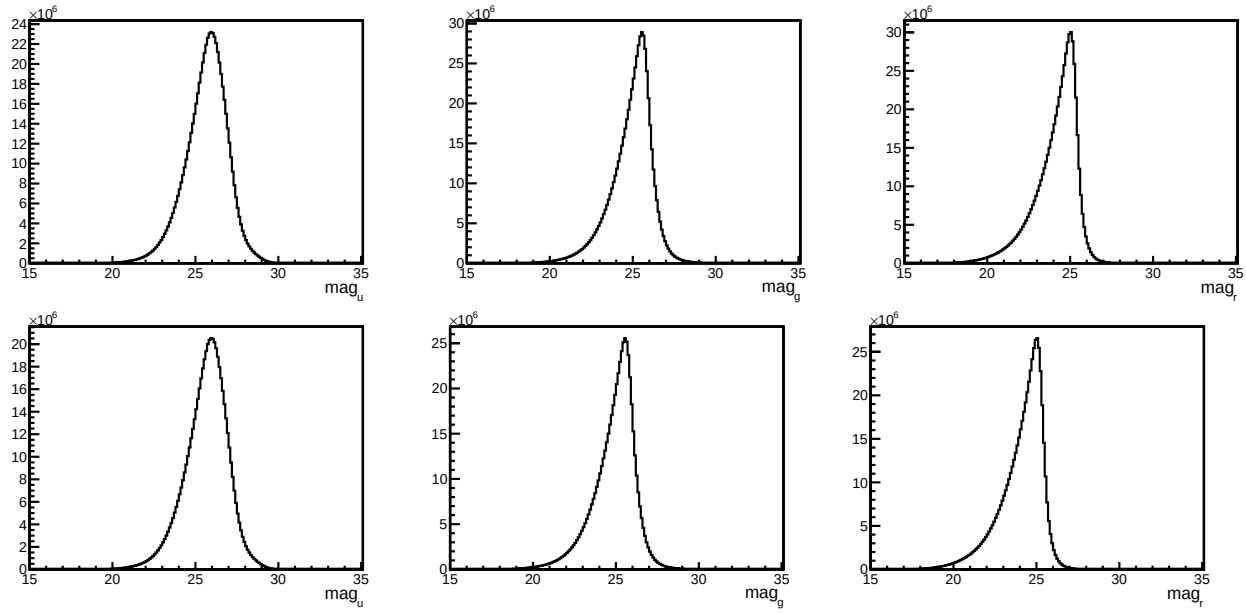

Figure 3.31: Magnitude distributions of Aarvark (top) and Buzzard (bottom) simulations in filters u, g and r.

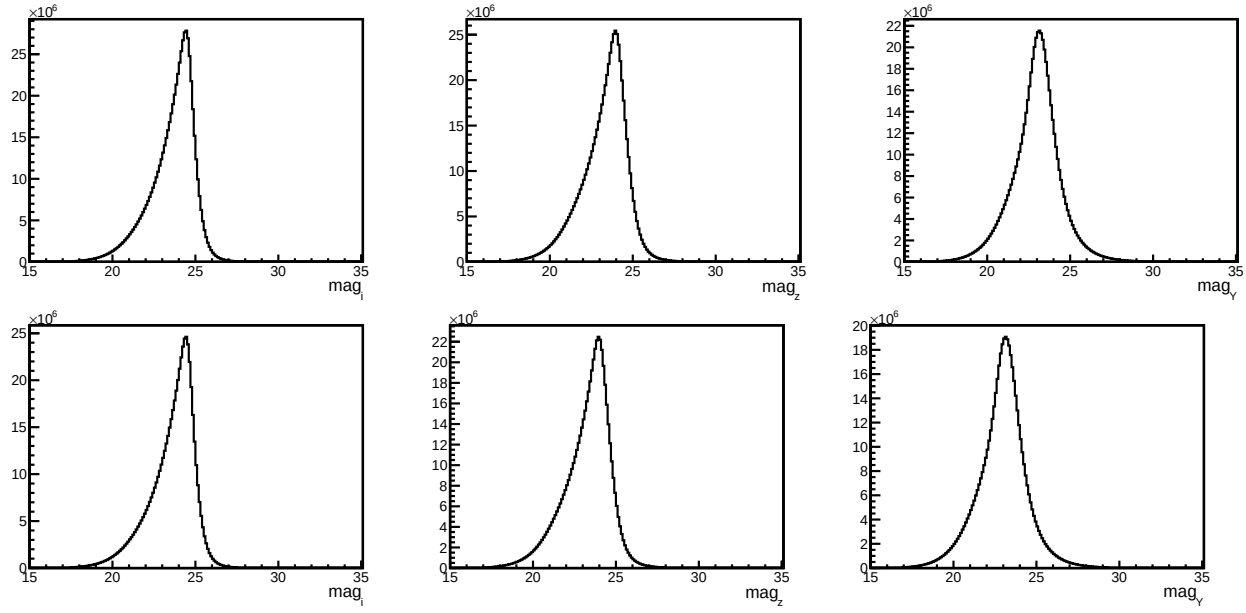

Figure 3.32: Magnitude distributions of Aarvark (top) and Buzzard (bottom) simulations in filters i, z and Y.

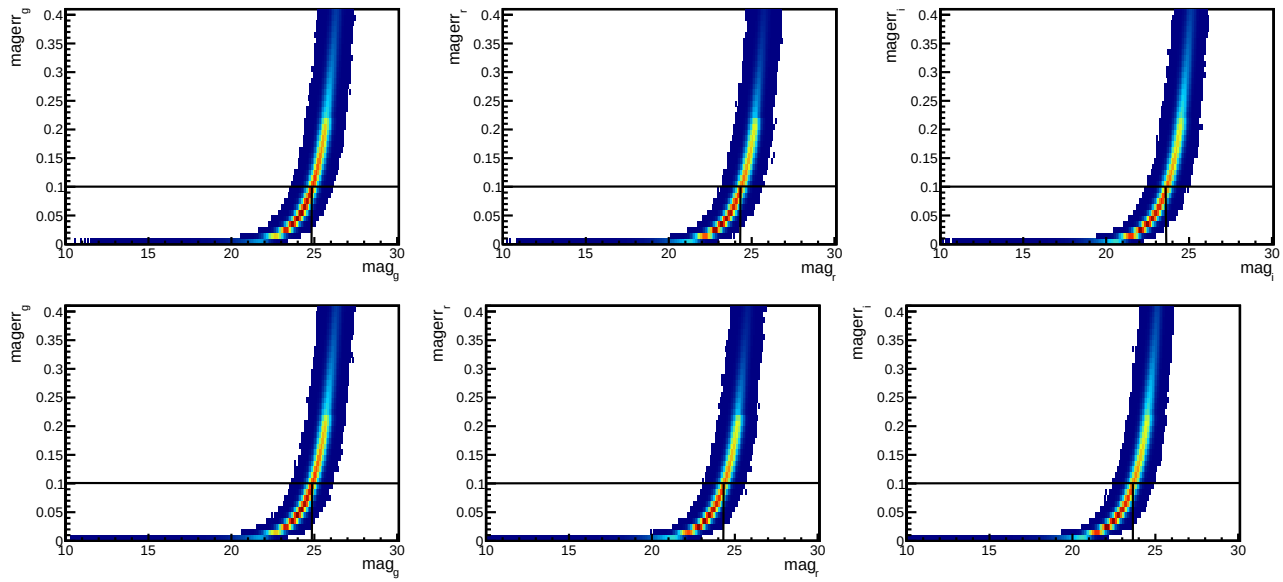

Figure 3.33: Magnitude error vs magnitude for Aarvark (top) and Buzzard (bottom) simulations in filters g, r and i. Limiting magnitudes are $maglim_g \approx 24.9$, $maglim_r \approx 24.2$ and $maglim_i \approx 23.8$.

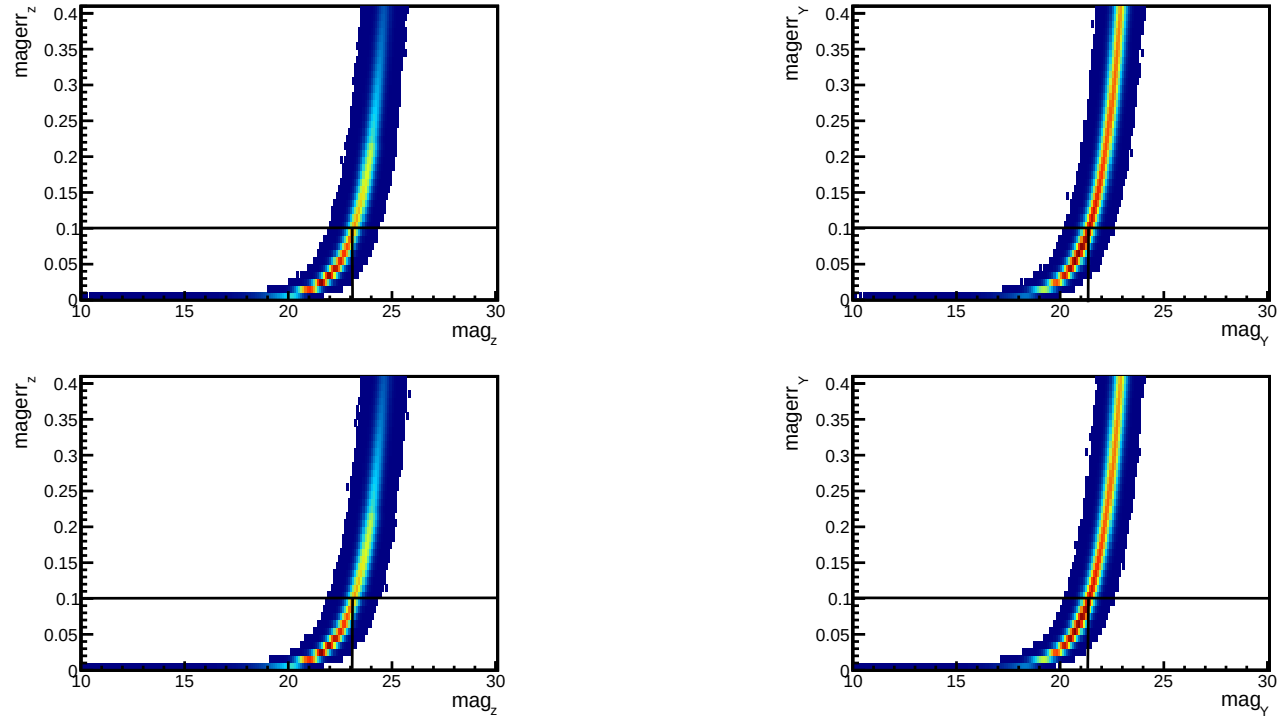

Figure 3.34: Magnitude error vs magnitude for Aarvark (top) and Buzzard (bottom) simulations in filters z and Y. Limiting magnitudes are $maglim_z \approx 23$ and $maglim_Y \approx 21.3$.

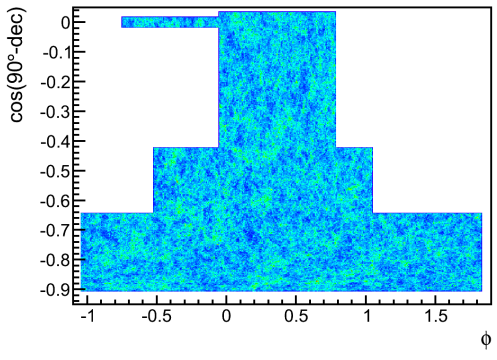

$0.2 < z_{phot} < 0.4$

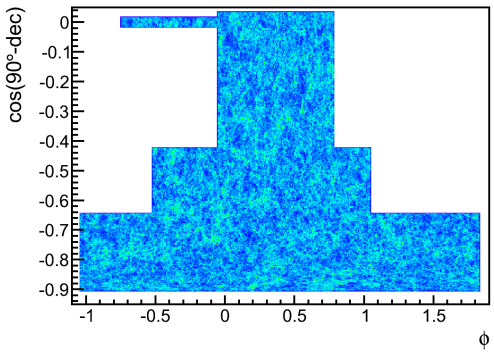

$0.4 < z_{phot} < 0.55$

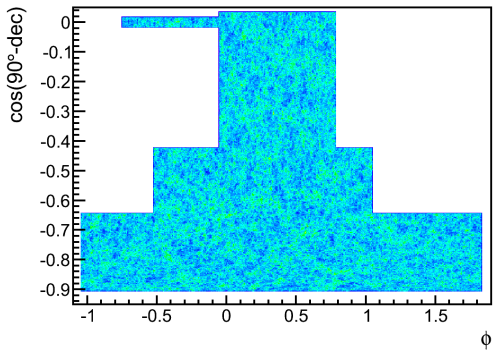

$0.55 < z_{phot} < 0.7$

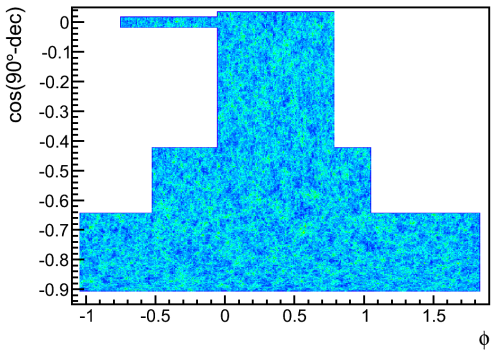

$0.7 < z_{phot} < 0.85$

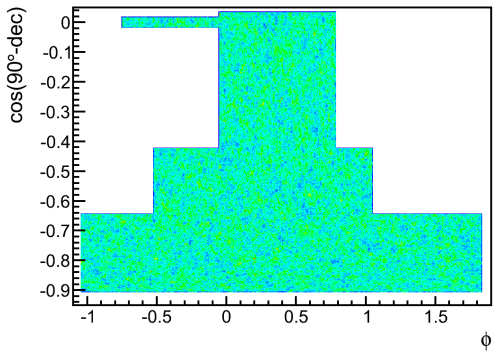

$0.85 < z_{phot} < 1.0$

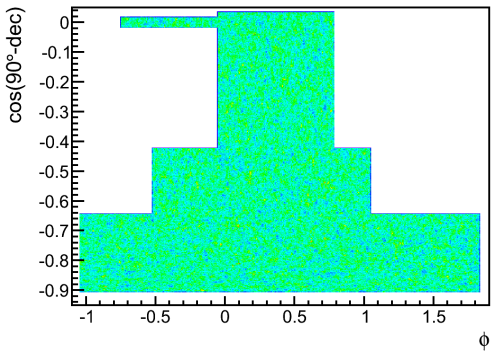

$1.0 < z_{phot} < 1.2$

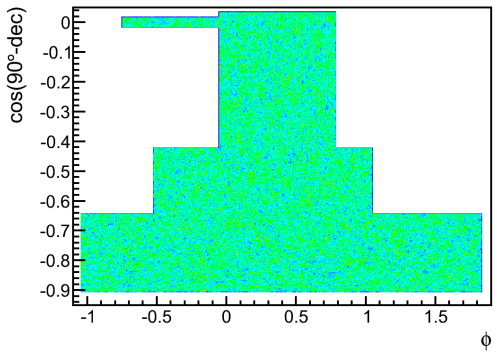

$1.2 < z_{phot} < 1.4$

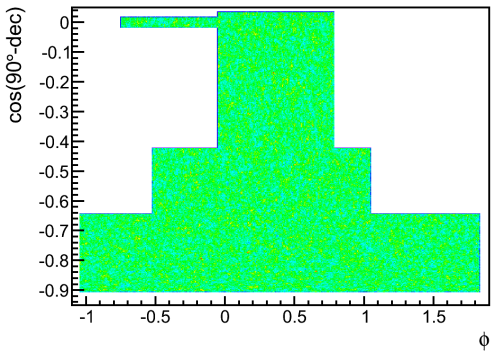

$1.4 < z_{phot} < 1.6$

Figure 3.35: Maps of Aardvark simulation.

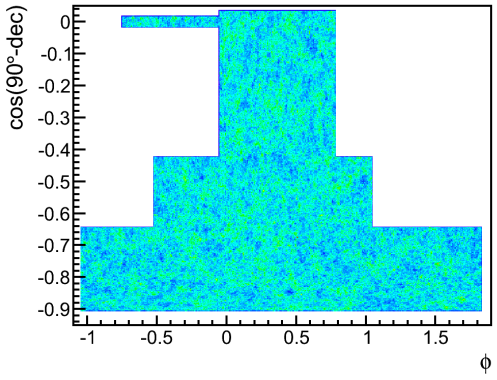

$0.2 < z_{phot} < 0.4$

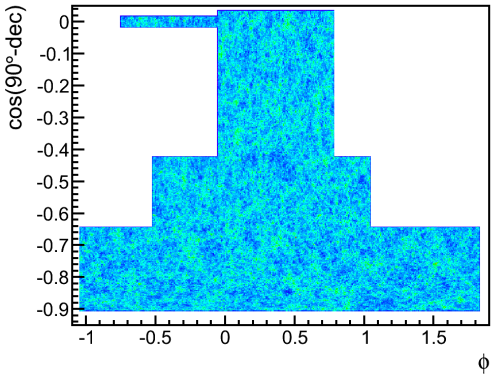

$0.4 < z_{phot} < 0.55$

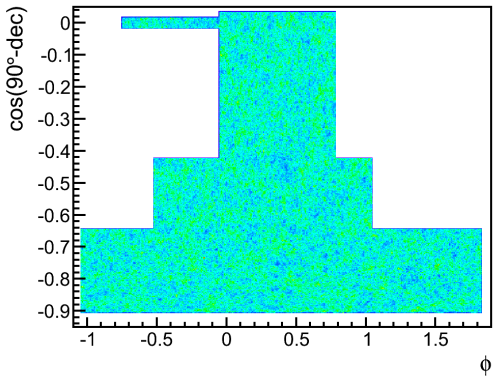

$0.55 < z_{phot} < 0.7$

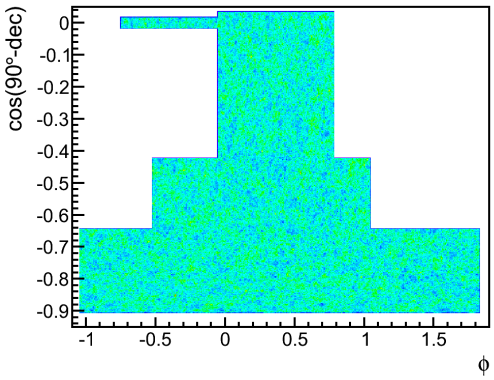

$0.7 < z_{phot} < 0.85$

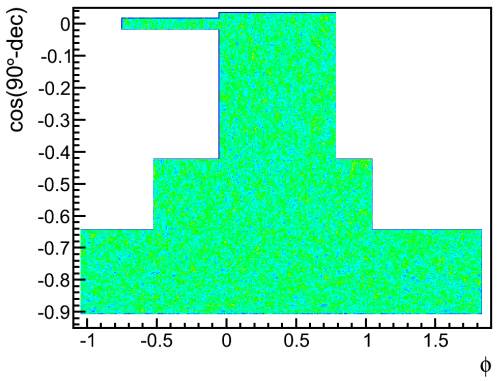

$0.85 < z_{phot} < 1.0$

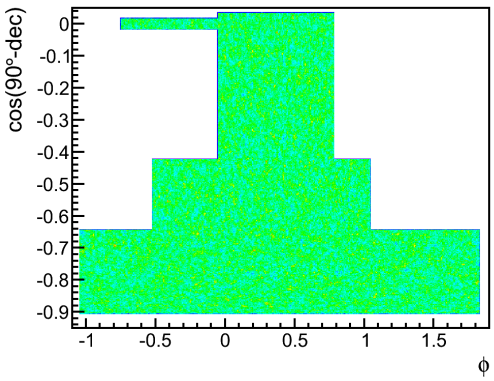

$1.0 < z_{phot} < 1.2$

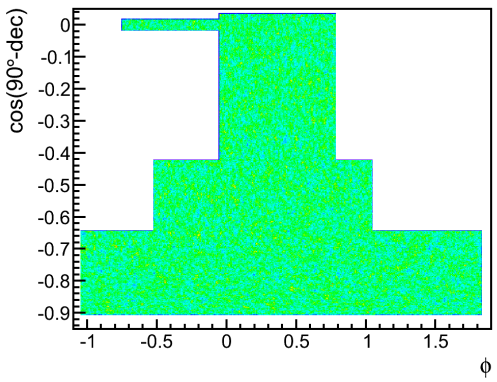

$1.2 < z_{phot} < 1.4$

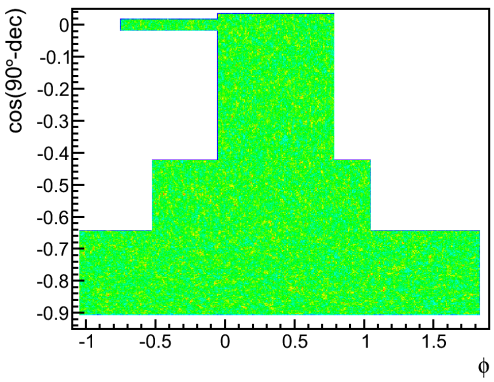

$1.4 < z_{phot} < 1.6$

Figure 3.36: Maps of Buzzard simulation.

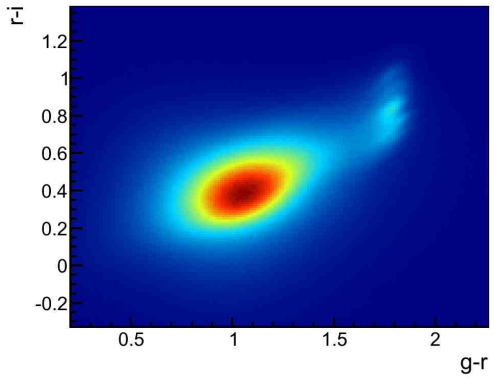

$g-r, r-i$ Aardvark $0.5 < photo-z < 0.6$

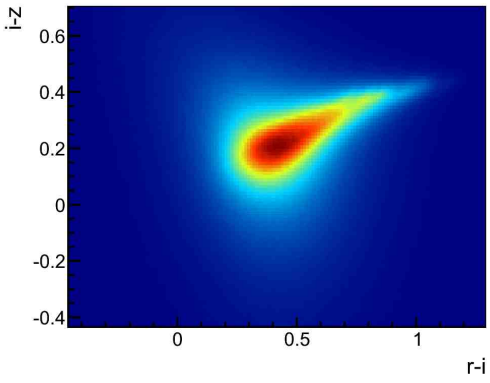

$r-i, i-z$ Aardvark $0.5 < photo-z < 0.6$

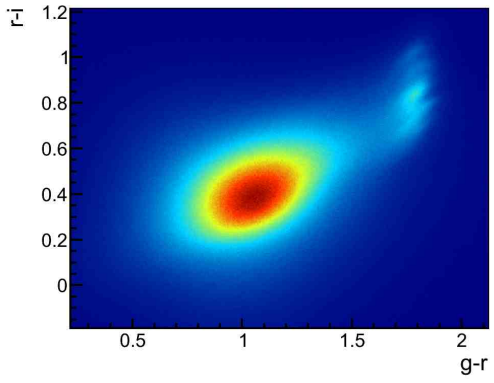

$g-r, r-i$ Buzzard $0.5 < photo-z < 0.6$

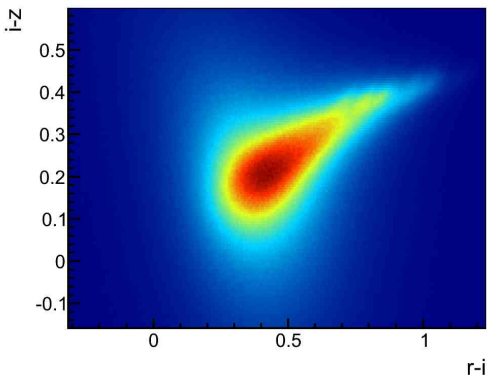

$r-i, i-z$ Buzzard $0.5 < photo-z < 0.6$

Figure 3.37: Example of color-color diagrams for Aardvark (top) and Buzzard (bottom).

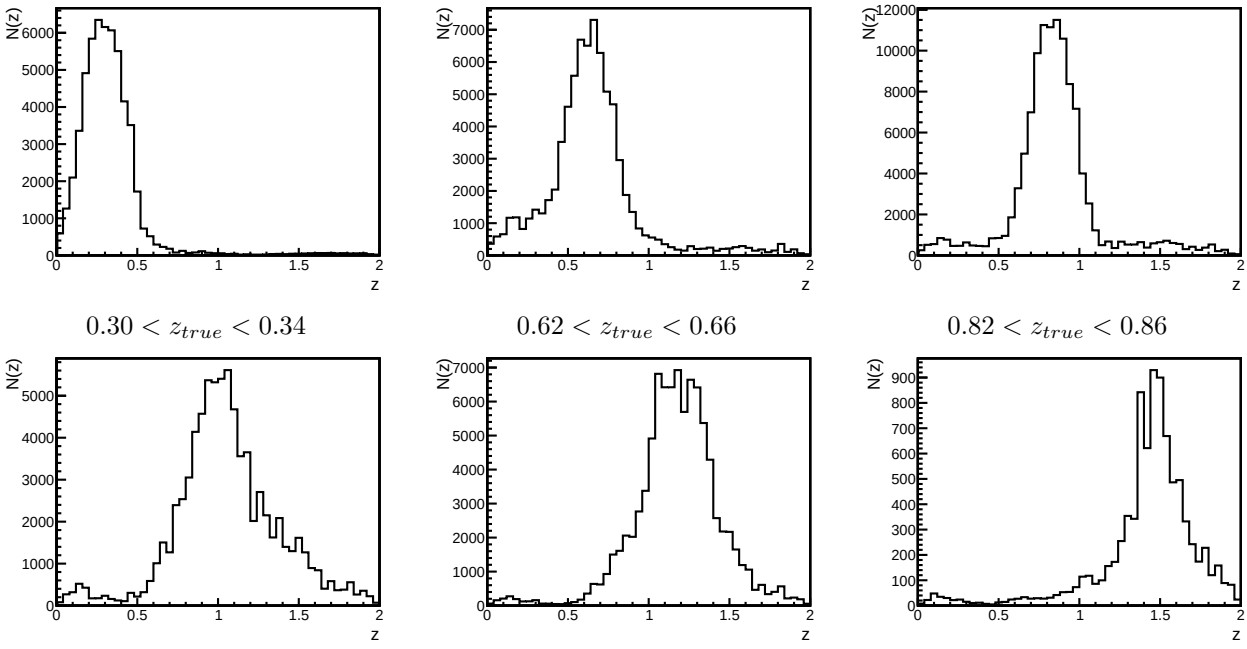

$0.30 < z_{true} < 0.34$ $0.62 < z_{true} < 0.66$ $0.82 < z_{true} < 0.86$

$1.02 < z_{true} < 1.06$ $1.18 < z_{true} < 1.22$ $1.38 < z_{true} < 1.42$

Figure 3.38: ArborZ true-z distributions.

Photo-z

An important issue is to choose the photo-z binning to calculate the angular correlation functions as demonstrated in [73]. A good knowledge and understanding of the photo-z is one of the key aspects in photometric surveys as DES. In particular, for our analysis we need a large volume and, in order to have stronger cosmological constraints, as many redshift bins as possible.

To understand the provided photo-z we proceeded reproducing the situation of real data. We selected 120,000 galaxies randomly as our calibration sample where the true redshift is known, and then, we constructed the true redshift distribution for 6 photo-z bins. The results in the Figure 3.38 show that it is not possible to divide the data into many independent bins because of the width of the probability distribution function (PDF) of the galaxies' photo-z.

We want the binwidths to be larger than the variance in order to avoid a strong correlation, but not too large because we want to minimize the projection effect. We concluded that for our analysis the optimal choice of photo-z binning is: $[0.2, 0.4]$, $[0.4, 0.55]$, $[0.55, 0.7]$, $[0.7, 0.85]$, $[0.85, 1]$, $[1, 1.2]$, $[1.2, 1.4]$ and $[1.4, 1.6]$. The photo-z behaviour is similar in both simulations, consequently we use the same photo-z bins.

After choosing our redshift bins, we have used two different methods to estimate their true-redshift distributions. First, we used the true-redshift information from the calibration sample to compute the distribution histograms for each photo-z bin. We also developed a second procedure. For every galaxy, we use its photo-z PDF and we assign to each redshift bin the full PDF weighted by its integral in the corresponding redshift bin. This method allows us to use every (well measured) galaxy in our sample since we only use observed quantities. Both procedures lead to similar results as it can be seen in Figure 3.39 which shows that the distributions are well behaved and match the true-redshift information properly.

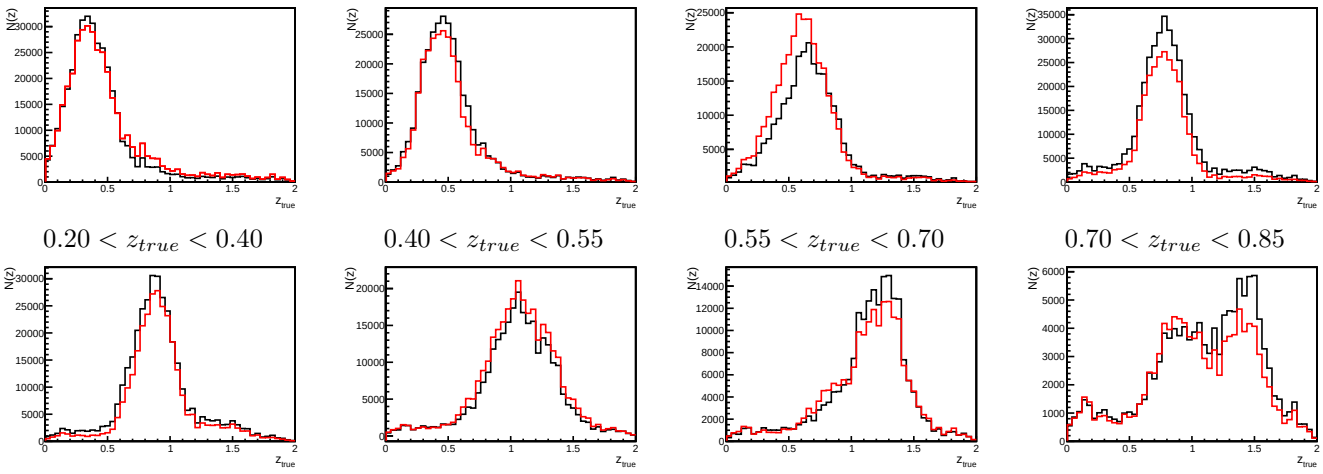

Figure 3.39: ArborZ true-z distributions weighting galaxies' PDFs by their integrals (black) and using true-z to select bins and accumulating PDFs (red).

Computation of the angular two point correlation function

The correlation function was computed in our selected redshift bins using a very fast pair-counting GPU code [99]. The code was modified to support logarithmic binning and pixel-based counting. Since data sample is very large, we used a pixel-based approach. We made 1024×1024 pixels maps in spherical coordinates (ra and $cos(90° - dec)$) covering 10000 deg^2. Only those pixels within the footprint are considered for the correlation function. Each galaxy contributes with a weight computed as the integral of its PDF in the corresponding redshift bin. This way, we minimize the correlation between redshift bins and use all the information avalaible. This number of pixels leads us to a resolution $\sim 0.09°$ in the correlation function which is more than enough for our purposes.
The calculation of the errors in the correlation function is done as we did for data, using the expression 2.48.
The results are shown in Figure 3.40 for Aardvark and Figure 3.41 for Buzzard. Once we have computed the correlation functions, the next step of our analysis is to extract the BAO peak.

BAO fit

The fitting procedure is described in [73]. We use a power law plus a Gaussian to fit the correlation function around the BAO peak. This constitutes an empirical description of the correlation function which allows a precise location of the BAO peak.

The fitting results are shown in Figure 3.40 for Aardvark and 3.41 for Buzzard. It can be seen that for the first two redshift bins the statistical significance is too low to claim any detection and, consequently, we ommited those bins in the extraction of cosmological constraints. The remaining redshift bins have a good significance BAO detection. The peak position and significance of the detection is shown in Figure 3.42. The statistical significance of the detection is given by the ratio D/σ_D where D is the amplitude of the Gaussian in the fitting formula given by 3.31.

$$\omega_{FIT}(\theta) = A + B\theta^{-C} + D\exp -\frac{(\theta - \theta_{FIT})^2}{2\sigma^2_{FIT}} \tag{3.31}$$

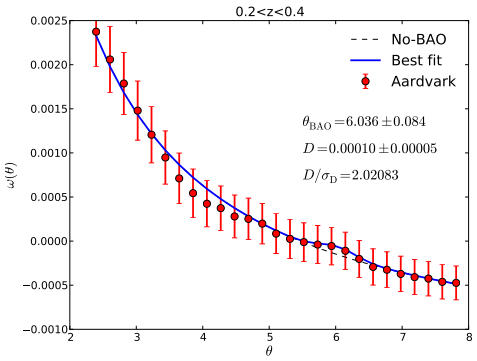

$0.20 < z < 0.40$

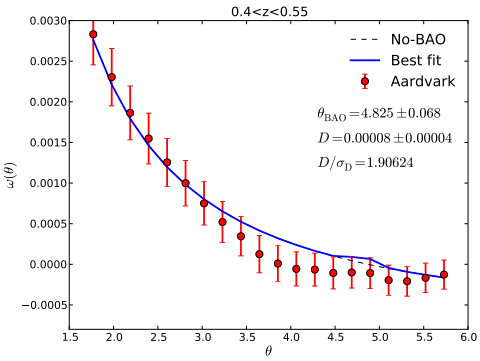

$0.40 < z < 0.55$

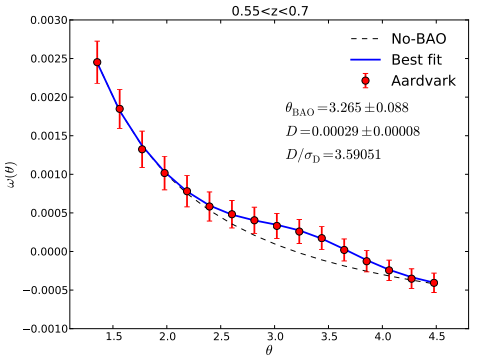

$0.55 < z < 0.70$

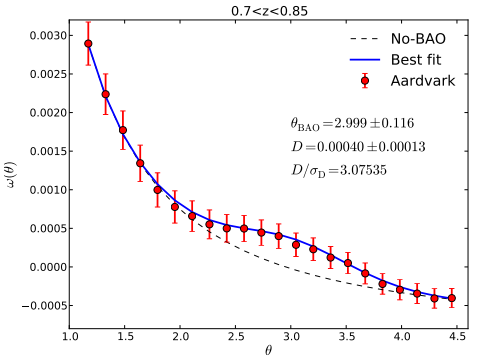

$0.70 < z < 0.85$

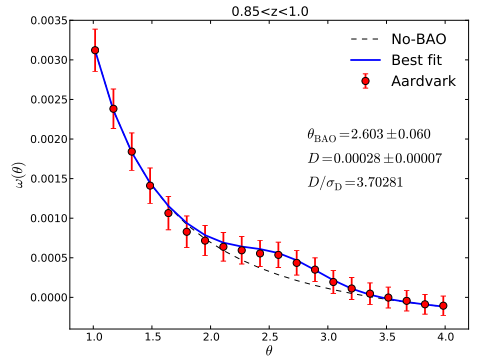

$0.85 < z < 1.00$

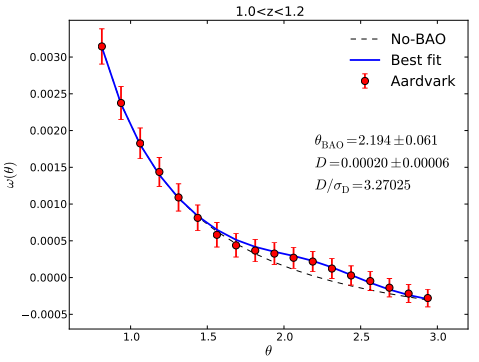

$1.00 < z < 1.20$

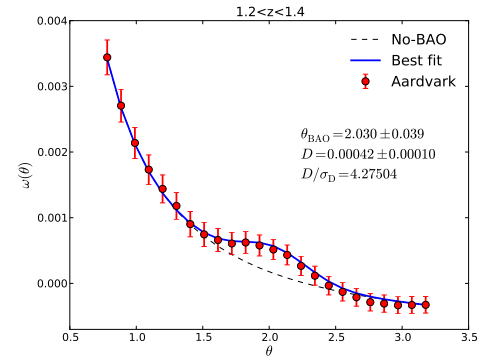

$1.20 < z < 1.40$

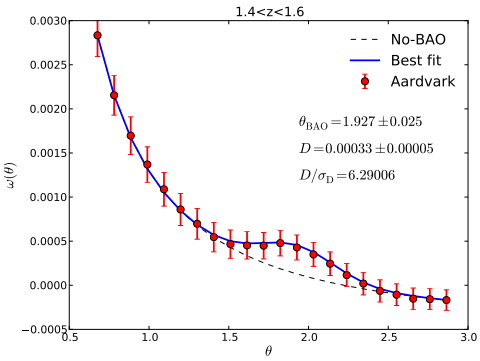

$1.40 < z < 1.60$

Figure 3.40: Angular correlation functions for Aardvark simulation using ArborZ photoz.

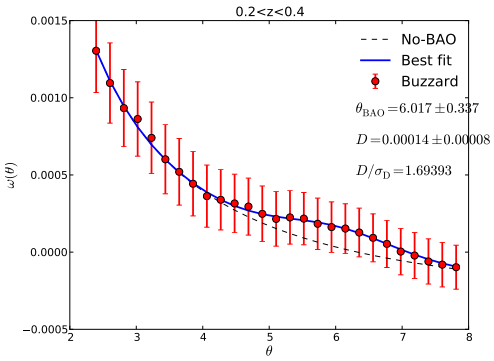

$0.20 < z < 0.40$

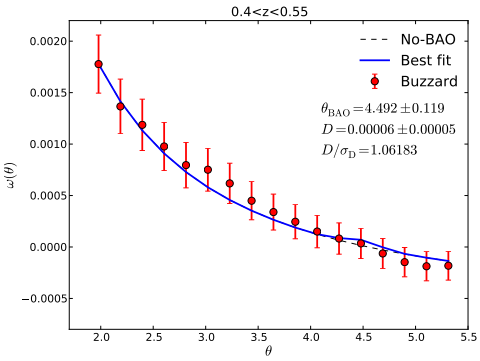

$0.40 < z < 0.55$

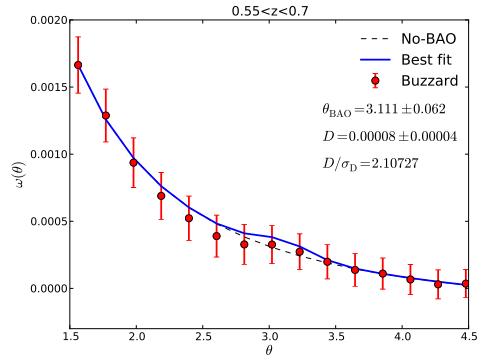

$0.55 < z < 0.70$

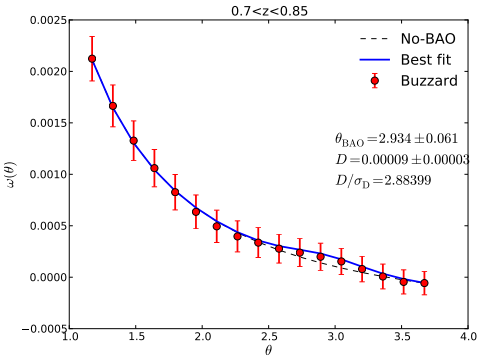

$0.70 < z < 0.85$

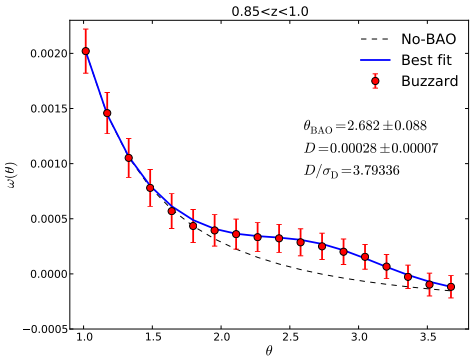

$0.85 < z < 1.00$

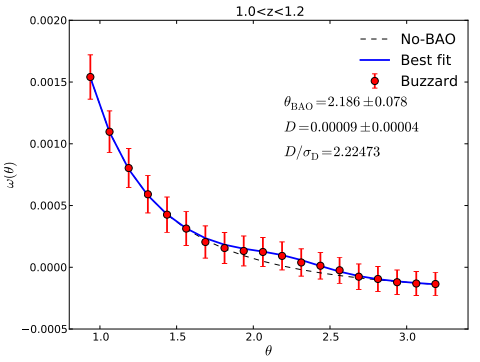

$1.00 < z < 1.20$

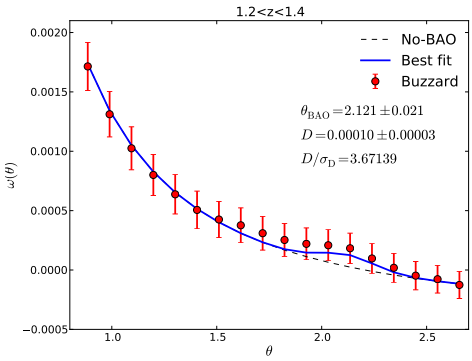

$1.20 < z < 1.40$

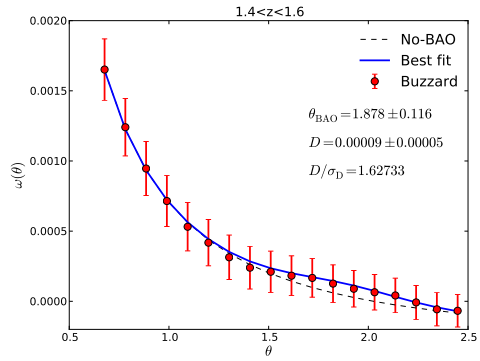

$1.40 < z < 1.60$

Figure 3.41: Angular correlation functions for Buzzard simulation using ArborZ photoz.

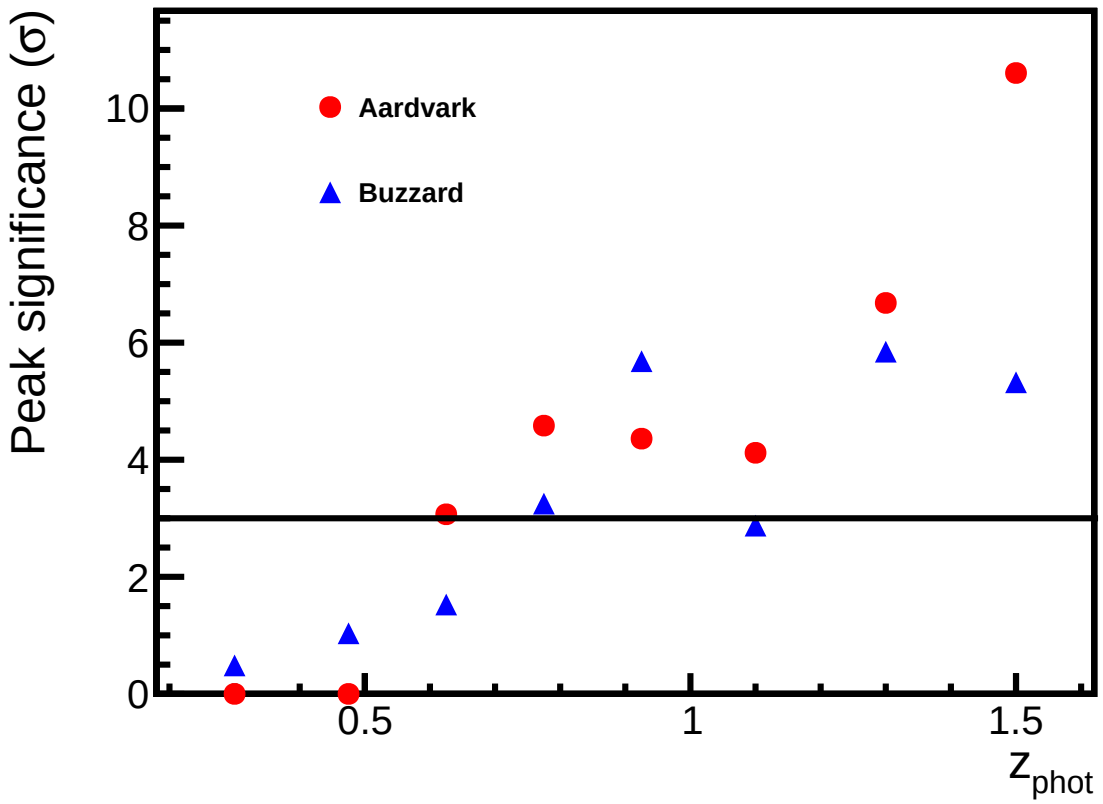

Figure 3.42: Significance of the BAO signal in each photo-z bin

Correction of the BAO peak position

The recovered position of the peak should be related to the position of the BAO peak at the mean redshift of the corresponding bin. These two positions are not equal due to the projection effect. This effect arises as a consequence of having wide redshift bins with non trivial distributions (Figure 3.39) due to the photometric nature of DES and the finite resolution of the redshift measurement. We can relate the peak position to the BAO using the calibration method explained in [73]. The calibration method depends only on the photo-z distributions and bins and is cosmology independent. Therefore, we can use any theoretical correlation function and compute the projection over a wide redshift bin. In our case these selection functions are the normalized photo-z distributions in Figure 3.39. The used input cosmological parameters were $h = 0.71$, $\Omega_m = 0.266$, $\Omega_b = 0.449$, $\Omega_\Lambda = 0.734$ but, the correction is cosmology independent.
After fitting these theoretical functions we compute the distortion due to the projection effect α:

$$\theta_{BAO} = \alpha\theta_{FIT} \tag{3.32}$$

where θ_{BAO} is the theoretical value of the BAO angular position given by:

$$\theta_{BAO} = \frac{r_s}{d_A(z)} \tag{3.33}$$

The results of the BAO measurement using the PLG method are shown in Figure 3.43. Systematic errors are included in the measurement. The main source of systematic errors are the method ($\sigma_{\theta_{BAO}} \leq 1\%$), the model ($\sigma_{\theta_{BAO}} \leq 1\%$), the correction ($\sigma_{\theta_{BAO}} \leq 1\%$) and the photoz ($\sigma_{\theta_{BAO}} \leq 5\%$) [73]. We find for these results a value of $\sigma_{\theta_{BAO}} = 5\%$ [73]. The recovered BAO scales for each one of the simulations are not clearly distinguishible, neither distinguishible from a flat ΛCDM model with WMAP 7 parameters.

Covariance Matrix

As we have seen, the BAO measurements from the different redshift bins are not independent. The correlation matrix between them is given by:

$$C_{ij} = \langle\omega_i^O(\theta)\omega_j^O(\theta)\rangle - \langle\omega_i^O(\theta)\rangle\langle\omega_j^O(\theta)\rangle = \sum_{k=1}^{N_{bins}} \left(r_{ik}^2 r_{jk}^2\right) \frac{\left(N_k^T\right)^4}{\left(N_i^O\right)^2\left(N_j^O\right)^2}\mathrm{Cov}(\theta,\theta') \tag{3.34}$$

where r_{ij} is the migration matrix, i.e., the probability of a galaxy originally in the bin i to be observed in bin j, N_i^T is the true number of galaxies in the i-th bin, and N_j^O is the number of galaxies observed in the j-th bin. The covariance matrices are shown in Figure 3.44.

Measuring cosmology from PLG (Power Law plus Gaussian)

Once we have measured the angular BAO scale and corrected the projection effect, we are ready to extract cosmological information. In order to do that, we plug the angular BAO scale measurements and the covariance matrix into the cosmoSIS MCMC code [100]. This code has been developed for DES and LSST collaborations. It contains a module which computes the likelihood for the angular BAO scale. It uses different MCMC samplers to estimate the likelihood and obtain the maximum likelihood values. Results are shown in 3.45.

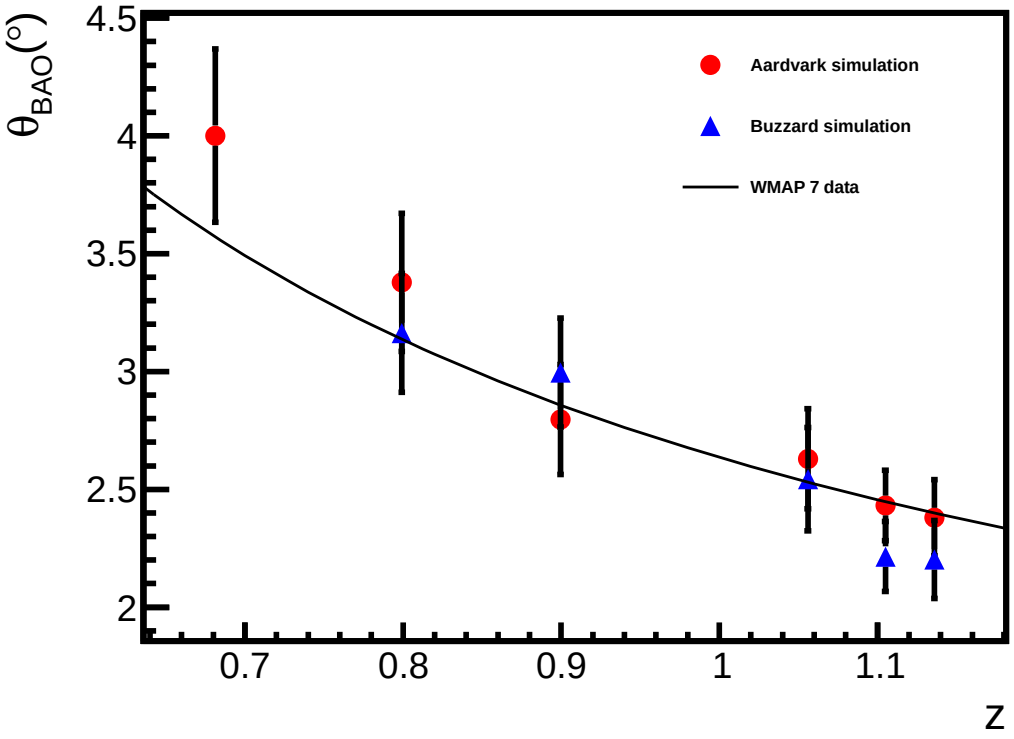

Figure 3.43: Recovered BAO position for Aardvark and Buzzard simulations using PLG method. Systematic errors are included.

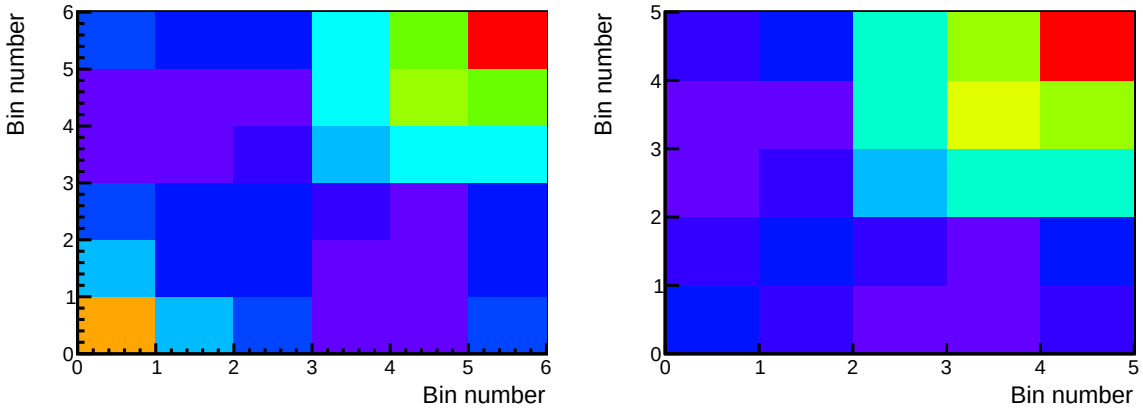

Figure 3.44: Covariance matrices for Aardvark (left) and Buzzard simulations (right).

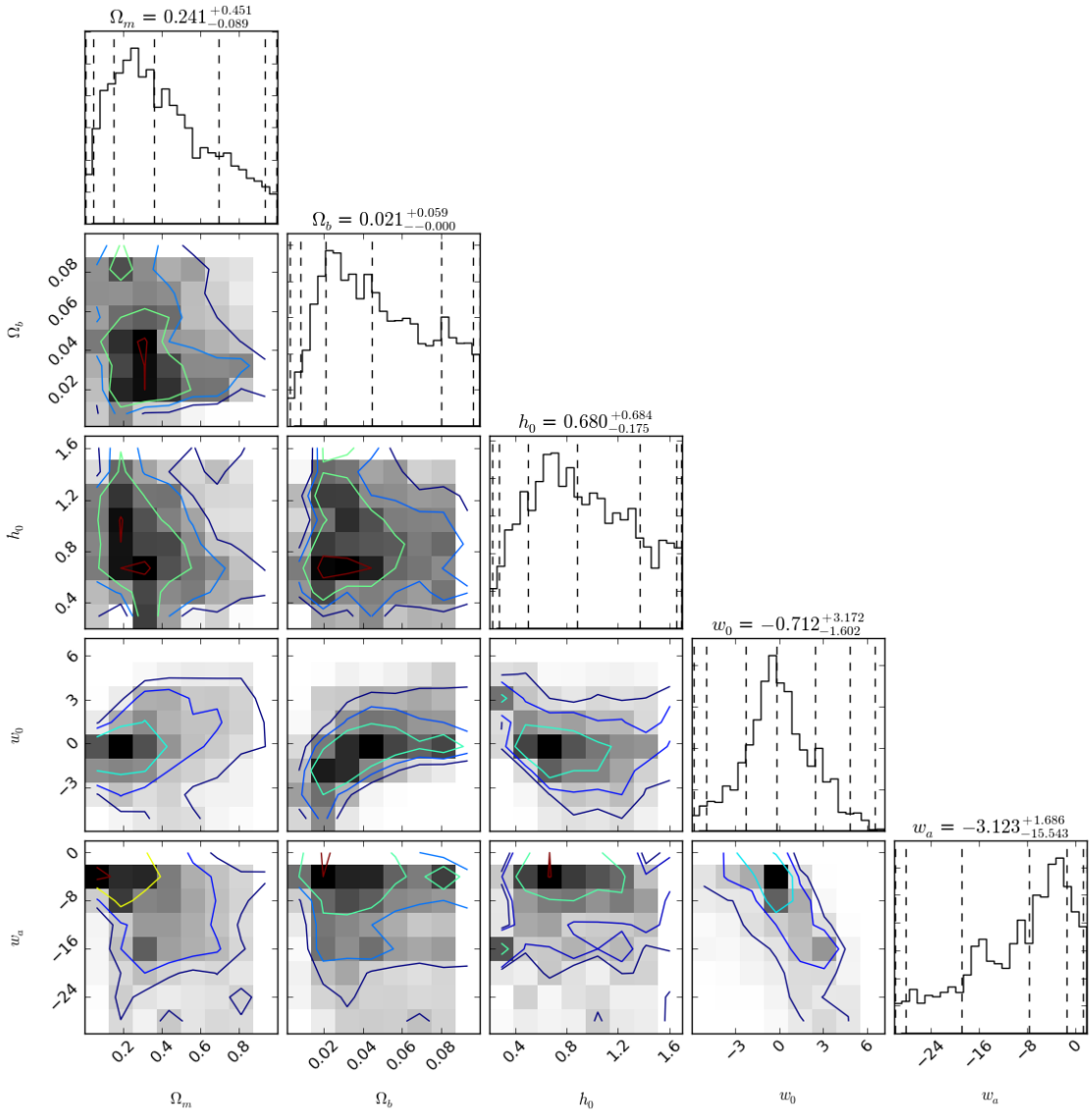

Figure 3.45: Measured cosmology for Aardvark. We recover the input flat ΛCDM cosmology $\Omega_m = 0.23$, $h = 0.72$, $\Omega_b = 0.042$.

3.3.4. Conclusions

We performed a full cosmological analysis of the angular BAO in the same way as it will be done with DES data. After performing some basic quality cuts on the simulated catalogs, we chose a set of photo-z bins as a compromise between minimizing bin correlations and projection effects. We then computed the angular two point correlation function for each bin and extracted the position of the BAO peak using the PLG method. Finally, we used the recovered values of $\theta_{\rm BAO}$ to constrain the values of the cosmological parameters using cosmoSIS. The results show that the BAO position only has no sensitivity to distinguish both simulations. Thus, the main difference in the cosmology of these simulations should be related to those parameters that are not strongly related to the BAO peak position.

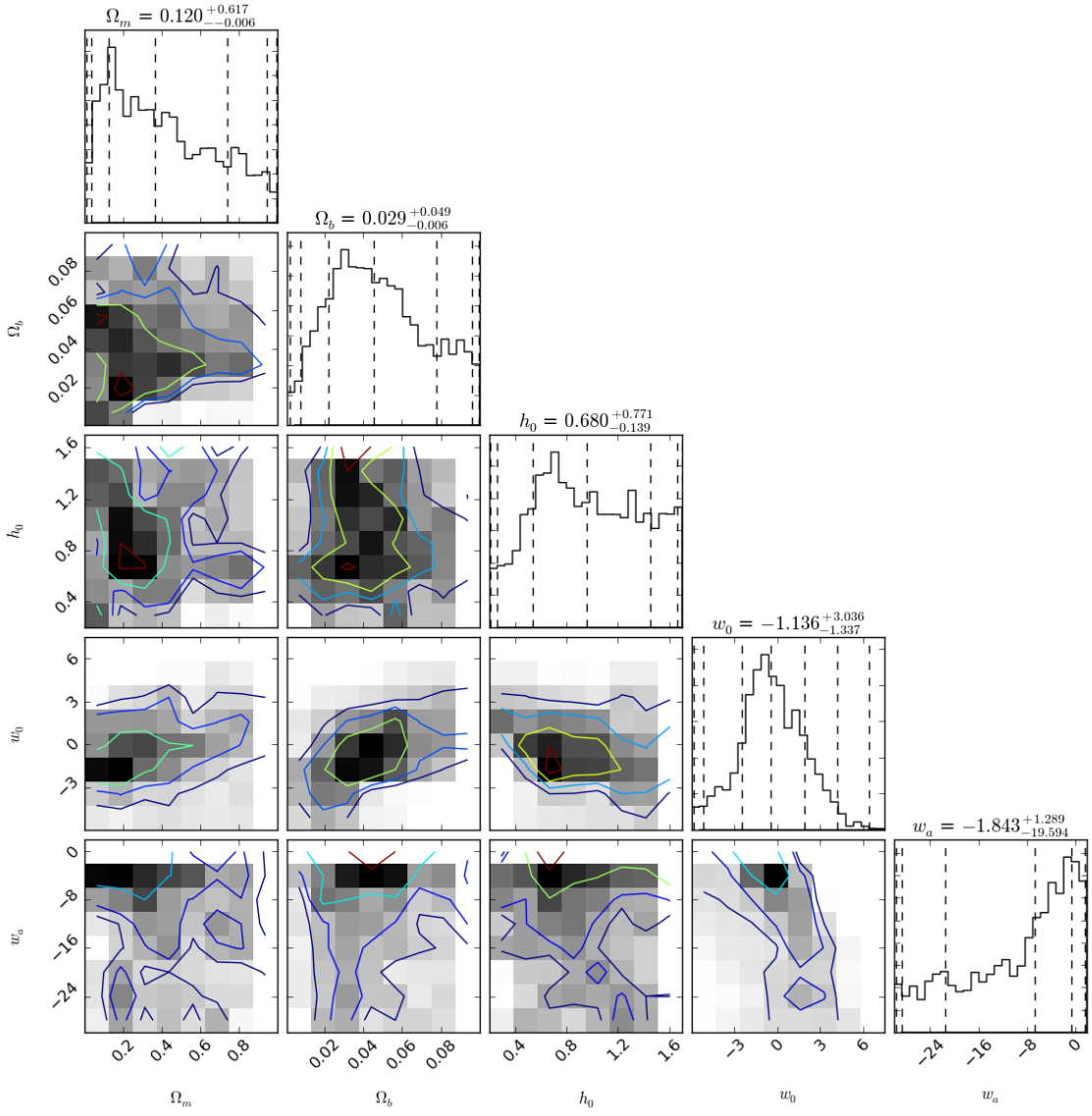

Figure 3.46: Measured cosmology for Buzzard.

3.3.5. Fit to the full-shape correlation function at low scales

The measurement of angular two point correlation function (2pcf) is one of the most powerful tools in modern cosmology, and it allows us to extract very valuable information. The photometric nature of DES makes difficult to measure redshift space distortions (RSD) or to make very narrow redshift bins. Besides, DES offers large statistics and allows us measurements of the angular 2pcf with negligible Poisson noise even for restricted area. Here we use the simulation to estimate the sensitivity to measure and analyze the constraining power of this measurement for two of the cosmological parameters: Ω_m and w.

Modelling the angular correlation function

In order to extract any information from the correlation function we will need a proper theoretical modelling. This modelling is provided by equation 2.55 and it includes the effect of redshift space distortions. If we proceed to compute the corresponding angular correlation function we have:

$$\begin{aligned}
\omega(\theta) &= \int_0^\infty dz_1\phi(z_1)\int_0^\infty dz_2\phi(z_2)\xi_s(z_1,z_2,\theta) \\
&= \int_0^\infty dz_1\phi(z_1)\int_0^\infty dz_2\phi(z_2)b^2(z_1,z_2)\left\{\left[1+\frac{2}{3}\beta(z_1,z_2)+\frac{1}{5}\beta(z_1,z_2)^2\right]\mathcal{P}_0(z_1,z_2,\theta)\xi_0(z_1,z_2,\theta)\right. \\
&+ \left[\frac{4}{3}\beta(z_1,z_2)+\frac{4}{7}\beta(z_1,z_2)^2\right]\mathcal{P}_2(z_1,z_2,\theta)\xi_2(z_1,z_2,\theta) \\
&+ \left.\frac{8}{35}\beta(z_1,z_2)^2\mathcal{P}_4(z_1,z_2,\theta)\xi_4(z_1,z_2,\theta)\right\}
\end{aligned}$$

Renaming $\Lambda_0 \equiv \mathcal{P}_0(\mu)\xi_0(r)$, $\Lambda_2 \equiv \mathcal{P}_2(\mu)\xi_2(r)$, and, $\Lambda_4 \equiv \mathcal{P}_4(\mu)\xi_4(r)$ and recalling that $\beta(z) = f(z)/b(z)$ we can rewrite:

$$\begin{aligned}
\omega(\theta) &= \int_0^\infty \phi(z_1)dz_1\int_0^\infty \phi(z_2)dz_2 b^2(z_1,z_2)\left[\Lambda_0(z_1,z_2,\theta)\right] \\
&+ b(z_1,z_2)f(z_1,z_2)\left[\frac{2}{3}\Lambda_0(z_1,z_2,\theta)+\frac{4}{3}\Lambda_2(z_1,z_2,\theta)\right] \\
&+ f^2(z_1,z_2)\left[\frac{1}{5}\Lambda_0(z_1,z_2,\theta)+\frac{4}{7}\Lambda_2(z_1,z_2,\theta)+\frac{8}{35}\Lambda_4(z_1,z_2,\theta)\right]
\end{aligned}$$

Now, we assume that the bias parameter varies slowly within the redshift bin, that is, $b(z_1,z_2) \approx b(\bar{z})$ thus, we have:

$$\begin{aligned}
\omega(\theta) &= b^2(\bar{z})\int_0^\infty \phi(z_1)dz_1\int_0^\infty \phi(z_2)dz_2\left[\Lambda_0(z_1,z_2,\theta)\right] \\
&+ b(\bar{z})\int_0^\infty \phi(z_1)dz_1\int_0^\infty \phi(z_2)dz_2 f(z_1,z_2)\left[\frac{2}{3}\Lambda_0(z_1,z_2,\theta)+\frac{4}{3}\Lambda_2(z_1,z_2,\theta)\right] \\
&+ \int_0^\infty \phi(z_1)dz_1\int_0^\infty \phi(z_2)dz_2 f^2(z_1,z_2)\left[\frac{1}{5}\Lambda_0(z_1,z_2,\theta)+\frac{4}{7}\Lambda_2(z_1,z_2,\theta)+\frac{8}{35}\Lambda_4(z_1,z_2,\theta)\right]
\end{aligned}$$

We use the power spectrum from HALOFIT to introduce the non-linearities and obtain the corresponding $\xi_l(r)$. When fitting to data we minimize a χ^2 function varying only the bias parameter and fixing the other parameters to their fiducial values:

$$\chi^2 = \sum_{i,j}[\omega(\theta_i)^{meas} - \omega(\theta_i)^{th}]C_{ij}^{-1}[\omega(\theta_j)^{meas} - \omega(\theta_j)^{th}] \tag{3.35}$$

This constitutes the base of our analysis.

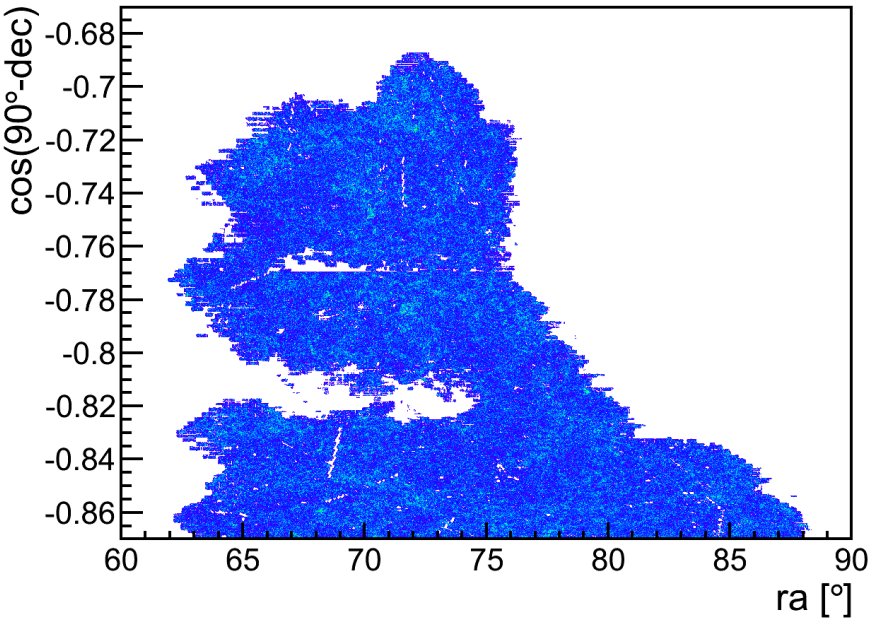

Figure 3.47: Patch of the Aardvark simulation used for the correlation function analysis.

Data selection

We selected the patch of the sky depicted in Figure 3.47. It is the same area that will be analyzed in the next chapter with DES SVA1 data (~ 135 deg^2).

Photo-z

In this case, we will use the Gaussian photo-z provided in the simulation for simplicity. The analysis procedure is the same regardless of the photo-z algorithm used. We analyze 5 different redshift bins: $[0.2, 0.4]$; $[0.4, 0.6]$; $[0.6, 0.8]$; $[0.8, 1.0]$ and $[1.0, 1.2]$. Since we have the true redshift information for all the galaxies in this simulation, we will use it to compute $\phi(z)$ in these bins. We show $\frac{dn(z)}{dz}$ in Figure 3.48. Remember that $\phi(z)$ is just $\frac{dn(z)}{dz}$ normalized to 1. The total number of objects in the sample is 13.3 million after selecting these bins and area.

Mesuring correlations.

In order to estimate the angular two point correlation function we proceed as in previoius sections. We use a modification of the GPU-based code presented in [99]. This allows us to reach very low angular scales ($\sim 10^{-7}$ deg) and also fast calculations by using pixellization for large scales. We use the Landy & Szalay estimator [82]:

$$\omega(\theta) = 1 + \frac{N_{rnd}^2}{N_{gal}^2}\frac{DD(\theta)}{RR(\theta)} - 2\frac{N_{rnd}}{N_{gal}}\frac{DR(\theta)}{RR(\theta)} \tag{3.36}$$

We use random catalogs with 3 times more objects than data[3]. We used 17 angular bins between 5×10^{-2} and 2 degrees.

[3]It is usual to use 10 times more randoms than objects but, in this case 3 times is more than enough due to the large statistics of DES

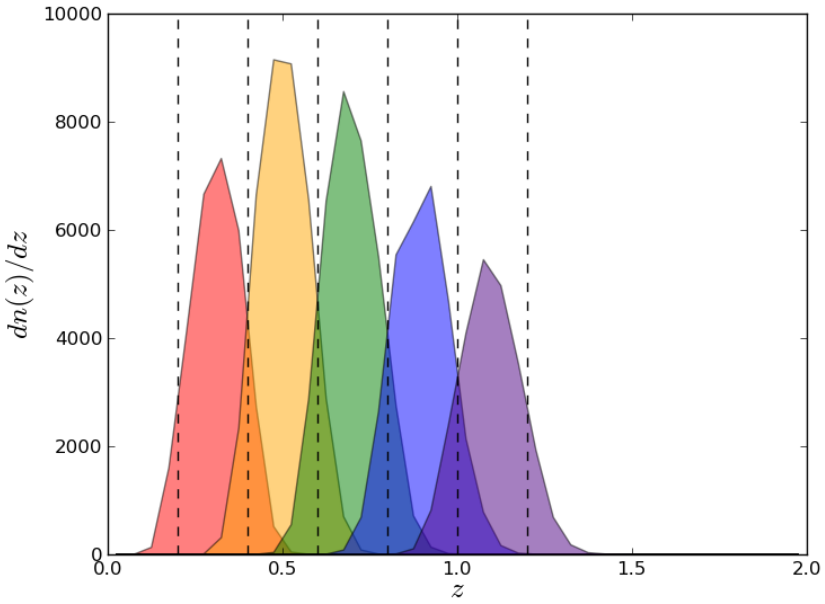

Figure 3.48: Photo-z bins used for the correlation function analysis from BCC-Aardvark simulation in units of hundreds of galaxies.

3.3.6. Covariance Estimation

One of the key parts of any cosmological analysis is the computation of the covariance matrices. In our case we will rely in the theoretical Gaussian approximation given by the expression from [62] (equation 2.48).

$$\mathrm{Cov}_{\theta\theta'} = \frac{2}{f_{sky}} \sum_{l\geq 0} \frac{2l+1}{(4\pi)^2} P_l(\cos\theta) P_l(\cos\theta') \left(C_l + \delta^D(\theta-\theta')\frac{1}{\bar{n}} \right)^2 \tag{3.37}$$

This theoretical estimation is consistent with the results from Jack-knife and random realizations [73].

3.3.7. Bias measurements

Following the aforementioned procedure, we computed the correlation function. We estimate the theoretical predictions for each one of the different redshift bins by fixing the cosmological parameters to the Aardvark values ($\Omega_m = 0.23$, $\Omega_b = 0.042$, $h = 0.72$, $\sigma_8 = 0.82$, $\Omega_\Lambda = 0.77$). Once we have the theoretical predictions we fit the linear bias parameter $b(z)$. We obtain the values shown in table 3.2 and the plots from Figure 3.49 and Figure 3.50 ,where the evolution of the bias with redshift is depicted. The fit is performed at the scales where we are confident of the linear bias approximation for the different redshift bins. The non-linearities at higher redshifts are propagated using the linear-growth. This makes that the scales where we are confident for the bins 0.4-0.6 and 0.6-0.8 are higher than the bin 0.2-0.4. Regardless, non-linearities are important in these three redshift bins at low scales.

3.3.8. Constraining w and Ω_m using the angular correlation function

We can go a step further and not only minimize the χ^2 fixing every parameter except the linear bias, but also we can fit Ω_m and w to obtain information about dark energy. The procedure is simple, we compute the

z	b	Δb	χ^2/ndof	p-value
0.2 - 0.4	1.08	0.06	0.11	0.99
0.4 - 0.6	0.95	0.08	1.02	0.41
0.6 - 0.8	1.10	0.09	0.95	0.47
0.8 - 1.0	1.33	0.03	0.88	0.60
1.0 - 1.2	1.74	0.04	0.56	0.90

Table 3.2: Best-fit bias values for Aardavark simulation.

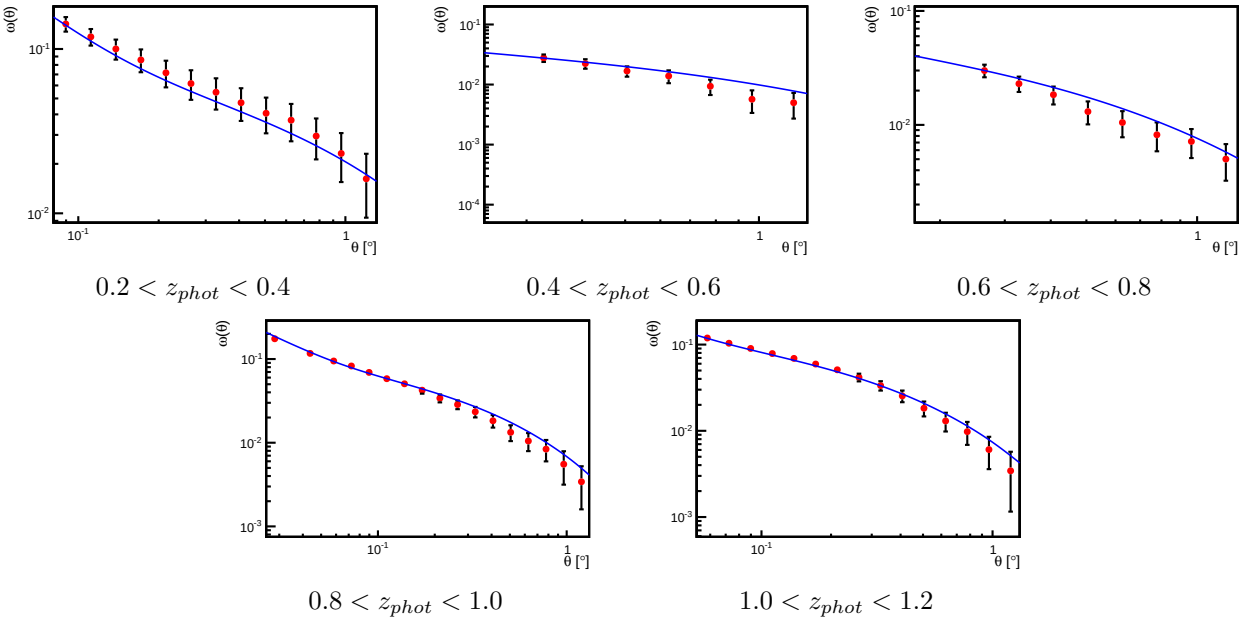

Figure 3.49: Best-fit bias to the Aardvark angular two point correlation function. The theoretical predictions are made using the non-linear power spectrum from HALOFIT [69].

theoretical angular correlation function for each set of cosmological parameters in the same way we did to fit the bias. A power spectrum is obtained from CAMB [59] using non-linearities from HALOFIT [69] for each set of parameters. Then we integrate for the wide redshift bins using the correspoding photo-z distributions and obtain the functions $\omega_{th}(\theta)$. Once we have these theoretical predictions, we minimize a χ^2 in the desired parameter space.

We restrict our analysis to just 2 parameters because the errors of the correlation function are still dominated by the area (see equation 2.48). Then our constraining power is reduced and we are sensitive just to certain combinations of them, in particular, the correlation function shape will be especially affected by Ω_m, and w. The overall amplitude will be affected by the bias parameter but, we will fix these values to the values we obtained in the last section. We make this assumption because the bias could be measured independently using methods like counts in cells[4]. Moreover, a small variation in cosmological parameters does not affect the best-fit values of the bias and viceversa. Thus, we can choose safely these values. However, we should keep in mind that this results will be optimistic since we are fixing the rest of cosmological parameters but, the correlation between w and Ω_m will remain the same and the uncertainties will be similar. The results are plotted in Figure 3.51 and they show that we recover the correct input cosmology within 1σ C.L. The performance of this

[4]The value of the bias will depend on the election of σ_8 so, the bias obtained by other methods should be normalized to the same value of σ_8 that is used in the theoretical predictions.

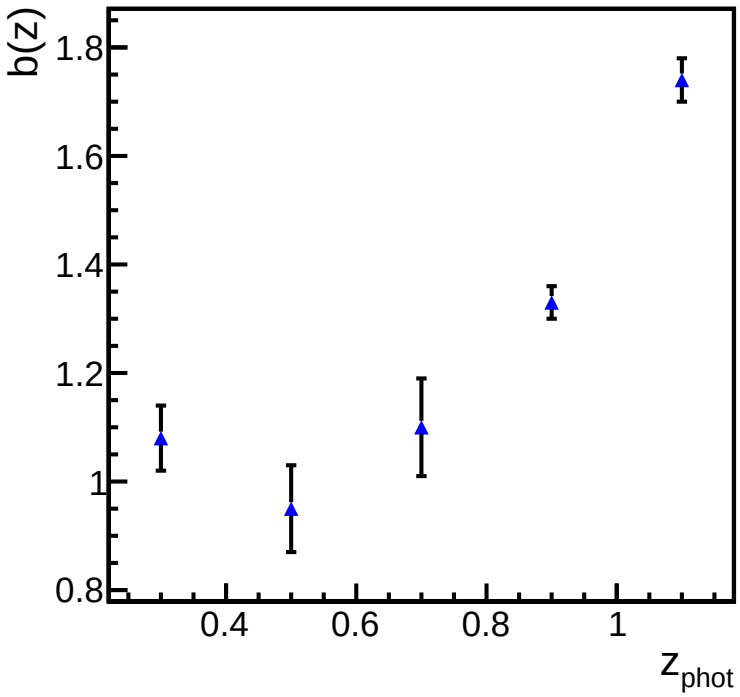

Figure 3.50: Evolution of the best-fit bias parameter for the Aardvark simulation.

measurements will improve when we have larger areas but, we wanted to test this method in a realistic scenario similar to the case of the DES Science Verification Data. In conclusion, we have used the angular two point correlation function as a probe of the cosmological parameters in photometric redshift surveys and we will use this technique with DES data in chapter 5.

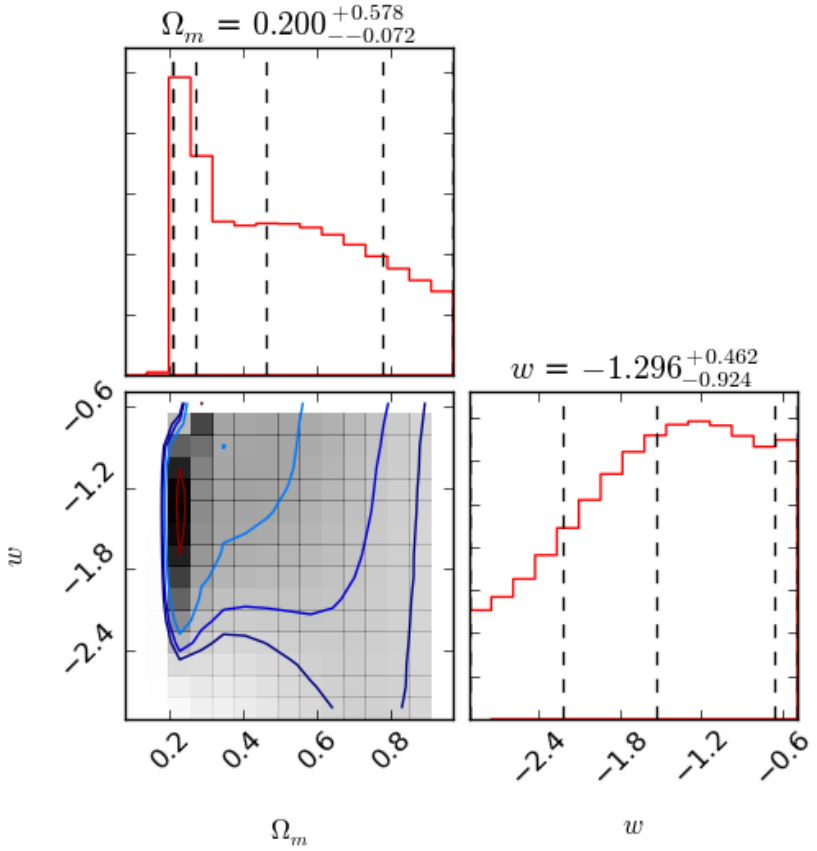

Figure 3.51: Results of the fits to Ω_m and w for the Aardvark simulation fixing n_s, $b_g(z)$, h_0 and the ratio Ω_b/Ω_m in a wCDM model.

Chapter 4

The Dark Energy Survey (DES)

The Dark Energy Survey (DES) [101] is a stage III [51] generation galaxy survey that relies on four probes to unveil the nature of dark energy. These probes are: the number of clusters as a function of redshift z (CL), the weak lensing effect in the distribution of galaxies (WL), the BAO measurement and the Hubble diagram of type Ia supernovae (SN). At the end of DES, 10000 clusters up to $z \sim 1.0$, 200 million galaxy shapes for WL measurements, 300 million galaxy positions up to $z \sim 1.4$ for BAO measurements, and, in addition to this, 3000 type Ia supernovae up to $z \sim 1$ will be measured. Combining the four probes it is expected to measure the dark energy equation of state parameter w_0 with a precision better than 0.05 and its evolution with time w_a with a precision around 0.3 (Figure 4.2).

DES is an international collaboration formed by more than 300 scientists participating from more than 20 institutions in the United States, Spain, the United Kingdom, Brazil, Germany, Switzerland and Australia. The collaboration has built a very sensitive 570 Megapixel digital camera, DECam, mounted on the Blanco 4-meter telescope at Cerro Tololo Inter-American Observatory (CTIO) high in the Chilean Andes. The initial data from Science Verification were recorded from September 2012 to February 2013 and the Survey period started in August 31st of 2013, countinuing for at least five years.

DES will observe 5000 deg^2 of the southern sky with five different filters from visible g, r, i to near infrared z, and Y up to magnitude i $\sim$ 24 at 10 sigma ($z_{max} \sim 1.5$). Moreover, DES will have a large overlap ($\sim$ 2500 deg^2) with the South Pole Telescope (SPT) [102] in order to measure the Sunyaev-Zel'dovich effect [31]. All the DES results presented in this thesis are based on the Science Verification data.

4.1. DECam

The Dark Energy Camera (DECam) [103] is the main instrument of DES (Figures 4.5, 4.6). The camera has five major systems:

- a 570 megapixel CCD imager,
- a low-noise electronic readout system,
- a wide-field optical corrector,
- a combination shutter-filter system,
- a hexapod adjustor to provide stability.

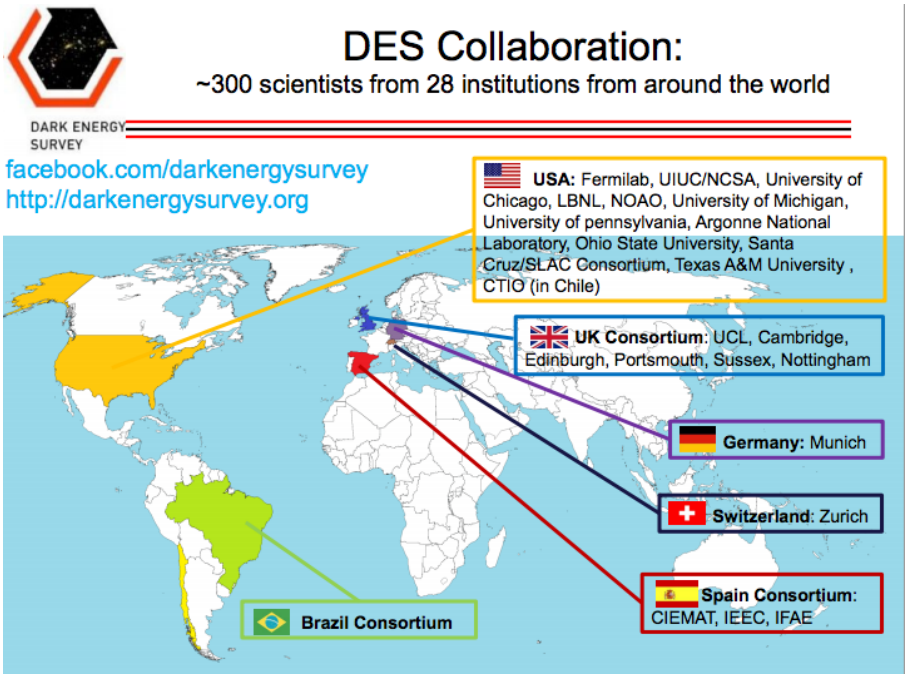

Figure 4.1: Countries and Institutions participating in DES collaboration. Picture Credit: Dark Energy Survey Collaboration.

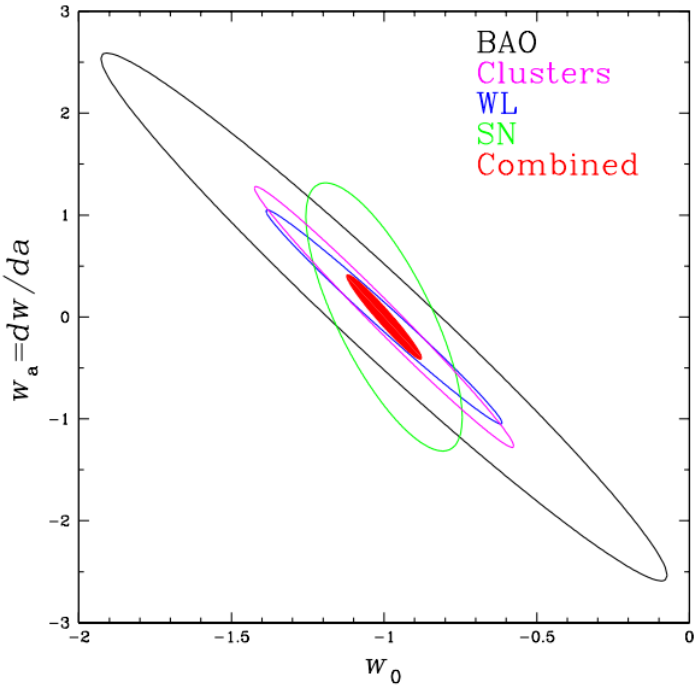

Figure 4.2: Forecast for the sensitivity of DES at the end of the project combining the four different probes to test the nature and evolution of dark energy [102].

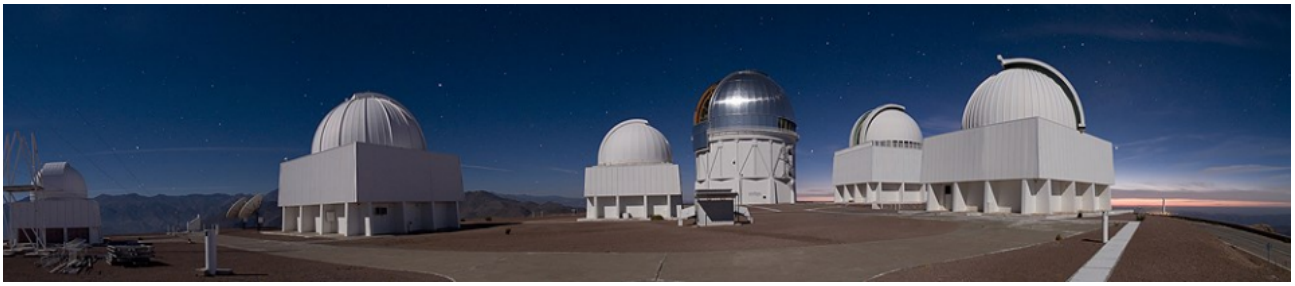

Figure 4.3: Cerro Tololo Inter-American Observatory. Picture Credit: Dark Energy Survey Collaboration.

In order to complete its science goals, DES uses CCDs that engineers at Lawrence Berkeley National Laboratory (LBNL) specifically designed to observe red light from distant galaxies. For example, the sensitivity of detecting long-wavelength light is increased when it travels through more silicon, so DES CCDs are about 10 times thicker (250 microns) than conventional CCDs. The DECam focal plane consists of a science array of sixty-two 2048×4096 CCDs (15 microns of pixel side that results on 0.27"/pixel in the Blanco). Additionally there are four 2048×2048 guider CCDs and eight 2048×2048 focus and alignment CCDs. The quantum efficiency of these CCDs with their anti-reflective coating is red optimized to be $> 90\%$ at 900nm and over 60% in the 400-1000nm range (see Figure 4.4). The DES CCDs were fabricated by Dalsa with further processing done by LBNL. They were packaged and tested by Fermilab.

DECam operates at 180 K in order to minimize noise and dark current with the cooling provided by liquid nitrogen. To prevent condensation on the surface of the CCDs, DECam operates at an extremely low vacuum pressure of 10^{-6} Torr.

The electronic system reads out and records an entire digital image (5×10^8 pixels) in 17 seconds, keeping an extremely low readout noise at the same time. This allows the camera to be read out in the same amount of time that it takes to the telescope to move to its next viewing position. The noise of the readout system is so low that, while an image may produce a full-well specification of 130,000 electrons, there are less than 25 electrons of noise in each pixel. The electronic system records the data in the form of a multi-extension fits (MEF) file and also provide real-time instrument health and quality checks. The electronic boards were produced in Spain, by CIEMAT and IFAE. The design process was carried out by Fermilab, CIEMAT, and IFAE.

The optical corrector system is a Wynne-style five lens, two asphere design. It provides a 2.2 degree field of view image at 0.27"/pixel while contributing less than 0.3" FWHM to the image quality. The biggest of these lenses is 98 cm in diameter and weighs approximately 190 kilograms.

The cartridge-style filter changer holds up to eight filters, which, at 62 cm in diameter, were the largest produced at the time of its manufacture. DES uses five filters, g, r, i, z, and Y (see Figure 4.7). Each one of these lets through a relatively broad wavelength. By comparing the relative amount of light detected through each filter for each object in an image, we can make a very good estimate of the redshift. The shutter is the largest of its kind.

The hexapods provide a real-time focus and alignment system to maintain high image quality.

4.1.1. The Blanco telescope

DECam is mounted on the Victor M. Blanco Telescope located at the Cerro Tololo Inter-American Observatory (CTIO) in the Chilean Andes at a height of 2200 meters. The observatory is 460 km north of Santiago and 80 km inland from the coastal city of La Serena. The telescope is operated by the Association of Universities

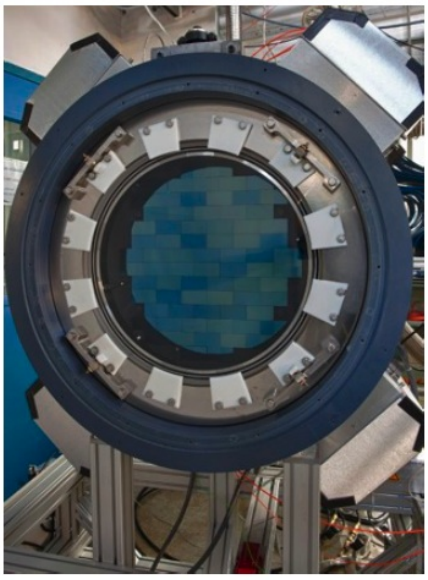

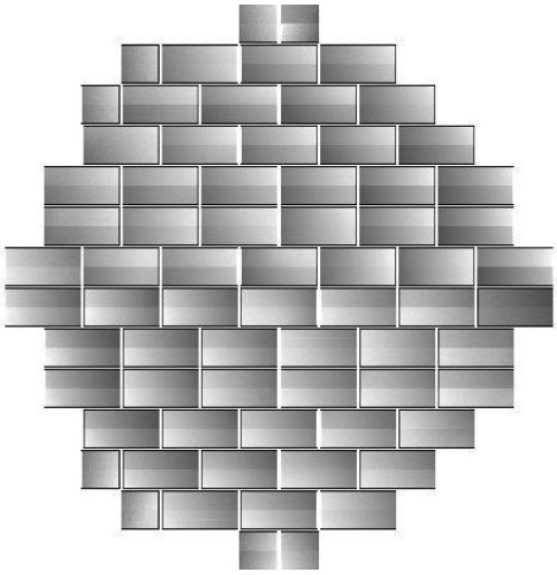

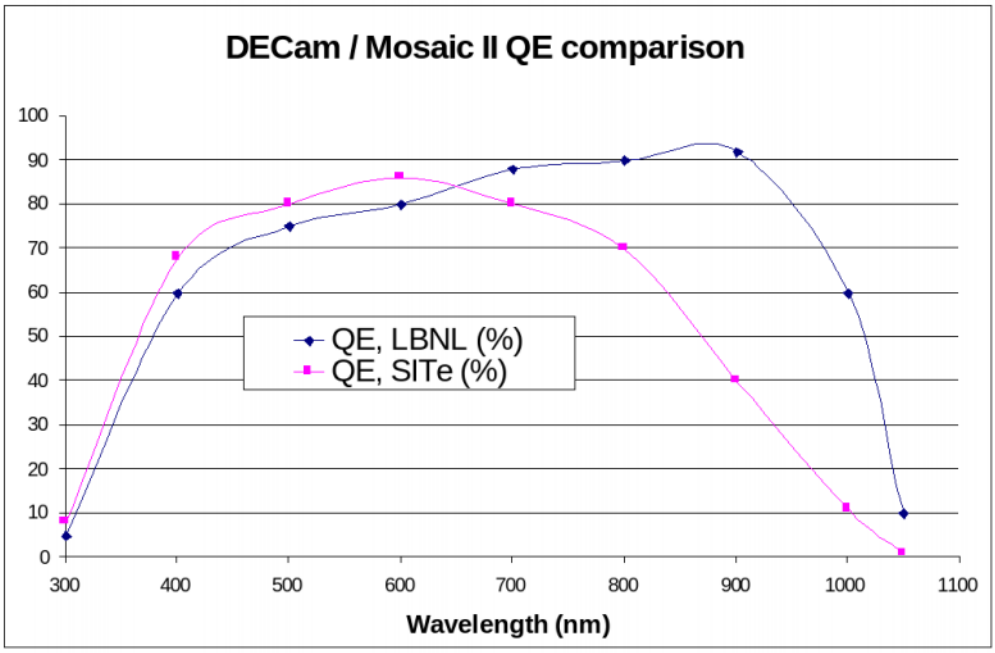

Figure 4.4: Quantum efficiency of DECAM CCDs and scheme of the focal plane of DECam. Picture Credit: Dark Energy Survey Collaboration.

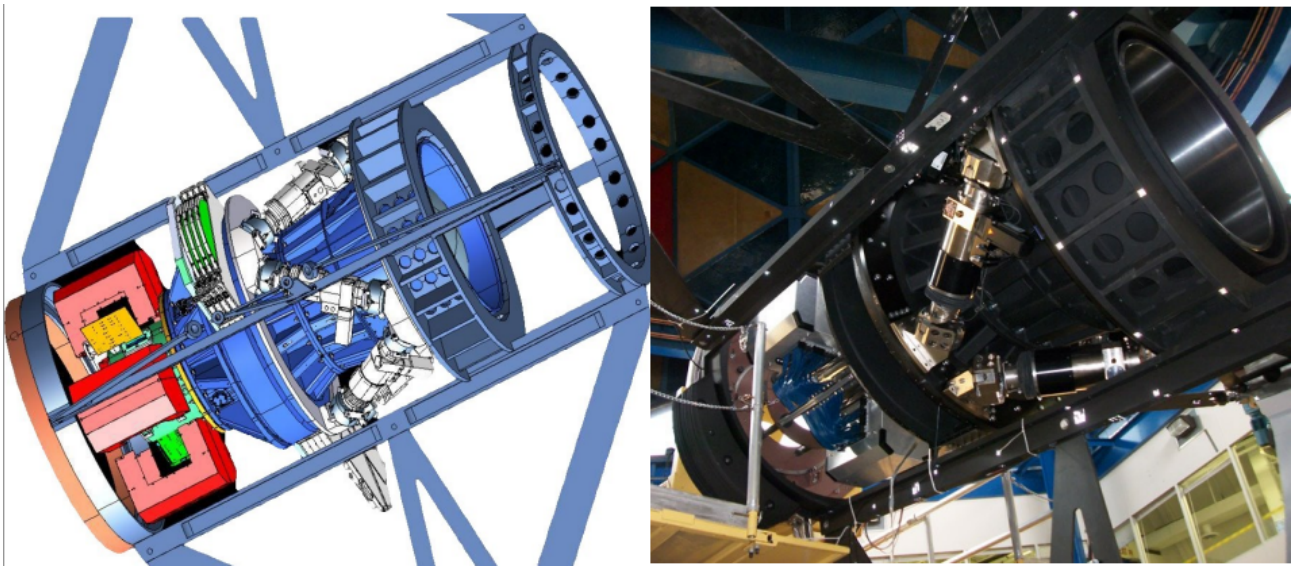

Figure 4.5: DECam scheme and picture at CTIO. Picture Credit: Dark Energy Survey Collaboration.

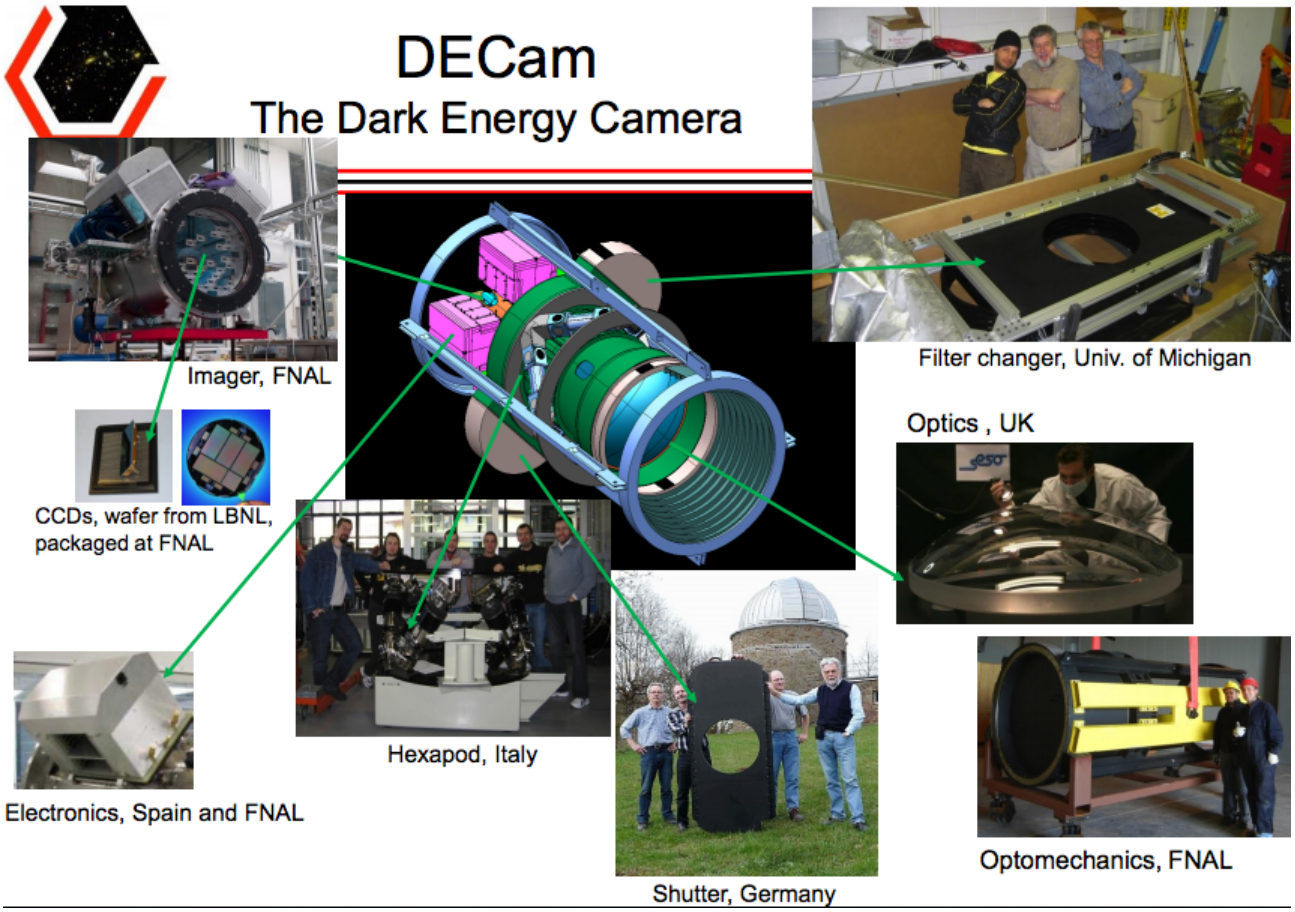

Figure 4.6: DECam and its components. Picture Credit: Dark Energy Survey Collaboration.

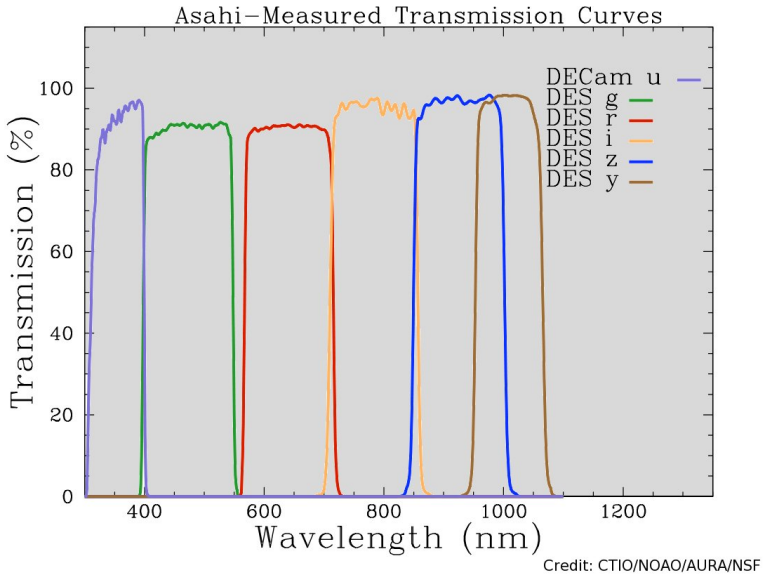

Figure 4.7: Transmittance curves of DES filters as measured by Asahi. Credit CTIO/NOAO/AURA/NSF. DES uses just g, r, i, z and Y.

for Research in Astronomy and funded by the U.S. National Science Foundation. This telescope hosted some of the observations of type Ia supernovae that led to the discovery of the accelerated expansion of the Universe by Riess, Perlmutter and Schmidt who earned the Nobel Prize by their discovery [104].

The Blanco is ideally suited to receive this new device because it was originally built to hold a heavy load at this top end. When it was built, people rode in the prime focus cage and took astronomical pictures using heavy glass photographic plates. Now, DECam takes pictures of roughly the same size with electronic CCD's.

In addition to its use for the Dark Energy Survey, DECam is a facility instrument on the Blanco telescope. This means that it is available for general use by the astronomical community, providing an order of magnitude increase in reach over the last Blanco imager, MOSAIC II (http://www.ctio.noao.edu/mosaic/). DES has updated the Blanco telescope as well as the associated installations and will use this telescope around 30% of its observation time (for 525 nights within 5 years). The rest of the time, DECam is avaible for the scientific community.

4.2. Dark Energy Survey Data Management (DESDM)

Each DECam image is a gigabyte in size. The Dark Energy Survey takes about 400 of these large images per night. This presents a very high data-collection rate for a cosmology experiment. The data are sent via a microwave link to La Serena. From there, an optical link forwards them to the National Center for Supercomputer Applications (NCSA) in Illinois for storage and "reduction". Reduction consists of standard image corrections of the raw CCD information to remove instrumental signatures and artifacts and the joining of these images into 0.5 square degree "combined images". Then galaxies and stars in the images are identified, catalogd, and finally their properties measured and stored in a database.

Data taken with DECam by astronomers during non-DES observing will be processed through the DECam Community Pipeline at the National Optical Astronomy Observatory and made available for analysis.

Figure 4.8: Image taken by DECam (left) and the moon superimposed over the same image to give a hint about the actual size of DES images. Credit: Dark Energy Survey Collaboration.

4.3. Survey strategy

The Dark Energy Survey has 525 nights of observation in 5 years. The plan is to cover 5000 deg^2 of the southern sky in the five photometric bands. The current footprint is depicted in Figure 4.9. The colored areas correspond to the patches of the sky covered during the first year of observations whereas the red line marks the complete planned footprint. With this footprint it is pretended to have a large connected area for large-scale structure studies, and also to have large areas to study Sunyaev-Zel'dovich effect and to cross-correlate with SPT-CMB maps. Zones with high extinction are avoided.

At the end of the survey, these 5000 deg^2 will be covered with 10 tilings. One tiling is one patch of the sky in one of the filters. In year one (Y1), 2000 deg^2 have been covered with 4 tilings and it is planned to cover approximately 3000 deg^2 with 3 more tilings during the next year of observations (Y2).

Nights with best seeing ($fwhm \leq 1.1$") are called photometric nights and for them, the observations are focused on the main survey. If seeing is worse than that, then, DES observes the supernovae fields. If there are 7 consecutive photometric nights the observations will focus on supernovae fields for one night.

Each year, DES has 105 nights of observations, the rest of the nights, DECam is avaible for the scientific community.

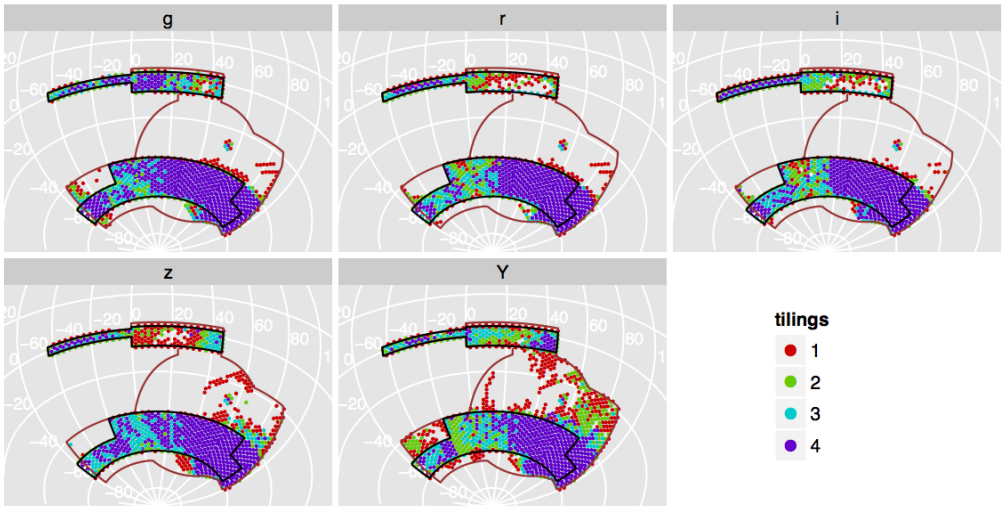

Figure 4.9: Current footprint of DES. The black line marks the first year covered area, colors specify the number of tilings in each filter. The red line marks the planned 5 year total area. Credit: Dark Energy Survey Collaboration.

Chapter 5

Galaxy clustering measurements on SVA-1

The Science Verification (SV) period (Nov. 12th, 2012 - Feb. 13th 2013) covered approximately 200 deg^2 that correspond to the red areas in Figure 5.1. This area, namely SVA-1, includes the fields corresponding to *SPT-E*, *SPT-W*, *El Gordo Cluster*, *Bullet Cluster*, *COSMOS*, *VVDS(14h)*, *SN-S*, *SN-X*, *SN-C*, *RXJ2248*, *SN-E*. These fields contain 45.3 million objects in total. The fields *SN-X*, *SN-C*, *VVDS(14h)* and *COSMOS* have been used to search for type Ia Supernovae and to calibrate the photometric redshifts because they overlap with spectroscopic redshift surveys [105]. In this chapter we will present the analysis performed on the DES SVA1 data. It is organized as follows: First, we will describe the sample for our analysis. Next we will discuss systematic uncertainties and how they are considered in the analysis. After that, we will proceed to describe the method of analysis to compute the two point correlation function, the theoretical framework and the scientific results.

5.1. SVA-1 SPTE Photometric sample

SVA-1 data were taken in order to verify DES capabilities for the nominal survey period. The main goal was to test each one of the different channels of DES to measure Dark Energy, *i.e.*, clusters, supernovae, weak lensing and galaxy clustering. The quality of these data confirmed the expectations and SVA-1 data enabled DES collaborators to make measurements such as weak lensing masses for galaxy clusters [106] as well as the discovery of new supernovae [107] or the usage of new photometric redshift algorithms [105]. Since we are interested in the Large-Scale Structure, for our analysis we will focus on SPT-E region since it is the largest contiguous one. For the SVA-1 Gold catalog the footprint selection was made for coverage with at least 1 CCD in g, r, i, z bands. The catalog includes magnitudes for the detected objects in the 5 DES filters g, r, i, z, Y with different criteria: `MAG_AUTO, MAG_MODEL, MAG_DETMODEL, MAG_APER4`, etc. These magnitudes are computed using SExtractor [108]. `MAG_AUTO` is computed from the flux above the background in an automatically selected aperture that depends on the shape of the object. `MAG_MODEL` is measured by fitting the object with a given model (by SDSS) and estimating the flux for this model. `MAG_DETMODEL` is similar to `MAG_MODEL` but first it makes the model fitting on the detection image, and then, it fits the overall normalization of this model to each single-band image separately. `MAG_DETMODEL` thus has a consistent galaxy model for the same galaxy across all filters, which is primarily useful for color measurements. Finally, `MAG_APER4` is measured computing the flux above the background in a 2 arcseconds circular aperture.
The catalog includes positions and a photometric redshift estimation using *DESDM* code [105]. We remove bad photometry regions, *i.e*, regions where it is very likely to have objects with colors not fulfilling $-1 < g - r < 4$ and $-1 < i - z < 4$ using `MAG_DETMODEL`. We use it because this algorithm makes a very precise estimation of the colors. In addition a cut was made at declination > -61 degrees to remove the Large Magellanic Cloud

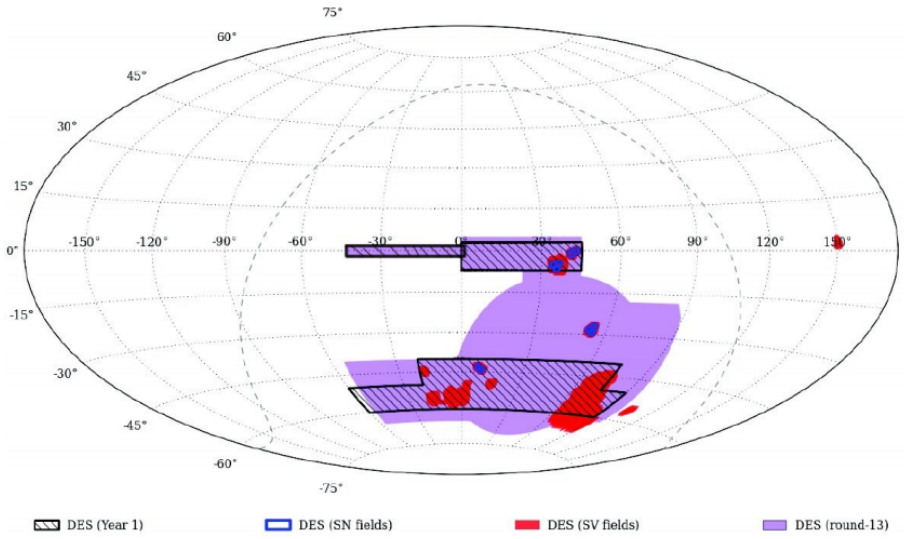

Figure 5.1: DES footprint in purple, the shadowed area corresponds to Y1 observations and the red area correspond to the SVA1 fields. SPT-E is the red colored region located at the lower right (South East) part of the map. Credit: Dark Energy Survey Collaboration.

(LMC) since in this area magnitudes cannot be accurately calibrated. This selection yields as a result a total area of ~ 150 deg^2 and ~ 24 million objects with redshifts spanning from $0.1 \leq z \leq 1.5$. In order to minimize the impact of systematic errors in this very first measurement of LSS in DES, additional cuts are required. The resulting sample is called the **Benchmark sample** and is described in the next section.

5.1.1. LSS Benchmark sample

The LSS benchmark sample consists in a subsample of the SVA-1 SPT-E data. We performed the following cuts:

$$18 < i_{AB} < 22.5 \tag{5.1}$$

Where i_{AB} is `MAG_AUTO` and

$$0 < g - r < 3$$
$$0 < r - i < 2$$
$$0 < i - z < 3$$

Using `MAG_MODEL` magnitudes since they are the best calibrated (as well as `MAG_DETMODEL`) to account for color outliers whereas `MAG_AUTO` gives a better overall estimation of the magnitude. These cuts were made in order to remove objects with poor photometry. The sample will be split in redshift bins for two different purposes:

1. Trace as well as possible the evolution of structure with redshift.
2. Make systematic uncertainties analysis easier since, most of these systematic effects will depend on redshift. The selected redshift bins are: $[0.2 < z < 0.4], [0.4 < z < 0.6], [0.6 < z < 0.8], [0.8 < z < 1.0]$ and, $[1.0 < z < 1.2]$, where z is the photometric redshift estimate that we are about to describe.

5.1.2. Photometric redshift

One of the key aspects of DES is its photometric nature. The DES collaboration has developed a large set of photometric redshfit algorithms. These algorithms are fully described in [105]. In particular, we will use the

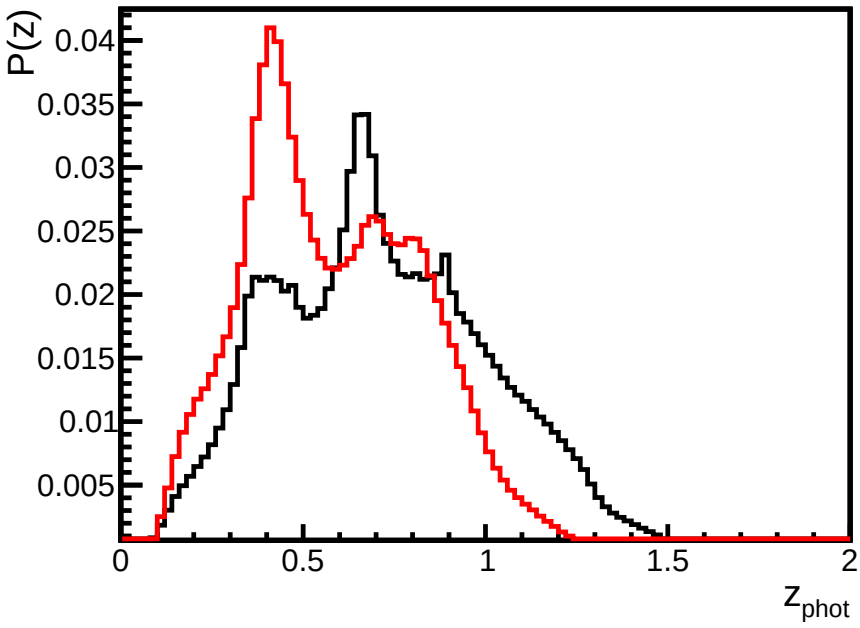

Figure 5.2: Photometric redshift probability distribution of the SPT-E objects for the Benchmark sample (red) and the Gold sample (black) using the DESDM photo-z.

default DES algorithm, the DESDM photo-z. It consists in an artificial neural network algorithm, the same that was used for SDSS DR6, detailed in [109]. This algorithm produces the $N(z)$ distributions depicted in Figure 5.2. The black line is for the whole DES SVA-1 SPTE sample whereas the red line corresponds to the Benchmark $N(z)$ distribution. In each one of the redshift bins objects are distributed as detailed in Figure 5.3. These distributions are consistent with the DES expectations [105]. Maps and number of galaxies in each bin can be found in Figure 5.10.
This code gives a very good performance and a good description of the $N(z)$ as it can be seen at [105].

5.2. Angular Footprint and Limiting Depth Mask

DES is a large photometric survey. This technique has the advantage of fast data acquisition and very large statistics, at the price of a smaller precision on the redshift measurement compared to the spectroscopic surveys and also, a very complex geometry. Since DES takes exposures of the different patches of the sky at different nights and, after 10 exposures, the images are co-added, some patches of the sky are observed deeper than others. The survey strategy is made in such a way that depth differences are as small as possible but, in any case, we have different depths because of different observing conditions during the survey. The mask is a tool made to quantify these effects and it eliminates regions where the observations had artificial effects (airplane or satellite trails, cosmic rays, etc) or where very bright stars appear. The depth variations are mapped using `MANGLE` [110]. `MANGLE` takes into account properties of DECam CCDs and the observing conditions during each night and gives an estimation of the depth for different regions. This depth is calculated for `MAG_APER4` magnitude estimation. This mask has a very high resolution but the inconvenience of using `MAG_APER_4` which is not used to measure galaxies and not very accurately calibrated. Thus, from the `MANGLE` mask, a new mask for every magnitude algorithm has been built since, the different algorithms relate with `MANGLE_MAGLIM` in a different, non-linear, position-dependent way. These differences are depicted in Figure 5.4 for `MAG_AUTO`. The procedure to build this new mask is the following: first, a high resolution (Nside=32768 $\Rightarrow$ 41.5 arcsec^2) HEALPix version

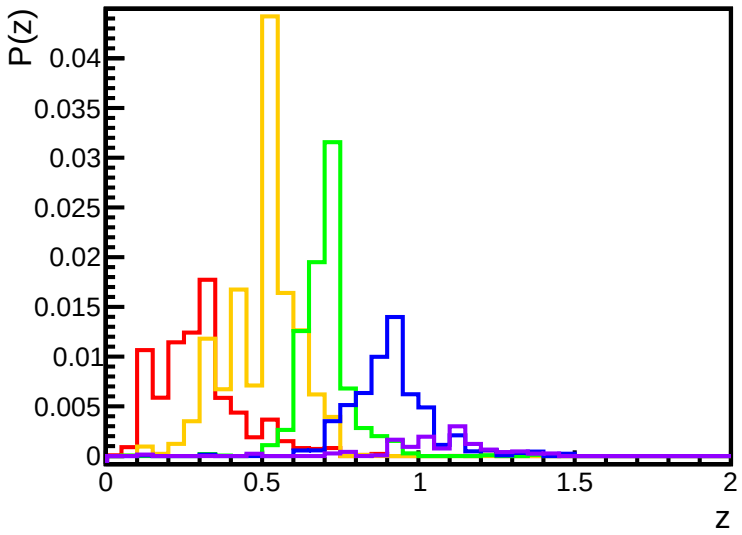

Figure 5.3: Probability distribution functions (PDFs) of each one of the considered redshift bins in our data sample.

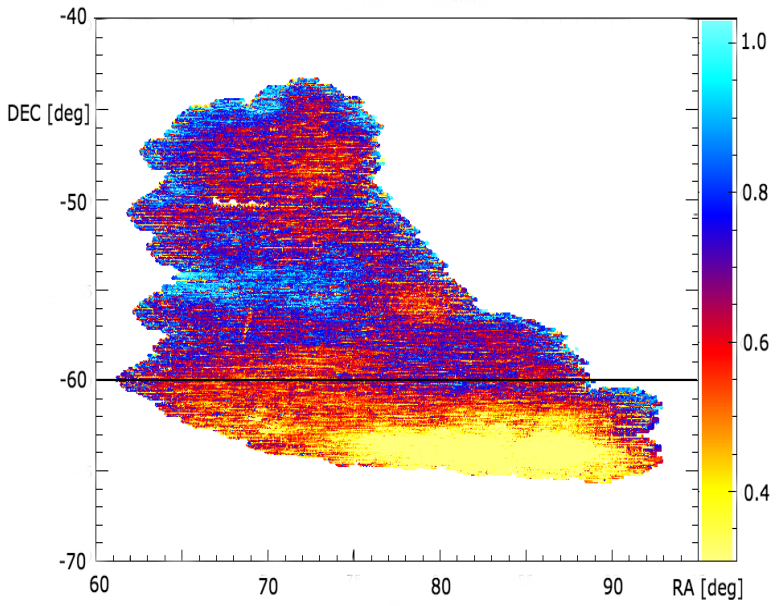

Figure 5.4: Differences between `MANGLE` mask and `MAG_AUTO_I` mask. Credit: Eli Rykoff

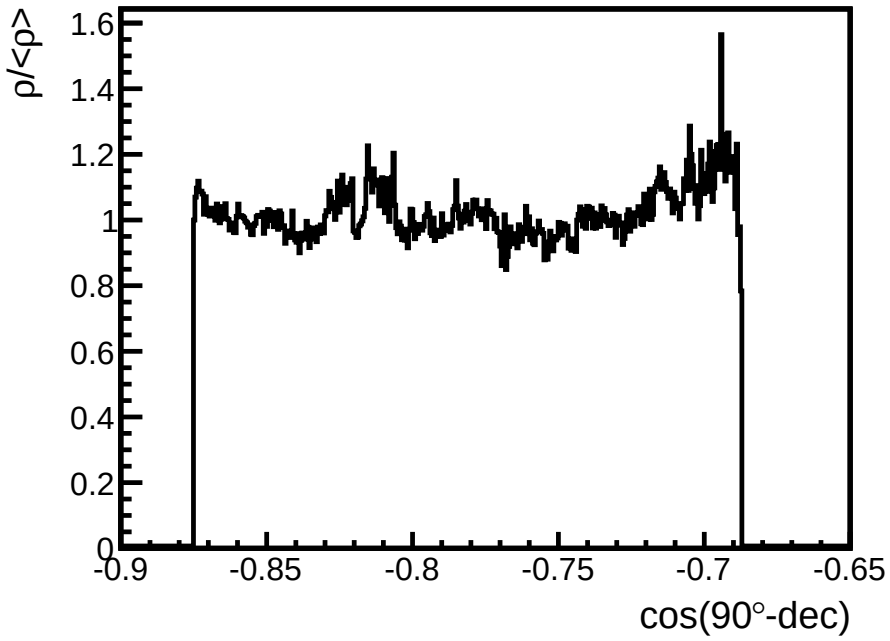

Figure 5.5: Ratio of density and mean density of objects along the declination axis. In order to avoid contamination from the LMC a cut in dec = -61° was made in the Benchmark sample.

of the `MANGLE` mask is made then for each one of the pixels is coarsed down to a 64 times lower resolution (Nside=4096 $\Rightarrow$ 0.75 arcmin^2) and the fraction of pixels where the limiting magnitude is misestimated by 0.1 mag or greater with respect to `MANGLE` is computed as well as the fraction of pixels observed. Then, each big pixel has the limiting magnitude of the average of the detected pixels and a second mask giving the fraction of well-behavioured pixels (`fracdet`).

The angular mask we chose for the Benchmark sample includes two cuts: the aforementioned one in declination to avoid the LMC, and the other one in depth to ensure completeness. We analyzed this cut in terms of density as depicted in Figure 5.5, and, as it is noticeable, density grows when we approximate to the -61 degrees cut which is in the limit. Going below -61 deg introduces a large fraction of objects with bad photometry from the LMC. We want to ensure completeness in our sample. To do that we analyze the density in terms of the limiting magnitude as seen in Figure 5.6. First, we make limiting magnitude bins with 0.1 binwidth, *i.e.*, we select those patches where the limiting magnitude is $m_{lim_i} \in [21.8, 21.9]; [21.9, 22.0]; ...; [23.4, 23.5]$. Then we compute density of objects with certain observed magnitude mag_i. From these plots we can see that selecting objects brighter than 22.5 we have the same density value, within statistical fluctuations, for every limiting magnitude larger than 22.5, thus, we add this new limiting magnitude cut $m_{lim_i} > 22.5$ using the `MAG_AUTO_I` for consistency purposes. The resulting compact $\sim$135 deg^2 area is depicted in Figure 5.7.

5.2.1. Star-Galaxy Separation and Stellar Contamination

The Benchmark sample includes a simple star/galaxy classifier called `MODEST_CLASS`. This variable is just a flag with the value 1 for galaxies, and 2 for stars. It also has different values for unidentified objects. The classifier relies on the `SPREAD_MODEL` and `SPREAD_MODEL_ERR` variables which are related to the shape of the object, the PSF and the FWHM. The two different populations can be seen in Figure 5.8. Using the DESDM code and the `MODEST_CLASS` separator we obtain a distribution of stars (as defined by MODEST_CLASS) as

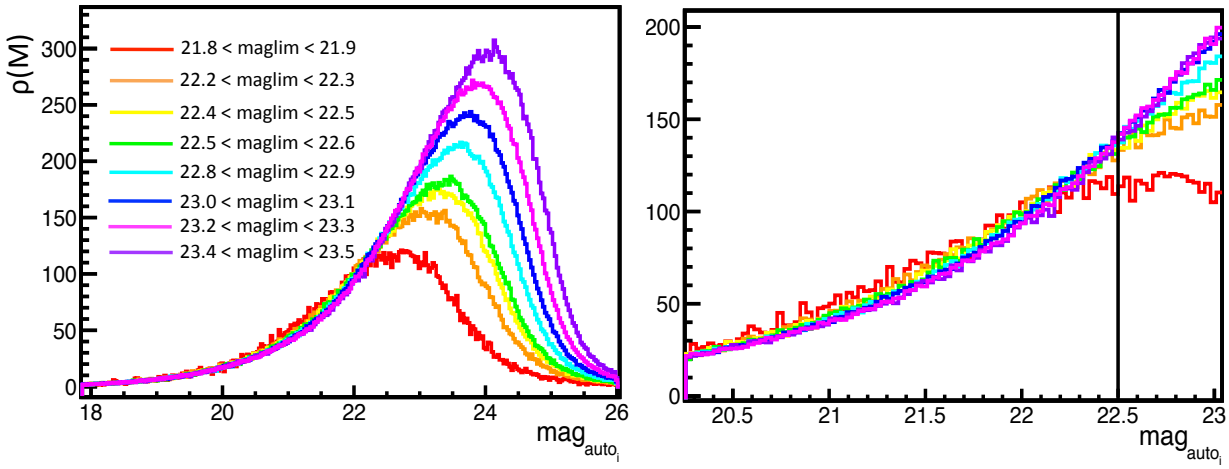

Figure 5.6: Density in function of magnitude for different limiting magnitude bins. It is shown that MAG_AUTO_I=22.5 is the faintest we can go with high completeness.

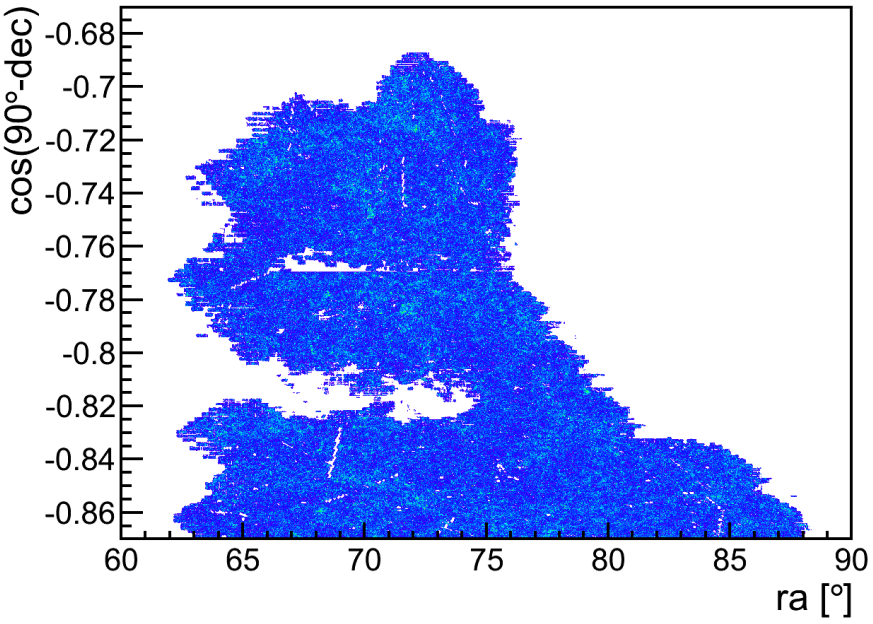

Figure 5.7: Benchmark sample angular footprint. The Figure shows a homogeneous random field distributed along this footprint.

described in Table 5.1. Additionally, we are interested in estimating the fraction of misclassified stars in the

$0.2 < z_{phot} < 0.4$	252399
$0.4 < z_{phot} < 0.6$	182550
$0.6 < z_{phot} < 0.8$	497031
$0.8 < z_{phot} < 1.0$	65167
$1.0 < z_{phot} < 1.2$	1120

Table 5.1: Number of stars per bin using the cuts corresponding to selection number 1.

Benchmark sample. To do that, let us now consider the following ratio:

$$\alpha_s = \frac{\langle \delta^O_{gal} \delta^O_{star} \rangle}{\langle \delta^O_{star} \delta^O_{star} \rangle} \tag{5.2}$$

Where the subscript *star* refers to stars and the subscript *gal* to galaxies, and we used the notation $\delta(\theta) = \delta$. The superscript O states for observed quantities. We will use the T superscript for true quantities. If we expand these terms,

$$\delta^O_{gal} = f\delta^T_{gal} + (1-f)\delta^T_{star} \tag{5.3}$$

$$\delta^O_{star} = g\langle\delta^T_{gal} + (1-g)\delta^T_{star} \tag{5.4}$$

f represents the fraction of galaxies contributing to the total observed galaxy-galaxy autocorrelation and g the fraction of galaxies contributing to the total observed star-star autocorrelation. Using the expressions above we can write,

$$\langle \delta^O_{gal} \delta^O_{star} \rangle = fg\langle \delta^T_{gal} \delta^T_{gal} \rangle + (1-f)(1-g)\langle \delta^T_{star} \delta^T_{star} \rangle + [f(1-g) + g(1-f)] \langle \delta^T_{gal} \delta^T_{star} \rangle \tag{5.5}$$

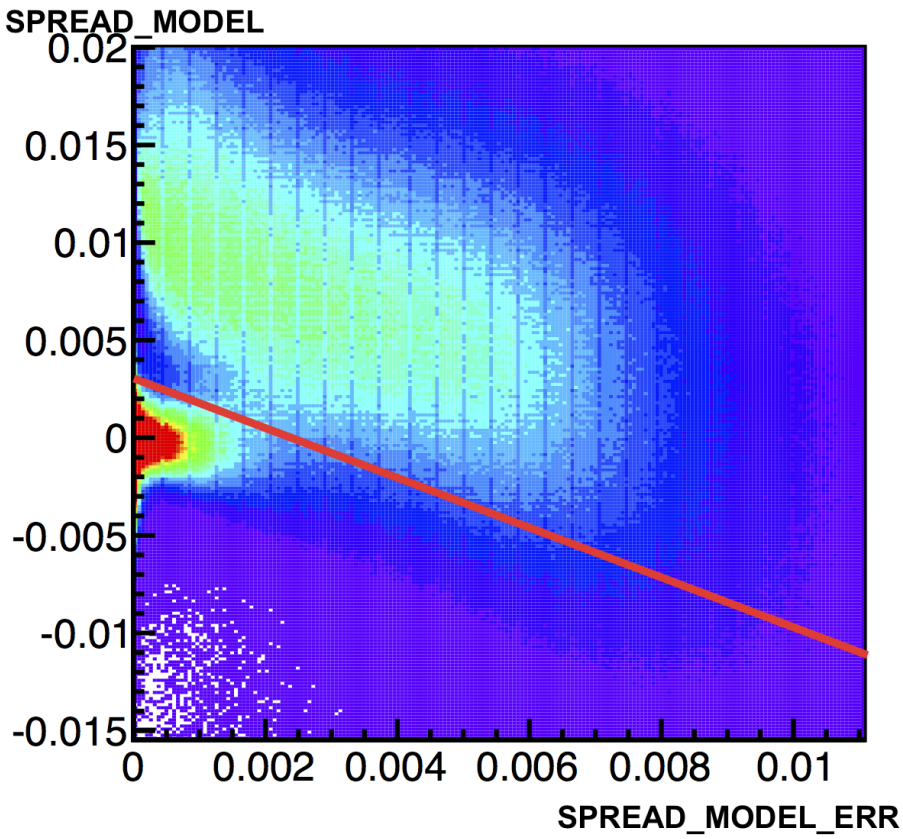

Figure 5.8: Plot showing SPREAD_MODEL vs SPREAD_MODEL_ERR, we can distinguish two different populations. We trace a simple straight line to separe them and create MODEST_CLASS star/galaxy separator.

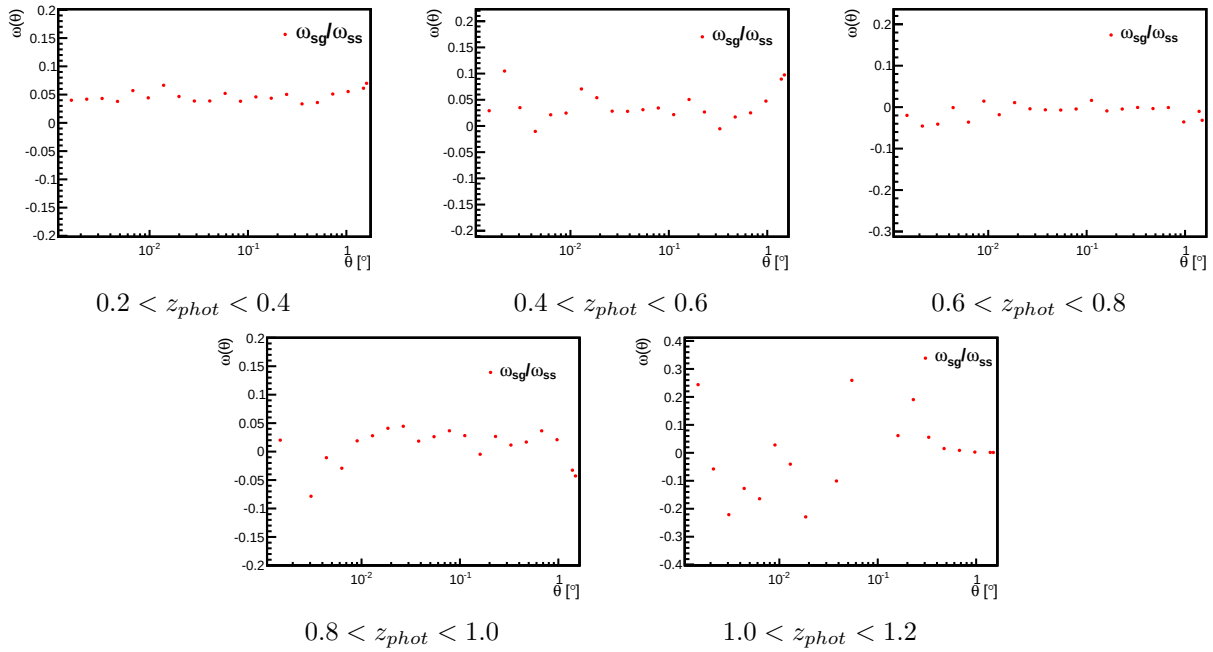

Figure 5.9: Estimation of the ratio of stars in each one of the considered redshift bins.

and

$$\langle \delta^O_{star} \delta^O_{star} \rangle = g^2 \langle \delta^T_{gal} \delta^T_{gal} \rangle + (1-g)(1-g) \langle \delta^T_{star} \delta^T_{star} \rangle + 2(1-g) g \langle \delta^T_{gal} \delta^T_{star} \rangle \tag{5.6}$$

Now, let us consider the following assumptions:

1. The galaxies that are confused with stars have the same clustering properties as the galaxies that are not confused.
2. The cross-correlation between true galaxies and true stars is negligible, *i.e.*, $\langle \delta^T_{gal} \delta^T_{star} \rangle \approx 0$.
3. The fraction of galaxies classified as stars is very low, *i.e.*, $g \approx 0$.

Under these conditions the α_s can be written as:

$$\alpha_s \approx \frac{(1-f)(1-g)\langle \delta^T_{star} \delta^T_{star} \rangle}{(1-g)^2 \langle \delta^T_{star} \delta^T_{star} \rangle} \approx 1 - f = \frac{N_{star}}{N_{star} + N_{gal}} \tag{5.7}$$

Thus, we can obtain an estimate of the stellar contamination by just using this ratio. Plots showing this ratio can be found at Figure 5.9 from which we can estimate a fraction of stars in between 2% and 4%. Then after selecting galaxies with `MODEST_CLASS = 1` and making the cuts mentioned above we obtain the galaxies depicted in Figure 5.10. These galaxies constitute the so-called Benchmark Sample.

5.2.2. Other Sources of Systematic Uncertainties: Map Projections.

There are other potential sources of systematic uncertainties related to the quality of the observations and, that could be correlated with other systematic uncertainties such as uncertainty in photo-z or star/galaxy separation. We will consider the following potential sources:

- Airmass: The airmass is the ratio between the optical depth at a given zenith angle and the optical depth at the zenith. The larger the airmass, the higher is the attenuation of the light. It is possible that a larger

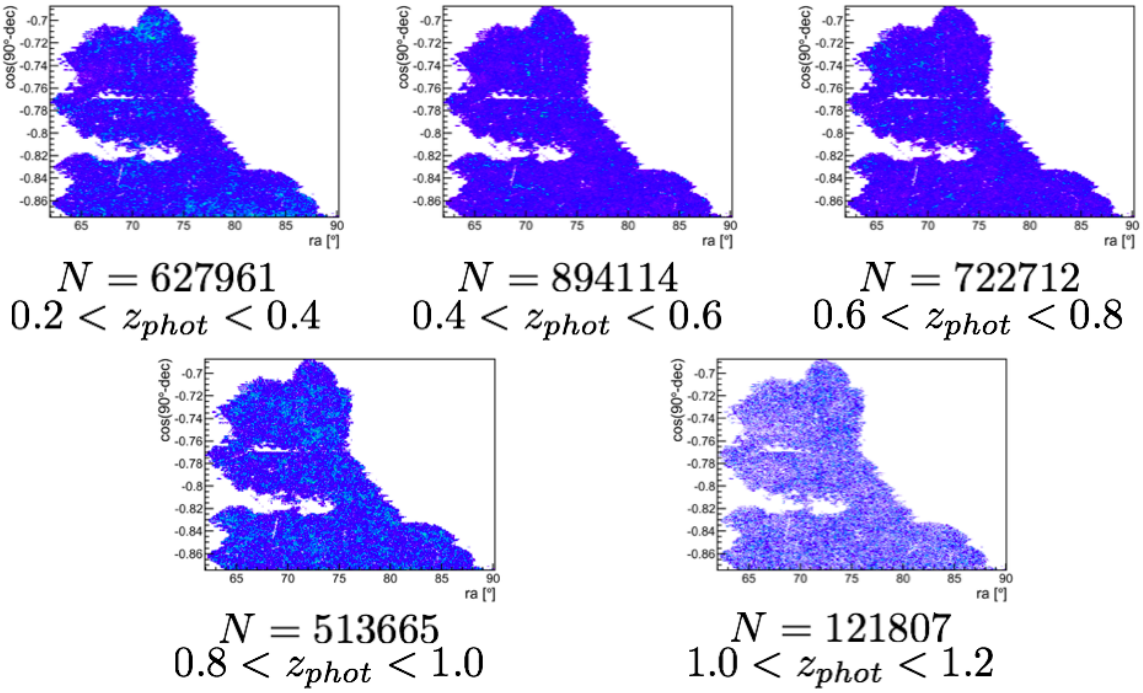

Figure 5.10: Maps and number of galaxies for the different redshift bins in the Benchmark sample using DESDM photo-z.

airmass can affect the photometry and therefore, the photo-z determination. It can also affect to the detection of fainter objects. This effect will be corrected using the cross-correlation between the galaxy map and the systematic map.

- Sky brightness: This gives us the brightness of a patch of the sky without direct light sources (no observed stars, no moonlight, etc). Several sources can be identified as the source of the intrinsic brightness of the sky, namely airglow, indirect scattering of sunlight, scattering of starlight, and artificial light pollution. Large skybrightness can lead to bad photometric determination and to prevent the detection of very faint objects. This effect will be corrected in a similar fashion as the airmass effect.

- Extinction: The extinction is the measurement of the magnitude reddening due to the presence of galactic dust. The reddening due to extinction affect mostly to photometry and photometric redshift determination. It also affects the detection of fainter objects.

- Seeing (FWHM): The seeing measures the atmospherical distortion of astronomical objects. A point source in the sky when the light comes through Earth's atmosphere suffers a distortion that we can measure and characterize just estimating the Full-Width-Half-Maximum (FWHM) of this point source. Large values of FWHM make objects to appear wider in the images so, some stars could be classified as galaxies and thus, affect the clustering. Seeing can also make worse the photometric redshift estimation since it can difficult the determination of magnitudes.

These systematics have negligible impact, except for the seeing that has a big impact depending on the redshift bin and the scale and thus, it should be corrected.

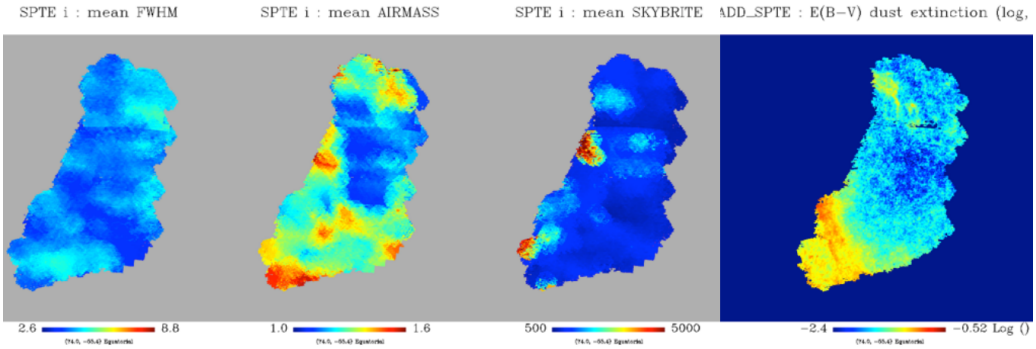

Figure 5.11: Spatial varying systematic uncertainties. These maps have been made avaible to the collaboration by Boris Leidstedt.

	Ω_m	Ω_Λ	Ω_b
Model 1	0.31	0.68	0.044
Model 2	0.5	0.5	0.071
Model 3	1	0	0.142

Table 5.2: Cosmological parameters of the different models we used to fit the galaxy bias.

5.3. Angular Clustering

5.3.1. 2 Point Angular Correlation Functions

We already presented a similar analysis in chapter 3. The main goal is to use the power of the correlation function to extract some cosmological information. The estimation of the two point correlation function is done in the same fashion as aforementioned. We use the same GPU-based code [99] with the same upgrades, and the Landy & Szalay estimator [82]:

$$\omega(\theta) = 1 + \frac{N_{rnd}^2}{N_{gal}^2}\frac{DD(\theta)}{RR(\theta)} - 2\frac{N_{rnd}}{N_{gal}}\frac{DR(\theta)}{RR(\theta)} \tag{5.8}$$

Once again, the random catalogs have 3 times the number of data objects. We use 10 angular bins between 5×10^{-2} and 2 degrees.

5.3.2. Covariance Estimation

We proceed the same way as before and use the theoretical Gaussian approximation given by the expression from [62] (equation 2.48).

5.3.3. Theoretical Predictions

We have computed the correlation function and extract the bias for three different cosmological ΛCDM models described in the Table 5.2. We follow the procedure presented in chapter 3. In order to construct the theoretical predictions we used the non-linear HALOFIT power-spectrum [69], we added redshift space distortions using the Kaiser approximation [63]. We want to minimize a χ^2 function varying only the bias parameter and fixing the other parameters to each one of the models. If we remind this χ^2 function is given by:

$$\chi^2 = \sum_{i,j}[\omega(\theta_i)^{meas} - \omega(\theta_i)^{th}]C_{ij}^{-1}[\omega(\theta_j)^{meas} - \omega(\theta_j)^{th}] \tag{5.9}$$

5.3.4. Systematic Errors

Correction of position dependent systematic effects

In general, the observed density contrast, δ_{obs}, will be a combination of the observed density contrast, δ_{true}, plus the variation due to the systematic effects, δ_{sys}, thus [111]:

$$\delta_{obs} = \delta_{true} + \sum_i \alpha_i \delta^i_{sys}, \text{ (i = seeing, airmass, stars...)} \tag{5.10}$$

If we assume that the true galaxy fluctuations do not correlate with the fluctuations induced by the systematics we have:

$$\langle \delta_{obs} \delta^j_{sys} \rangle = \sum_i \alpha_i \langle \delta^i_{sys} \delta^j_{sys} \rangle \tag{5.11}$$

If we define

$$\omega_{cross,j} \equiv \langle \delta_{obs} \delta^j_{sys} \rangle \tag{5.12}$$

$$\omega_{auto,ij} \equiv \langle \delta^i_{sys} \delta^j_{sys} \rangle \tag{5.13}$$

We can rewrite equation 5.11 as:

$$\omega_{cross,j} = \sum_i \alpha_i \omega_{auto,ij} \tag{5.14}$$

Thus,

$$\vec{\alpha} = \vec{\omega}_{cross} \cdot (\omega_{auto})^{-1} \tag{5.15}$$

Hence, if we have N systematic maps, we have to invert a $N \times N$ matrix for each θ bin. So, the correlation function that we want to calculate is:

$$\omega(\theta)_{true} = \omega(\theta)_{obs} - \vec{\alpha} \cdot \vec{\omega}_{cross} \tag{5.16}$$

Given a galaxy sample g, with a true density contrast δ^T and an observed one δ^O, we define $\omega^T_{g,g} = \langle \delta^T_g \delta^T_g \rangle$, $\omega^O_{g,g} = \langle \delta^O_g \delta^O_g \rangle$. In the case of one systematic s with a density contrast δ_s and autocorrelation $\omega_{s,s}$, we can write:

$$\omega^T_{g,g} = \omega^O_{g,g} - \frac{(\omega^O_{g,s})^2}{\omega_{s,s}} \tag{5.17}$$

Let us consider the case of two correlated systematics $s1$, and $s2$ and the galaxy sample g. We have the following system of equations:

$$\omega_{g,s1}(\theta) = \alpha_1 \omega_{s1,s1}(\theta) + \alpha_2 \omega_{s1,s2}(\theta) \tag{5.18}$$

$$\omega_{g,s2}(\theta) = \alpha_1 \omega_{s1,s2}(\theta) + \alpha_2 \omega_{s2,s2}(\theta) \tag{5.19}$$

The solutions for this system are:

$$\alpha_1 = \frac{\omega_{g,s1}\omega_{s2,s2} - \omega_{g,s1}\omega_{s1,s2}}{\omega_{s1,s1}\omega_{s2,s2} - \omega^2_{s1,s2}} \tag{5.20}$$

$$\alpha_2 = \frac{\omega_{g,s2}\omega_{s1,s1} - \omega_{g,s2}\omega_{s1,s2}}{\omega_{s1,s1}\omega_{s2,s2} - \omega^2_{s1,s2}} \tag{5.21}$$

And the expression for the galaxy-galaxy autocorrelation yields:

$$\omega^T_g = \omega^O_g - \alpha_1^2 \omega_{s1,s1} - \alpha_2^2 \omega_{s2,s2} - 2\alpha_1 \alpha_2 \omega_{s1,s2} \tag{5.22}$$

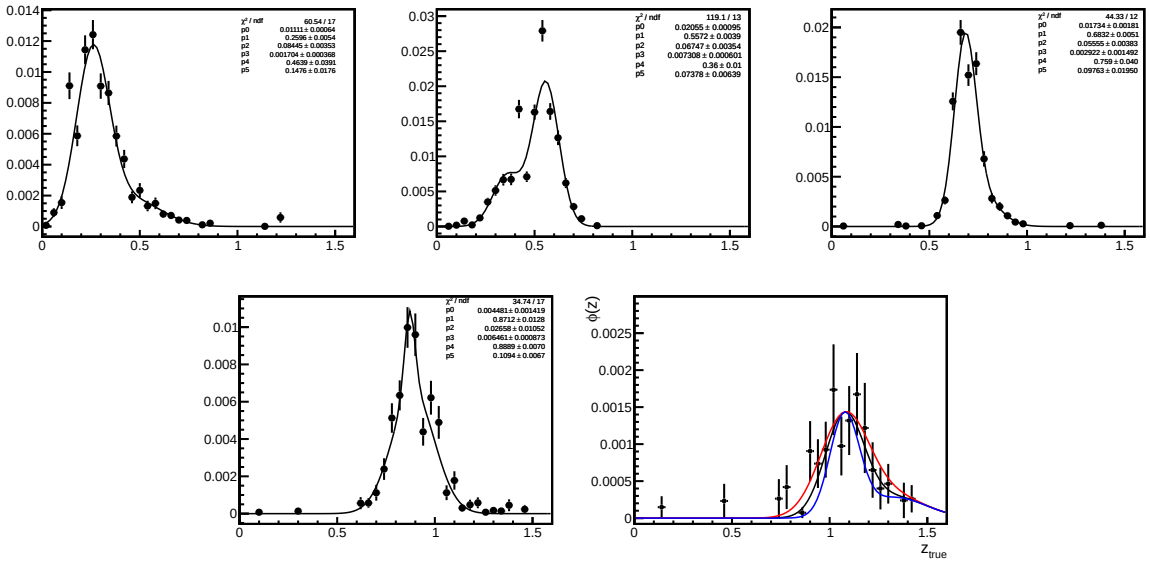

Figure 5.12: Fits to the PDFs using a sum of two Gaussians to evaluate the systematic error due to the photo-z. Redshift bins are depicted in ascending order ($0.2 < z < 0.4$ top left, $1.0 < z < 1.2$ bottom right).

Photometric redshift

The photometric redshift estimation is the most important source of systematic uncertainty. It has been verified that the calibration sample is a good representation of the full sample. However, the size of the calibration sample is small and we need to propagate the statistical error in the determination of $\phi(z)$.

To evaluate this uncertainty, we fitted the redshift distribution within each redshift bin to the sum of two Gaussians and we vary the width between the best-fit value and the best-fit value plus its error:

$$\phi_1(z) = Ae^{-\frac{(z-z_1)^2}{2(\sigma_1+\Delta\sigma_1)^2}} + Be^{-\frac{(z-z_2)^2}{2\sigma_2^2}} \tag{5.23}$$

$$\phi_2(z) = Ae^{-\frac{(z-z_1)^2}{2(\sigma_1-\Delta\sigma_1)^2}} + Be^{-\frac{(z-z_2)^2}{2\sigma_2^2}} \tag{5.24}$$

Finally, we use these distributions to make a theoretical prediction using a ΛCDM model with Planck parameters. The error is computed as the relative difference between these correlation functions, i.e,

$$\omega_1(\theta) = \int_0^\infty dz_a \phi_1(z_a) \int_0^\infty dz_b \phi_1(z_b) \xi(\theta, z_a, z_b) \tag{5.25}$$

$$\omega_2(\theta) = \int_0^\infty dz_a \phi_2(z_a) \int_0^\infty dz_b \phi_2(z_b) \xi(\theta, z_a, z_b) \tag{5.26}$$

$$\sigma_{phot} = \frac{|\omega_1(\theta) - \omega_2(\theta)|}{2\omega_1(\theta)} \tag{5.27}$$

We estimate this error to be $\sigma_{photo-z} < 4\%$ and add these errors in quadrature to the statistical error.

Declination cut

The declination cut to avoid the LMC could be a source of systematic uncertain since it correlates with bad photometry regions. The declination cut at dec $= -61°$ shows stability in terms of clustering as it is noticeable

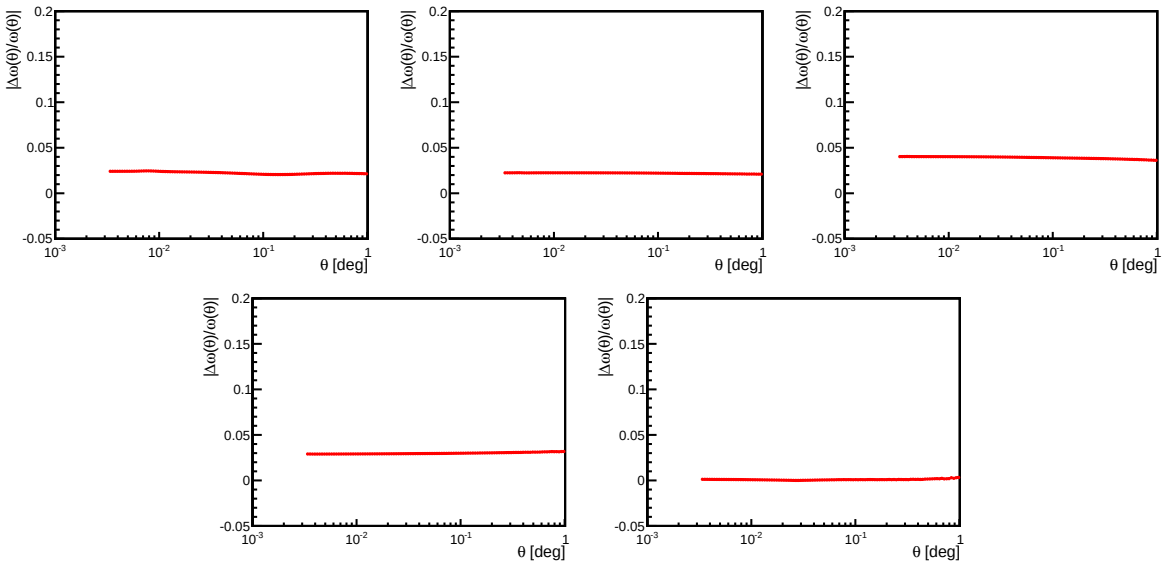

Figure 5.13: Relative error of the correlation function due to the photo-z distortion. Redshift bins are depicted in ascending order ($0.2 < z < 0.4$ top left, $1.0 < z < 1.2$ bottom right).

z_{phot}	$\chi^2/ndof$	p	b	Δb
0.2 - 0.4	0.158	0.992	1.09	0.14
0.4 - 0.6	0.286	0.985	1.05	0.06
0.6 - 0.8	0.763	0.659	0.93	0.06
0.8 - 1.0	0.633	0.786	1.29	0.05
1.0 - 1.2	0.659	0.747	1.86	0.05

Table 5.3: Results of the fit to Planck ΛCDM model leaving the galaxy bias b as a free parameter.

in Figure 5.14 where we analyzed the relative difference of the correlation function for the different declination cuts in the selected redsfhit bins.

Stellar contamination

Stars are a source of systematic uncertainty in galaxy clustering measurements. They affect in two different ways: On the one hand, stars and galaxies have different clustering properties so, if we unknowingly classify stars as galaxies this will change the clustering signal. There is another effect called star obscuration. Bright stars prevent us to detect faint objects around them. It is better to lose area and do a conservative masking around those stars than to have the obscuration effect. Using the aforementioned classifier, we evaluate the systematic uncertainty by cross-correlating stars with galaxies and the correction due to star contamination. Results in Figure 5.15 show that this effect is very low (see Table 5.1) and we neglect the correction.

5.3.5. Results

In this section we present the results of the measurement of the Benchmark Sample angular two point correlation function, and the measurement of the linear galaxy bias. Proceeding the same way as we did for the simulations, and fixing the cosmological parameters to the Planck results, we obtain the results depicted in Figure 5.17 and Figure 5.18, and described in Table 5.3. We also analyzed evolution with redshift of the best-fit bias and compared it with the results we obtained in the simulation. In Figure 5.16 we can see that

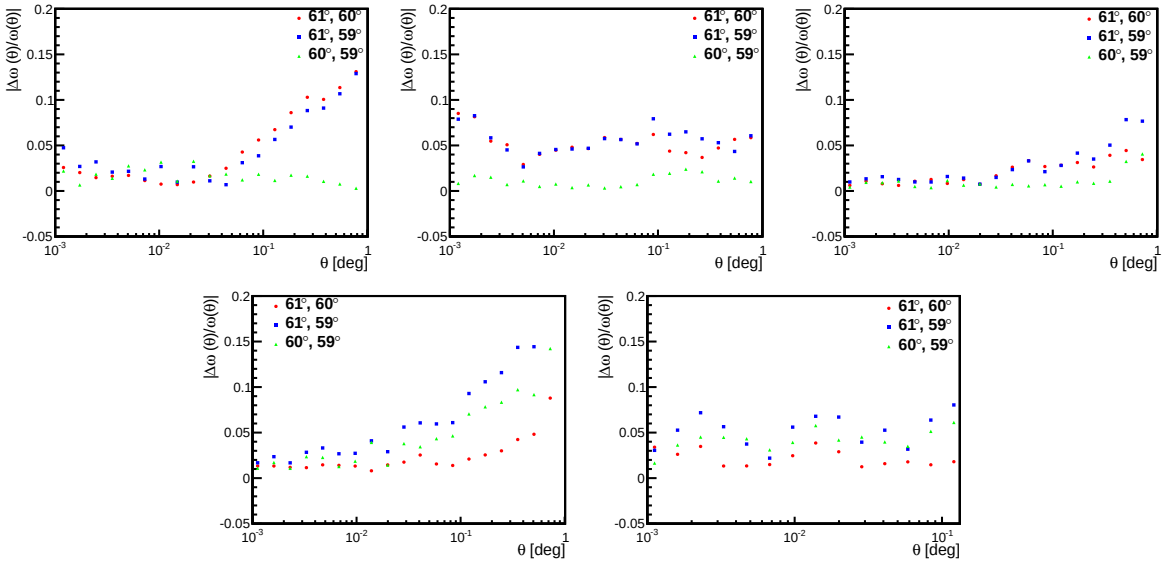

Figure 5.14: Relative variation of the correlation function due to the selection. Redshift bins are depicted in ascending order ($0.2 < z < 0.4$ top left, $1.0 < z < 1.2$ bottom right).

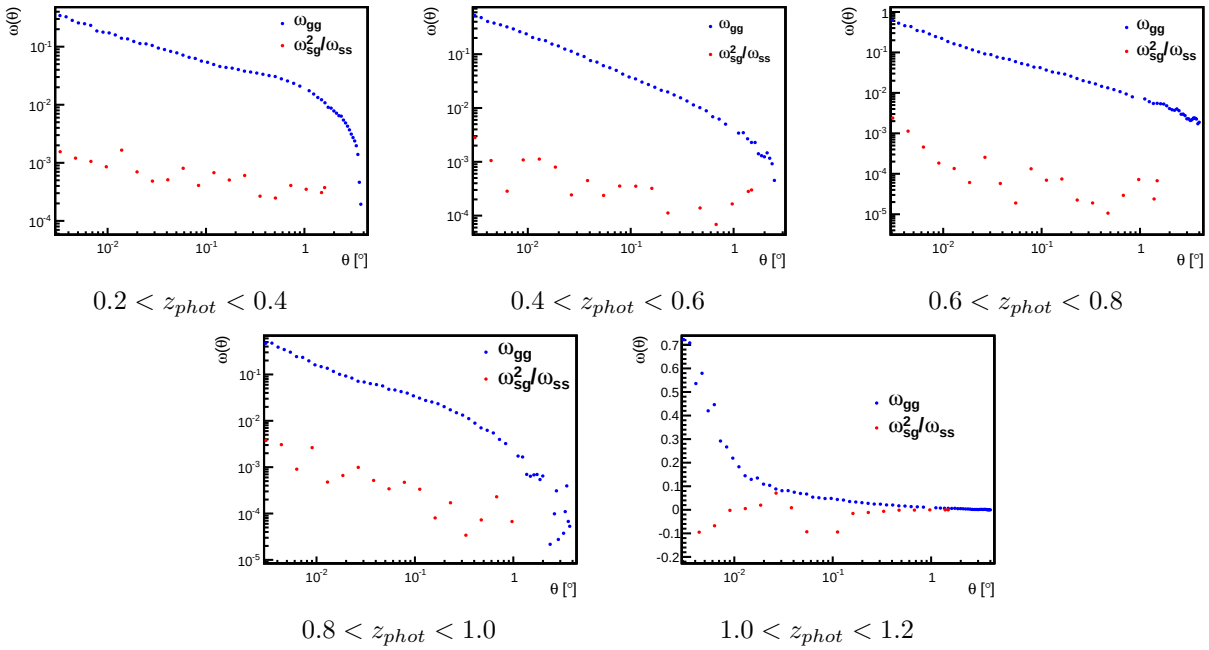

Figure 5.15: Correction in the correlation function due to star contamination for each redshift bin.

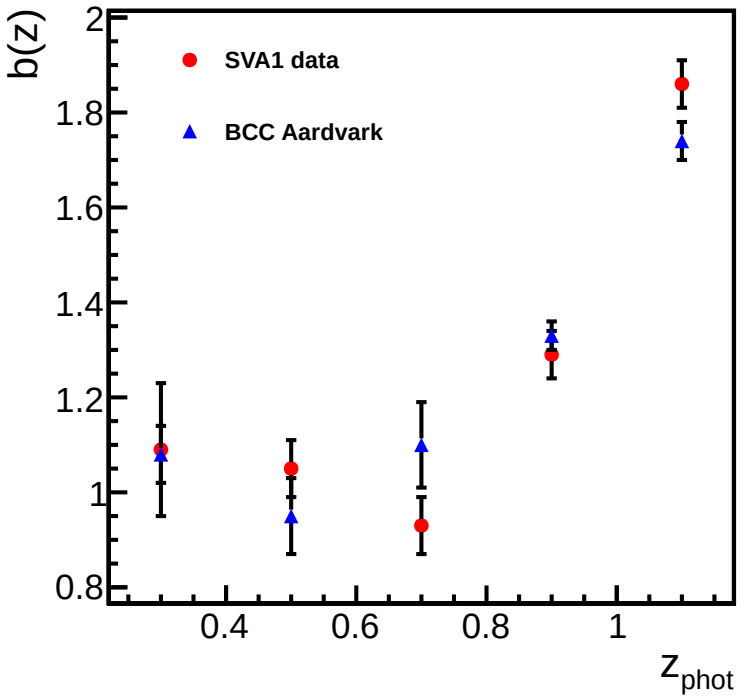

Figure 5.16: Evolution of the galaxy bias with redshift for the SVA-1 data (red points). We compare the evolution with the BCC Aardvark simulation (blue triangles). It is noticeable that both measurements follow a similar trend.

the simulation and the data have a similar behaviour and the values of the best-fit bias are close, even though the simulation has different cosmological parameters to the ones we assume to the fits for data. The best fit results for the remaining two models are depicted as well in Figure 5.19. Notice that, the number of points we have used for the fits is not the same for every redshift bin. This is related to the aforementioned higher photo-z uncertainty in the lowest and highest redshift bins. It is critical to have a good determination of the selection function to make a robust theoretical prediction. At very low scales, the determination of $\phi(z)$ plays a very important role. Small differences in $\phi(z)$ translate into noticeable differences in the theoretical prediction at scales lower than 0.5 degrees. Also, in the lowest redshift bin, at large scales the variation of the correlation function is very fast, then, the determination of $\phi(z)$ becomes critical. Besides, for the last redshift bin, since SVA-1 does not map a very large area, we cannot reach very large scales so, the last points are not accounted for the fit. These results show the high quality of the DES measurements and the constraining power of the angular two point correlation function. Even on their own, and with this small fraction of the DES area, we are capable to rule out the Einstein-de Sitter model which is very significant and promising for the upcoming DES data.

5.4. Constraining w and Ω_m

In order to extract some cosmological information from the correlation function we proceed as we did in simulations in Chapter 3. We compare the value of the correlation function for different theoretical models and minimize the χ^2 function. We use the same covariance matrices and the same points that we used to extract the bias. We use Planck [15] best-fit values for h_0, n_s, A_s, σ_8 and we fix the ratio Ω_b/Ω_m as priors and make a grid of 20 times 20 bins for w and Ω_m. There is a correlation between the bias parameter and these two parameters,

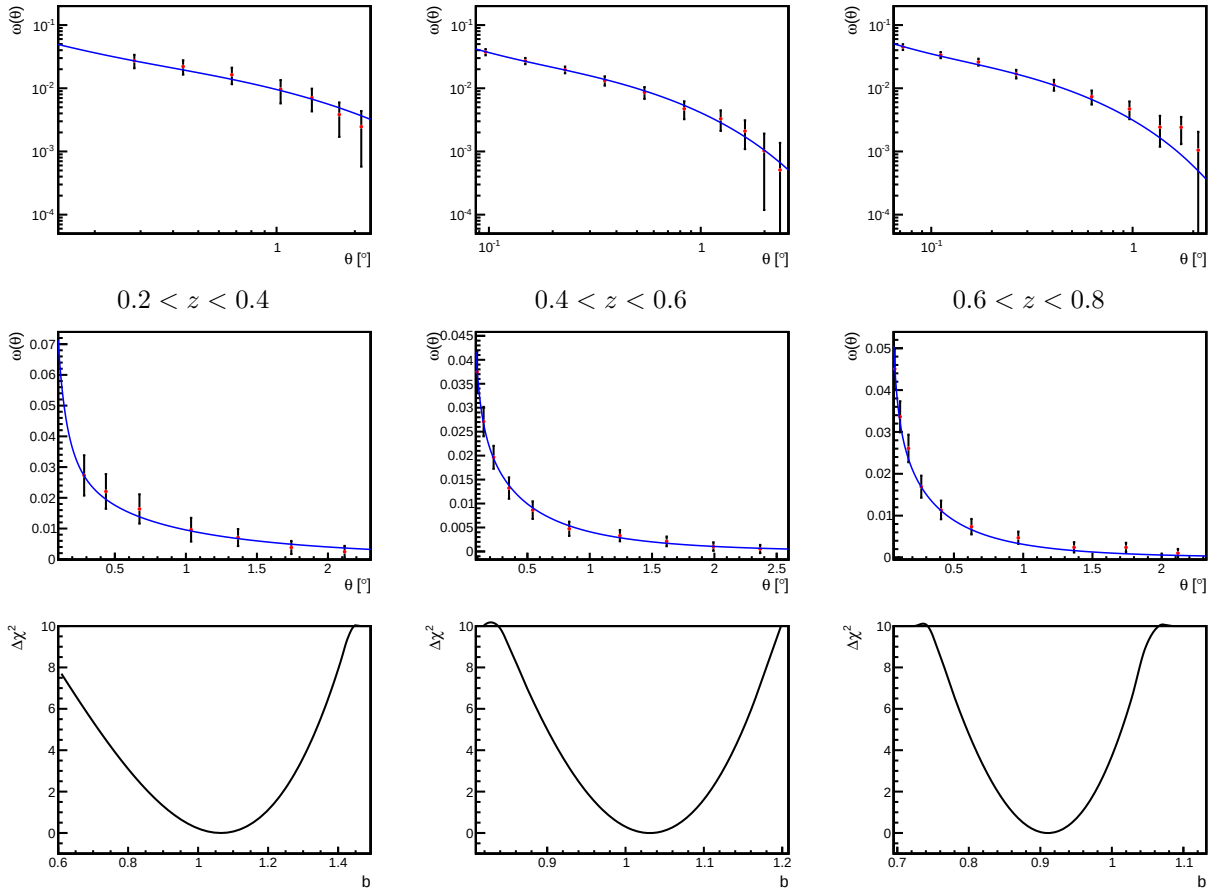

Figure 5.17: Results of fitting the angular correlation function to a ΛCDM model with Planck cosmological parameters in log-log scale (top), in linear scale (center) and χ^2 for different galaxy bias.

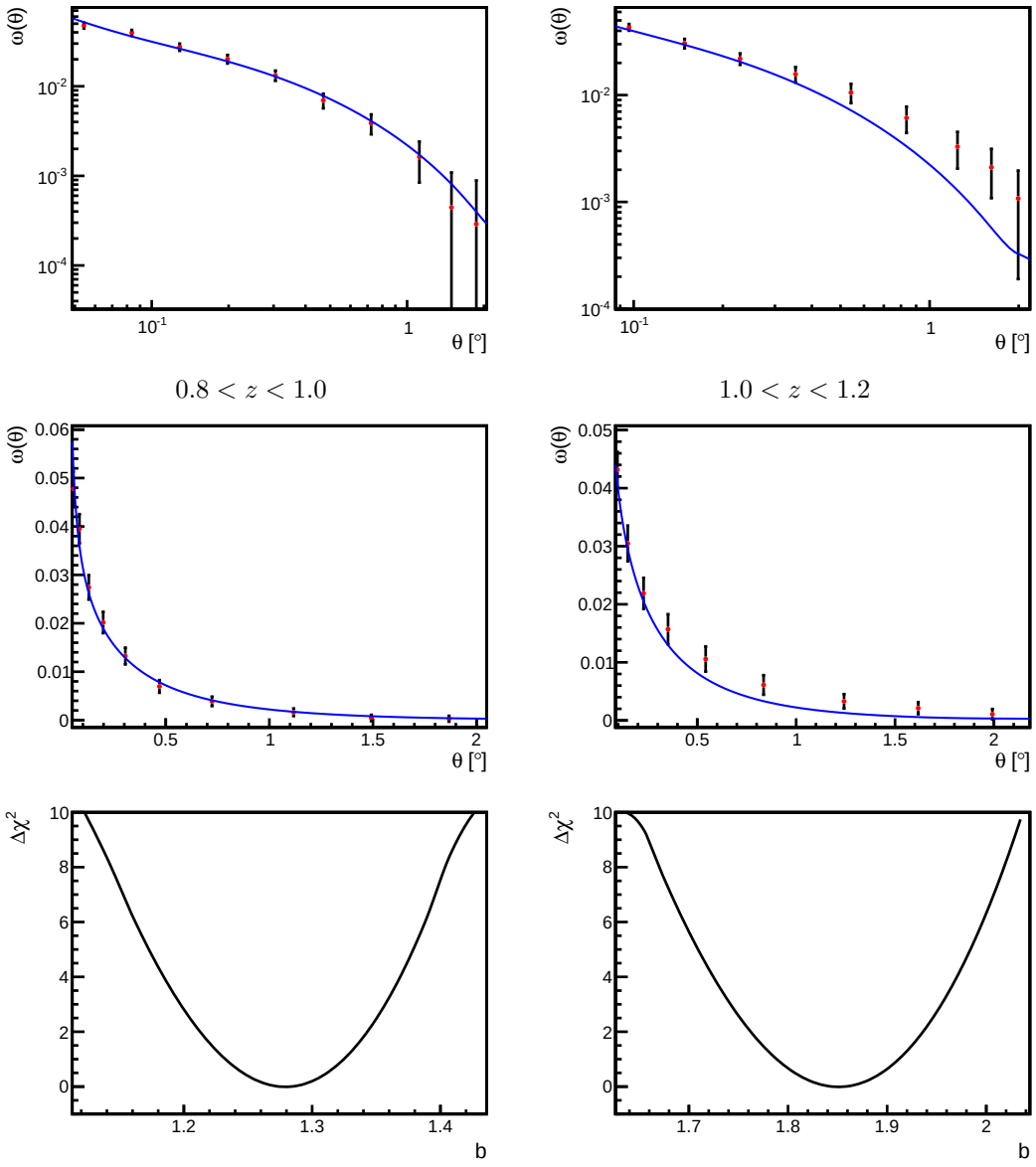

Figure 5.18: Results of fitting the angular correlation function to a ΛCDM model with Planck cosmological parameters in log-log scale (top), in linear scale (center) and χ^2 for different galaxy bias.

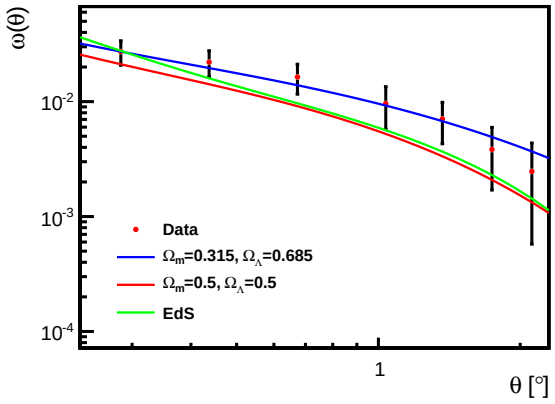

$0.2 < z < 0.4$

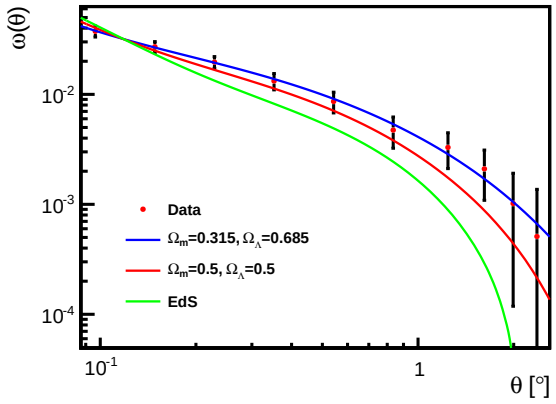

$0.4 < z < 0.6$

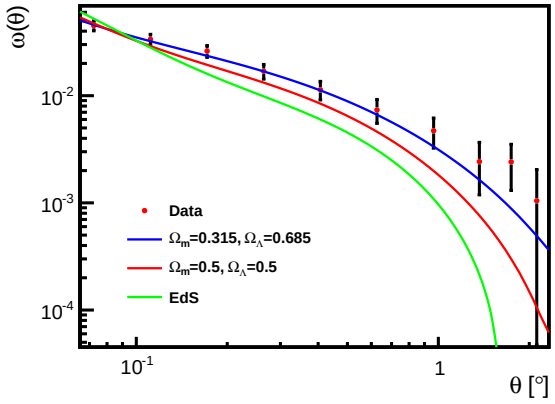

$0.6 < z < 0.8$

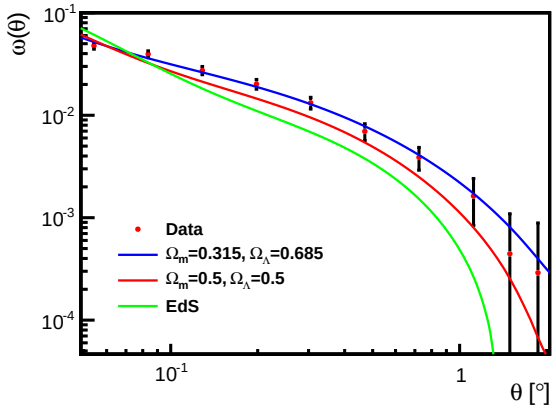

$0.8 < z < 1.0$

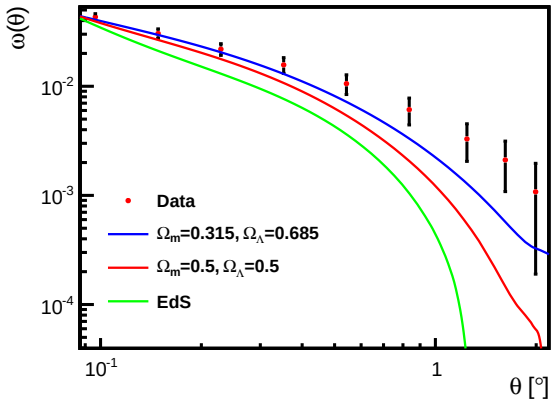

$1.0 < z < 1.2$

Figure 5.19: Comparison of the fits of the three models considered in table 5.2.

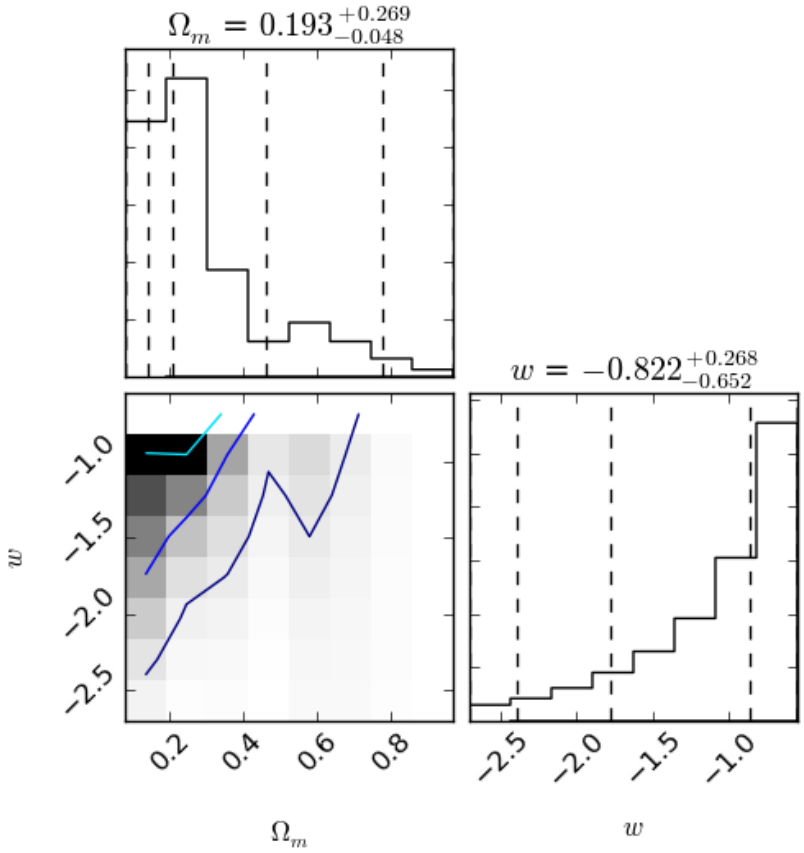

Figure 5.20: Contours showing the fit results for the parameters Ω_m and w fixing the rest of parameters to Planck [15]. We recover the Planck values at 1σ. This gives the idea of robustness of the DES-SV data.

and, if we leave the bias as a free parameter, w and Ω_m can have degenerate values with no physical meaning. Thus, we adopt the best-fit bias of the previous section as the bias for each one of the redshift bins. This assumption will make the results shown here to be optimistic. However, the systematic error due to assuming these bias parameters is negligible if the true underlying cosmology is close to the assumed one. The results are shown in Figure 5.20.

These results show that even though we are dealing with the Science Verification data we are able to introduce a new methodology to measure cosmological parameters and we are able to recover a measurement that is compatible and consistent with Planck at 1σ. Thus, this data and these measurements are a good start for DES since its data show a high degree of robustness.

5.5. Pushing to the limit: Going fainter than 22.5

The results for the Benchmark sample are robust and consistent and constitute a very good first step for DES clustering analysis. However, we can go further and be more ambitious pushing DES to its limit. We can try to go beyond the 22.5 limit. Given the results in the Figure 5.6 we cannot go fainter without losing area if we want to keep the analysis with the standard methodology, *i.e.*, making a random catalog where every patch

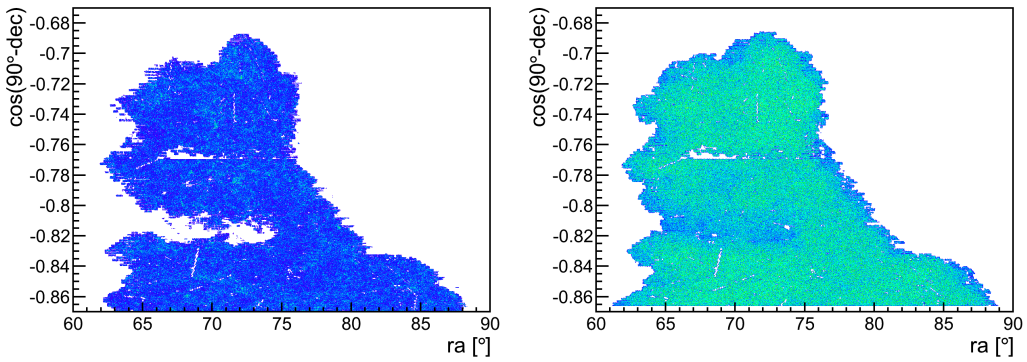

Figure 5.21: Comparison between uniform (left) and non uniform (right) randoms in the SPT-E area.

in the footprint has the same mean density. If we want to go further we must take into account the variations in mean density given by the variations in depth. The simplest way to do this is using a weighted random catalog.

5.5.1. Generation of random catalogs

As long as depth differences appear (see Figure 5.6), they have to be taken into account for any cosmological analysis. In the case of 2pcf or CiC, the easiest way to quantify this effect is using a depth-variable random catalog *a.k.a* non-uniform randoms.

We have developed a technique to build random catalogs that match the differences in depth of the DES SVA1 footprint. The key idea behind the random construction process is that more depth implies a larger mean density The proposed technique works as follows:

1. Map the depth variation in your survey.
2. Make magnitude limit bins. On the one hand they should be large enough to cover regions where you can avoid sample variance. On the other hand, you should do as many bins as possible in order to trace well the density differences.
3. Compute density $\rho(m)$ in function of magnitude in those bins (Figure 5.6).
4. Assign weights according to the integral of those $\rho(m)$ histograms. In our case, if we do N bins we assign the deepest bin a weight $w_N = 1$ and the others follow:

$$w_i = \frac{\int_{m_{min}}^{m_{max}} dm \rho_i(m)}{\int_{m_{min}}^{m_{max}} dm \rho_N(m)} \tag{5.28}$$

5.5.2. The Faint Selection

The Benchmark sample has as an advantage that it is possible to use the traditional random approach, you can safely forget about depth variations across the footprint. The main disadvantage is that a fraction of area is lost, total area is 135 deg^2 instead 150 deg^2 and we lose a non-negligible fraction of objects (see Figure 5.23). We propose a new selection that we will call *Faint Selection* with the following cuts:

- $15 < mag_{i_{auto}} < 26$.
- $21 < mag_{i_{auto,lim}} < 24.2$.

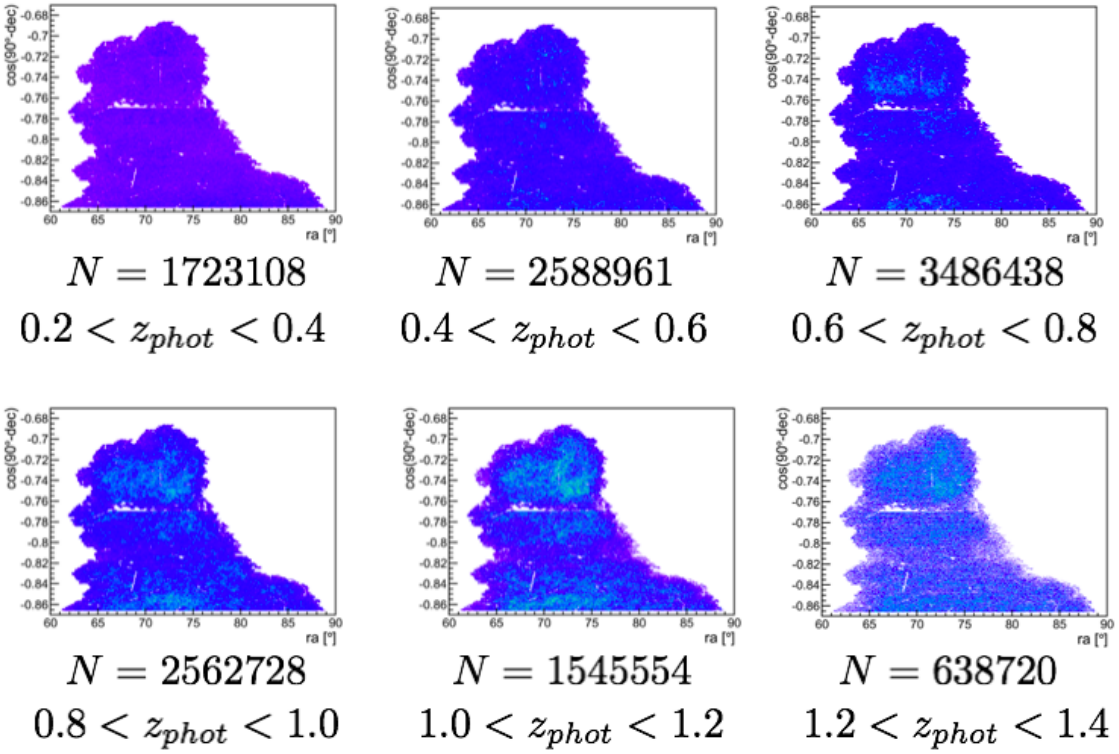

Figure 5.22: Maps and number of galaxies for objects located at regions where 24.2 > MAGLIM_AUTO_I > 21, with $15 < mag_{i_{auto}} < 26$ and MODEST_CLASS= 1.

- `MODEST_CLASS = 1`.

The corresponding maps for this selection are depicted in the Figure 5.22. The Faint Selection has more area and more objects, specially for the deepest redshift bins but the determination of the photo-z is less precise. The correlation function for these two samples should be different since, these selections have different photo-z distributions and, most probably, different bias.

5.5.3. Angular 2 Point Correlation Function

We will proceed as we did for the Benchmark sample but for the Faint Selection we use our method to build a non-uniform random (see Figure 5.21) and then, we compute the correlation function. The correlation functions of the Benchmark Sample and the Faint Selection are depicted in Figure 5.24.

5.6. Conclusions

In this chapter it has been presented the analysis of the DES Science Verification data using the angular two point correlation function. Since we are dealing with a new experiment, some particularities arise. In our case, DES is a large photometric redshift survey and has a complicated masking scheme. Thus, we did a completeness study, and we developed a technique to calculate the correlation function with variable depth footprints. From this study we concluded that the best cut to ensure completeness and go as deep as possible was using patches with `MAG_LIM_AUTO_I`> 22.5 and objects that fulfill `MAG_AUTO_I`< 22.5. For the first time in cosmology, the

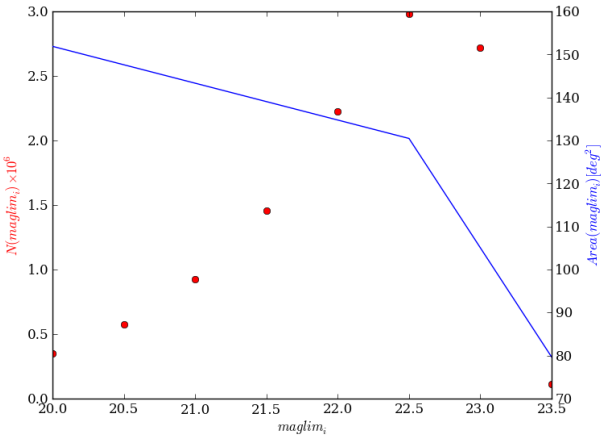

Figure 5.23: Evolution of the area and number of objects available with different limiting magnitude selections.

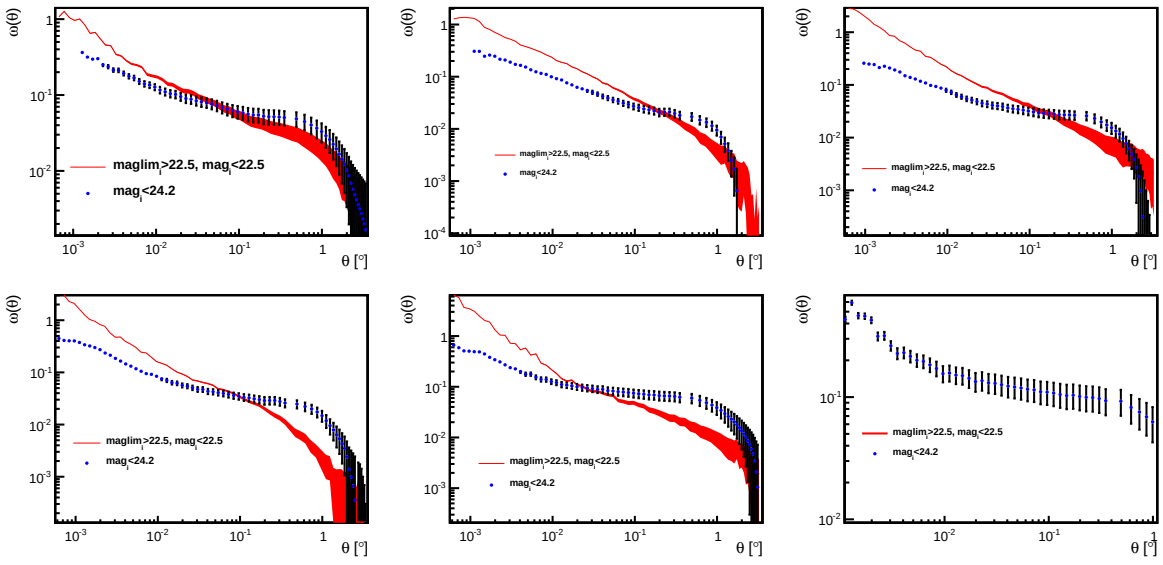

Figure 5.24: Comparison between the correlation functions obtained using the uniform and non-uniform randoms for the two different samples. Since we are treating with different samples, the results are expected to be different but results seem to be reasonable. Every redshift bin is depicted, from $0.2 < z_{phot} < 0.4$ (top left) to $1.2 < z_{phot} < 1.4$ (bottom right) in increasing order.

correlation function is computed using a new weights based technique to account depth fluctuations due to observational effects. In this chapter, we also present the first measurements of the galaxy-galaxy angular correlation function in the redshift range $0.75 < z < 1.4$. These measurements were used to recover the galaxy bias by fixing three different ΛCDM models with different cosmological parameters and fitting the data. From these fits, it is clear that, even with Science Verification data, DES is able to put cosmological constraints and rule out Einstein-de Sitter models, or equivalently, it manifests the need for dark energy for the ΛCDM model. Constraints over Ω_m and w are obtained as well once we fix the other parameters. This is the first time that this method is applied in a photometric redshift survey in these scales. The results obtained are compatible with ΛCDM with Planck [15] cosmological parameters. These constraints are just an example of the power of the measurements and data quality of DES.

Chapter 6

Conclusions

In this thesis two main results are presented: on the one hand, novel methods to study the large-scale structure of the Universe and dark energy have been presented. On the other hand, the first measurement of the large-scale structure of the Universe in the DES project has been performed. This work is the result of an active participation in DES and PAU collaborations. The results and methods presented here will be used in the future by DES and PAU publications. In particular, the results from chapter 5 will be part of the upcoming DES galaxy clustering article. The work presented in this thesis resulted in three publications [76], [112], and [113].

One of the most powerful dark energy probes is the Baryon Acoustic Oscillation (BAO) scale. A method to measure the BAO scale in the direction of the line-of-sight has been developed and tested in simulations. The strength of this method consists in the fact that it relies on observable quantities only. In combination with the angular BAO method presented in [73] it yields to a precission similar to the standard method but with several advantages. It is model independent, *i.e.* any model of dark energy can be tested if an observable BAO scale is given, and moreover, it is unsensitive to most of the systematic uncertainties sources. This methodology is feasible in spectroscopic surveys such as BOSS and DESI.

The study of the large-scale structure of the Universe is usually done with methods that rely in the Cosmological Principle. Thus, it is important to test this assumption. An unbiased method to test the homogeneity in photometric catalogs has been introduced and tested. We can distinguish fractal models from non-fractal models with a 1.5% precision with a DES-like survey and measure the degree of homogeneity in large-scales. This method has been used in a recent work to measure the homogeneity in the 2MPZ survey [113].

After that, a test of the angular BAO method from [73] using a photometric catalog that provides a probability distribution function (PDF) for each galaxy is presented. To do this, we had to compute for the first time the angular correlation function weighting the galaxies by its photo-z PDF. This technique will be used in the upcoming DES data and it can be potentially used in large photometric surveys like LSST.

Two point statistics are one of the main probes in modern cosmology, in particular, for galaxy surveys the two point correlation function is one of the most sensitive measurements to study dark energy and LSS. We have performed the first measurement of $\omega(\theta)$ from the Dark Energy Survey Science Verification data. The results are compatible with the latest release of Planck data [15]. These results show the robustness of DES Science Verification data. The errors in the correlation function are still dominated by the area. With a larger area they will decrease and the constraining power will increase. The measurement reliability and sensitivity have been verified in large simulations. This technique can be potentially used for the upcoming data releases of DES where more area will be available. When this method, is combined with measurements from weak lensing, clusters and supernovae it will provide the best constaints constraints on (w_0, w_a) of the dark energy. Of course,

this methodology is directly applicable to other photometric redshift galaxy surveys.

In this work we have also introduced a new technique to measure the correlation function in photometric redshift surveys with non-homogeneous depth. This technique will be of utmost importance for the upcoming DES measurement campaigns.

The techniques introduced in this work are also applicable to other galaxy surveys such as PAU, eBOSS, DESI, LSST, WFIRST or EUCLID but, also some of them can be easily extended to the case of 21-cm intensity line measurements. DES and these experiments will shed light on the nature of the evasive dark energy.

Resumen

6.1. Introducción

Averiguar la naturaleza de la energía oscura es uno de los más intrigantes problemas de la física moderna. La energa oscura es la responsable última de la expansión acelerada del Universo pero las predicciones del modelo estándar están en desacuerdo con las observaciones por ~ 50 órdenes de magnitud. Por este motivo, la comunidad científica está realizando grandes esfuerzos, agrupándose en inmensas colaboraciones para afrontar los retos que plantea el problema de la energía oscura. En el marco de una de estas colaboraciones, Dark Energy Survey (DES), se ha realizado este trabajo de tesis doctoral. El objetivo último de esta tesis es el estudio de la energía oscura a través del análisis de la estructura a gran escala del Universo. Para ello, se han desarrollado nuevas técnicas de análisis: se propone una técnica para la caracterización de la escala de oscilaciones acústicas de bariones (BAO) en la línea de visión. Asimismo, se propone una técnica no sesgada para la medida de la fractalidad en cartografiados fotométricos de galaxias. Esta técnica permite probar el rango de validez del Principio Cosmológico, de vital importancia para muchas de las medidas cosmológicas que se realizan en la actualidad. Además, se desarrolla un método para medir la función de correlación de galaxias usando distribuciones de probabilidad fotométricas y, posteriormente, se extrae la escala angular de oscilaciones acústicas de bariones. A partir de esta medida se obtiene información sobre los parámetros cosmológicos. Posteriormente, se presenta la medida del denominado *bias* galáctico y de los parámetros cosmológicos, a partir del ajuste de la función de correlación angular a modelos teóricos. También se presenta un método para la medida de la función de correlación en cartografiados de profundidad variable. Finalmente, se exponen las conclusiones de este trabajo.

La Teoría del *Big Bang* (o de la Gran Explosión) describe con precisión la evolución del Universo y es la pieza central del llamado Modelo Estándar cosmológico o modelo ΛCDM, basado en el Principio Cosmológico, la Teoría de la Relatividad General y la inflación cósmica. El éxito de este modelo reside en que ha realizado diversas predicciones que se han corroborado posteriormente mediante observaciones. En particular, ΛCDM predice la existencia de las oscilaciones acústicas de bariones, la polarización del fondo cósmico de microondas (CMB) y la existencia de lentes gravitacionales débiles.

Las pruebas observacionales más fuertes de este modelo son la existencia y propiedades del CMB y sus anisotropías; y la predicción de la abundancia de elementos ligeros. Sin embargo, este modelo exige de dos componentes que no están presentes en el modelo estándar de física de partículas: la materia oscura y la energía oscura.

La existencia de materia oscura se infiere de la velocidad de rotación de las galaxias. La materia observada no es suficiente para explicar las velocidades de rotación que se medían. Por tanto, se propuso la existencia de materia que no emite radiación (o que su radiación es extraordinariamente débil) pero que tiene una gran masa y sufre interacción gravitatoria. Existen multitud de candidatos como materia oscura. Muchos de estos candidatos serán puestos a prueba en los numerosos experimentos dedicados a la investigación de la materia oscura como: CDMS, DAMA/LIBRA, CANDLES, PAMELA, MAGIC, CTA, ArDM, AMS o los experimentos del LHC.

Por otra parte, la necesidad de introducir en el modelo la energía oscura surge en el momento en el que se observa la expansión acelerada del Universo a través de experimentos que miden luminosidad en explosiones de

supernovas tipo Ia en 1998 por los equipos de Riess, Perlmutter y Schmidt. La energía oscura se suele describir y parametrizar como un fluido en el que se define el parámetro w como el cociente entre la presión, p, y la densidad, ρ, del mismo:

$$w = \frac{p}{\rho} \tag{6.1}$$

Dependiendo del valor de este parámetro la energía oscura tiene una naturaleza distinta. Así, si $w = -1$, la energía oscura se corresponde con la constante cosmológica, Λ. En el caso de $w < -1$ se tiene lo que se llama energía oscura fantasma y en el caso en el que $-1 < w < -1/3$ se da la quintaesencia. Las observaciones actuales son compatibles con el caso de constante cosmológica, sin embargo, se requiere más precisión para conocer la evolución de w a través de la historia del Universo. Normalmente, w se parametriza como:

$$w = w_0 + w_a(1-a) = w_0 + w_a\frac{z}{1+z} \tag{6.2}$$

donde a es el factor de escala y z el corrimiento al rojo cosmológico.

El objetivo final de esta tesis es dar una medida de este parámetro w y uno de los objetivos finales de DES es mejorar la precisión en la medida de w_0 y w_a. Una de las formas de conseguir este objetivo es a través del estudio de la estructura a gran escala del Universo que vamos a describir a continuación.

Las no homogeneidades en la distribución de materia en el Universo nos dan información sobre el origen, evolución y naturaleza de sus componentes. Según los modelos inflacionarios, las perturbaciones de densidad de materia están generadas por fluctuaciones Gaussianas en un campo escalar. Por tanto, dichas fluctuaciones son un campo Gaussiano aleatorio. Dicho campo queda completamente definido por el espectro de potencias $P(k)$ definido como:

$$\langle\hat{\delta}(\vec{k})\hat{\delta}(\vec{k'})\rangle = (2\pi)^3\delta^D(\vec{k}-\vec{k'})P(\vec{k}) \tag{6.3}$$

Donde δ^D es la delta de Dirac y $\hat{\delta}(\vec{k})$ es el llamado contraste de densidad. Dadas la densidad $\rho(\vec{k})$ y $\bar{\rho}$ la densidad media, se define como:

$$\hat{\delta}(\vec{k}) = \frac{\rho(\vec{k})}{\bar{\rho}} - 1 \tag{6.4}$$

Es por esto que para el estudio de la estructura a gran escala del Universo se utiliza el espectro de potencias, o de forma equivalente, su transformada de Fourier, que recibe el nombre de función de correlación a dos puntos $\xi(\vec{r})$:

$$P(\vec{k}, z) = \int d^3\vec{r}\xi(\vec{r}, z)\exp\left(i\vec{k}\cdot\vec{r}\right) \tag{6.5}$$

La función de correlación se define como el exceso de probabilidad de encontrar un par de objetos a una distancia $\vec{r}$ respecto a una distribución aleatoria y uniforme con la misma densidad media. Por tanto, el número esperado de objetos dada una galaxia en dV_1 y otra en dV_2 en un campo cuyo número medio de objetos es $\bar{n}$ es:

$$\langle n_{pair}\rangle = \bar{n}^2\left[1+\xi(\vec{r})\right]dV_1dV_2 \tag{6.6}$$

En nuestro caso, dado que gran parte de este trabajo se realiza en el contexto de cartografiados fotométricos, vamos a estar interesados en la denominada función de correlación angular $\omega(\theta)$. Esta función de correlación angular no es más que la proyección al plano de la función de correlación $\xi(\vec{r})$.

$$\omega(\theta) \equiv \langle\delta(\hat{n}_1)\delta(\hat{n}_2)\rangle = \int_0^\infty dz_1\phi(z_1)\int_0^\infty dz_2\phi(z_2)\xi(z_1, z_2, \theta) \tag{6.7}$$

Donde la separación angular θ está relacionada con la distancia $r = |\vec{r}|$ a través de:

$$r \equiv \sqrt{x_1^2 + x_2^2 - 2x_1x_2\cos(\theta)} \tag{6.8}$$

Donde los x_i son las distancias comóviles al corrimiento al rojo correspondiente z_i y $\phi(z_i)$ es la denominada función de selección. Esta función de selección relaciona la distribución de corrimiento al rojo fotométrico en una capa ancha con su distribución espectroscópica.

$$\phi(z) \propto \frac{dN}{dz} \int_{z_{p1}}^{z_{p2}} dz_p \frac{dN_p}{dz_p} P(z_p|z) \tag{6.9}$$

Esta información se suele obtener a partir de la muestra de calibración de los algoritmos que calculan el corrimiento al rojo fotométrico, ya que para esta muestra se dispone de medidas tanto fotométricas como espectroscópicas.

En los cartografiados de galaxias no se tiene acceso directo a la distancia a las mismas. En su lugar, se mide el corrimiento al rojo. Este corrimiento al rojo se ve distorsionado por los movimientos peculiares de las galaxias, lo que produce anisotropías en la función de correlación. Este efecto es conocido con el nombre de distorsiones en el espacio del corrimiento al rojo o por sus siglas en inglés RSD. Además, generalmente, estamos interesados en la distribución subyacente de materia que relacionamos con la distribución de galaxias a través del llamado parámetro de *bias* galáctico, $b(z)$. Dicho parámetro da cuenta de la relación entre las acumulaciones de materia luminosa y materia oscura y depende del tipo de población de galaxias que se seleccione para la medida. Teniendo en cuenta dichos efectos y, en aproximación plano-paralela [63], podemos escribir la función de correlación observada en términos de multipolos de la función de correlación ξ_l de la distribución de materia subyacente.

$$\xi(r,\mu) = b(z)^2 \left\{ \left[1 + \frac{2}{3}\beta + \frac{1}{5}\beta^2 \right] \mathcal{P}_0(\mu)\xi_0(r) + \left[\frac{4}{3}\beta + \frac{4}{7}\beta^2 \right] \mathcal{P}_2(\mu)\xi_2(r) + \frac{8}{35}\mathcal{P}_4\xi_4(r) \right\} \tag{6.10}$$

donde $\mathcal{P}_l$ son los polinomios de Legendre, μ es el coseno del ángulo que forman la línea que une el par y la línea de visión y β está definido por:

$$\beta = \frac{1}{b(z)} \frac{d\ln D_+}{d\ln a} \tag{6.11}$$

Donde D_+ es el factor de crecimiento lineal.

Además del efecto de las RSD, existen otros efectos que modifican la forma del espectro de potencias. Estos efectos son las no linealidades, que aparecen debido a que a partir de cierto momento, los términos no lineales que se desprecian en las ecuaciones de fluidos para poder calcular el espectro de potencias teórico, empiezan a ser relevantes. Hay diversas aproximaciones para tratar este problema. Durante el desarrollo de este trabajo usaremos el software `HALOFIT` [69] en el paquete CAMB para estimar el espectro de potencias no lineal. Este software no es más que un ajuste paramétrico a medidas del espectro de potencias en simulaciones de N-cuerpos de alta resolución.

Otro efecto importante que distorsiona la forma del espectro de potencias y que, además, posee valiosa información cosmológica, son las oscilaciones acústicas de bariones, también conocidas por sus siglas en inglés BAO. Las BAO no son más que el resultado de la competición de la presión de radiación con la atracción gravitatoria en el plasma primordial. En etapas tempranas del Universo, cuando el plasma estaba ionizado, el recorrido libre medio de un fotón era mucho más pequeño que el horizonte del Universo. Los fotones se comportaban como un fluido acoplado a las partículas cargadas. La presión de radiación tiende a separar el plasma mientras que la atracción gravitatoria tiende a colapsar el mismo. La acción de estas dos fuerzas provoca oscilaciones en el plasma de fotones y bariones. Una vez que la temperatura del Universo baja a 3000 K, los fotones se desacoplan de los bariones. La sobredensidad de bariones debida a las oscilaciones, atrae gravitatoriamente a la materia oscura y a otros bariones, y sigue creciendo. Esta escala se queda *congelada* a través de la evolución del Universo y viene dada por:

$$r_s(z_{dec}) = \frac{c}{\sqrt{3}} \int_0^{1/(1+z_{dec})} \frac{da}{a^2 H(a)\sqrt{1 + (3\Omega_b/\Omega_\gamma)a}} \text{ Mpc h}^{-1} \tag{6.12}$$

Donde z_{dec} es el corrimiento al rojo en el momento del desacoplo y también depende del valor de los parámetros cosmológicos (ver capítulo 2).

6.2. Medida de la escala radial de BAO

En esta tesis se desarrolla y prueba un método de medida que usa únicamente cantidades observables para la determinación de la escala de oscilaciones acústicas de bariones en la línea de visión. Esta escala viene dada por:

$$\Delta z_{BAO} = H(z) r_s \tag{6.13}$$

Donde $H(z)$ es la constante de Hubble evaluada en el corrimiento al rojo para el que se efectúa la medida. Asimismo, esta medida se complementa con la medida de la escala angular de BAO que se expresa como:

$$\theta_{BAO} = \frac{r_s}{(1+z) d_A(z)} \ , \tag{6.14}$$

siendo d_A la distancia por diámetro angular al corrimiento al rojo en el que medimos la señal.

En primer lugar, para la determinación de la escala radial se mide la función de correlación de dos puntos en la dirección radial. $\xi_{\parallel}(\Delta z)$. Para ello se usa el estimador de Landy & Szalay [82] en una muestra de galaxias. Para este análisis consideramos colineales todas aquellas galaxias que estén en un píxel cuadrado de 0.5 grados de lado. El tamaño de este píxel puede variar en función de las condiciones del cartografiado.

En segundo lugar, una vez medida la función de correlación, se procede a ajustar dicha función a la siguiente expresión:

$$\xi_{\parallel}(\Delta z) = A + B e^{-C\Delta z} + D e^{-E\Delta z} + F e^{-\frac{(\Delta z - \Delta z_{BAO})^2}{2\sigma^2}} \tag{6.15}$$

De esta expresión se obtiene directamente el valor de la escala radial de BAO, Δz_{BAO}.

Para demostrar la validez y capacidades del método se presentan medidas en la simulación MICE [77], [78], [79] asimilada a un cartografiado espectroscópico (o fotométrico que nos permita tener $\Delta z < 0{,}0025$). Se divide la muestra en cuatro capas anchas de corrimiento al rojo: (0.2, 0.45); (0.45, 0.75); (0.75,1.1); (1.1, 1.4); que se pueden observar en la figura 6.1. Consideramos los casos de cartografiados con áreas de 200, 500 y 1000 grados cuadrados pero la significancia estadística de las detecciones era en todos estos casos baja. Con lo cual, el análisis exige áreas del orden de 5000 grados cuadrados. En dichas capas de corrimiento al rojo y considerando como colineales todos aquellos objetos que estén en el mismo píxel de 0.5 grados de lado, se calcula la función de correlación usando el estimador de Landy & Szalay [82]. Posteriormente, procedemos al ajuste según la fórmula en la ecuación 6.15 y se obtienen los resultados de la figura 6.2. Los resultados de la medida de la escala de oscilaciones acústicas de bariones se muestran en la figura 6.3. Además, se muestran las medidas en capas de corrimiento al rojo ligeramente desplazadas (triángulos azules) para validar las medidas. Para el análisis cosmológico sólo se utilizarán los resultados dados en los puntos rojos, sin embargo se ve que todos los puntos concuerdan con la predicción teórica para la cosmología subyacente en la simulación.

La estimación de los errores en la función de correlación se realizó utilizando dos métodos complementarios. Por un lado, se midió la misma cantidad en diferentes regiones de la simulación y se calculó la dispersión de la medida para ellas. El segundo método consiste en usar la expresión teórica que aparece en el capítulo 3 [112]. El error tiene dos contribuciones principales: por un lado, está el error de Poisson y por otro lado, la varianza cósmica. Los errores pueden verse en la figura 6.4 siendo la varianza cósmica la contribucin dominante.

En cuanto a los errores sistemáticos, tenemos de dos tipos: los genéricos en las medidas de función de correlación como son el modelado de las no linealidades, los rangos que se usan para el ajuste y el *bias* galáctico; y el otro tipo de sistemáticos son los inherentes a este método. En este caso se trata del error que se comete

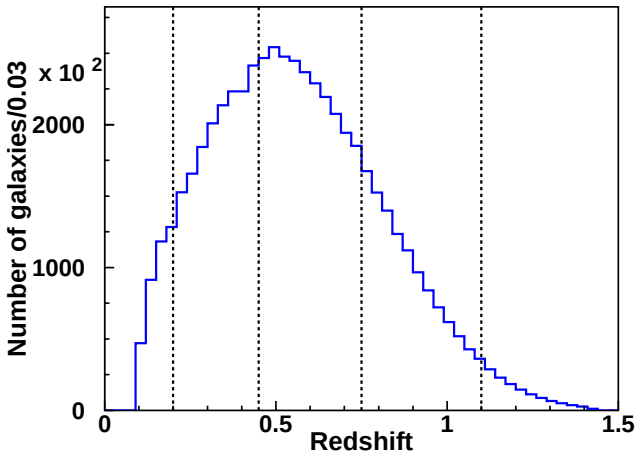

Figura 6.1: $N(z)$ del catálogo MICE. La simulación contiene 55 millones de galaxias en el rango de corrimiento al rojo $0.1 < z < 1.5$. Las líneas verticales indican los límites de las capas anchas utilizadas en este análisis.

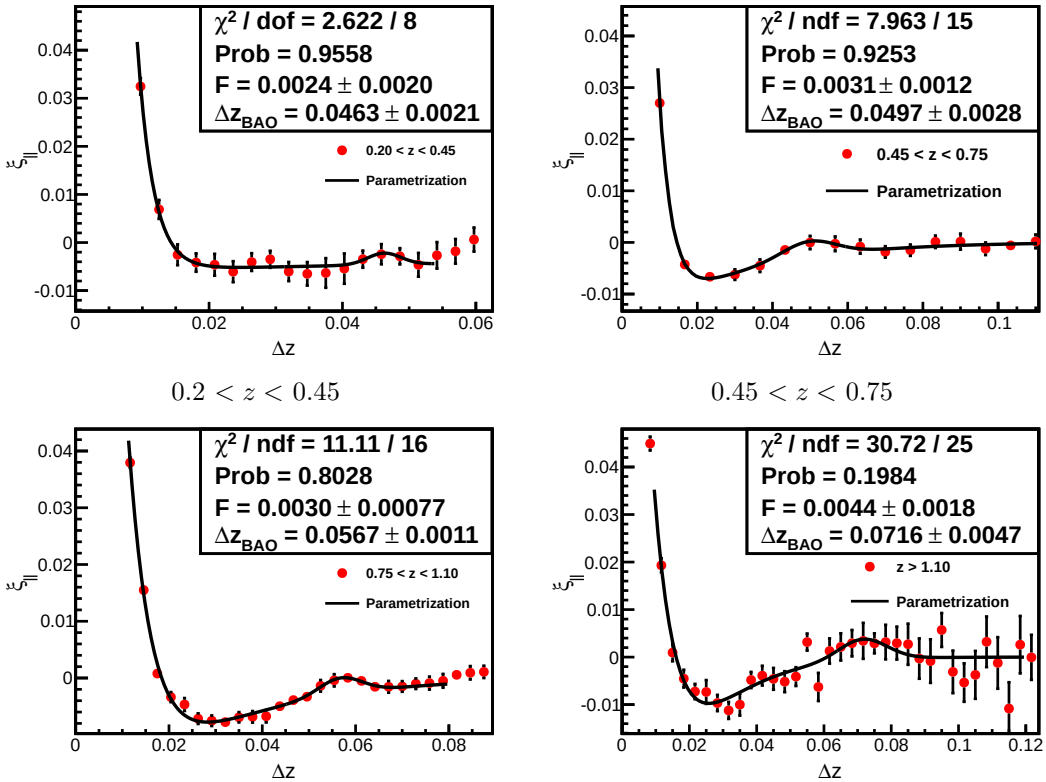

$0.2 < z < 0.45$ $0.45 < z < 0.75$

$0.75 < z < 1.05$ $1.05 < z < 1.2$

Figura 6.2: Funciones de correlación radial medidas en la simulación MICE para las cuatro capas de corrimiento al rojo usando un píxel de 0.25 grados cuadrados. Se compara el resultado con la parametrización propuesta (línea negra). La significancia estadística de la medida en la primera capa es baja y, por tanto, no se utiliza en el análisis cosmológico.

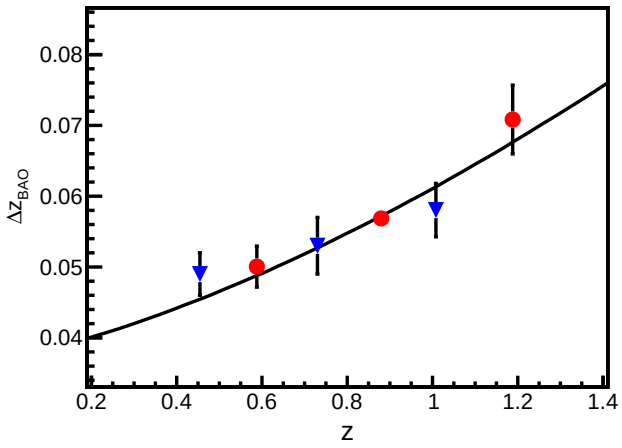

Figura 6.3: Escala de BAO radial en función del corrimiento al rojo en MICE. Los puntos son las capas nominales y los triángulos corresponden a capas ligeramente desplazadas y medidas únicamente con propósitos de validación. Todas las medidas están en buen acuerdo con la predicción teórica (línea negra).

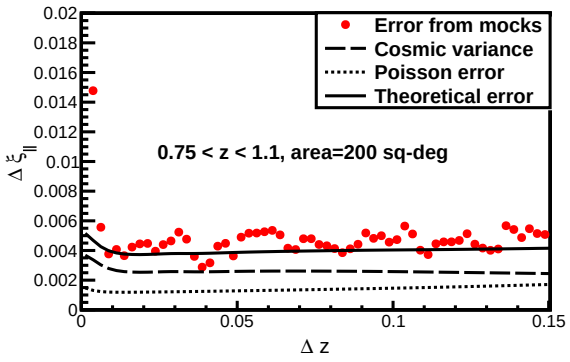

Figura 6.4: Comparativa entre los distintos métodos de estimación para la función de correlación. Los puntos corresponden a estimaciones a través de simulaciones y la línea corresponde al cálculo teórico. Ambas estimaciones concuerdan en la región de interés para el análisis del BAO. El desacuerdo a baja escala viene de la descripción incompleta de las no linealidades ya que no hemos tenido en cuenta el acoplo entre modos. Además los efectos de borde afectan a las medidas en las regiones del cielo. Estos efectos no afectan en las escalas que estamos estudiando. Se muestran las distintas contribuciones al error: ruido de Poisson (línea de puntos) y varianza cósmica (línea de guiones)

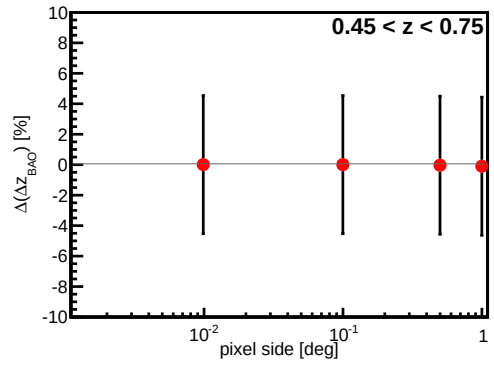

$0{,}45 < z < 0{,}75$

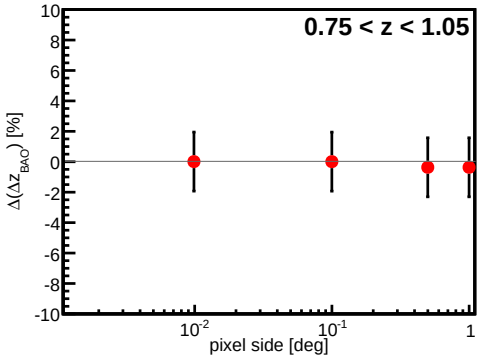

$0{,}75 < z < 1{,}05$

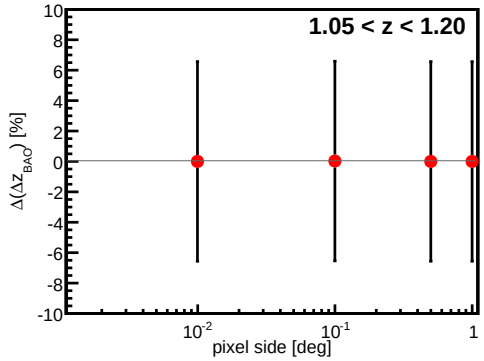

$1{,}05 < z < 1{,}2$

Figura 6.5: Variación de la escala BAO radial en función del tamaño angular del píxel para las diferentes capas de corrimiento al rojo. Los resultados son estables y la variación es siempre mucho menor del 1 %. Las barras de error indican el tamaño del error estadístico para el tamaño de píxel nominal en la simulación que cubre un octante del cielo.

al considerar galaxias en un píxel de tamaño no infinitesimal como colineales. Este error sistemático ha sido estudiado variando el tamaño del píxel y recalculando la función de correlación. En la figura 6.5 se aprecia que, efectivamente, el cambio en el tamaño angular del píxel modifica el comportamiento de la función de correlación. Específicamente, la función de correlación se ve muy afectada para escalas bajas, sin embargo, a la escala BAO las medidas son consistentes para los distintos tamaños de píxel escogidos que cubren un rango de escalas de dos órdenes de magnitud diferentes. El error sistemático asociado se estima en $\delta(\Delta z_{BAO}) = 0{,}20\,\%$ siendo dicho error mucho más pequeño que el estadístico.

Pasando a los sistemáticos genéricos, se ha analizado el sistemático del efecto de las no linealidades de manera conservadora como la diferencia relativa entre las funciones de correlación lineal y no lineal a las escalas de BAO y se obtiene una incertidumbre $\delta(\Delta z_{BAO}) = 0{,}10\,\%$.

Del mismo modo, también se ha estudiado el efecto del *bias* galáctico. Dicho parámetro afectará únicamente a la bondad de ajuste de la parametrización. Para conocer el impacto de este parámetro hemos repetido el análisis para distintos valores del *bias* obteniendo que a las escalas de interés la incertidumbre es $\delta(\Delta z_{BAO}) = 0{,}15\,\%$. Además, se ha analizado el comportamiento de la presencia de un *bias* dependiente de la escala y se asume un modelo-Q para el mismo, dando lugar a variaciones en la función de correlación entre el 1 % y el 6 %. Sin embargo, la escala de BAO permanece prácticamente inalterada, estimándose el error en $\delta(\Delta z_{BAO}) = 0{,}20\,\%$.

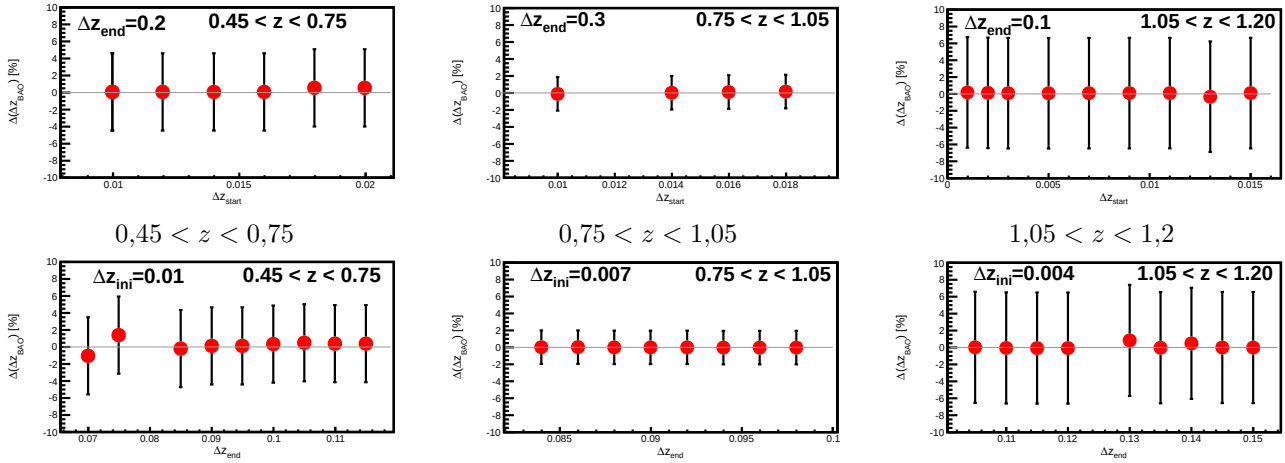

Figura 6.6: Evolución de Δz_{BAO} en función de los puntos inicial y final del ajuste. los resultados son estables y confirman que el error sistemático asociado es pequeño. Las barras de error representan al error estadístico e incluyen el ruido de Poisson y la varianza cósmica en la simulación que cubre un octante del cielo.

Por último, se estima la influencia del rango de ajuste en la determinación de la escala BAO. Para ello se han variado los puntos inicial y final del ajuste. En la figura 6.6 se puede observar que se tiene un comportamiento estable para los distintos valores inicial y final y que la variación debido a este efecto es mucho menor que la varianza cósmica que se representa con las barras de error.

Dado que las diferentes fuentes de error sistemático son independientes, el error sistemático total se calcula como suma en cuadratura, obteniendo $\delta(\Delta z_{BAO})_{tot} = 0{,}33\,\%$. Existen otras fuentes potenciales de error sistemático como la magnificación cósmica, que pueden introducir una correlación entre los distintos puntos y capas de corrimiento al rojo, pero este efecto es muy pequeño y lo hemos despreciado a la hora de realizar el análisis.

Las medidas de la figura 6.3 demuestran que el método funciona. Cuando estas medidas se traducen a estimaciones de los parámetros cosmológicos se obtienen los resultados de la figura 6.7. Cuando estos resultados se combinan con la medida de la escala BAO angular usando el método que se presenta en [73] la sensibilidad mejora. Si comparamos con el método habitual [38] obtenemos lo descrito en la figura 6.8.

En conclusión, se ha desarrollado y probado en simulación un método basado únicamente en cantidades observables y robusto a errores sistemáticos para extraer la escala radial de BAO. En combinación con el método presentado en [73] da unas incertidumbres en los parámetros cosmológicos similares al método estándar, con la ventaja de que el método presentado es completamente independiente del modelo.

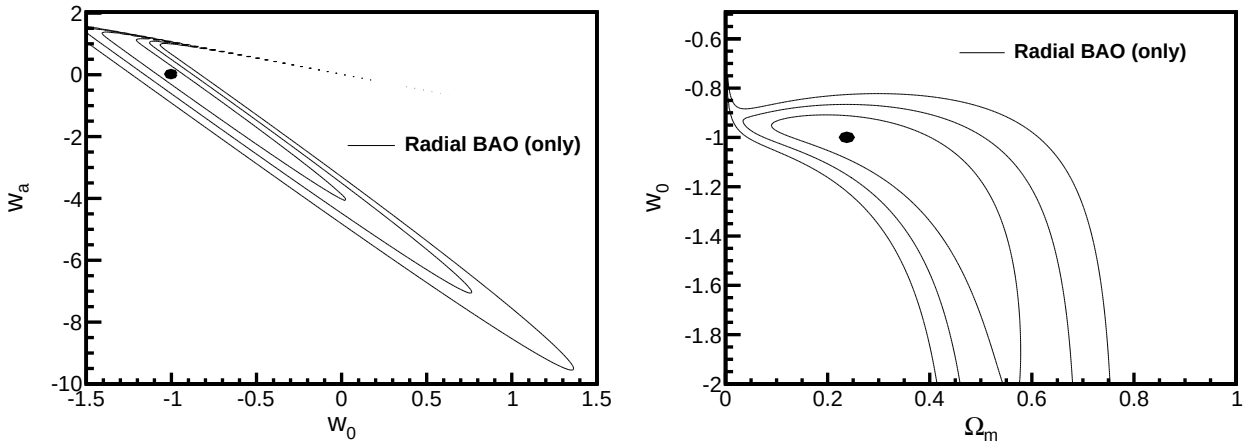

Figura 6.7: Contornos a 1σ, 2σ y 3σ de nivel de confianza en el plano (w_0, w_a) (izquierda) y en el plano (Ω_M, w_0) (derecha) obtenidos del análisis del BAO radial. El punto muestra el valor de los parámetros en la simulación MICE.

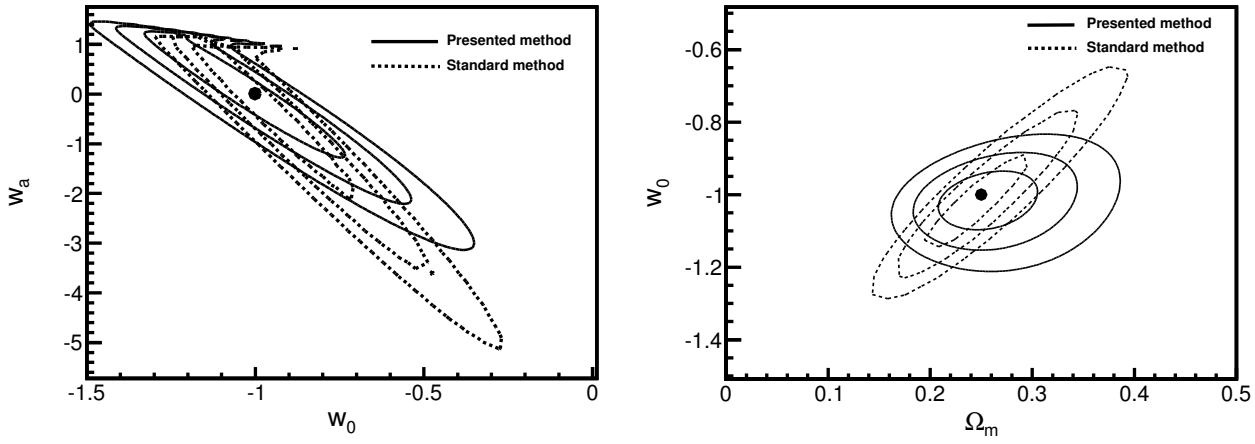

Figura 6.8: Contornos a 1, 2, y 3σ de nivel de confianza en los planos (w_0, w_a) (izquierda) y $(\Omega_{\rm M}, w_0)$ (derecha). Los contornos con línea continua corresponden a nuestra combinación de la información radial y angular. Los contornos con línea discontinua son los resultados usando el método estándar. La diferente correlación entre parámetros se debe al distinto tratamiento de las RSD.

6.3. Medida de la transición hacia la homogeneidad

En este trabajo se presenta asimismo un nuevo método para probar el Principio Cosmológico en cartografiados fotométricos de galaxias. Como se señala en el capítulo 1, el Principio Cosmológico es una de las bases del modelo ΛCDM y afirma que el Universo, en escalas grandes, es homogéneo e isótropo. Esto significa que son necesarios cartografiados de gran volumen para poder testarlo en observaciones. Por esto, cartografiados fotométricos como DES son ideales para este tipo de pruebas. El problema es que debido a su naturaleza fotométrica, se pierde precisión en la determinación de la distancia en la línea de visión. Por ello, aquí se desarrolla un estimador de homogeneidad para cartografiados fotométricos de galaxias. Este estimador es el índice de homogeneidad angular $H_2(\theta)$.

$H_2(\theta)$ se define en términos de la integral de correlación en dos dimensiones. La integral de correlación en dos dimensiones no es más que el número medio de puntos dentro de un casquete esférico de radio θ centrado en otros puntos de la distribución. Entonces $H_2(\theta)$ se define como:

$$H_2(\theta) = \frac{d\log G_2(\theta)}{d\log V(\theta)} \tag{6.16}$$

Donde V es el volumen de un casquete esférico. Estas cantidades se pueden modelar en términos de la función de correlación y su media:

$$G_2(\theta) = 1 + \bar{N}(\theta)\,[1 + \hat{\omega}(\theta)] \tag{6.17}$$

$$H_2(\theta) = 1 - \frac{\hat{\omega}(\theta) - \omega(\theta)}{1 + \hat{\omega}(\theta)} - \frac{1}{\hat{N}(\theta)} \tag{6.18}$$

$$\hat{N}(\theta) = 2\pi\hat{\sigma}(1 - \cos\theta) \tag{6.19}$$

Donde $\hat{\sigma}$ es la densidad angular media y $\hat{\omega}$ se define como

$$\hat{\omega}(\theta) = \frac{1}{1 - \cos\theta}\int_0^\theta \omega(\theta')\sin\theta' d\theta' \tag{6.20}$$

Para estimar $H_2(\theta)$ consideramos tres estimadores distintos que describimos más adelante. En el caso tridimensional, si para la i-ésima galaxia del cartografiado definimos $n_i^d(< r)$ como el número de galaxias en el cartografiado dentro de una esfera de radio r alrededor de i y $n_i^r(< r)$, la misma cantidad, pero para una distribución aleatoria. Para N_c galaxias usadas como centros, se define el número de cuentas en esferas escalado $\mathcal{N}(r)$ como

$$\mathcal{N}(r) = \frac{1}{N_c}\sum_{i=1}^{N_c}\frac{n_i^d(< r)}{f_r n_i^r(< r)} \tag{6.21}$$

Con $f_r = D/R$ la proporción de número de galaxias y número de objetos de la distribución aleatoria. A partir de estas magnitudes definimos los estimadores:

- E1: Es el caso más conservador, no realiza ningún tipo de asunción sobre la distribución de galaxias. Sólo tiene en cuenta aquellas esferas cuyo volumen esté competamente contenido en el cartografiado. En este caso $n_i^r = \hat{N}(r) = \frac{4}{3}\pi r^3\hat{n}_d$. Donde $\hat{n}_d$ es la densidad media del cartografiado y hemos asumido $f_r = 1$.
- E2: Se siguen usando únicamente esferas completamente contenidas en el cartografiado pero además se usa un catálogo de galaxias artificial aleatorio que incorpora los mismos efectos observacionales que los datos para estimar $n_i^r(< r)$.
- E3: Se usan todas las galaxies del cartografiado para todos los radios. Esto implica que se usan esferas que tienen parte fuera del cartografiado, hecho que es compensado por el catálogo aleatorio que sirve para estimar $n_i^r(< r)$ para los mismos radios.

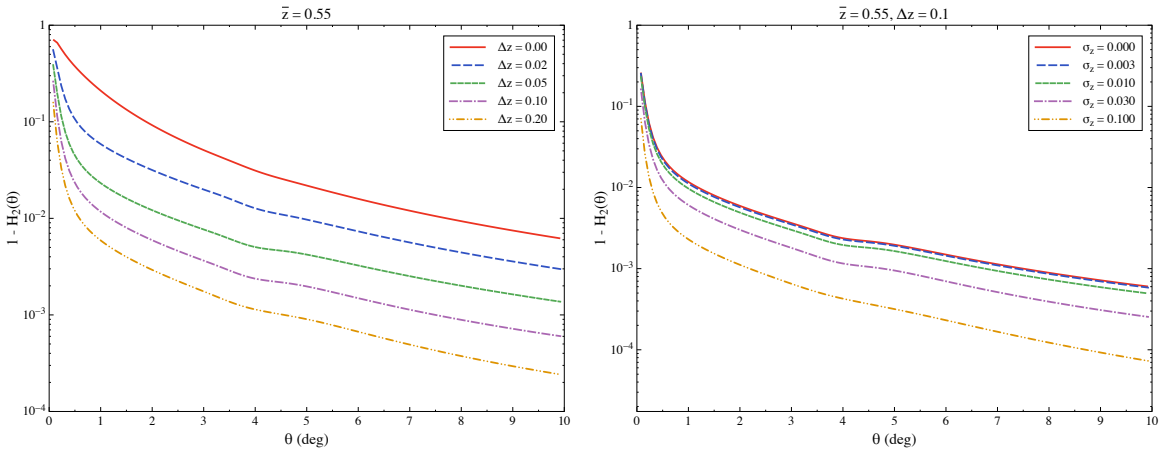

Figura 6.9: $\Delta H_2(\theta)$ en función de θ para distintas anchuras de la capa de corrimiento al rojo (izquierda) y distinta incertidumbre en el corrimiento al rojo fotométrico (derecha). El uso de capas anchas de corrimiento al rojo produce una distribución más homogénea cuando se proyecta en la esfera, reduciendo la amplitud de la correlación.

Por tanto, en analogía con el caso tridimensional se estima $H_2(\theta)$ usando el número de cuentas en casquetes esféricos escalado $\mathcal{N}(\theta)$ definido como:

$$\mathcal{N}(\theta) = \frac{1}{N_c} \sum_{i=1}^{N_c} \frac{n_i^d(<\theta)}{f_r n_i^r(<\theta)} \tag{6.22}$$

Donde se usan las diferentes prescripciones para el cálculo de N_c y $n_i^r(<\theta)$.

Para el modelado teórico de $H_2(\theta)$ simplemente se emplean las expresiones anteriores que lo relacionan con $\omega(\theta)$. Para obtener los valores teóricos de $\omega(\theta)$ usamos códigos numéricos como `HALOFIT` [69] para obtener el espectro de potencias. Este mismo se integra y se obtiene la función de correlación ξ_r y, finalmente, se proyecta sobre una capa ancha de corrimiento al rojo para obtener $\omega(\theta)$. La descripción detallada se encuentra en el capítulo 2. Existen distintos efectos que modifican $H_2(\theta)$, entre otros, están el efecto de proyección a capas de corrimiento al rojo anchas, el efecto del *bias* galáctico y el efecto de las no linealidades del espectro de potencias. Todos estos efectos se pueden incluir en las predicciones teóricas y han sido cuantificados en este trabajo.

El efecto de proyección en una capa ancha de corrimiento al rojo mezcla las distintas escalas e introduce pares no correlacionados en los mismos casquetes esféricos. Este efecto, provoca que cuanto más ancha sea la capa de corrimiento al rojo más homogénea parezca la muestra, tal y como se aprecia en la figura 6.9.

El efecto del *bias* galáctico es el contrario, una muestra con un *bias* más alto presenta mayores acumulaciones y desviaciones más altas de la homogeneidad. Por tanto, la escala de homogeneidad aumentará para muestras con mayor *bias* tal y como se aprecia en la figura 6.10.

En cuanto al efecto de las no linealidades en el espectro de potencias, se tiene que $H_2(\theta)$ es una cantidad integral y, por tanto, se mezclan escalas grandes y pequeñas. El efecto de las mismas se puede observar en la figura 6.11.

$H_2(\theta)$ también depende de los parámetros cosmológicos, aunque esta dependencia es suave y, por tanto, la medida cualitativa de homogeneidad será válida para cualquier modelo que tienda a la homogeneidad.

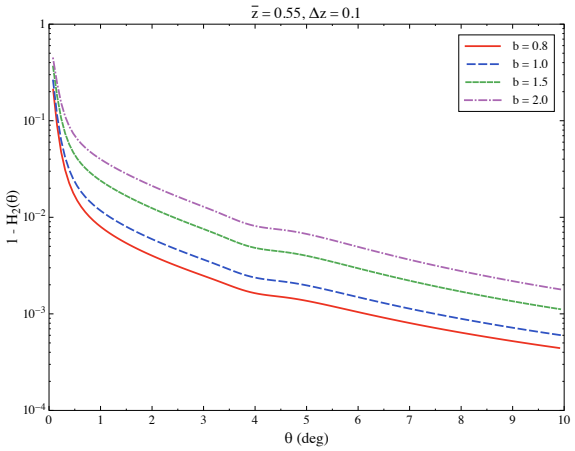

Figura 6.10: $\Delta H_2(\theta)$ en función de θ para distintos valores del *bias*. Una población con valores de *bias* altos formará mayores acumulaciones y mostrará desviaciones respecto a la homogeneidad más evidentes.

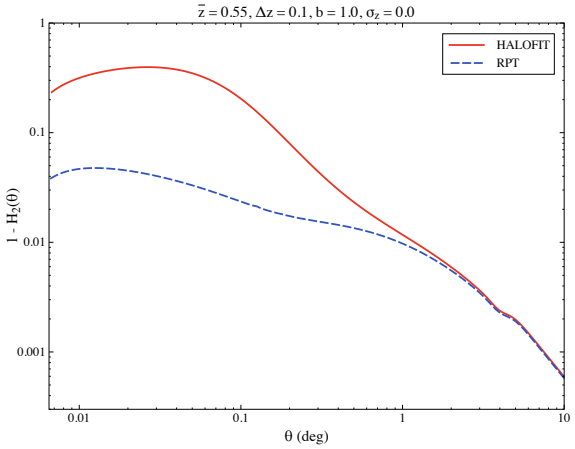

Figura 6.11: $\Delta H_2(\theta)$ en función de θ para dos prescripciones distintas de las no linealidades. Dado que $H_2(\theta)$ depende de una cantidad integral, contiene información sobre escalas pequeñas. Por tanto es importante describir los efectos no lineales de manera correcta. La línea roja continua corresponde a la predicción usando `HALOFIT` y describe correctamente nuestras simulaciones. La predicción usando únicamente el amortiguamiento de la escala de BAO (línea discontinua azul) da valores más altos de homogeneidad a escalas pequeñas aunque esta desviación se corrige a escalas angulares grandes.

	E2		E3	
Bin limits	$\theta_H >$	$r_H >$	$\theta_H >$	$r_H >$
$0{,}2 - 0{,}3$	6,1	75	7,5	93
$0{,}3 - 0{,}4$	5,6	94	7,8	131
$0{,}4 - 0{,}5$	5,5	11	7,1	149
$0{,}5 - 0{,}6$	5,0	126	6,3	158
$0{,}6 - 0{,}7$	4,9	140	6,0	174
$0{,}7 - 0{,}8$	4,7	151	5,6	182
$0{,}8 - 0{,}9$	4,7	169	5,4	192
$0{,}9 - 1{,}0$	4,8	185	5,3	206
$1{,}0 - 1{,}2$	4,2	180	4,8	207

Cuadro 6.1: Límite inferior en la escala de homogeneidad calculada para nueva capas de corrimiento al rojo en cien realizacioes lognormal. La escala angular de homogeneidad se da en grados y la escala comóvil en Mpc/h.

Como se ha señalado anteriormente, el Principio Cosmológico sostiene que el Universo a grandes escalas es homogéneo. Sin embargo, no hay ningún tipo de prescripción para saber cuándo se alcanza dicha homogeneidad. En esta tesis se proponen dos prescripciones:

1. Una posibilidad es definir la escala de homogeneidad como aquella escala en la que la diferencia entre la medida de $H_2(\theta)$ (o cualquier observable que caracterice el nivel de fractalidad de la muestra) y su valor homogéneo ($H_2(\theta) = 1$) sea menor que la incertidumbre de la medida. El problema es que la incertidumbre de la medida va a depender de las características concretas del cartografiado.

2. Otra posibilidad es definir la escala de homogeneidad como aquella en la que la dimensión fractal se diferencia en cierto porcentaje, arbitrariamente asignado, del valor homogéneo. Por ejemplo, un 1 %. La ventaja de esta prescripción es que es independiente del cartografiado, la desventaja, es la arbitrariedad de dicho valor.

En este trabajo se ha seguido la primera prescripción. Consideramos homogeneidad cuando:

$$\Delta H_2(\theta) \leq q\sigma_{H_2}(\theta) \tag{6.23}$$

donde hemos escogido $q = 1$ para el estimador E2 y $q = 2$ para el estimador E3, ya que el primero tiene errores mucho más grandes al considerar menos galaxias. Para probar el método hemos utilizado simulaciones lognormal con parámetros basados en las observaciones de Planck 2013 [39] y $1{,}2 \times 10^8$ galaxias distribuidas en un octante del cielo. Se le añade una distorsión Gaussiana en el corrimiento al rojo para simular un cartografiado fotométrico con $\sigma_z = 0{,}03(1 + z)$.

A partir de los estimadores E2 y E3, usando 100 realizaciones lognormal, se estima el límite inferior de la escala de homogeneidad siguiendo la prescripción citada anteriormente. El error se estima a partir de la desviación estándar de la medida de las 100 realizaciones. Posteriormente se estima la escala tridimensional de homogeneidad r_H como

$$r_H(z) = (1 + z)d_A\theta_H(z) \tag{6.24}$$

Siendo d_A la distancia por diámetro angular a corrimiento al rojo z. Los resultados para las distintas capas de corrimiento al rojo se pueden encontrar en la tabla 6.1 y se pueden observar en la figura 6.12.

En este trabajo también estudiamos en las simulaciones el comportamiento de las matrices de covarianza, en el que se observan mayores correlaciones para el estimador E2 que para el E3, y el efecto de proyección para ambos estimadores en las simulaciones. También se estudia la máxima escala angular a la que se puede estimar $H_2(\theta)$ para cartografiados de 500, 1000, 3000 y 5000 grados cuadrados.

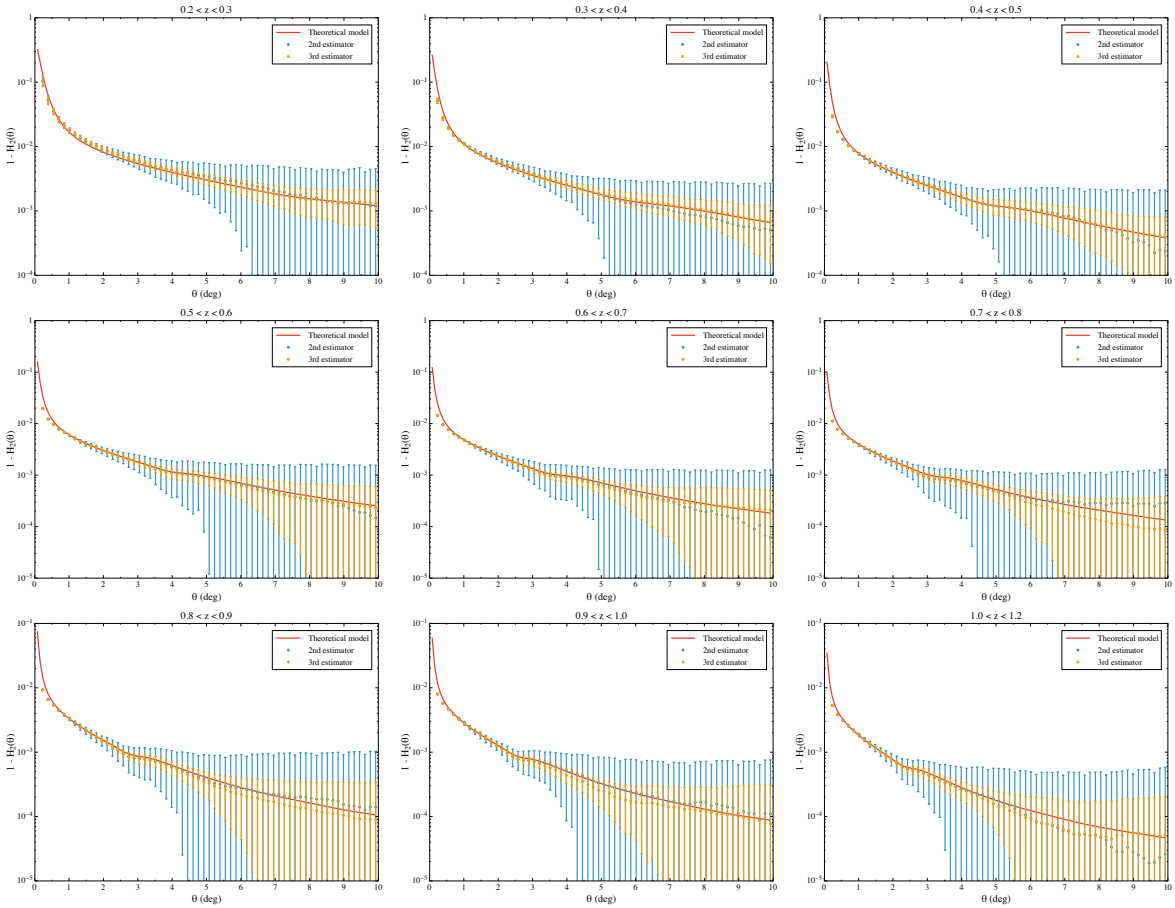

Figura 6.12: $\Delta H_2(\theta)$ en función de θ calculado para 100 realizaciones lognormal para las 9 capas de corrimiento al rojo de la tabla 6.1. Los puntos azules con barras de error corresponden a la media y desviación estándar de los 100 catálogos para el estimador E2, mientras que los puntos amarillos corresponden al estimador E3. La línea roja muestra la predicción teórica.

Por último, se prueba la robustez del método para verificar que es capaz de distinguir un modelo fractal en 3 dimensiones de un modelo homogéneo usando únicamente información angular. Para ello, se usa un modelo de Rayleigh-Levy y un modelo β. Ambos están descritos en el capítulo 3. Exploramos estos modelos para diversos valores de α y de la dimensión fractal D. Los resultados de estas medidas se observan en las figuras 6.13 y 6.14. Observamos que los modelos de Rayleigh-Levy son fácilmente distinguibles de un modelo ΛCDM, mientras que los modelos β sólo son distinguibles para ciertos valores de D. En concreto, con un cartografiado de 5000 grados cuadrados podemos distinguir modelos de hasta $D = 2{,}95$. Por encima de este umbral no los distinguimos de un modelo ΛCDM homogéneo.

Además de estos modelos fractales, también realizamos una prueba en una simulación de un modelo LTB. Estos modelos ponen al observador en el centro de una infradensidad. La distribución es no homogénea en tres dimensiones pero su proyección aparece homogénea. Este es el principal motivo por el que no se puede distinguir con el método presentado de un modelo ΛCDM. En conclusión, se ha presentado un método para estudiar la transición hacia la homogeneidad en cartografiados fotométricos. Esta técnica es una extensión de la metodología usual para realizar estudios de fractalidad. Este método es no sesgado puesto que no asume ningún

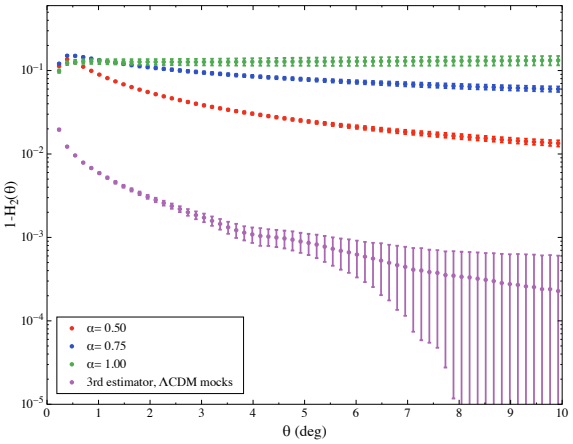

Figura 6.13: $\Delta H_2(\theta)$ en función de θ para tres conjuntos de vuelos 2D de Rayleigh-Levy con $\alpha = 1{,}0$ (verde), $\alpha = 0{,}75$ (azul) y $\alpha = 0{,}5$ (rojo), junto con el resultado de los catálogos lognormal (morado). Podemos distinguir estos modelos de un modelo ΛCDM.

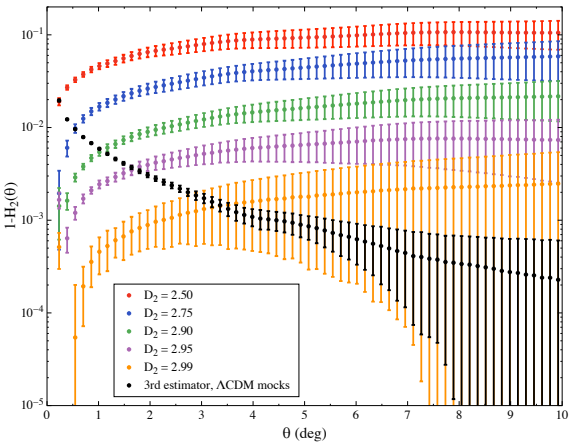

Figura 6.14: $\Delta H_2(\theta)$ en función de θ para un modelo β en la capa $0{,}5 < z < 0{,}6$ para diferentes valores de D_2 desde 2.5 (arriba) hasta 2.99 (abajo), junto con la predicción para ΛCDM obtenida de los catálogos lognormal (negro). Podemos distinguir modelos no-fractales de homogéneos para valores de $D \lesssim 2{,}95$.

tipo de cosmología fiducial. Además permite su uso en la nueva generación de experimentos fotométricos como DES o LSST. En un cartografiado como DES, nos permite distinguir modelos con dimensión fractal D de hasta 2.95.

6.4. Medida de la escala de BAO angular

Como se ha mencionado anteriormente, la escala de BAO es una de las pruebas más importantes para la determinación de la naturaleza de la energía oscura. Dentro del proyecto DES es una de las pruebas más importantes. Para predecir la precisión de la medida en DES, la colaboración fue provista de dos simulaciones cuyos parámetros cosmológicos eran desconocidos. Tras la medida de los mismos, los creadores de la simulación los harían públicos. En el contexto de este ejercicio, se presenta en este trabajo la medida de la escala angular BAO en estas simulaciones utilizando el método presentado en [73].

Las simulaciones consisten en 1.36 $\times 10^9$ galaxias distribuidas en dos octantes del cielo y disponen de varios estimadores de su corrimiento al rojo fotométrico. En nuestro caso, escogimos el código `ArborZ` ya que provee de una distribución de probabilidad (PDF) de corrimiento al rojo para cada galaxia. Después de ciertas medidas de la calidad de la simulación, que incluyen histogramas de magnitud, color, corrimiento al rojo, mapas, etc., se procedió a cortar el catálogo de forma similar a la que se realiza en los datos. Se exige una detección a 10σ de nivel de confianza y se aplica la llamada máscara de DES. Esta máscara, en el caso de la simulación, no es más que un mapa que señala las zonas del cielo observadas.

Una de las partes más importantes para este tipo de análisis es la selección de capas de corrimiento al rojo. Para ello, lo que se hizo fue acumular las distintas PDFs de galaxias y ver la distribución para distintos anchos de dichas capas. Una vez observadas estas distribuciones se eligieron las capas óptimas, que resultaron ser: [0.2, 0.4], [0.4, 0.55], [0.55, 0:7], [0.7, 0.85], [0.85, 1], [1, 1.2], [1.2, 1.4] y [1.4, 1.6]. Además, dada la naturaleza probabilística de estas medidas de corrimiento al rojo, hay diferentes maneras de acumular estas probabilidades: la primera de ellas consiste en acumular la PDF completa de cada galaxia en la capa a la que corresponda el máximo de probabilidad. La segunda forma consiste en acumular la PDF de una galaxia en todas las capas pero, que en cada capa, la PDF, esté normalizada a la integral en dicha capa de su distribución. Si las probabilidades están bien calculadas, los resultados serán consistentes. Este es el caso que nos ocupa tal y como se puede apreciar en la figura 6.15.

Para la medida de la función de correlación angular nos centraremos en estas capas de corrimiento al rojo. Además, usaremos el método de pesado por la PDF para el cálculo de las mismas. Este procedimiento es novedoso y además tiene ciertas ventajas, como minimizar el error sistemático debido a la incertidumbre en el corrimiento al rojo fotométrico. Por otra parte, se utiliza un código basado en unidades gráficas de cálculo o tarjetas gráficas (GPU) para calcular las mismas [99]. La ventaja de este paradigma de computación es el gran nivel de paralelismo que, para este tipo de cálculo, resulta en aceleraciones del orden de un factor 60. Los errores en la función de correlación se estiman usando la expresión teórica de la ecuación 2.48. A estas medidas de la función de correlación se les aplica el denominado método PLG [73], que consiste en la parametrización de la función de correlación angular en una ley de potencias más una Gaussiana. Los resultados de estas medidas se pueden observar en la figura 6.16 y 6.17. La significancia de las medidas se representa en la figura 6.18.
Una vez que se realizan las medidas de θ_{FIT}, se procede a la corrección de las mismas debido al efecto de proyección, tal y como se indica en [73], para obtener la escala de BAO angular representada en la figura 6.19. Una vez obtenida dicha escala, se puede constreñir la cosmología subyacente haciendo una minimización de una función χ^2 en el espacio multiparamétrico que se desee. En nuestro caso, optamos por usar una cadena de Markov Montecarlo (MCMC) integrada en el *software* cosmoSIS. Este mismo se está desarrollando en el seno de las grandes colaboraciones cosmológicas, como DES y LSST. En este programa, se calcula la posición teórica de la escala angular de oscilaciones acústicas de bariones para distintas combinaciones de valores de los parámetros cosmológicos y, posteriormente, se calcula la probabilidad de ajuste del mismo. Finalmente,

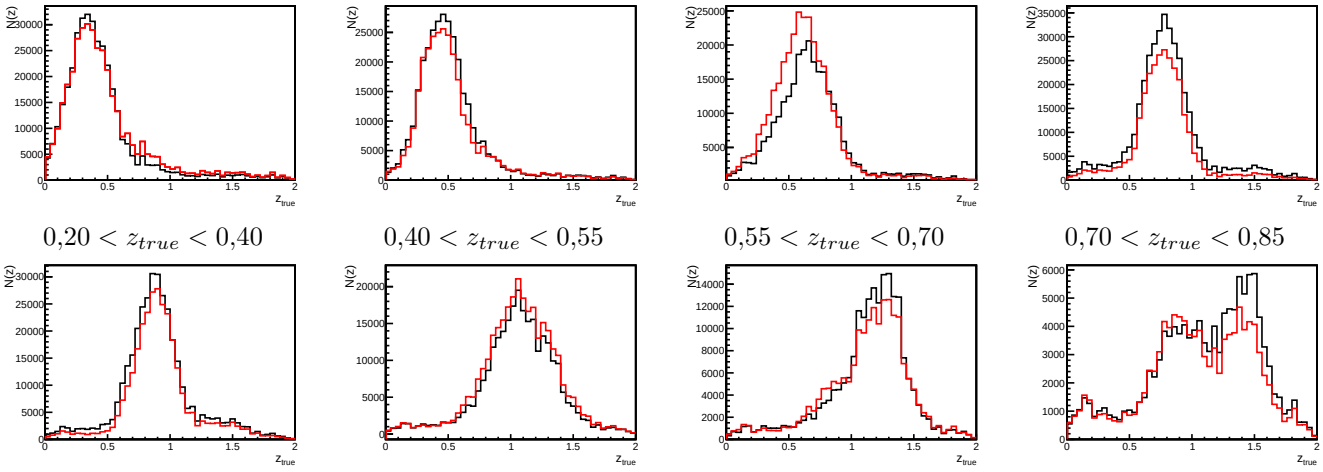

Figura 6.15: Funciones de selección de ArborZ pesando las galaxias por la integral de su PDF (negro) o usando su corrimiento al rojo real para acumular la PDF completa en dicha capa. Los resultados son equivalentes y esto demuestra el buen comportamiento del código.

mediante una MCMC se obtiene una muestra significativa del espacio de parámetros y el valor de máxima probabilidad (se maximiza la función de verosimilitud). Los resultados de la marginalización sobre el espacio multiparamétrico se muestran en la figura 6.20 para Aardvark y 6.21 para Buzzard. En el caso de Aardvark, se desveló posteriormente el valor de los parámetros cosmológicos de entrada y se recuperan a 1σ de nivel de confianza. Se trata de una cosmología ΛCDM plana con valores $\Omega_m = 0{,}23$, $\Omega_\Lambda = 0{,}77$, $h_0 = 0{,}72$, $\sigma_8 = 0{,}82$, $\Omega_b = 0{,}042$.

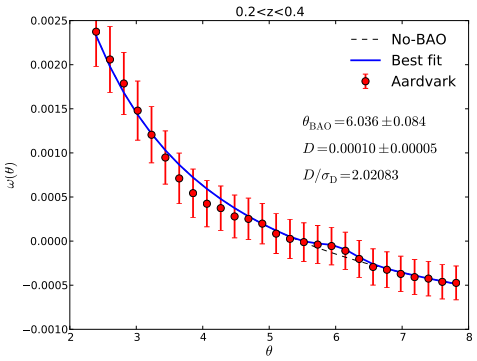

$0{,}20 < z < 0{,}40$

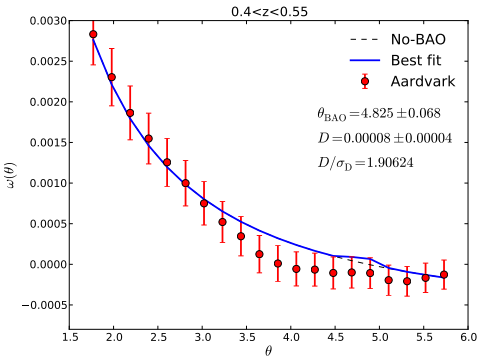

$0{,}40 < z < 0{,}55$

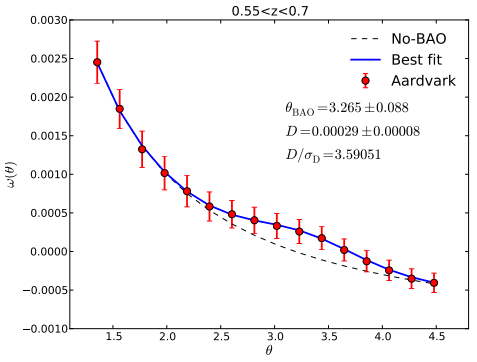

$0{,}55 < z < 0{,}70$

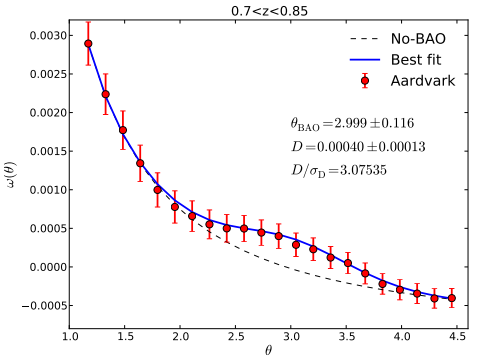

$0{,}70 < z < 0{,}85$

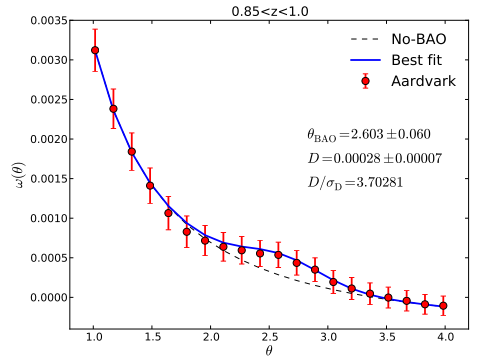

$0{,}85 < z < 1{,}00$

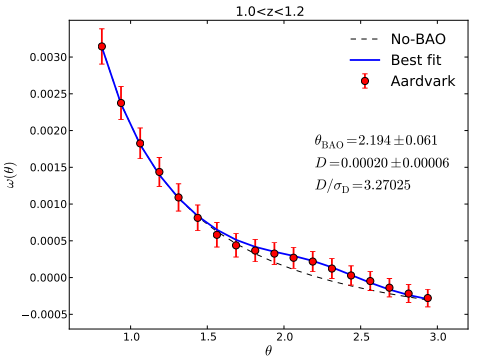

$1{,}00 < z < 1{,}20$

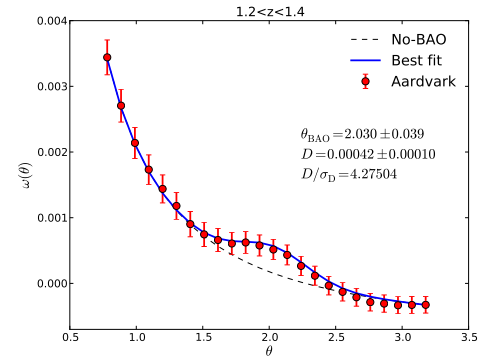

$1{,}20 < z < 1{,}40$

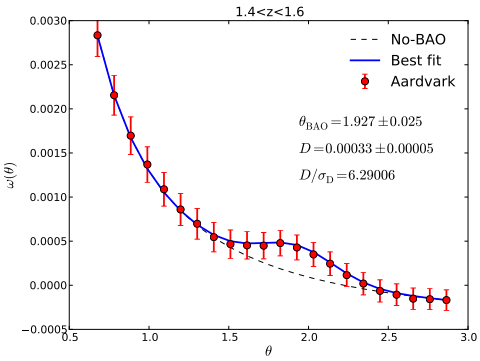

$1{,}40 < z < 1{,}60$

Figura 6.16: Ajustes a la función de correlación angular, usando el método PLG, en la simulación Aardvark para 3×10^8 galaxias en 5000 grados cuadrados pesando cada galaxia por su PDF de ArborZ.

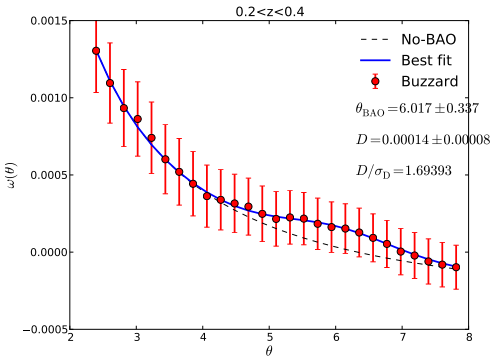

$0{,}20 < z < 0{,}40$

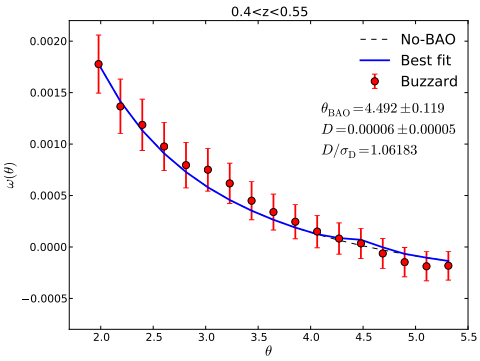

$0{,}40 < z < 0{,}55$

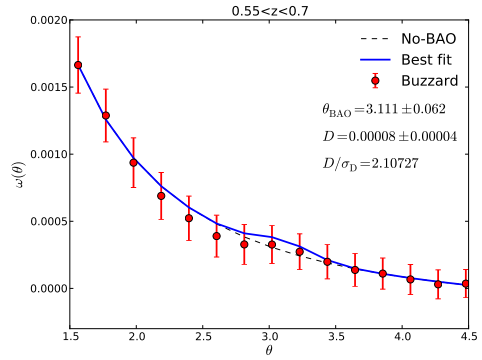

$0{,}55 < z < 0{,}70$

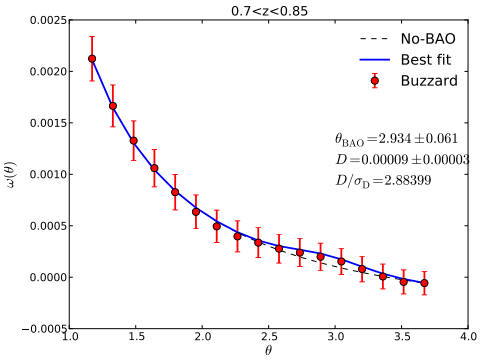

$0{,}70 < z < 0{,}85$

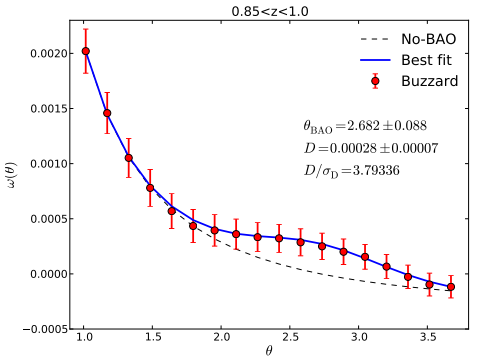

$0{,}85 < z < 1{,}00$

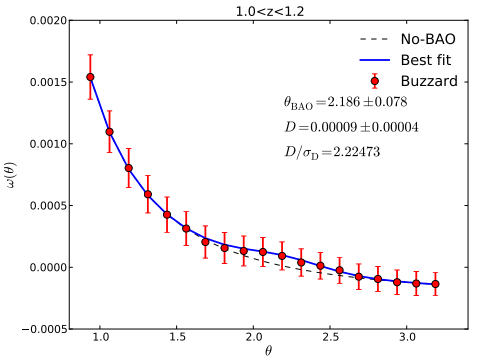

$1{,}00 < z < 1{,}20$

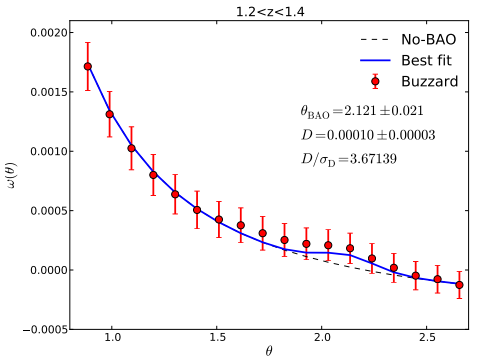

$1{,}20 < z < 1{,}40$

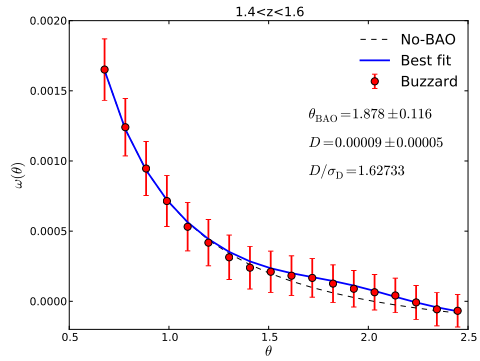

$1{,}40 < z < 1{,}60$

Figura 6.17: Ajustes a la función de correlación angular, usando el método PLG, en la simulación Buzzard para 3×10^8 galaxias en 5000 grados cuadrados pesando cada galaxia por su PDF de ArborZ.

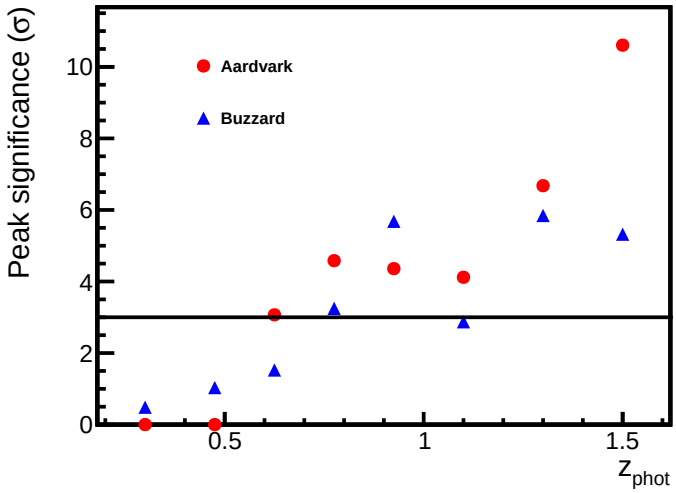

Figura 6.18: Significancia de la medida de la señal de BAO angular en cada capa de corrimiento al rojo.

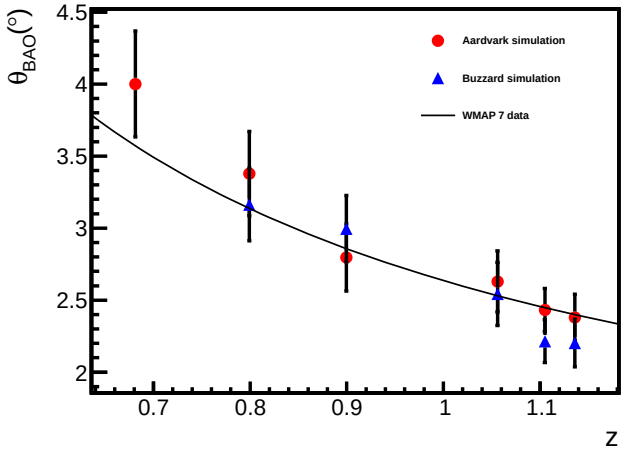

Figura 6.19: Escala BAO medida en las simulaciones Aardvark y Buzzard usando el método PLG.

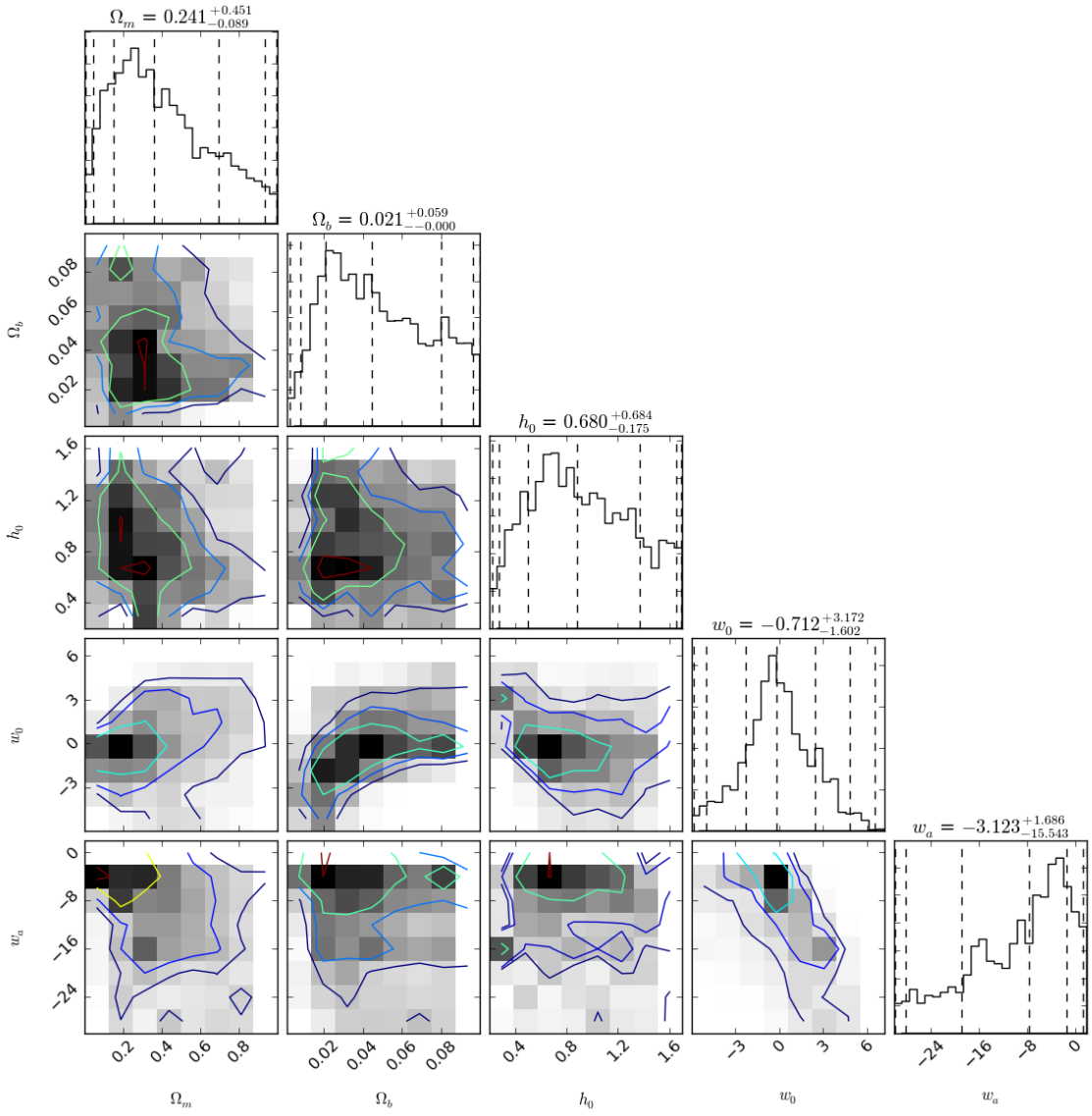

Figura 6.20: Medidas cosmológicas para Aardvark. Se recupera la cosmología plana ΛCDM con $\Omega_m = 0{,}23$, $h = 0{,}72$, $\Omega_b = 0{,}042$.

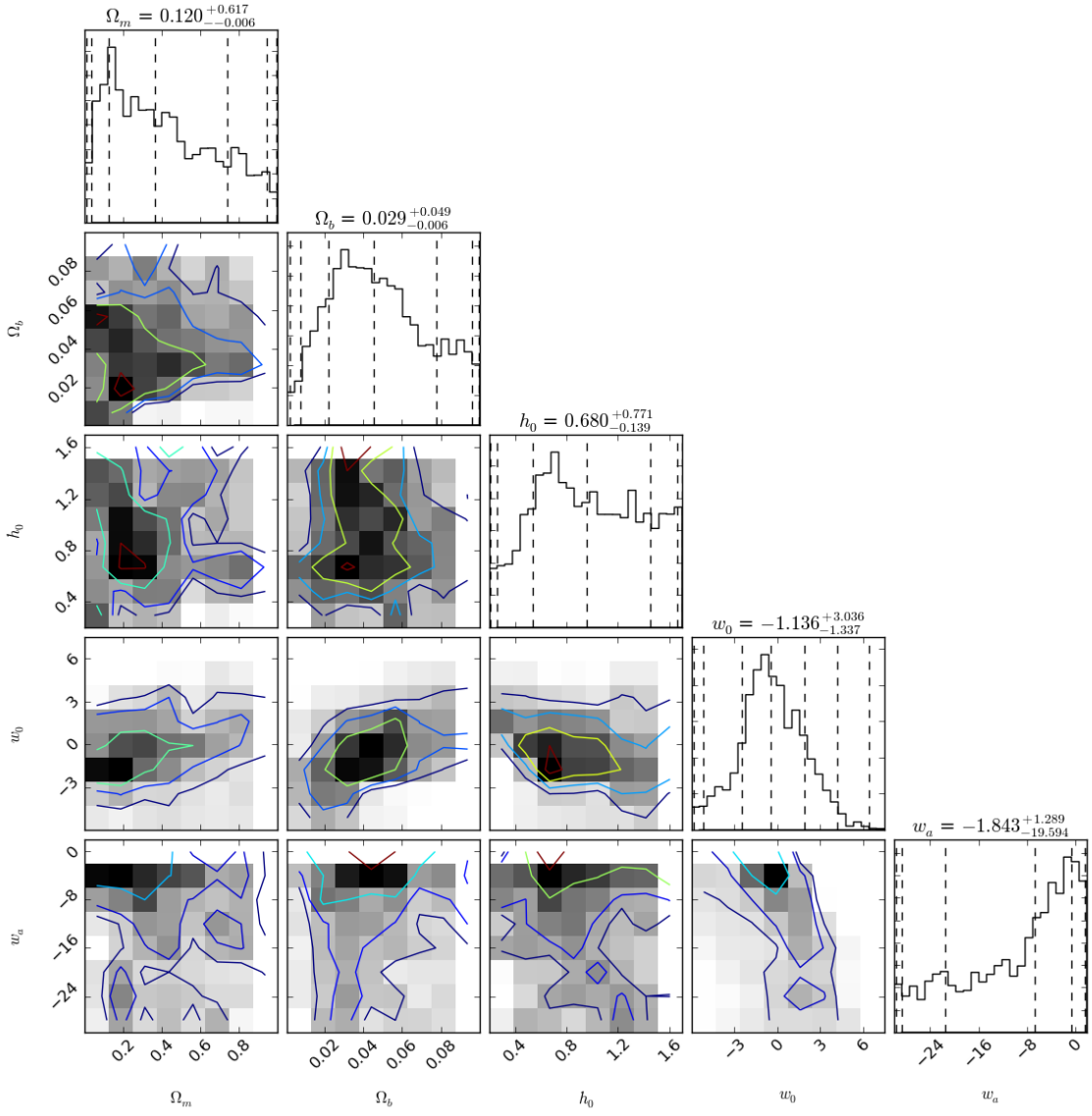

Figura 6.21: Cosmología de la simulación Buzzard. Sólo sabemos que responde a un modelo wCDM.

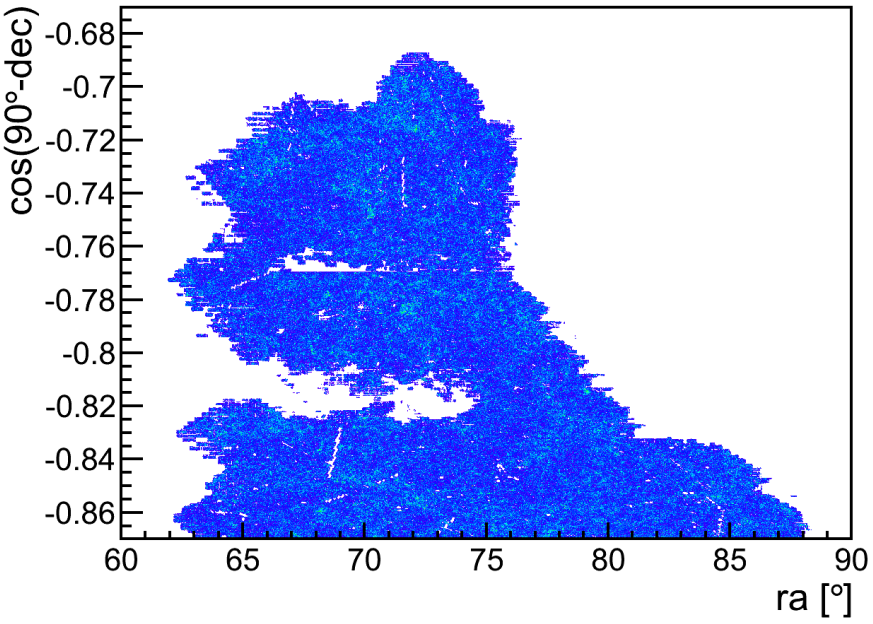

Figura 6.22: Región del cielo utilizada para la medida de la función de correlación a baja escala en la simulación Aardvark.

6.5. Medida cosmológica a partir de la función de correlación a baja escala

En este trabajo, se utiliza por primera vez un ajuste completo a la función de correlación angular a partir de su modelo teórico para un cartografiado fotométrico. En primer lugar, probamos este método en la simulación Aardvark en condiciones similares a las de los datos de verificación de DES, es decir, se usan 135 grados cuadrados con la geometría que se muestra en la figura 6.22. En esta región, se mide la función de correlación angular. Para este caso, se usa una distribución Gaussiana de corrimiento al rojo en cada capa, dividiéndose la muestra en 5 capas: [0.2, 0.4], [0.4,0.6], [0.6, 0.8], [0.8, 1.0], [1.0, 1.2]. En primer lugar, lo que se hace es la medida del *bias* galáctico. Para ello, se fijan los parámetros cosmológicos al valor fiducial en la simulación. Posteriormente, se calculan las predicciones teóricas de la función de correlación en las capas de corrimiento al rojo anteriormente mencionadas, y se usa un espectro de potencias no lineal a partir de `HALOFIT`. Finalmente, se varía el parámetro del *bias* usando RSD, y se obtienen los valores de mejor ajuste que se muestran en la tabla 6.2. Las medidas y ajustes de la función de correlación se muestran en la figura 6.23. La evolución con el corrimiento al rojo que se tiene en esta simulación se muestra en la figura 6.24. Además de extraer el *bias*, se puede obtener información

z	b	Δb	χ^2/ndof	p-value
0.2 - 0.4	1.08	0.06	0.11	0.99
0.4 - 0.6	0.95	0.08	1.02	0.41
0.6 - 0.8	1.10	0.09	0.95	0.47
0.8 - 1.0	1.33	0.03	0.88	0.60
1.0 - 1.2	1.74	0.04	0.56	0.90

Cuadro 6.2: Resultados de los ajustes de *bias* galáctico para la simulación Aardvark.

de otros parámetros cosmológicos. En nuestro caso, vamos a estar interesados en w y Ω_m ya que son dos de los

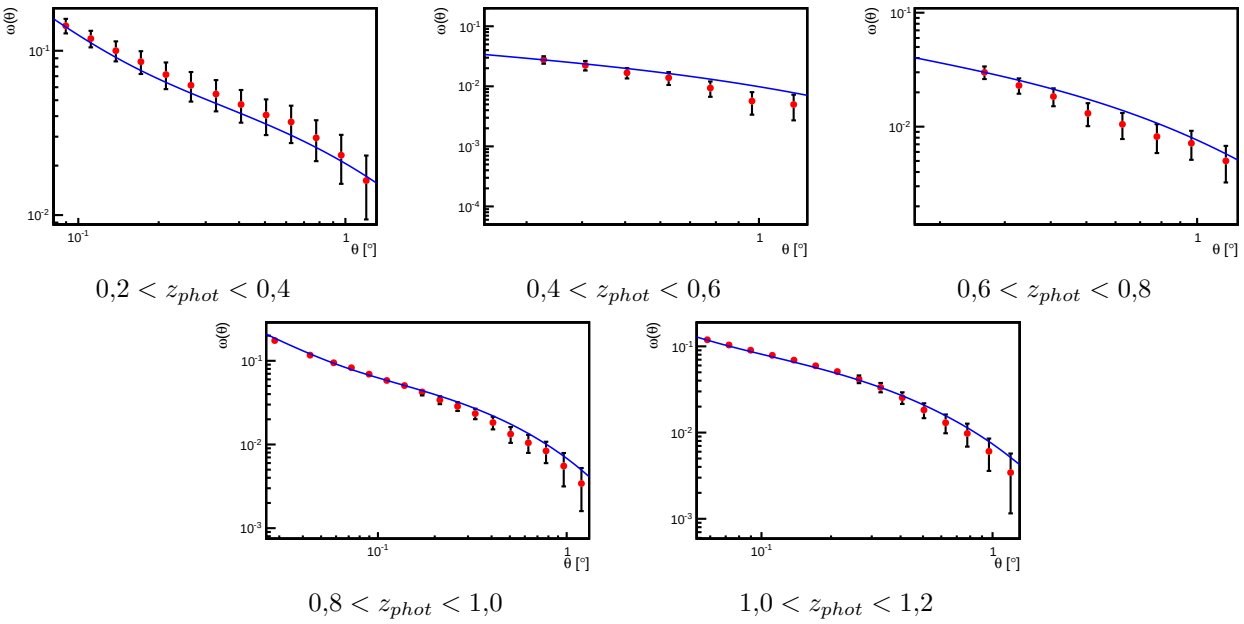

Figura 6.23: Valores de mejor ajuste de *bias* para Aardvark en la región de verificación de DES. Las predicciones teóricas se han obtenido incluyendo RSD en aproximación plano-paralela a partir de un espectro de potencias no lineal de `HALOFIT`.

que más afectan la forma de la función de correlación angular. Para ello, fijamos el resto de parámetros a sus valores fiduciales y el *bias* galáctico a los valores que hemos obtenido anteriormente. Efectivamente, esto puede producir un sesgo de las medidas, sin embargo, los valores del *bias* no afectan tanto a la forma de la función de correlación como a su amplitud y, además, están referidos al valor de σ_8 que hemos fijado para su obtención. Por otra parte, siempre que los parámetros cosmológicos sean cercanos a la cosmología que se va a medir, los valores del *bias* no van a cambiar de manera abrupta y, por otra parte, existen métodos para obtener el *bias* de forma independiente. Por tanto, esta suposición no es tan fuerte como en un principio puede parecer. Las constricciones que encontremos con este método serán en cualquier caso optimistas, puesto que se trata del caso más favorable de medida.

Una vez fijados todos los parámetros, hacemos un recorrido en una red bidimensional de valores de w y Ω_m y calculamos sus predicciones teóricas usando `HALOFIT` y calculamos el χ^2 para cada una de las predicciones como:

$$\chi^2 = \sum_{i,j}(\omega(\theta_i) - \omega_{TH}(\theta_i)C_{ij}^{-1}(\omega(\theta_j) - \omega_{TH}(\theta_j)) \tag{6.25}$$

Los valores que obtenemos para los parámetros cosmológicos son los que se muestran en la figura 6.25. Se aprecia que se recuperan los valores originales de los parámetros a 1-σ de nivel de confianza. Hemos probado por tanto, la validez del método y, si bien los resultados obtenidos son optimistas, nos dan la idea del poder de constricción de DES.

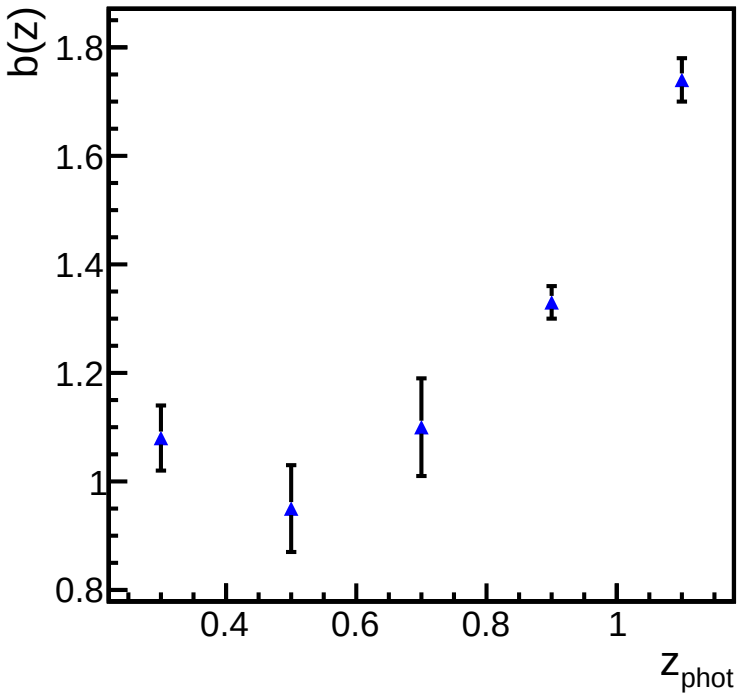

Figura 6.24: Evolución con el corrimiento al rojo del *bias* en la simulación Aardvark.

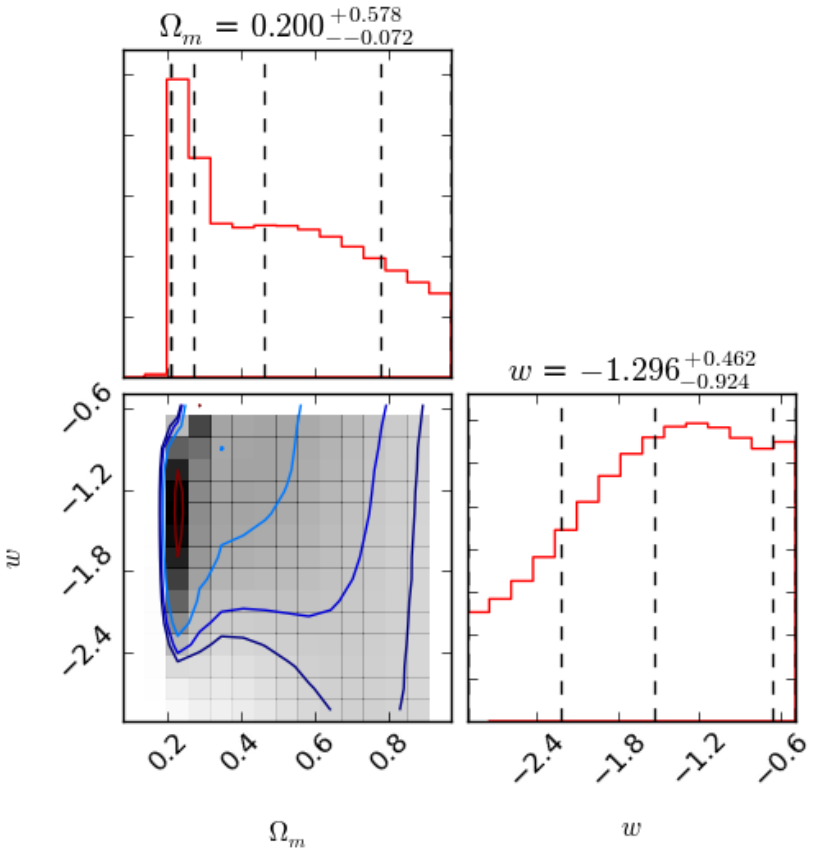

Figura 6.25: Resultados del ajuste a Ω_m y w para la simulación Aardvark fijando los valores de n_s, $b_g(z)$, h_0 y la fracción Ω_b/Ω_m en un modelo wCDM. Se aprecia que se recuperan los valores iniciales de la simulación $\Omega_m = 0{,}23$ y $w = -1$ a 1-σ de nivel de confianza.

6.6. Medida de parámetros cosmológicos en DES

Hasta el momento se han introducido numerosos métodos y técnicas para el estudio de la estructura a gran escala del Universo. Dichos métodos han sido probados en simulaciones. A continuación, presentamos el uso de uno de estos métodos en los datos de verificación del proyecto DES.

El instrumento principal del proyecto DES es la DECam, una cámara de 570 Mpx muy sensible a la radiación infrarroja instalada en el Telescopio Víctor M. Blanco de 4.2 m en Chile. El proyecto, que se encuentra actualmente en su segunda campaña de medidas oficial, tiene como objetivo mejorar la caracterización de la energía oscura mediante cuatro canales diferentes: lentes gravitacionales, cúmulos de galaxias, supernovas y BAO. En total se prevé que, en los 5 años de duración del proyecto, se detecten fotométricamente unos 300 millones de objetos (con una significancia de 10σ) distribuidos en un octante del Cielo Sur. Estos objetos se encuentran a distancias de hasta $z = 2$. El corrimiento al rojo se mide usando filtros anchos en las bandas g, r, i, z, Y.

Los datos disponibles en la actualidad son los correspondientes al área de verificación de DES. Estos cubren aproximadamente unos 200 grados cuadrados, y solapan con varios cartografiados espectroscópicos que se usan para calibrar los algoritmos que calculan el corrimiento al rojo. Además, también solapa, en gran medida, con el experimento SPT que mide la radiación de fondo de microondas y el efecto Sunyaev-Zel'dovich. De estos datos seleccionamos el área contigua más grande. Este campo se llama SPT-E. A dicho campo, se le aplican distintos cortes para asegurar la completitud y pureza de la muestra. Se exige que los objetos cumplan mag_i <22.5 y se seleccionan aquellas zonas del campo cuya magnitud límite sea mayor que 22.5. Este corte asegura que la densidad media no va a variar debido a la diferencia de profundidad en la observación. También se eliminan los objetos con fotometría dudosa y aquellas zonas cuyo calibrado es complicado debido a la alta densidad estelar. En concreto, para nuestro estudio se eliminan todas las regiones cercanas a la Gran Nube de Magallanes.

Una vez hechos estos cortes, el área resultante es de algo menos de 135 grados cuadrados. Lo que se hace posteriormente es seleccionar objetos en 5 capas de corrimiento al rojo. La selección de estos objetos, se hace acorde al corrimiento al rojo calculado según el algoritmo implementado en el tratamiento automático de datos de DES, llamado DESDM. Seleccionaremos objetos en los siguientes rangos de corrimiento al rojo: [0.2, 0.4], [0.4, 0.6], [0.6, 0.8], [0.8, 1.0], [1.0, 1.2]. A partir de los datos de calibración, obtenemos las distribuciones reales de corrimiento al rojo en cada capa de corrimiento al rojo fotométrico. Estas distribuciones $\phi(z)$ serán utilizadas para realizar las predicciones teóricas de las funciones de correlación correspondientes. Un problema común en los cartografiados de galaxias es la confusión entre estrellas y galaxias. Generalmente, se usan variables de observación asociadas a la forma del objeto para distinguir entre estrellas y galaxias. En este caso, para los datos de verificación de DES, se usa una variable llamada MODEST_CLASS que se basa en las variables SPREAD_MODEL y SPREAD_MODEL_ERROR. Estas variables nos dan la idea de cómo de extensa es la fuente luminosa en un CCD, y tienen en cuenta la distorsión que causa el cielo y los diferentes instrumentos ópticos del experimento. Básicamente, SPREAD_MODEL usa información morfológica a nivel de píxel y compara el perfil de cada objeto con la PSF local y SPREAD_MODEL_ERROR es su error. En cualquier caso, no existe ningún método de separación que asegure un 100 % de eficiencia. Se tiene cierta contaminación estelar que hemos estudiado en este trabajo y que se presentará más adelante. En el catálogo seleccionamos los objetos que tienen MODEST_CLASS=1.

Tras realizar todos estos cortes y seleccionar las capas de corrimiento al rojo anteriormente citadas, nos quedan unos 3.5 millones de objetos. Es la denominada *benchmark sample* o muestra de referencia de DES.

En este trabajo se evalúan los distintos efectos sistemáticos que afectan la medida de la función de correlación angular en DES. En primer lugar, evaluamos la fracción de contaminación estelar utilizando la correlación cruzada entre estrellas definidas por MODEST_CLASS, y galaxias también definidas por este separador. El resultado se sitúa entre el 2 y el 4 %. La contaminación estelar puede inducir un exceso de potencia a escalas

grandes. Este exceso se corrige usando el método presentado en [111]. También se corrigen los errores sistemáticos debidos a diversos efectos de observación, como son la presencia de polvo (extinción), la cantidad de aire por encima del horizonte, el brillo del cielo y la visibilidad de la noche de observación. Esta última está relacionada con la magnitud de las turbulencias atmosféricas de la noche en cuestión. La colaboración DES dispone de distintos mapas que cuantifican estos efectos. Lo que se hace es calcular el grado de correlación entre estos mapas y los mapas de galaxias, y así, corregir su contribución usando la misma técnica que usamos para las estrellas [111]. El sistemático que más afecta a la medida, en nuestro caso, es la visibilidad ya que, debido al cambio en la misma, es más sencillo confundir estrellas con galaxias y tener una contaminación de una población desconocida mayor.

No sólo tenemos estos efectos sistemáticos, también se debe tener en cuenta el error sistemático debido a la incertidumbre en la función de selección $\phi(z)$. Este error proviene de que se dispone de una muestra de calibrado finita. Dicho efecto lo evaluamos ajustando $\phi(z)$ a la suma de dos Gaussianas y variando las anchuras de estas Gaussianas en los intervalos de confianza del ajuste. Una vez hemos variado las mismas, usamos estas distribuciones para calcular las predicciones teóricas. La diferencia relativa entre las curvas teóricas nos da el error. El resultado es que el sistemático es inferior al 4 %. Otro efecto sistemático que se evalúa es el efecto de cortar la Gran Nube de Magallanes. Para asegurarnos que este corte es robusto y la contaminación estelar debida a la misma es baja, realizamos otros cortes en declinación. Una vez realizados estos cortes comparamos la medida de la función de correlación y calculamos su diferencia relativa. El resultado se muestra estable y la diferencia relativa es inferior al 7 %, mucho menor que el error estadístico. En cualquier caso, estos errores sistemáticos se añaden en cuadratura al error estadístico para realizar una estimación conservadora de los mismos.

Teniendo en cuenta estos efectos, medimos la función de correlación angular de galaxias usando el mismo código basado en GPU que utilizamos para las simulaciones. Se calcula la misma entre 0.05 y 2 grados en 10 puntos. Las matrices de covarianza se estiman usando la aproximación Gaussiana de la expresión 2.48. Una vez hecha la medida, procedemos a la corrección de los diversos efectos sistemáticos. Posteriormente, se calculan las predicciones teóricas para 3 modelos distintos: un modelo ΛCDM con los parámetros de Planck 2013 [39], un modelo con Ω_m =0.5, Ω_Λ =0.5 y un modelo de Einstein-de Sitter y se ajusta el *bias*. Se obtienen los resultados que se muestran en la figura 6.26 Además, en la figura 6.27 observamos la medida y evolución del *bias* para los parámetros basados en Planck. Es notable que la evolución es bastante similar a la que tiene la simulación. Las pequeñas diferencias residen en que los cortes en magnitud que se aplican son diferentes en cada caso.

Por otra parte, procedemos de la misma forma que lo hicimos en simulaciones. A partir de estas medidas de la función de correlación, obtenemos ciertos valores para los parámetros cosmológicos. Se usa exactamente el mismo método que para la simulación Aardvark y se fijan todos los parámetros, incluyendo el *bias*, a los valores para Planck [15] y se dejan libres Ω_m y w. Se calculan las predicciones teóricas para una red bidimensional en dicho espacio de parámetros y se obtiene la probabilidad de cada valor de los mismos. Finalmente, los resultados que se tienen son los de la figura 6.28. Vemos que los valores que medimos son compatibles con Planck [15] a 1σ. La sensibilidad a dichos parámetros no es muy elevada y además la estimación del error en los mismos es optimista, sin embargo, hemos introducido un nuevo método de medida y hemos comprobado la consistencia de los datos de verificación del experimento, viendo que tienen una gran calidad.

Por último, en este trabajo, se introduce una nueva técnica para medir la función de correlación de galaxias en cartografiados fotométricos con profundidad variable. Dependiendo de las condiciones de observación, algunos parches del cielo son observados durante un tiempo mayor que otros. Esto hace que aparezcan variaciones de densidad en el catálogo de galaxias que no son debidos a los procesos físicos entre galaxias, sino a las condiciones de observación. Estos efectos se suelen solucionar realizando cortes en magnitud y magnitud límite para asegurar una muestra completa. El coste de esta aproximación es que el área y número de galaxias se ve reducido, en algunos casos, muy considerablemente. La solución para el cómputo de la función de correlación consiste en crear un catálogo aleatorio que tenga los mismos efectos observacionales. Es decir, que dependiendo de la profundidad de observación de dicha zona tenga una densidad media mayor o menor. Para ello, lo que se

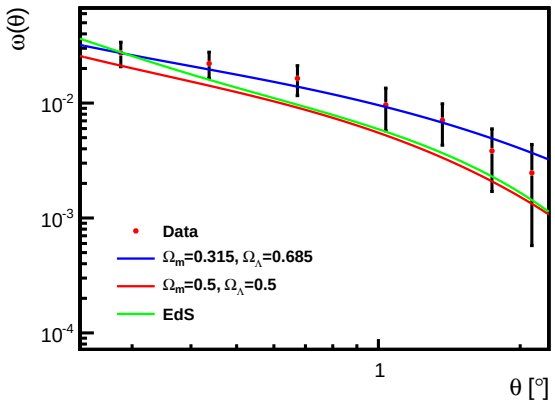

$0.2 < z < 0.4$

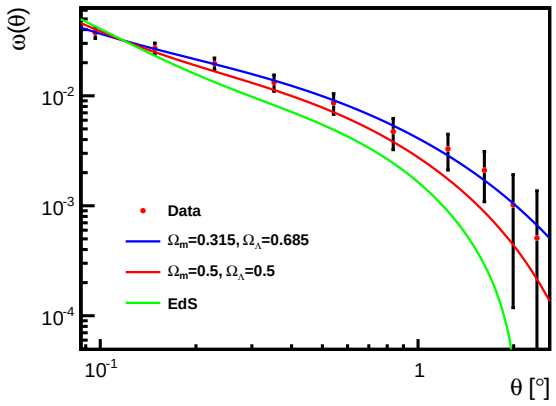

$0.4 < z < 0.6$

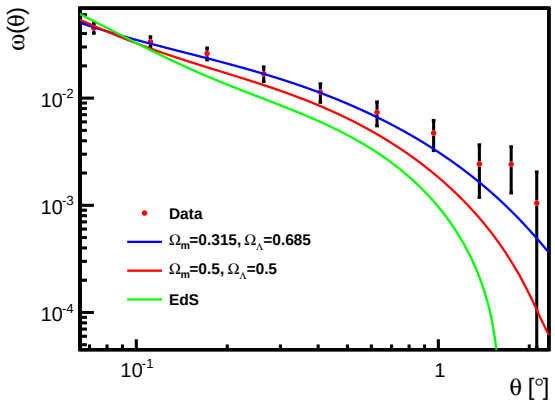

$0.6 < z < 0.8$

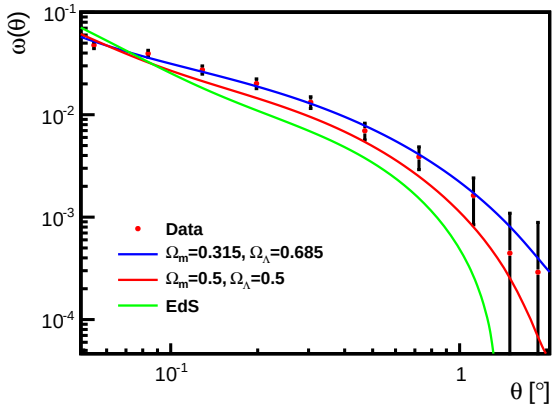

$0.8 < z < 1.0$

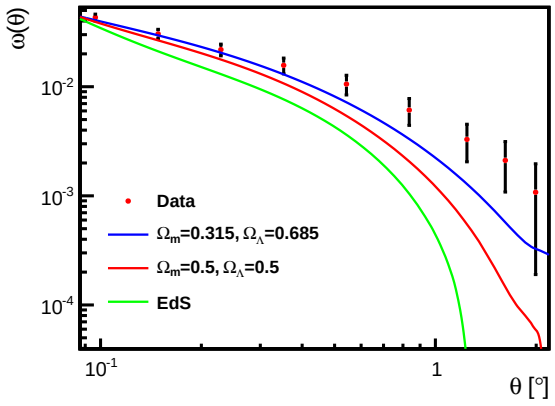

$1.0 < z < 1.2$

Figura 6.26: Comparativa de los ajustes para un modelo ΛCDM basado en Planck (azul), un modelo ΛCDM con $\Omega_m = \Omega_\Lambda$ =0.5 y un modelo de Einstein-de Sitter (EdS). Se puede ver que el modelo EdS no ajusta bien para todo el rango de corrimiento al rojo y lo mismo pasa con el modelo de $\Omega_m = \Omega_\Lambda$ =0.5. Esto nos da la idea de la sensisbilidad de la función de correlación como prueba cosmológica.

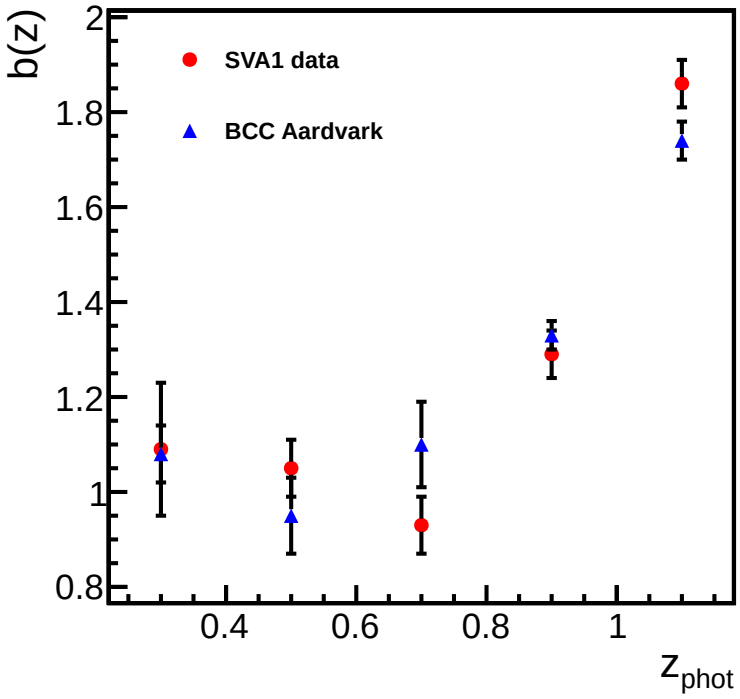

Figura 6.27: Evolución del *bias* galáctico con el corrimiento al rojo en la muestra de referencia (puntos rojos). También se muestran los resultados de la simulación Aardvark (triángulos azules). Ambas medidas tienen una evolución similar.

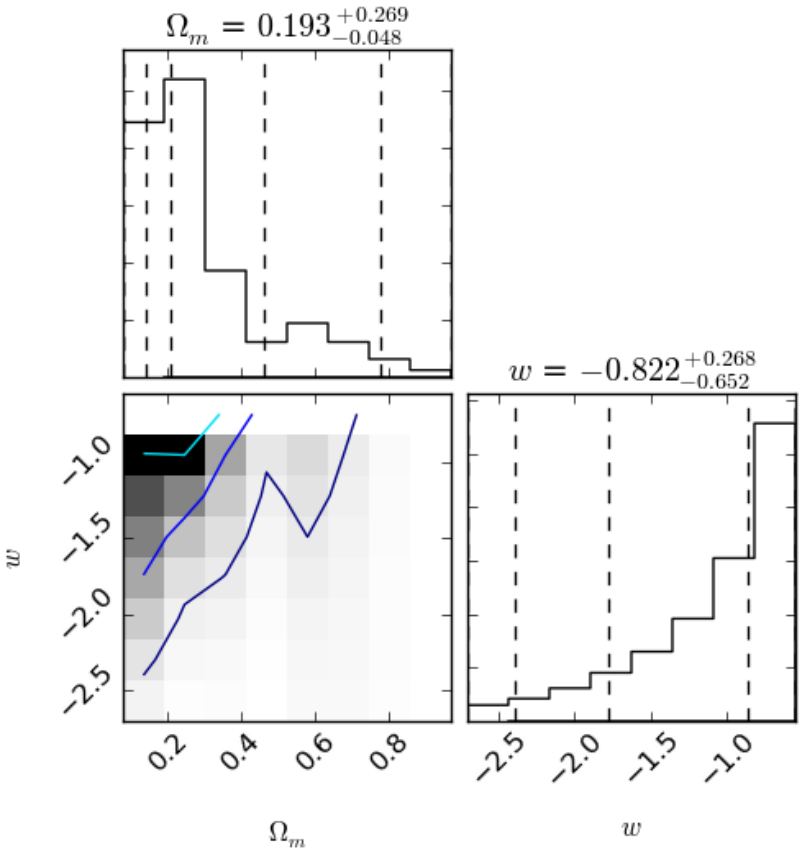

Figura 6.28: Contornos mostrando 1σ, 2σ y 3σ de nivel de confianza para los parámetros w y Ω en la muestra de referencia de DES. Se han fijado previamente los valores de los demás parámetros a los valores arrojados por Planck. El hecho de recuperar los valores de Planck a 1σ nos demuestra que la muestra es robusta.

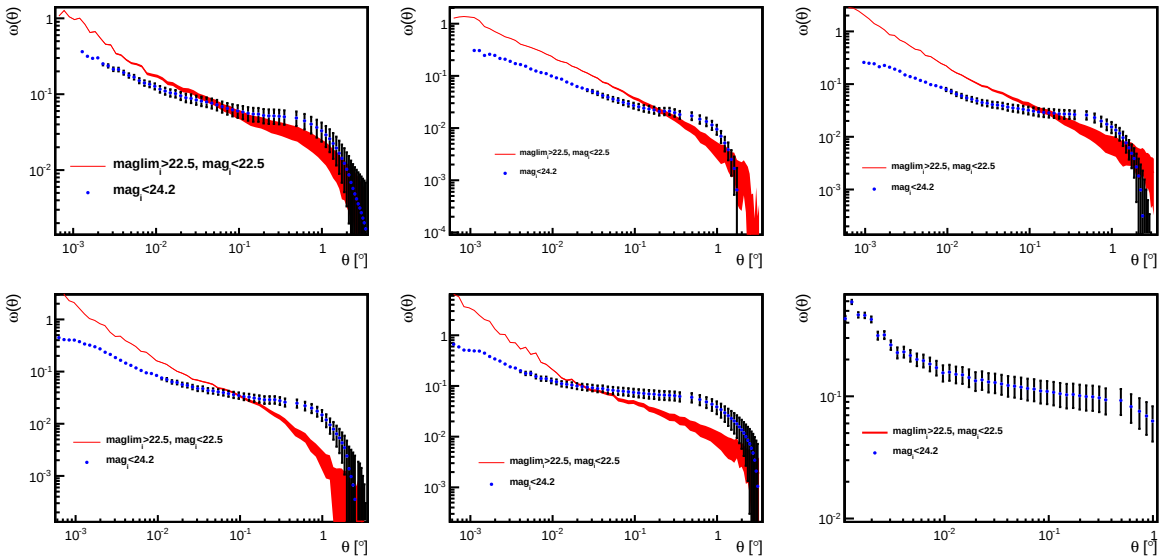

Figura 6.29: Comparativa de las funciones de correlación considerando un campo aleatorio uniforme y no uniforme para las distintas muestras que se presentan en este trabajo. Como estamos tratando diferentes muestras los resultados deben ser diferentes. Sin embargo, estos resultados parecen tener un comportamiento razonable. Se muestran todas las capas de corrimiento al rojo en orden creciente desde $0{,}2 < z < 0{,}4$ (arriba a la izquierda) a $1{,}2 < z < 1{,}4$ (abajo a la derecha).

hace es usar los histogramas de magnitud para capas anchas de magnitud límite, es decir, agrupamos todas las galaxias que se encuentran en una zona con cierto rango de magnitud límite y construimos el histograma de magnitudes. Una vez hecho esto, se normalizan todos los histogramas al área de cielo que cubren los distintos parches que lo componen. Finalmente, se refieren todos los histogramas al de mayor profundidad. Es decir, se le da un peso a cada zona del cielo que es el cociente entre la integral de su histograma de magnitud y el más profundo.

Este método lo aplicamos a la muestra de verificación de DES en el campo SPTE. El resultado es que se tiene un número de objetos mucho mayor, unos 13 millones de objetos, y un área ligeramente más grande, unos 150 grados cuadrados. En estas condiciones, medimos la función de correlación angular obteniendo los resultados de la figura 6.29. En esta figura comparamos los resultados de esta última muestra con los de la muestra de referencia de DES. Como conclusión, hemos introducido un nuevo método de medida de la función de correlación de galaxias usando un esquema de pesos para compensar efectos observacionales que será de gran utilidad en los cartografiados fotométricos venideros.

6.7. Conclusiones

En esta tesis hemos estudiado la energía oscura a través de la estructura a gran escala del Universo. Hemos desarrollado diversas técnicas como son la medida de la escala radial de BAO usando únicamente cantidades observables, la medida de fractalidad en cartografiados fotométricos y la medida de los parámetros cosmológicos usando la función de correlación angular de galaxias. Hemos probado estos métodos en simulaciones y, finalmente, hemos realizado la medida en la muestra de verificación de DES. Estas medidas están en acuerdo con ΛCDM [15] y, además, confirman la robustez y calidad de los datos de DES. Se ha desarrollado un método para medir la función de correlación usando cartografiados de profundidad variable que será vital para las campañas de medida venideras en los distintos cartografiados fotométricos, y hemos puesto a prueba la sensibilidad de la escala angular de BAO en un cartografiado de galaxias como DES.

Este trabajo es fruto de la participación activa en las colaboraciones DES y PAU. Además, ha dado lugar a tres publicaciones en revistas de reconocido prestigio internacional. Las técnicas presentadas en este trabajo podrán ser usadas en futuros cartografiados de galaxias como PAU, DESI, EUCLID, LSST, WFIRST o eBOSS y son extensibles a otras pruebas como los mapas de intensidad de 21 cm. Estos experimentos junto con DES arrojarán luz sobre la esquiva naturaleza de la energía oscura.

Fits to ΛCDM and EdS

z_{phot}	$\chi^2/ndof$	p	b	Δb
0.2 - 0.4	0.591	0.764	1.27	0.18
0.4 - 0.6	1.560	0.112	1.03	0.08
0.6 - 0.8	2.664	0.003	0.86	0.07
0.8 - 1.0	5.200	1.13×10^{-7}	1.14	0.06
1.0 - 1.2	0.659	0.747	1.86	0.05

Table 3: Results of the fit to EdS ΛCDM model leaving the galaxy bias b as a free parameter.

z_{phot}	$\chi^2/ndof$	p	b	Δb
0.2 - 0.4	0.222	0.981	1.20	0.11
0.4 - 0.6	0.525	0.874	1.08	0.06
0.6 - 0.8	1.280	0.234	0.93	0.06
0.8 - 1.0	2.163	0.017	1.27	0.07
1.0 - 1.2	0.659	0.747	1.86	0.07

Table 4: Results of the fit to $\Omega_m = 0.5$ and $\Omega_\Lambda = 0.5$ ΛCDM model leaving the galaxy bias b as a free parameter.

Bibliography

[1] G. Lemaître. "Un Univers homogène de masse constante et de rayon croissant rendant compte de la vitesse radiale des nébuleuses extra-galactiques." In: *Annales de la Societe Scietifique de Bruxelles* 47 (1927), pp. 49–59.

[2] Edwin Hubble. "A relation between distance and radial velocity among extra-galactic nebulae." In: *Proceedings of the National Academy of Sciences* 15.3 (1929), pp. 168–173. DOI: 10.1073/pnas.15.3.168. eprint: http://www.pnas.org/content/15/3/168.full.pdf+html. URL: http://www.pnas.org/content/15/3/168.short.

[3] R. A. Alpher, H. Bethe, and G. Gamow. "The Origin of Chemical Elements." In: *Physical Review* 73 (Apr. 1948), pp. 803–804. DOI: 10.1103/PhysRev.73.803.

[4] A. A. Penzias and R. W. Wilson. "A Measurement of Excess Antenna Temperature at 4080 Mc/s." In: *Astrophysical Journal* 142 (July 1965), pp. 419–421. DOI: 10.1086/148307.

[5] Steven Weinberg. *Gravitation and Cosmology: Principles and Applications of the General Theory of Relativity*. Wiley & Sons, 1972. ISBN: 0-471-92567-5.

[6] A. Einstein. "Die Grundlage der allgemeinen Relativitätstheorie." In: *Annalen der Physik* 354.7 (1916), pp. 769–822. ISSN: 1521-3889. DOI: 10.1002/andp.19163540702. URL: http://dx.doi.org/10.1002/andp.19163540702.

[7] A. Einstein. "Zur Elektrodynamik bewegter Körper." In: *Annalen der Physik* 322.10 (1905), pp. 891–921. ISSN: 1521-3889. DOI: 10.1002/andp.19053221004. URL: http://dx.doi.org/10.1002/andp.19053221004.

[8] Sean Carroll. *Spacetime and Geometry: An Introduction to General Relativity*. Benjamin Cummings, 2003. ISBN: 0805387323. URL: http://www.amazon.com/Spacetime-Geometry-Introduction-General-Relativity/dp/0805387323.

[9] S. Tsujikawa. "Introductory review of cosmic inflation." In: *ArXiv High Energy Physics - Phenomenology e-prints* (Apr. 2003). eprint: hep-ph/0304257.

[10] A.A. Starobinsky. "A new type of isotropic cosmological models without singularity." In: *Physics Letters B* 91.1 (1980), pp. 99 –102. ISSN: 0370-2693. DOI: http://dx.doi.org/10.1016/0370-2693(80)90670-X. URL: http://www.sciencedirect.com/science/article/pii/037026938090670X.

[11] Alan H. Guth. "Inflationary universe: A possible solution to the horizon and flatness problems." In: *Phys. Rev. D* 23 (2 1981), pp. 347–356. DOI: 10.1103/PhysRevD.23.347. URL: http://link.aps.org/doi/10.1103/PhysRevD.23.347.

[12] A. D. Linde. "A new inflationary universe scenario: A possible solution of the horizon, flatness, homogeneity, isotropy and primordial monopole problems." In: *Physics Letters B* 108 (Feb. 1982), pp. 389–393. DOI: 10.1016/0370-2693(82)91219-9.

[13] A. Albrecht and P. J. Steinhardt. "Cosmology for grand unified theories with radiatively induced symmetry breaking." In: *Physical Review Letters* 48 (Apr. 1982), pp. 1220–1223. DOI: 10.1103/PhysRevLett.48.1220.

[14] A. Linde. *Lecture notes of the 100th Les Houches Summer School: Post-Planck Cosmology*. Oxford University Press, 2014.

[15] Planck Collaboration et al. "Planck 2015 results. XIII. Cosmological parameters." In: *Astronomy and Astrophysics* (Jan. 2015).

[16] Andrew R. Liddle and David H. Lyth. *Cosmological inflation and large-scale structure*. English. Cambridge: Cambridge University Press, 1999. DOI: 10.1017/CBO9781139175180.

[17] A. Riotto. "Inflation and the Theory of Cosmological Perturbations." In: *ArXiv High Energy Physics - Phenomenology e-prints* (Oct. 2002). eprint: hep-ph/0210162.

[18] A. Linde. "Recent Progress in Inflationary Cosmology." In: *Cosmological Constant and the Evolution of the Universe*. Ed. by K. Sato, T. Suginohara, and N. Sugiyama. 1996, p. 133. eprint: astro-ph/9601004.

[19] G. Hinshaw et al. "Nine-year Wilkinson Microwave Anisotropy Probe (WMAP) Observations: Cosmological Parameter Results." In: *ApJs* 208, 19 (Oct. 2013), p. 19. DOI: 10.1088/0067-0049/208/2/19. arXiv:1212.5226 [astro-ph.CO].

[20] M. Betoule et al. "Improved cosmological constraints from a joint analysis of the SDSS-II and SNLS supernova samples." In: *Astron.Astrophys.* (2014). arXiv:1401.4064 [astro-ph.CO].

[21] P. J. Steinhardt. "Cosmological Perturbations:" in: *Modern Physics Letters A* 19 (2004), pp. 967–982. DOI: 10.1142/S0217732304014252.

[22] Latham A. Boyle, Paul J. Steinhardt, and Neil Turok. "Inflationary Predictions for Scalar and Tensor Fluctuations Reconsidered." In: *Phys. Rev. Lett.* 96 (11 2006), p. 111301. DOI: 10.1103/PhysRevLett.96.111301. URL: http://link.aps.org/doi/10.1103/PhysRevLett.96.111301.

[23] A. Loeb and M. Zaldarriaga. "Measuring the Small-Scale Power Spectrum of Cosmic Density Fluctuations through 21cm Tomography Prior to the Epoch of Structure Formation." In: *Physical Review Letters* 92.21, 211301 (May 2004), p. 211301. DOI: 10.1103/PhysRevLett.92.211301. eprint: astro-ph/0312134.

[24] G. F. Smoot. "COBE observations and results." In: *3K cosmology*. Ed. by L. Maiani, F. Melchiorri, and N. Vittorio. Vol. 476. American Institute of Physics Conference Series. May 1999, pp. 1–10. DOI: 10.1063/1.59326. eprint: astro-ph/9902027.

[25] R. A. Alpher and R. C. Herman. "On the Relative Abundance of the Elements." In: *Physical Review* 74 (Dec. 1948), pp. 1737–1742. DOI: 10.1103/PhysRev.74.1737.

[26] G. Gamow. "The Origin of Elements and the Separation of Galaxies." In: *Phys. Rev.* 74 (4 1948), pp. 505–506. DOI: 10.1103/PhysRev.74.505.2. URL: http://link.aps.org/doi/10.1103/PhysRev.74.505.2.

[27] Y. B. Zeldovich. "A hypothesis, unifying the structure and the entropy of the Universe." In: *MNRAS* 160 (1972), 1P.

[28] E. R. Harrison. "Fluctuations at the Threshold of Classical Cosmology." In: *PRD* 1 (May 1970), pp. 2726–2730. DOI: 10.1103/PhysRevD.1.2726.

[29] P. J. E. Peebles and J. T. Yu. "Primeval Adiabatic Perturbation in an Expanding Universe." In: *ApJ* 162 (Dec. 1970), p. 815. DOI: 10.1086/150713.

[30] J. Silk. "Cosmic Black-Body Radiation and Galaxy Formation." In: *ApJ* 151 (Feb. 1968), p. 459. DOI: 10.1086/149449.

[31] R. A. Sunyaev and Y. B. Zeldovich. "The Observations of Relic Radiation as a Test of the Nature of X-Ray Radiation from the Clusters of Galaxies." In: *Comments on Astrophysics and Space Physics* 4 (Nov. 1972), p. 173.

[32] R. K. Sachs and A. M. Wolfe. "Perturbations of a Cosmological Model and Angular Variations of the Microwave Background." In: *Astrophysical Journal* 147 (Jan. 1967), p. 73. DOI: 10.1086/148982.

[33] C. Bertulani. *Nuclei in the Cosmos*. World Scientific, 2013.

[34] J. Guy et al. "The Supernova Legacy Survey 3-year sample: Type Ia supernovae photometric distances and cosmological constraints." In: *AAP* 523, A7 (Nov. 2010), A7. DOI: 10.1051/0004-6361/201014468. arXiv:1010.4743 [astro-ph.CO].

[35] M. Sako et al. "The Data Release of the Sloan Digital Sky Survey-II Supernova Survey." In: *ArXiv e-prints* (Jan. 2014). arXiv:1401.3317 [astro-ph.CO].

[36] F. Beutler et al. "The 6dF Galaxy Survey: baryon acoustic oscillations and the local Hubble constant." In: *MNRAS* 416 (Oct. 2011), pp. 3017–3032. DOI: 10.1111/j.1365-2966.2011.19250.x. arXiv:1106.3366 [astro-ph.CO].

[37] N. Padmanabhan et al. "A 2 per cent distance to z = 0.35 by reconstructing baryon acoustic oscillations - I. Methods and application to the Sloan Digital Sky Survey." In: *MNRAS* 427 (Dec. 2012), pp. 2132–2145. DOI: 10.1111/j.1365-2966.2012.21888.x. arXiv:1202.0090 [astro-ph.CO].

[38] L. Anderson et al. "The clustering of galaxies in the SDSS-III Baryon Oscillation Spectroscopic Survey: baryon acoustic oscillations in the Data Release 9 spectroscopic galaxy sample." In: *MNRAS* 427 (Dec. 2012), pp. 3435–3467. DOI: 10.1111/j.1365-2966.2012.22066.x. arXiv:1203.6594 [astro-ph.CO].

[39] Planck collaboration et al. "Planck 2013 results. XV. CMB power spectra and likelihood." In: *ArXiv e-prints* (Mar. 2013). arXiv:1303.5075 [astro-ph.CO].

[40] F. Zwicky. "Die Rotverschiebung von extragalaktischen Nebeln." In: *Helvetica Physica Acta* 6 (1933), pp. 110–127.

[41] V. C. Rubin, W. K. J. Ford, and N. . Thonnard. "Rotational properties of 21 SC galaxies with a large range of luminosities and radii, from NGC 4605 /R = 4kpc/ to UGC 2885 /R = 122 kpc/." In: *Astrophysical Journal* 238 (June 1980), pp. 471–487. DOI: 10.1086/158003.

[42] T. S. van Albada, J. N. Bahcall, K. Begeman, and R. Sancisi. "Distribution of dark matter in the spiral galaxy NGC 3198." In: *ApJ* 295 (Aug. 1985), pp. 305–313. DOI: 10.1086/163375.

[43] B. Moore and J. Silk. "Dynamical and observable constraints on RAMBOs: Robust associations of massive baryonic objects." In: *ApJ* 442 (Mar. 1995), pp. L5–L8. DOI: 10.1086/187802. eprint: astro-ph/9407023.

[44] CDMS Collaboration et al. "Silicon Detector Dark Matter Results from the Final Exposure of CDMS II." In: *ArXiv e-prints* (Apr. 2013). arXiv:1304.4279 [hep-ex].

[45] ArDM Collaboration et al. "The ArDM experiment." In: *ArXiv e-prints* (June 2010). arXiv:1006.5335 [physics.ins-det].

[46] Kfir Blum, Boaz Katz, and Eli Waxman. "AMS-02 Results Support the Secondary Origin of Cosmic Ray Positrons." In: *Phys. Rev. Lett.* 111 (21 2013), p. 211101. DOI: 10.1103/PhysRevLett.111.211101. URL: http://link.aps.org/doi/10.1103/PhysRevLett.111.211101.

[47] W. B. Atwood et al. "The Large Area Telescope on the Fermi Gamma-Ray Space Telescope Mission." In: *ApJ* 697 (June 2009), pp. 1071–1102. DOI: 10.1088/0004-637X/697/2/1071. arXiv:0902.1089 [astro-ph.IM].

[48] O. Adriani et al. "Measurement of Boron and Carbon Fluxes in Cosmic Rays with the PAMELA Experiment." In: *ApJ* 791, 93 (Aug. 2014), p. 93. DOI: 10.1088/0004-637X/791/2/93. arXiv:1407.1657 [astro-ph.HE].

[49] CMS Collaboration. "Search for dark matter, extra dimensions, and unparticles in monojet events in proton-proton collisions at sqrt(s) = 8 TeV." In: *ArXiv e-prints* (Aug. 2014). arXiv:1408.3583 [hep-ex].

[50] A.S. Al-Rawaf and M.O. Taha. "Cosmology of general relativity without energy conservation." In: (1994).

[51] A. Albrecht et al. "Report of the Dark Energy Task Force." In: *ArXiv Astrophysics e-prints* (Sept. 2006). eprint: astro-ph/0609591.

[52] J. A. Frieman, M. S. Turner, and D. Huterer. "Dark Energy and the Accelerating Universe." In: *Annual Review of Astronomy and Astrophysics* 46 (Sept. 2008), pp. 385–432. DOI: 10.1146/annurev.astro.46.060407.145243. arXiv:0803.0982.

[53] W. H. Press and P. Schechter. "Formation of Galaxies and Clusters of Galaxies by Self-Similar Gravitational Condensation." In: *Astrophysical Journal* 187 (Feb. 1974), pp. 425–438. DOI: 10.1086/152650.

[54] A. H. Guth and S.-Y. Pi. "Fluctuations in the new inflationary universe." In: *Physical Review Letters* 49 (Oct. 1982), pp. 1110–1113. DOI: 10.1103/PhysRevLett.49.1110.

[55] R. H. Brandenberger. "Quantum field theory methods and inflationary universe models." In: *Reviews of Modern Physics* 57 (Jan. 1985), pp. 1–60. DOI: 10.1103/RevModPhys.57.1.

[56] P.J.E. Peebles. *The Large-Scale Structure of the Universe*. Princeton University Press, 1980.

[57] J. M. Bardeen, J. R. Bond, N. Kaiser, and A. S. Szalay. "The statistics of peaks of Gaussian random fields." In: *Astrophysical Journal* 304 (May 1986), pp. 15–61. DOI: 10.1086/164143.

[58] D. J. Eisenstein and W. Hu. "Baryonic Features in the Matter Transfer Function." In: *Astrophysical Journal* 496 (Mar. 1998), pp. 605–614. DOI: 10.1086/305424. eprint: astro-ph/9709112.

[59] Antony Lewis, Anthony Challinor, and Anthony Lasenby. "Efficient Computation of CMB anisotropies in closed FRW models." In: *Astrophys. J.* 538 (2000), pp. 473–476. eprint: astro-ph/9911177.

[60] U. Seljak and M. Zaldarriaga. "A Line-of-Sight Integration Approach to Cosmic Microwave Background Anisotropies." In: *Astrophysical Journal* 469 (Oct. 1996), p. 437. DOI: 10.1086/177793. eprint: astro-ph/9603033.

[61] Z. Ma, W. Hu, and D. Huterer. "Effects of Photometric Redshift Uncertainties on Weak-Lensing Tomography." In: *Astrophysical Journal* 636 (Jan. 2006), pp. 21–29. DOI: 10.1086/497068. eprint: astro-ph/0506614.

[62] M. Crocce, A. Cabré, and E. Gaztañaga. "Modelling the angular correlation function and its full covariance in photometric galaxy surveys." In: *MNRAS* 414 (June 2011), pp. 329–349. DOI: 10.1111/j.1365-2966.2011.18393.x. arXiv:1004.4640 [astro-ph.CO].

[63] N. Kaiser. "Clustering in real space and in redshift space." In: *MNRAS* 227 (July 1987), pp. 1–21.

[64] W. J. Percival. "Large Scale Structure Observations." In: *ArXiv e-prints* (Dec. 2013). arXiv:1312.5490 [astro-ph.CO].

[65] S. Dodelson. *Modern Cosmology*. Academic Press. ISBN: 9780122191411. Academic Press, 2003.

[66] L. Samushia et al. "The clustering of galaxies in the SDSS-III Baryon Oscillation Spectroscopic Survey: measuring growth rate and geometry with anisotropic clustering." In: *MNRAS* 439 (Apr. 2014), pp. 3504–3519. DOI: 10.1093/mnras/stu197. arXiv:1312.4899.

[67] M. Crocce and R. Scoccimarro. "Renormalized cosmological perturbation theory." In: *PRD* 73.6, 063519 (Mar. 2006), p. 063519. DOI: 10.1103/PhysRevD.73.063519. eprint: astro-ph/0509418.

[68] M. Crocce and R. Scoccimarro. "Nonlinear evolution of baryon acoustic oscillations." In: *PRD* 77.2, 023533 (Jan. 2008), p. 023533. DOI: 10.1103/PhysRevD.77.023533. arXiv:0704.2783.

[69] R. Takahashi et al. "Revising the Halofit Model for the Nonlinear Matter Power Spectrum." In: *Astrophysical Journal* 761, 152 (Dec. 2012), p. 152. DOI: 10.1088/0004-637X/761/2/152. arXiv:1208.2701 [astro-ph.CO].

[70] D. J. Eisenstein et al. "Detection of the Baryon Acoustic Peak in the Large-Scale Correlation Function of SDSS Luminous Red Galaxies." In: *Astrophysical Journal* 633 (Nov. 2005), pp. 560–574. DOI: 10.1086/466512. eprint: astro-ph/0501171.

[71] W. J. Percival et al. "Measuring the Baryon Acoustic Oscillation scale using the Sloan Digital Sky Survey and 2dF Galaxy Redshift Survey." In: *MNRAS* 381 (Nov. 2007), pp. 1053–1066. DOI: 10.1111/j.1365-2966.2007.12268.x. arXiv:0705.3323.

[72] L. Anderson et al. "The clustering of galaxies in the SDSS-III Baryon Oscillation Spectroscopic Survey: baryon acoustic oscillations in the Data Release 9 spectroscopic galaxy sample." In: *MNRAS* 427 (Dec. 2012), pp. 3435–3467. DOI: 10.1111/j.1365-2966.2012.22066.x. arXiv:1203.6594 [astro-ph.CO].

[73] E. Sánchez et al. "Tracing the sound horizon scale with photometric redshift surveys." In: *MNRAS* 411 (Feb. 2011), pp. 277–288. DOI: 10.1111/j.1365-2966.2010.17679.x. arXiv:1006.3226 [astro-ph.CO].

[74] N. Padmanabhan et al. "The clustering of luminous red galaxies in the Sloan Digital Sky Survey imaging data." In: *MNRAS* 378 (July 2007), pp. 852–872. DOI: 10.1111/j.1365-2966.2007.11593.x. eprint: astro-ph/0605302.

[75] N. G. Busca et al. "Baryon acoustic oscillations in the Lyα forest of BOSS quasars." In: *Astronomy and astrophysics* 552, A96 (Apr. 2013), A96. DOI: 10.1051/0004-6361/201220724. arXiv:1211.2616 [astro-ph.CO].

[76] E. Sánchez et al. "Precise measurement of the radial baryon acoustic oscillation scales in galaxy redshift surveys." In: *MNRAS* 434 (Sept. 2013), pp. 2008–2019. DOI: 10.1093/mnras/stt1146. arXiv:1210.6446 [astro-ph.CO].

[77] P. Fosalba, E. Gaztañaga, F. J. Castander, and M. Manera. "The onion universe: all sky lightcone simulations in spherical shells." In: *MNRAS* 391 (Nov. 2008), pp. 435–446. DOI: 10.1111/j.1365-2966.2008.13910.x. arXiv:0711.1540.

[78] P. Fosalba, M. Crocce, E. Gaztanaga, and F. J. Castander. "The MICE Grand Challenge Lightcone Simulation I: Dark matter clustering." In: *ArXiv e-prints* (Dec. 2013). arXiv:1312.1707 [astro-ph.CO].

[79] M. Crocce et al. "The MICE Grand Challenge Lightcone Simulation II: Halo and Galaxy catalogues." In: *ArXiv e-prints* (Dec. 2013). arXiv:1312.2013 [astro-ph.CO].

[80] M. Levi et al. "The DESI Experiment, a whitepaper for Snowmass 2013." In: *ArXiv e-prints* (Aug. 2013). arXiv:1308.0847 [astro-ph.CO].

[81] J. Amiaux et al. "Euclid mission: building of a reference survey." In: *Society of Photo-Optical Instrumentation Engineers (SPIE) Conference Series*. Vol. 8442. Society of Photo-Optical Instrumentation Engineers (SPIE) Conference Series. Sept. 2012. DOI: 10.1117/12.926513. arXiv:1209.2228 [astro-ph.IM].

[82] S. D. Landy and A. S. Szalay. "Bias and variance of angular correlation functions." In: *Astrophysical Journal* 412 (July 1993), pp. 64–71. DOI: 10.1086/172900.

[83] J. G. Cresswell and W. J. Percival. "Scale-dependent galaxy bias in the Sloan Digital Sky Survey as a function of luminosity and colour." In: *MNRAS* 392 (Jan. 2009), pp. 682–690. DOI: 10.1111/j.1365-2966.2008.14082.x. arXiv:0808.1101.

[84] E. Komatsu et al. "Seven-year Wilkinson Microwave Anisotropy Probe (WMAP) Observations: Cosmological Interpretation." In: *ApJS* 192, 18 (Feb. 2011), p. 18. DOI: 10.1088/0067-0049/192/2/18. arXiv:1001.4538 [astro-ph.CO].

[85] E. Komatsu et al. "Five-Year Wilkinson Microwave Anisotropy Probe Observations: Cosmological Interpretation." In: *Astrophysical Journal Supplement* 180 (Feb. 2009), pp. 330–376. DOI: 10.1088/0067-0049/180/2/330. arXiv:0803.0547.

[86] X. Xu et al. "Measuring D_A and H at z=0.35 from the SDSS DR7 LRGs using baryon acoustic oscillations." In: *MNRAS* 431 (May 2013), pp. 2834–2860. DOI: 10.1093/mnras/stt379. arXiv:1206.6732 [astro-ph.CO].

[87] Ruth Durrer. "What do we really know about Dark Energy?" In: *Phil.Trans.Roy.Soc.Lond.* A369 (2011). Cosmological Tests of General Relativity, pp. 5102–5114. arXiv:1103.5331 [astro-ph].

[88] V. J. Martínez and E. Saar. "Statistics of galaxy clustering." In: *Statistical Challenges in Astronomy*. Ed. by E. D. Feigelson and G. J. Babu. 2003, pp. 143–160.

[89] J. S. Bagla, Jaswant Yadav, and T. R. Seshadri. "Fractal dimensions of a weakly clustered distribution and the scale of homogeneity." In: *Monthly Notices of the Royal Astronomical Society* 390.2 (2008), pp. 829–838. DOI: 10.1111/j.1365-2966.2008.13793.x. eprint: http://mnras.oxfordjournals.org/content/390/2/829.full.pdf+html. URL: http://mnras.oxfordjournals.org/content/390/2/829.abstract.

[90] F. de Simoni et al. "Large-scale analysis of the SDSS-III DR8 photometric luminous galaxies angular correlation function." In: *MNRAS* 435 (Nov. 2013), pp. 3017–3027. DOI: 10.1093/mnras/stt1496. arXiv:1308.0630 [astro-ph.CO].

[91] P. Coles and B. Jones. "A lognormal model for the cosmological mass distribution." In: *MNRAS* 248 (Jan. 1991), pp. 1–13.

[92] M. White, J. L. Tinker, and C. K. McBride. "Mock galaxy catalogues using the quick particle mesh method." In: *MNRAS* 437 (Jan. 2014), pp. 2594–2606. DOI: 10.1093/mnras/stt2071. arXiv:1309.5532 [astro-ph.CO].

[93] R. Durrer et al. "Angular projections of fractal sets." In: *EPL (Europhysics Letters)* 40 (Dec. 1997), pp. 491–496. DOI: 10.1209/epl/i1997-00493-3. eprint: astro-ph/9702116.

[94] A. Nusser and O. Lahav. "The Lyman α forest in a truncated hierarchical structure formation." In: *MNRAS* 313 (Apr. 2000), pp. L39–L42. DOI: 10.1046/j.1365-8711.2000.03441.x. eprint: astro-ph/9910177.

[95] Chris Clarkson. "Establishing homogeneity of the universe in the shadow of dark energy." In: *Comptes Rendus Physique* 13 (2012), pp. 682–718. DOI: 10.1016/j.crhy.2012.04.005. arXiv:1204.5505 [astro-ph.CO].

[96] J. García-Bellido and T. Haugbølle. "The radial BAO scale and cosmic shear, a new observable for inhomogeneous cosmologies." In: *JCAP* 9, 028 (Sept. 2009), p. 28. DOI: 10.1088/1475-7516/2009/09/028. arXiv:0810.4939.

[97] D. Alonso, J. García-Bellido, T. Haugbølle, and J. Vicente. "Large scale structure simulations of inhomogeneous Lemaître-Tolman-Bondi void models." In: *Physical Review Letters D* 82.12, 123530 (Dec. 2010), p. 123530. DOI: 10.1103/PhysRevD.82.123530. arXiv:1010.3453 [astro-ph.CO].

[98] D. W. Gerdes et al. "ArborZ: Photometric Redshifts Using Boosted Decision Trees." In: *Astrophysical Journal* 715 (June 2010), pp. 823–832. DOI: 10.1088/0004-637X/715/2/823. arXiv:0908.4085 [astro-ph.CO].

[99] R. Ponce et al. "Application of GPUs for the Calculation of Two Point Correlation Functions in Cosmology." In: *Astronomical Data Analysis Software and Systems XXI*. Ed. by P. Ballester, D. Egret, and N. P. F. Lorente. Vol. 461. Astronomical Society of the Pacific Conference Series. Sept. 2012, p. 73. arXiv:1204.6630 [astro-ph.IM].

[100] J. Zuntz et al. "CosmoSIS: modular cosmological parameter estimation." In: *ArXiv e-prints* (Sept. 2014). arXiv:1409.3409.

[101] B. Flaugher. "The Dark Energy Survey." In: *International Journal of Modern Physics A* 20 (2005), pp. 3121–3123. DOI: 10.1142/S0217751X05025917.

[102] The Dark Energy Survey Collaboration. "The Dark Energy Survey." In: *ArXiv Astrophysics e-prints* (Oct. 2005). eprint: astro-ph/0510346.

[103] T. Diehl and Dark Energy Survey Collaboration. "The Dark Energy Survey Camera (DECam)." In: *Physics Procedia* 37 (2012), pp. 1332–1340. DOI: 10.1016/j.phpro.2012.02.472.

[104] Adam G. Riess et al. "Observational Evidence from Supernovae for an Accelerating Universe and a Cosmological Constant." In: *The Astronomical Journal* 116.3 (1998), p. 1009. URL: http://stacks.iop.org/1538-3881/116/i=3/a=1009.

[105] C. Sánchez et al. "Photometric redshift analysis in the Dark Energy Survey Science Verification data." In: *ArXiv e-prints* (June 2014). arXiv:1406.4407 [astro-ph.IM].

[106] P. Melchior et al. "Mass and galaxy distributions of four massive galaxy clusters from Dark Energy Survey Science Verification data." In: *ArXiv e-prints* (May 2014). arXiv:1405.4285.

[107] M. Smith et al. "Discovery and Classification of 8 SNe from the Dark Energy Survey." In: *The Astronomer's Telegram* 6515 (Sept. 2014), p. 1.

[108] E. Bertin and S. Arnouts. "SExtractor: Software for source extraction." In: *Astronomy and Astrophysics* 117 (June 1996), pp. 393–404.

[109] H. Oyaizu et al. "A Galaxy Photometric Redshift Catalog for the Sloan Digital Sky Survey Data Release 6." In: *Astrophysical Journal* 674 (Feb. 2008), pp. 768–783. DOI: 10.1086/523666. arXiv:0708.0030.

[110] M. E. C. Swanson, M. Tegmark, A. J. S. Hamilton, and J. C. Hill. "Methods for rapidly processing angular masks of next-generation galaxy surveys." In: *MNRAS* 387 (July 2008), pp. 1391–1402. DOI: 10.1111/j.1365-2966.2008.13296.x. arXiv:0711.4352.

[111] S. Ho et al. "Clustering of Sloan Digital Sky Survey III Photometric Luminous Galaxies: The Measurement, Systematics, and Cosmological Implications." In: *Astrophysical Journal* 761, 14 (Dec. 2012), p. 14. DOI: 10.1088/0004-637X/761/1/14. arXiv:1201.2137 [astro-ph.CO].

[112] D. Alonso et al. "Measuring the transition to homogeneity with photometric redshift surveys." In: *MNRAS* 440 (May 2014), pp. 10–23. DOI: 10.1093/mnras/stu255. arXiv:1312.0861 [astro-ph.CO].

[113] D. Alonso et al. "Homogeneity and isotropy in the 2MASS Photometric Redshift catalogue." In: *ArXiv e-prints* (Dec. 2014). arXiv:1412.5151.